

UNDERGRADUATE RESEARCH AT THE SWANSON SCHOOL OF ENGINEERING

2017

INGENiUM





Highlighting Undergraduate Research
at the University of Pittsburgh Swanson School of Engineering

Spring 2017

The University of Pittsburgh is an affirmative action, equal opportunity institution.
Published in cooperation with the Department of Communications Services. DCS110241

Please note that neither *Ingenium* nor the Swanson School of Engineering retains any copyright of the original work produced in this issue. However, the Swanson School does retain the right to nonexclusive use in print and electronic formats of all papers as published in *Ingenium*.

University of Pittsburgh
Swanson School of Engineering
Benedum Hall
3700 O'Hara Street, Pittsburgh, PA 15261 USA

INGENIUM

UNDERGRADUATE RESEARCH AT THE SWANSON SCHOOL OF ENGINEERING

Table of Contents

4 A Message from the Associate Dean for Research

5 A Message from the Co-Editors-in-Chief

6 Editorial Board Members

Articles

7 Self-supported Monolith Formation of Silica Nanoparticles with Hollow Nickel Core

Patrick Asinger, Sharlee Mahoney, Yahui Yang, and Götz Veser

Department of Chemical and Petroleum Engineering

12 Verifying Normality of Ocular Tissue Through Development of a Semi-automated Optic Nerve Axon Counting Method

Katelyn Axman, Addison Kaufmann, Sundaresh Ram, and Jonathan P. Vande Geest

Department of Bioengineering

16 Design of an Active Trunk Control and Balancing System to Reduce Fatigue During Walking with an Exoskeleton

Joshua Barron, Dr. Nitin Sharma

Neuromuscular Control and Robotics Laboratory, Swanson School of Engineering, Department of Mechanical Engineering and Materials Science

21 Electromyography Based Control for Lower Limb Assistive Therapy

Amanda Boyer and Dr. Nitin Sharma

Neuromuscular Control and Robotics Laboratory, Swanson School of Engineering, Department of Mechanical Engineering and Materials Science

26 Atomic Scale Topology Optimization Based on Finite Element Methods

Clement N. Ekaputra, Albert C. To, PhD

Department of Mechanical Engineering and Materials Science

31 Investigating Antibacterial Properties of Plasma Cleaned Polypropylene

Anthony Galante and Paul Leu

Laboratory of Advanced Materials in Pittsburgh, Department of Industrial Engineering

35 Cell Recoverability After Exposure to Complex Engineered Nanoparticles

Julie Hartz, Sharlee Mahoney, Thomas Richardson, Ipsita Banerjee, and Götz Veser

Department of Chemical and Petroleum Engineering

40 Modeling Amplifiers in Linear Stages

Gabriel Hinding, Tim Ryan, and Dr. Jeffrey Vipperman

Department of Mechanical Engineering and Materials Science

44 Additive Manufacturing of Magnetocaloric Material for High-Efficiency Cooling

Katerina Kimes , Erica Stevens , Jakub Toman , Amir Mostafaei, and Markus Chmielus

Department of Mechanical Engineering and Materials Science

51 Addressing Infusion Pump Management Challenges Through Implementation of a PAR Stock System

Kelly R. Larson and Dr. Bryan A. Norman

Department of Industrial Engineering

56 Chemical Looping for Syngas Production

Isaac Mastalski, Amey More, and Götz Veser

Department of Chemical and Petroleum Engineering

61 Anti-tumor (M1) Macrophages Secrete Cytokines that Prime Breast Cancer Cells for Apoptosis

Maya McKeown; Jennifer Guerriero, PhD; and Anthony Letai, MD, PhD

Department of Bioengineering, Swanson School of Engineering

66 Creating an Osteochondral Bioreactor for the Screening of Treatments for Osteoarthritis

Derek A. Nichols, Inderbir S. Sondh, Paolo Zunino, and Riccardo Gottardi

Department of Mechanical Engineering and Materials Science

71 Microphysiological Model to Study Transport Across the Osteochondral Junction

Kalon J. Overholt, Riccardo Gottardi, and Rocky S. Tuan

Department of Bioengineering

76 Assessment of Schwann Cell Migration After Peripheral Nerve Injury and Treatment with Tissue-Specific Extracellular Matrix Hydrogel

Mara C. Palmer, Travis A. Prest, and Bryan N. Brown

Department of Bioengineering

83 Analysing the Porosity of Low-Cost Ceramic Water Filters through X-Ray Microtomography

Rafael Rodriguez, Qinghao Zang, and Ian Nettleship

Department of Mechanical Engineering and Materials Science

88 Glutaraldehyde Efficacy Against Microbial Species Found in Produced Water

Cassandra Valcourt, Daniel Lipus, and Kyle Bibby

Department of Civil and Environmental Engineering

94 Design of Highly Efficient Bifunctional Metal-Organic Framework Catalysts for Tandem Catalysis by Shortening the Reaction Pathway

Benjamin Yeh, Zhigang Hu, and Dan Zhao

Department of Chemical and Petroleum Engineering

100 Development of Computational Tools for 3-D *In Vivo* Morphometry and Analysis of Deformations of Monkey Optic Nerve Head

Ziyi Zhu, Huong Tran, Andrew P. Voorhees, Jacob Wallace, Andrew Moore, Matthew A. Smith, Gadi Wollstein, and Ian A. Sigal

Department of Mechanical Engineering and Materials Science



David A. Vorp, PhD

A Message from the Associate Dean for Research

“ ‘Ingenium’ is medieval English vernacular for ‘an ingenious contrivance.’ In his book *Ingenium: Five Machines That Changed the World*, Mark Denny describes ‘useful and ingenious applications of physical principles.’ To celebrate the ‘ingenium’ inherent in the practice of engineering, the University of Pittsburgh Swanson School of Engineering presents *Ingenium: Undergraduate Research at the Swanson School of Engineering*.”

—From the inaugural edition of *Ingenium*, 2015

The Swanson School of Engineering proudly presents its third edition of *Ingenium: Undergraduate Research at the Swanson School of Engineering*, a compilation of reports representing the achievements of selected Swanson School undergraduate students who have demonstrated excellence in our 2016 summer research program. To quote Bill Nye, “There’s nothing I believe more strongly in than getting young people interested in science and engineering for a better tomorrow for all humankind.” Indeed, our students are our legacy; our students are our future. To see them learn how to apply what they learn both inside and outside the classroom is very gratifying. But we hope that it does not stop there. We envision and hope that these experiences make a lasting impact on the students and their careers and help them, even in some small way, to produce “a better tomorrow for all humankind.”

The student authors of the articles contained in this edition of *Ingenium* studied mostly under the tutelage of a faculty mentor in the Swanson School. In some cases, the research took place at other institutions, both in the United States and abroad. At the conclusion of the program, students were asked to submit an abstract summarizing the results of their research, which were then reviewed by the *Ingenium* Editorial Board made up of Swanson School graduate student volunteers. The authors of the highest-ranking abstracts were invited to submit full manuscripts for consideration for inclusion in *Ingenium*, and those that were submitted were reviewed by the Editorial Board. Therefore, *Ingenium* serves as more than a record of our undergraduate student excellence in research; it also serves as a practical experience for our undergraduate students in scientific writing and the author’s perspective of the peer review process. In addition, it provides practical experience for our graduate students in editorial review and the reviewer’s perspective of the peer review process.

I would like to acknowledge the hard work and dedication of the co-editors-in-chief of this edition of *Ingenium*, Amir Mostafaei and Amey More, as well as the production assistance of Melissa Penkrot and the team at the Department of Communications Services. This issue also would not have been possible without the hard work of the graduate student volunteers who constituted the *Ingenium* Editorial Board and who are listed on page 6. It also is altogether fitting to thank the faculty mentors and other co-authors of the reports included in this edition.

Finally, we are grateful to the PPG Industries Foundation, which generously supported 11 of our undergraduate students as 2016 summer undergraduate research fellows. Two of the fellows—Clement Ekaputra and Julie Hartz—have contributed articles to this year’s edition of *Ingenium*.

On behalf of U.S. Steel Dean of Engineering Gerald Holder and the entire Swanson School of Engineering community, I hope that you enjoy reading this third edition of *Ingenium* and that the many talents of our students inspire the engineers of the future!

A handwritten signature in black ink, appearing to read "David A. Vorp".

David A. Vorp, PhD
Associate Dean for Research
University of Pittsburgh Swanson School of Engineering

**Amey More****Amir Mostafaei**

A Message from the Co-Editors-in-Chief

Greetings! We are delighted to bring you the third edition of *Ingenium: Undergraduate Research at the Swanson School of Engineering*. *Ingenium* was instituted as a platform to communicate peer-reviewed undergraduate research to students, faculty, and friends, both at the University of Pittsburgh and outside. The community warmly received the previous editions, motivating us to put together *Ingenium* 2017, a multifarious affair comprising 19 contributions across five departments at the Swanson School of Engineering. Successful production of this issue has been enabled by the *Ingenium* team—the editorial board; faculty advisors; and, of course, the undergraduate students, all of whom contributed their time and effort in conceiving, developing, and polishing the research published here. We take this opportunity to acknowledge each one of them—thank you!

All submissions to *Ingenium* went through a standard two-step single-blind review process. The extended abstracts and the full manuscripts were comprehensively reviewed by an editorial board consisting of graduate student volunteers from all departments of the Swanson School. This all-round participation of undergraduate and graduate students has been the characteristic spirit of *Ingenium* as a scientific publication by the students.

We are grateful to Associate Dean for Research David Vorp and Melissa Penkrot for their invaluable guidance and help in putting this issue together. The team at the Department of Communications Services has done a fantastic job in producing this issue in its current professional and aesthetic form.

Finally, we hope that this modest showcase portrays the Swanson School of Engineering as the vibrant and enthusiastic research community it is. And we sincerely hope that you, the reader, enjoy this morsel of exciting research we do at Pitt!

A handwritten signature in black ink that reads "Amey More".

Amey More
Co-Editor-in-Chief

A handwritten signature in black ink that reads "Amir Mostafaei".

Amir Mostafaei
Co-Editor-in-Chief

Editorial Board Members

Ingenium: Undergraduate Research at the Swanson School of Engineering

Co-Editors-in-Chief:

Amey Sudhir More (Chemical and Petroleum Engineering) and
Amir Mostafaei (Mechanical Engineering and Materials Science)

Name	Department
Anhalt, Ashley.....	Industrial Engineering
Cardoza, Alvaro.....	Electrical and Computer Engineering
Chen, Jingming.....	Bioengineering
Durka, Michael	Mechanical Engineering and Materials Science
Dziki, Jenna.....	Bioengineering
Esmaili, Nazanin.....	Industrial Engineering
Ferrer, Gerald	Bioengineering
Gade, Piyusha	Bioengineering
Gau, David	Bioengineering
Gustafson, Jonathan	Bioengineering
Hasik, Vaclav	Civil and Environmental Engineering
Heusser, Michelle.....	Bioengineering
Iftikhar, Aimon.....	Bioengineering
Kher, Rajan	Chemical Engineering
Krishnan, Lavanya.....	Industrial Engineering
Lee, Yoojin	Bioengineering
Long, Daniel	Bioengineering
Mehmachi, Erfan.....	Industrial Engineering
More, Amey**	Chemical Engineering
Mostafaei, Amir**	Mechanical Engineering and Materials Science
Nolfi, Alexis	Bioengineering
Oborski, Matthew	Bioengineering
O'Connell, Caitlin.....	Bioengineering
Pliner, Erika	Bioengineering
Rodriguez, Gianfranco.....	Chemical Engineering
Siying, Liu.....	Chemical Engineering
Stabryla, Lisa	Civil and Environmental Engineering
Stevens, Erica.....	Mechanical Engineering and Materials Science
Taylor, Michael	Chemical Engineering
Tran, Huong	Bioengineering
van der Merwe, Yolandi	Bioengineering
Vora, Nemi	Civil and Environmental Engineering
Wang, Ker Jiun.....	Electrical and Computer Engineering/Bioengineering
Wang, Yan	Civil and Environmental Engineering
Wei, Qiaoyi (Joey)	Mechanical Engineering and Materials Science
Wieserman, Laura	Electrical and Computer Engineering
Zheng, Xin (Sally)	Bioengineering

** Co-Editors-in-Chief 2017

Self-supported Monolith Formation of Silica Nanoparticles with Hollow Nickel Core

Patrick Asinger, Sharlee Mahoney, Yahui Yang, and Götz Veser

*Department of Chemical and Petroleum Engineering, Swanson School of Engineering,
University of Pittsburgh, Pittsburgh, PA, USA*

Abstract

Sintering of nanoparticles poses a major issue for their sustainable use. Structures utilizing a stable oxide shell, such as silica, show promise for prolonged stability of an encapsulated metallic nanomaterial. While applications in high-temperature heterogeneous catalysis and CO₂ sorption are enabled by the hollow-core shell structure of our hollow nickel on silica (hNi@SiO₂) nanoparticles, these materials are still in their nano-powder form, and hence pose serious health and engineering issues. Traditional inert monolithic supports address these issues, but do so with the cost and energy penalty of introducing excess material. Our work demonstrates the ability of hNi@SiO₂ to form self-supporting monoliths with bimodal porosity by templating around polymeric microspheres. The strength of the initially mechanically fragile monoliths is addressed by interconnecting the hNi@SiO₂ nanoparticles via an additional reaction of SiO₂ onto the previously formed superstructure. It is found that an acid-catalyzed morphology is significantly more conducive to strengthening the network of nanoparticles compared to base-catalyzed conditions, and this facet is attributed to the morphology formed in each case.

Keywords: monolith core-shell silica nickel

1. Introduction

1.1 Nanoparticle Features

Structures with features defined on the nanoscale (1-100 nm), known as nanomaterials, have found numerous applications in medicine, energy, catalysis, optics, electronics, and more [1]. The high surface area to volume ratio of nanoparticles affords a higher surface energy, bringing about properties that differ from the bulk material. While these particles possess unique characteristics, thermodynamics drive them to form larger particles through processes referred to as Oswald ripening and coalescence. In the case of catalytic nanoparticles operating at temperatures above 300 °C, a mixture of

the Oswald ripening and coalescence persist and the overall thermal deactivation is referred to as sintering [2]. As these processes evolve and the relevant length scale grows, the nanomaterials unfortunately lose their “nano-effects.”

1.2 Stability via Core-shell Nanoparticles

Significant work addresses the issue of catalytic nanoparticle sintering, namely by utilizing core-shell architectures. In this format, the active metal nanoparticles reside in the core of the particle while a stable oxide shell, such as silica, protects adjacent metal nanoparticles from coalescing [3, 4]. To this end, our lab has previously shown that silica nanoparticles with hollow nickel core (hNi@SiO₂, Figure 1) are stable up to 800 °C [4], compared to 300 °C when nickel nanoparticles are unprotected [5].

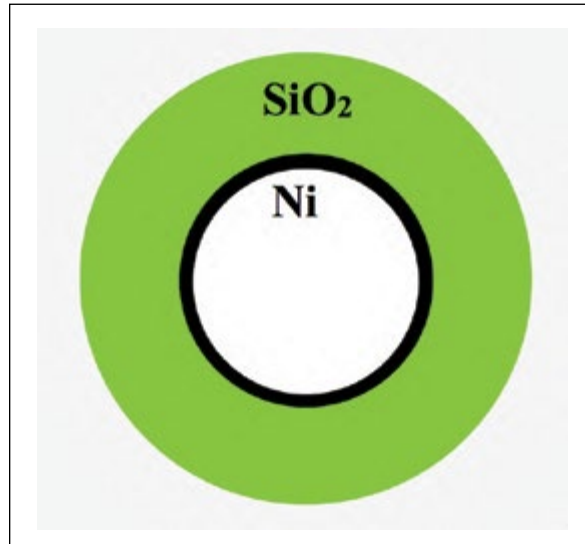


Figure 1. hNi@SiO₂ – a mesoporous SiO₂ shell 35 nm in diameter and 10 nm thick (green) surrounds a hollow core lined with nickel (black).

1.3 Applications of hNi@SiO₂

The improved thermal stability of hNi@SiO₂ compared to unprotected nickel nanoparticles enables their use at higher temperatures, which is especially advantageous for high-temperature heterogeneous catalysis. Considering the Arrhenius dependence of reaction rate on temperature, performing reactions at 800 °C will yield marked increases in production compared to 300 °C. Nickel nanoparticles are utilized in a variety of important heterogeneous catalysis reactions such as CO oxidation, CO₂ hydrogenation, dehydrogenation of H₃NBH₃, and others [4, 6, 7].

Beyond heterogeneous catalysis, the hollow core of hNi@SiO₂ has been demonstrated to be an effective nano-cavity for the loading of liquid CO₂ sorbents. The increased uptake kinetics and capacity of this core-shell-liquid-sorbent system is attributed to the nanoconfinement of the liquid sorbent [8].

1.4 Formation of Monolithic hNi@SiO₂

While the core-shell configuration shows great promise for robust application of nanoparticles, these materials are synthesized as a nano-powder and hence constitute significant health and safety concerns. Furthermore, nano-powders pose an engineering challenge due to excessive pressure drop when used in a catalytic bed, for example. While these issues could be overcome by depositing these core-shell structures onto conventional supports, a self-supporting monolithic structure made from such core-shell materials would be a uniquely efficient and potentially flexible configuration.

In the present work, we demonstrate forming self-supporting monolithic structures of hNi@SiO₂ without any sacrificial binders or additional inert support material. In a procedure potentially allowing flexibility of the macroporosity, hNi@SiO₂ is templated around polymeric microspheres; the subsequent removal of polymer via calcination creates macroporous voids. The porosity of these hNi@SiO₂ monoliths is anticipated to be high (> 90%) owing to the hollow core of hNi@SiO₂, mesoporosity in the SiO₂ shell, and macroporosity from polymeric template removal. The initial fragility of these highly porous structures is addressed by reacting an additional layer of SiO₂ onto the surface of the superstructure. Acid-catalyzed conditions, as opposed to base-catalyzed conditions, are expected to yield a mechanically stronger monolith; this facet is attributed to the interconnected morphology more pronounced with acid-catalyzed conditions [9].

2. Experimental

2.1 Materials

Brij58, cyclohexane, NiCl₂, hydrazine, isopropanol, NH₄OH (30% NH₃ basis), tetraethyl orthosilicate (TEOS), and 100 μm polymethacrylate (PMA) spheres (10 wt%) were obtained from Sigma-Aldrich. Cetyltrimethylammonium bromide (CTAB, Sigma-Aldrich) was used as a 0.5 M solution. Methanol and hydrochloric acid (Fisher Scientific) were used as received. Deionized water was used in all components of the experiments. Stainless steel molds (5.3 mm ID, 12.7 mm height) were obtained from Swagelok.

2.2 Synthesis of hNi@SiO₂ Core-shell Nanoparticles

Waiting 1 h between the addition of each reagent, Brij58 (10 g, 8.9 mmol), 2.0 M NiCl₂ (1.5 mL, 3 mmol), 1.5 mL hydrazine, 10 g TEOS, and 3 mL NH₄OH were added to 50 mL cyclohexane at 50 °C. The reaction was allowed to proceed for 2 h at 50 °C under cold water reflux. hNi@SiO₂ was precipitated by adding isopropanol and washed three times by centrifuge and redispersion. The powder was calcined at 500 °C for 2 h to remove organic compounds. Rehydroxylation of the SiO₂ was achieved by heating in excess water at 95 °C. The particles were dried under vacuum for at least 2 d before use.

2.2 Formation and Strengthening of Self-supported hNi@SiO₂ Monoliths

For each monolith, 21.6 mg hNi@SiO₂ powder was combined with excess DI (deionized) water and solutions of PMA and CTAB. In all cases the volume ratio of PMA:CTAB solutions remained 38.5:1. The mass ratio of PMA:hNi@SiO₂ varied from 0.97:2.18. The contents were mixed and dried at 100 °C in a vacuum oven overnight. All of the dry powder contents were randomly mixed by shaking and packed into molds. The contents were wetted with a few drops of NH₄OH or HCl, stored at 50 °C overnight, and calcined in air at 0.2 SCCM at 500 °C for 6 h with a 5 °C/min ramp.

In order to enhance the mechanical strength of the initially fragile monoliths, a chemical strengthening procedure was conducted. For acid-catalyzed conditions, TEOS was added dropwise onto the surface of the monolith. For base-catalyzed conditions, monoliths were soaked at room temperature in a solution of 1400 μL methanol, 51.4 μL DI water, 544 μL NH₄OH, and 4.5 μL TEOS for 20 to 115 h and dried at 50 °C overnight. For acid-catalyzed conditions, TEOS was added dropwise onto the

monolith surface until saturated. The monolith then aged in a solution of HCl (1-100 vol% in methanol) at 50 °C overnight.

Compression-to-rupture testing was performed on a Brookfield CT3 Texture Analyzer. The rupture point was marked by a sudden drop in load of 20-50 g.

3. Results and Discussion

3.1 Formation of Self-supported hNi@SiO₂ Monoliths

Fully self-supported monoliths of hNi@SiO₂ were formed by templating hNi@SiO₂ powder around 100 μm PMA spheres, as outlined in Figure 1. PMA microspheres are

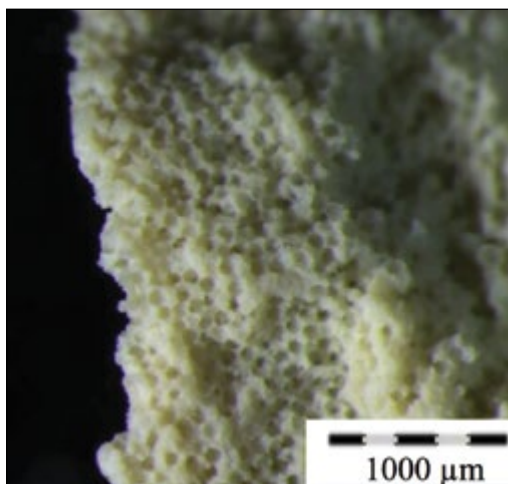


Figure 2. Removal of the polymer template creates 100 μm pores. Accounting for the hollow core of the hNi@SiO₂ nanoparticles, the overall structure is more than 90% porous.

received with a negative surface charge and the silanol groups of silica NP surfaces make hNi@SiO₂ negatively charged [8]. Thus, PMA microspheres and hNi@SiO₂ naturally repel, and adhesion of hNi@SiO₂ onto PMA does not occur without another force counteracting the repulsion of the two negatively charged species. To this end, cetyltrimethylammonium bromide (CTAB) was added to the aqueous mixture of PMA and hNi@SiO₂. The cationic end of CTAB mediates the negative charges between the two species and the hydrophobic tail ensures attraction between CTAB-coated silica surfaces and PMA hydrophobic surfaces [9]. Furthermore, the addition of CTAB was found to be useful in reducing the amount of static clinging of PMA microspheres to containers and tools, ensuring the nominal value of PMA added is nearly the true amount. When calcined at 500 °C, the PMA and CTAB are burned away and the void created by PMA provides macroporosity to the monolith. Additionally at 500 °C, the surface silanol groups of adjacent nanoparticles condense together to form siloxane bonds, making the individual silica particles solidify into a uniform monolithic superstructure. However, the siloxane bond formation does not occur without flux. Some regions are not interconnected well and thus are more prone to fracture.

The monoliths formed are highly porous (Figure 2). Accounting for only the hollow core of the hNi@SiO₂ nanoparticles and the macroporosity from polymeric template removal, it was found that the monolith structure is 90% porous. The porosity is in fact higher than this since the SiO₂ shells are porous as well. As a result

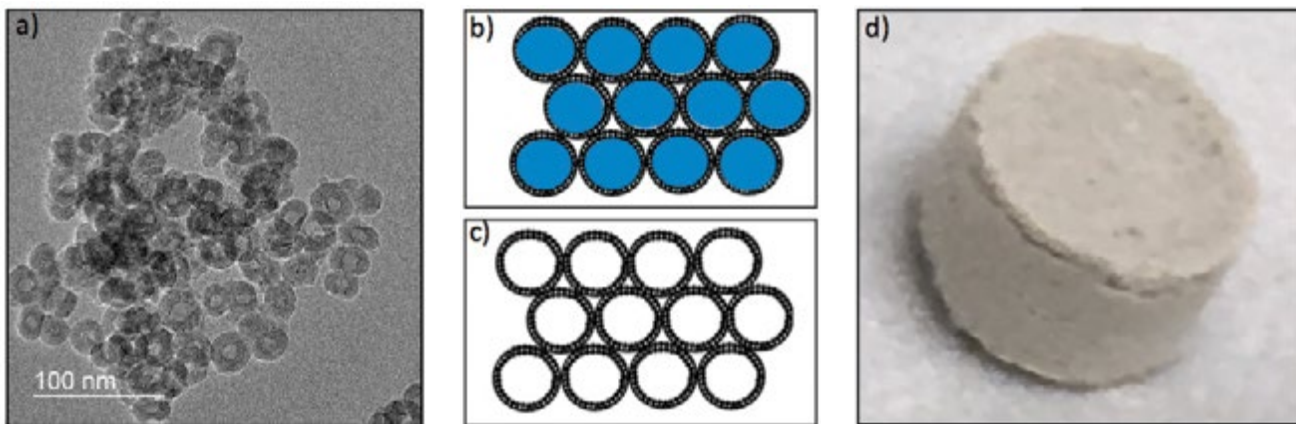


Figure 3. A schematic of templating hNi@SiO₂ onto PMA spheres. a) TEM image of hNi@SiO₂. b) hNi@SiO₂ (black) templates around 100 μm PMA spheres (blue). c) After 500 °C calcination, PMA spheres are removed. d) Image of self-supported hNi@SiO₂

of the high porosity, the monoliths formed with only the aforementioned procedure are mechanically fragile. We sought to improve the strength by reacting an additional layer of silica onto the monolith surface.

3.2 Strengthening of Self-supported hNi@SiO₂ Monoliths

Strengthening of the monoliths was achieved by reacting TEOS, an SiO₂ precursor, onto the previously formed superstructure of hNi@SiO₂ nanoparticles. In the case of base-catalyzed conditions, we see relatively low rupture strengths (Figure 4) compared to acid-catalyzed conditions (Figure 5). Even after long periods of aging for base-catalyzed samples, the acid-catalyzed samples strongly outperform in terms of mechanical strength.

The effect of acid concentration was investigated for its effect on the resulting strength. The rupture strength

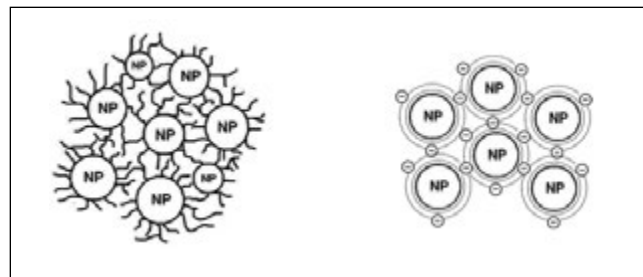


Figure 6. Acid-catalyzed strengthening (left) yields an interconnected morphology. Base-catalyzed strengthening (right) yields a lightly crosslinked network of “colloidal particles”.

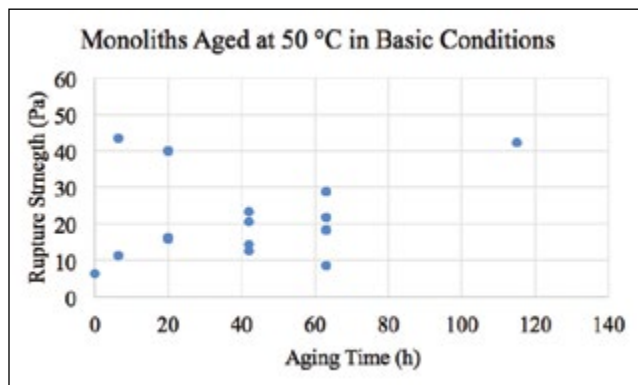


Figure 4. Rupture strength of monoliths after strengthening with TEOS under base-catalyzed conditions over various periods of time

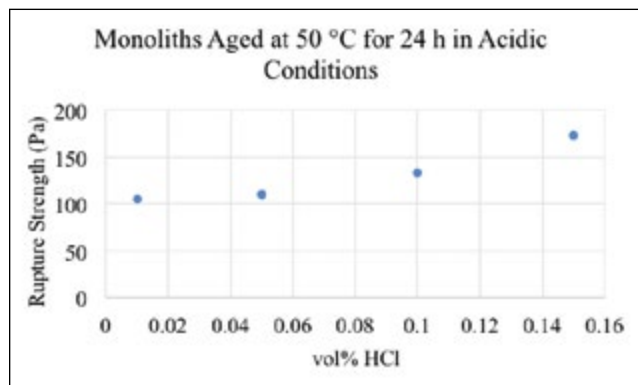


Figure 5. Increasing concentration of HCl yields a higher rupture strength. At 24 h of aging in acidic conditions, the rupture strength surpasses that of basic conditions at any timescale.

increases as the concentration of HCl increases (Figure 4). This facet can be attributed to a higher reaction rate with more acid catalyst, creating more network-forming bonds within the 24 h timespan.

The distinct difference in strength of basic and acidic conditions results from the morphology that is created in each case (Figure 6). The key difference is that acid-catalyzed conditions form long, linear extensions while base-catalyzed conditions tend to form highly branched “colloidal particle” networks [9]. The exact cause for the acid-catalyzed morphology is currently uncertain, but it is frequently utilized when an interconnected network is desired. Base-catalyzed conditions afford a repulsion between the negative charge of adjacent SiO₂ surfaces, preventing their aggregation into an interconnected network. Colloidal SiO₂ nanoparticles are typically synthesized under base-catalyzed conditions for this reason. For these reasons it is expected that acid-catalyzed conditions yield a higher rupture strength (max. 173 Pa) than base-catalyzed conditions (max. 43.6 Pa).

4. Conclusion

hNi@SiO₂ has been exploited as a hollow nanostructure that has a surface functionality enabling formation of a monolith entirely composed of one catalytic nanoparticle type. We demonstrated the ability to template hNi@SiO₂ around PMA spheres and subsequently create macroporosity via calcination. We intend to demonstrate the possibility of using various polymer sphere sizes while also finding trends relating the mass transport properties to the tunable macroporosity.

We believe the monolith we have created, one that is uniformly made of porous nanomaterials, to be the first

of its kind. The monolith presented here is more than 90% porous; both the hollow nanomaterials and polymer microsphere voids contribute to the overall porosity. The fragility of the monoliths is addressed with a chemical strengthening procedure which has shown an 18-fold increase in crushing strength under acid-catalyzed conditions. Related work that intends to create a covalently bonded network of silica nanoparticles can build upon the principle emphasized here of reacting additional silica under acidic conditions to preferentially form the desired morphology. Further characterization of the silica-coated monoliths will help elucidate whether the coating mechanism will in any way inhibit catalytic activity of the monolith.

Acknowledgment

The Mascaro Center for Sustainable Innovation and Dr. Len Peters provided funding. Dr. Sachin Valenkar kindly allowed us to use the appropriate equipment for mechanical rupture strength testing.

References

- [1] Rao, C. N. R., and A. K. Cheetham. "Science and technology of nanomaterials: current status and future prospects." *Journal of Materials Chemistry* 11.12 (2001): 2887-2894.
- [2] Hansen, Thomas W., et al. "Sintering of catalytic nanoparticles: particle migration or Ostwald ripening?." *Accounts of chemical research* 46.8 (2013): 1720-1730.
- [3] Joo, Sang Hoon, et al. "Thermally stable Pt/mesoporous silica core-shell nanocatalysts for high-temperature reactions." *Nature materials* 8.2 (2009): 126-131.
- [4] Cao, Anmin, Rongwen Lu, and Götz Veser. "Stabilizing metal nanoparticles for heterogeneous catalysis." *Physical Chemistry Chemical Physics* 12.41 (2010): 13499-13510.
- [5] Matsuno, Misa, et al. "In situ sintering of Ni nanoparticles by controlled heating." *Microscopy and Microanalysis* 17.S2 (2011): 524-525.
- [6] Wang, Wei, et al. "Mesoporous nickel catalyst supported on multi-walled carbon nanotubes for carbon dioxide methanation." *International Journal of Hydrogen Energy* 41.2 (2016): 967-975.
- [7] Metin, Önder, et al. "Monodisperse nickel nanoparticles and their catalysis in hydrolytic dehydrogenation of ammonia borane." *Journal of the American Chemical Society* 132.5 (2010): 1468-1469.
- [8] Palm, David W., Robert M. Enick, and Götz Veser. "Nanoconfined Amine-Functionalized Silicone Oil Sorbents for Rapid CO₂-Capture." *Industrial & Engineering Chemistry Research* 53.42 (2014): 16476-16484.
- [9] Brinker, C. J. "Hydrolysis and condensation of silicates: effects on structure." *Journal of Non-Crystalline Solids* 100.1 (1988): 31-50.

Verifying Normality of Ocular Tissue Through Development of a Semi-automated Optic Nerve Axon Counting Method

Katelyn Axman¹, Addison Kaufmann², Sundaresh Ram², and Jonathan P. Vande Geest¹

*Department of Bioengineering, Swanson School of Engineering,
University of Pittsburgh¹, Pittsburgh, PA, USA*

*Department of Electrical and Computer Engineering, Soft Tissue Biomechanics
Laboratory University of Arizona², Tucson, AZ, USA*

Abstract

Glaucoma is the second leading cause of irreversible blindness and vision loss worldwide. Although inception of the disease in patients is somewhat ambiguous, race and ethnicity are proven risk factors in glaucoma prevalence. Examining the biomechanical differences between eyes of different racial/ethnic backgrounds will lead to a better understanding of the reason for this disparity. The goal of this work is to identify baseline axon counts for optic nerves from donors of African Descent (AD), European Descent (ED) and Hispanic Ethnicity (HE) as a means of verifying that the ocular tissue is healthy and nonglaucomatous. Optic nerves were received from AD ($n=2$), HE ($n=2$) and ED ($n=3$) donors, which were then cut cross-sectionally, processed on slides, and montage imaged at 60x magnification. These images were analyzed using a MATLAB code, which prompted the user to click on the axons in 10 smaller, randomly selected sections of the optic nerve image. These averaged counts were used to extrapolate and obtain an axon count for the entire nerve cross section. All samples were determined to be within an axon count range that confirmed ocular tissue normality (AD: $928,274 \pm 264,783$, ED: $979,725 \pm 83,118$, HE: $807,148 \pm 65,167$). Thus, future work will explore other possible biomechanical differences between these confirmed nonglaucomatous eyes of varying racial/ethnic backgrounds that could cause a disparity in glaucoma prevalence. The healthy axon counts obtained in this work are also valuable for comparison to both healthy and glaucomatous optic nerve axon counts calculated in other studies, which may provide further insight into prevention of axonal loss in glaucoma and potential treatment for patients suffering from vision loss.

Keywords: glaucoma, axon count, normality, race/ethnicity

Abbreviations: African Descent (AD), European Descent (ED), Hispanic Ethnicity (HE), right eye (OD), left eye (OS), Midwest Eye Bank (MWEB), San Diego Eye Bank (SDEB), Banner Health Eye Bank (BH)

1. Introduction

Glaucoma is the second leading cause of irreversible blindness around the world, affecting more than 200,000 people every year. It has been shown that primary open angle glaucoma disproportionately affects those of African Descent (AD) and Hispanic Ethnicity (HE) over those of European Descent (ED) [1,2]. Though this phenomenon may be due in part to a disparity in socioeconomic factors, it is reasonable to assume that certain biomechanical and morphological differences between the eyes of AD, HE and ED individuals may play an important role. Because axons of retinal ganglion cells that traverse the optic nerve become considerably degraded and are eventually lost in patients with glaucoma, resulting in vision loss [3,4], the axon count of optic nerve samples is one method to confirm the normality of donor ocular tissues. The goal of this work is to identify baseline axon counts for optic nerves from those of AD, HE and ED race/ethnicity. The information gathered in this work will be useful for ensuring that the biomechanical and structural endpoints being measured in separate studies in this laboratory are solely due to racial and/or ethnic differences. This data will also be useful as a control group for future experiments investigating how axon counts may be different in glaucomatous samples as a function of racial/ethnic background. As full manual axon counting is extremely grueling and time intensive, semi-automated methods are widely used in the literature. Previous studies detailing similar semi-automated axon counting methods to that used in this work predominantly examine non-human tissue [5,6]. Thus, identifying baseline healthy human optic nerve axon counts using a semi-automated extrapolation method will prove especially valuable to the study of glaucoma in humans and allow for better understanding of the disease's adverse effect on these retinal ganglion cells that results in permanent vision loss.

2. Materials and Methods

2.1 Sample Preparation and Processing

Optic nerves were received from Midwest Eye Bank (MWEB) ($n=4$), San Diego Eye Bank (SDEB) ($n=2$), and Banner Health (BH) ($n=1$), containing nerves from both the left (OS) ($n=5$) and right (OD) ($n=2$) eyes, from AD ($n=2$), HE ($n=2$) and ED ($n=3$) donors. Donors of each racial/ethnic background did not differ significantly in age (AD: 69 ± 4.24 , ED: 75 ± 3 , HE: 71.5 ± 20.5 ; $P = .8288$). Within four hours of death, the optic nerves were cut and fixed in Poly/LEM at their respective eye banks, at which point they were sent to our laboratory. Once received, the nerves were transferred to vials containing 2.5% glutaraldehyde and stored for 24 hours. Finally, they were transferred to PBS and stored at 4°C until they were sent out for processing (Figure 2). During processing, optic nerve samples were cut cross-sectionally, stained with OsO₄, and embedded onto slides that were visualized on a Nikon Eclipse 90i microscope. Each cross section was individually imaged at 60x magnification using Nikon NIS-Elements software; 15% overlap as well as autofocus capabilities were used for each pixel, allowing for successful and detailed image montaging. A full optic nerve image montage is shown in Figure 3.



Figure 2. Image of a donor optic nerve sample, as it is received post-enucleation

2.2 Image Analysis: Obtaining Axon Counts

Semi-automated axon counts were executed using image processing techniques in MATLAB, and methodology adapted from that previously described in Teixeira et al [6]. Each montaged image was read one at a time through a program written to perform a semi-automated axon count across 100% of the given optic nerve cross section. A single experienced user performed all axon counts on the samples examined in this study. The user was first prompted to identify the bounds of the optic nerve cross section in order to crop the image. Contrast-limited adaptive histogram equalization was applied to the cropped image to improve user accuracy of axon identification. Ten individual small sections of axons of equal area throughout the entire image were randomly selected and presented one at a time, and the user was asked to manually click on the axons in each section. A magnified section of axons can be seen in Figure 3. These manual counts for each section were added together and averaged corresponding to their fraction of the total cropped cross-sectional area, providing an average axon density for the section. Counting 10 of these images and calculating this average count was done to create a more accurate representation of the average axon density in these sections with respect to the entire optic nerve area,

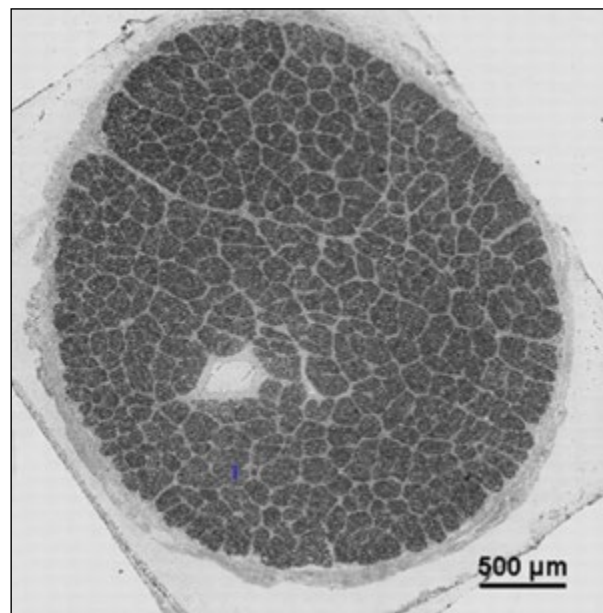


Figure 3. Microscope image montage of full optic nerve cross section at 60x magnification, from 66-year-old AD sample, OS. Dark sections indicate bundles of axons, separated by the lighter septae of collagenous connective tissue

as axon distribution can be somewhat non-uniform by nature. This calculated density was then used to extrapolate across the entire cross-section in order to give an estimated axon count for the whole optic nerve. Each image was run through the program four times for repeatability purposes, and an average and standard deviation for the axon count of each optic nerve was calculated.

3. Results

Of the seven samples tested, mean semi-automated axon counts ranged from 741,045 to 1,031,924. Calculated standard deviations indicated a minimum axon count of 601,240 for AD OS sample age 72, and a maximum axon count of 1,351,184 for AD OS sample age 66.

Mean axon counts with standard deviations for each individual sample are shown in Figure 1. For samples of African Descent ($n=2$), mean axon count was $928,274 \pm 264,783$. Samples of European Descent ($n=3$) yielded a mean axon count of $979,725 \pm 83,118$, and mean axon count for samples of Hispanic Ethnicity ($n=2$) was $807,148 \pm 65,167$. The mean axon count for all ($n=7$) samples tested was $915,717 \pm 143,965$. A one-way ANOVA test between axon counts from the three racial/ethnic backgrounds yielded a p-value of 0.50, and thus no significant difference between axon counts for optic nerves of European Descent, African Descent, and Hispanic Ethnicity was found.

4. Discussion

Full human optic nerve axon counts have been reported in the literature as ranging from 777,000 to 1,679,000

[7]. A t-test indicated that the mean human eye axon counts in our study did not vary significantly from those reported in Mikelberg et al [8], returning a p-value of .52. However, the mean axon count for all optic nerves in this study was determined to be significantly lower ($P < .05$) than the investigation of Jonas et al., which published a mean axon count of $1,158,000 \pm 222,000$ [7]. This disagreement is likely due to the difference in age between subjects in the two studies, which is significant ($P < .05$); the average age of donors in this work was 72.3 ± 9.14 while the average age published by Jonas et al was 54.7 ± 19.8 . It has been shown in multiple studies that there are generally fewer axons in the eyes of older individuals, as a number of retinal ganglion cells are lost every year and do not regenerate [9,10, 11]. In comparison to axon counts performed by Kerrigan-Baumrind et al. [12] on glaucomatous human eyes, our axon count mean proved significantly higher ($P < .05$), indicating healthy, non-glaucomatous tissue. By confirming normality of the ocular tissues studied in this work, our laboratory can continue to explore biomechanical factors affecting glaucoma prevalence between races. Loss of human optic nerve retinal ganglion cells during glaucoma causes irreversible blindness [3,4]. Comparing the baseline healthy axon counts gathered in this study and others to the axon counts of glaucomatous samples will refine characterization of the mechanism by which axons are degraded in the optic nerve, and potentially lead to improvement in vision loss treatment and prevention for glaucoma patients. A one-way ANOVA test between optic nerves from the three racial/ethnic backgrounds ($P = 0.50$) indicated no significant difference between axon

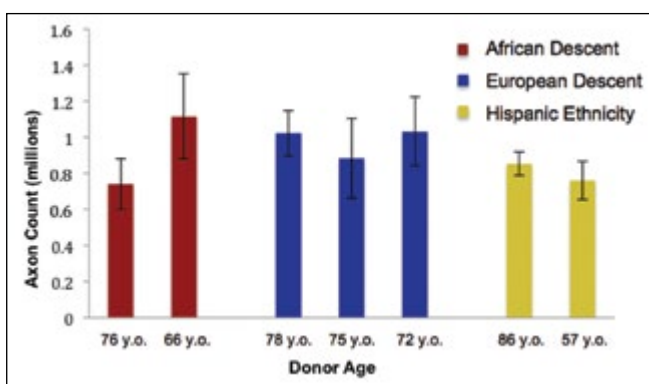


Figure 1. Bar graph showing the human optic nerves of different aged donors from AD, ED, and HE backgrounds and the calculated axon counts with standard deviations for each sample

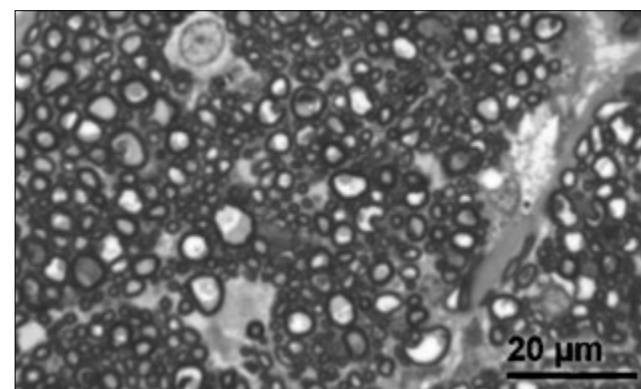


Figure 4. This is a small, 60x magnified section of retinal ganglion cell axons taken from the cross section of a human optic nerve. These axons, varying in size, are characterized by their circular shape and lighter centers surrounded by dark myelin sheaths.

counts for individuals of European Descent, African Descent, and Hispanic Ethnicity. This would suggest that race does not play a role in the number of axons that traverse the human optic nerve. We intend to continue to compare optic nerve axon counts between races to further substantiate this observation. A single experienced user counted axons for the samples used in this work to ensure repeatability and consistency. However, since axon shapes and sizes are nonuniform by nature, it may be important to include counts from multiple users in future work in order to account for inter-user variability. Development of a fully automated axon counting code is another notable endeavor for future work, and would be useful to improve count accuracy.

5. Conclusions

When optic nerve cross sections from donors of three backgrounds were imaged and axon counts obtained from the samples, no significant difference in axon count was found between races. Axon counts indicated that the eyes examined in this work were healthy and nonglaucomatous, allowing further experimentation on the other parts of these donor eyes. In examining ocular biomechanical differences solely as a function of racial background, we hope to better characterize their role in the disparity in glaucoma prevalence between races/ethnicities. Identifying these baseline healthy optic nerve axon counts in humans is valuable in order to better understand the adverse effect glaucoma has on retinal ganglion cell axons, since the permanent loss of these axons is what causes irreversible blindness in glaucoma.

6. Acknowledgments

The author would like to thank Dr. Jonathan P. Vande Geest, his NIH grant NEI 5R01EY020890-05, the SSOE Department of Bioengineering, and the Office of the Provost at the University of Pittsburgh for contributing to the funding that facilitated this research.

7. References

- [1] J.M. Tielsch, A. Sommer, J. Katz, R.M. Royall, H.A. Quigley, and J. Javitt, Racial variations in the prevalence of primary open-angle glaucoma. *The Baltimore Eye Survey*. *Jama*, 266 (1991) 369-74.
- [2] A. Sommer, J.M. Tielsch, J. Katz, H.A. Quigley, J.D. Gottsch, J.C. Javitt, J.F. Martone, R.M. Royall, K.A. Witt, and S. Ezrine, Racial differences in the cause-specific prevalence of blindness in east Baltimore. *N Engl J Med*. 325 (1991) 1412-7.
- [3] H.A. Quigley, R.M. Hohman, E.M. Addicks, R.W. Massof, W.R. Green. Morphologic changes in the lamina cribrosa correlated with neural loss in open-angle glaucoma. *Am. J. Ophthalmol.* 95 (1983) 673–691.
- [4] R.W. Nickells. The cell and molecular biology of glaucoma: mechanisms of retinal ganglion cell death. *Invest Ophthalmol Vis Sci*. 53 (2012) 2476-2481.
- [5] Ebneter A, Casson RJ, Wood JP, Chidlow G. Estimation of axon counts in a rat model of glaucoma: comparison of fixed-pattern sampling with targeted sampling. *Clin Exp Ophthalmol*. 2012 (6) 626-33
- [6] L.C. Teixeira, K.A. Buhr, O. Bowie, F.D. Duke, T.M. Nork, R.R. Dubielzig, G.J. McLellan. Quantifying optic nerve axons in a cat glaucoma model by a semi-automated targeted counting method. *Molecular Vision*. 20 (2014) 376-385.
- [7] J.B. Jonas, A.M. Schmidt, J.A. Müller-Bergh, U.M. Schlötzer-Schrehardt, G.O. Naumann. Human optic nerve fiber count and optic disc size. *Invest Ophthalmol Vis Sci*. 33 (1992) 2012-2018.
- [8] F.S. Mikelberg, S.M. Drance, M. Schulzer, H.M. Yidegiligne, M.M. Weis. The normal human optic nerve. Axon count and axon diameter distribution. *Ophthalmol*. 96 (1989) 1325-1328.
- [9] A.G. Balazsi, J. Rootman, S.M. Drance, M. Schulzer, G.R. Douglas. The effect of age on the nerve fiber population of the human optic nerve. *Am J Ophthalmol*. 97 (1984) 760–766.
- [10] B.M. Johnson, M. Miao, A.A. Sadun. Age-related decline of human optic nerve axon populations. *Age*. 10 (1987) 5–9.
- [11] M.X. Repka, H.A. Quigley. The effect of age on normal human optic nerve fiber number and diameter. *Ophthalmology*. 96 (1989) 26–32.
- [12] L.A. Kerrigan-Baumrind, H.A. Quigley, M.E. Pease, D.F. Kerrigan, R.S. Mitchel. Number of ganglion cells in glaucoma eyes compared with threshold visual field tests in the same persons. *Invest Ophthalmol Vis Sci*. 41 (2000) 741-748.

Design of an Active Trunk Control and Balancing System to Reduce Fatigue During Walking with an Exoskeleton

Joshua Barron^{1,2}, Dr. Nitin Sharma^{1,2}

Neuromuscular Control and Robotics Laboratory, Swanson School of Engineering, Department of Mechanical Engineering and Materials Science, University of Pittsburgh, Pittsburgh, PA, USA

Abstract

Spinal cord injuries cause approximately 5,100 people to be diagnosed with paraplegia each year in the United States. One potential device to help restore walking in such patients is the use of a gait restoration device such as a hybrid neuroprosthesis. However, because there is no support beyond the lower limbs in these systems, the test subjects must resort to using a walker to remain upright and maintain balance while using the exoskeleton. The implementation of a gyroscopic trunk control system would provide stability during use, and allow the subjects to perform actions with their upper limbs. A gyroscopic balancing device relies on rotating flywheels to produce a reactive torque by restricting gyroscopic procession. To meet the requirements of the project, a system was designed utilizing two flywheels to generate the necessary torque. The flywheel sizes were optimized based on patient size, and simulations were performed to determine the effectiveness of the system.

Keywords: gyroscopes, exoskeleton, balance, trunk

Abbreviations: Spinal cord injury (SCI), functional electrical stimulation (FES), control moment gyroscope (CMG)

1. Introduction

One potential device to help restore walking in patients with paraplegia is the use of a gait restoration device such as an exoskeleton. Powered exoskeletons are orthoses with an external source of actuation at the joints. These are a viable type of powered orthoses, and much advancement has been made on the subject in recent years [1, 2, 3]. Hybrid exoskeletons include both external joint actuation and functional electrical stimulation (FES). FES is the application of moderate electrical charges to the muscles of a patient to cause either extension or flexion of the muscle. A hybrid exoskeleton is currently under development in Dr. Nitin Sharma's lab. One problem with this type of orthosis is that it is hard for the patient to balance during use, as the forced actuation adds many

disturbances. Since there is no support beyond the lower limbs, the test subjects must resort to using a walker to remain upright and maintain balance while using the exoskeleton. This causes fatigue in the subject, and prevents the use of the upper limbs for other activities of daily living.

It was hypothesized that a gyroscope-based balancing device could be used to help patients achieve balance while using an orthosis. Currently, gyroscopic systems are most commonly used in self-balancing vehicles and positioning systems in satellites. The basics of these designs were taken as inspiration for implementation on an exoskeleton. In the interest of building a benchtop prototype, research was done on the balancing of an inverted pendulum about a fixed pivot axis. These designs commonly used a device with two flywheels, with the center of mass of the gyroscope assembly aligned with the axis of the pendulum [4].

2. Materials and Methods

For this project, the end goal was to design a full-scale device for use on an exoskeleton used by a SCI patient. However, for proof of concept, a benchtop prototype was also desired because it provides a simple and cheap way to test the effectiveness and safety of the device. Additionally, the smaller prototype would allow testing and implementation of further safety measures to ensure the welfare of the subject when using the full-scale device. The prototype was designed to be smaller in scale, and was expected to have comparable characteristics to the full-scale model, so the behavior of both systems would be similar. If the design and performance of the prototype satisfied all requirements, the final version could simply be scaled up for use on human patients.

To design an effective device, an accurate model of the human trunk was critical. To simplify the dynamics, the trunk was idealized as an inverted pendulum with a single-plane pivot axis. The gyroscopes generate a torque τ_{gyros} about the pivot axis, which balances the torques

created by the mass of the pendulum and the mass of the device itself. The torque generated by the gyroscopes is calculated as

$$\tau_{\text{gyros}} = 2(\dot{\beta} \times I\omega) \quad (1)$$

where $\dot{\beta}$ is the gimbal speed, and ω is the angular velocity of the flywheel, which is held constant in this application. The complete system is modeled in (2) and Figure 1.

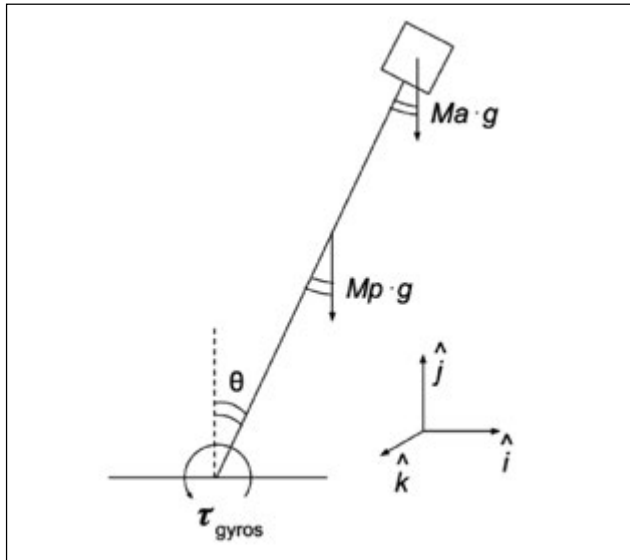


Figure 1: Inverted pendulum model of human trunk

$$\ddot{\theta} = \frac{2\dot{\beta}\omega \cos(\beta) - g \sin(\theta)(m_p \frac{L_p}{2} + m_a L_a)}{I_o} \quad (2)$$

Where L_p and L_a represent the length of the pendulum and the distance from the pivot to the gyroscope assembly, respectively, and I_o is the combined inertia of the whole system. For the full-scale model, the pendulum had a mass of 50 kg and a length of 0.5 meters, while the scaled down pendulum was the same height with a smaller radius weighing 10.63 kg.

Gyroscopes utilize two forms of rotational motion to generate torque. The flywheels spin about their main axis, and utilize a gimbal motor to pivot the gyroscope about an axis perpendicular to the main axis, generating a torque whose direction obeys the right-hand rule. As the flywheel pivots about the gimbal axis, its torque develops a Sine and Cosine component, generating torque about two different axes. In this case, torque is only required about one axis to stabilize the subject, and excess torque out of plane could impede stabilization or even cause harm to the subject. To avoid this, a design implement-

ing two flywheels was selected. The flywheels rotate and gimbal in opposite directions, which causes out-of-plane torques to cancel and assistive torques to add.

Due to cost limitations, the material of the flywheels was chosen to be steel. Higher density materials would create a larger moment of inertia, but were found to be too expensive. The torque required to stabilize the system was calculated from the static model in Figure 1 for any angle, ignoring accelerations of the pendulum. Referring to equation (2), the torque required from the gyroscopes at any given angle θ to bring the pendulum back to vertical is calculated as

$$g \sin(\theta) (m_p \frac{L_p}{2} + m_a L_a) \quad (3)$$

This torque is dependent on the mass of the gyroscope assembly, which means larger flywheels would generate more torque but would also cause the system to require more torque to balance. The dynamics of the model were derived from a simplification that considered the trunk as static, and thus ignored accelerations imparted on the systems. Outside accelerations were considered to be negligible compared to those generated by the gyroscopes; an expansion on this topic can be found in section 4.1. Figure 2 shows the required torque to balance the system versus the amount of torque produced by the flywheels as a function of the radius of the flywheels. The point of intersection of the two curves is the critical radius of the flywheels; any radius smaller than the value

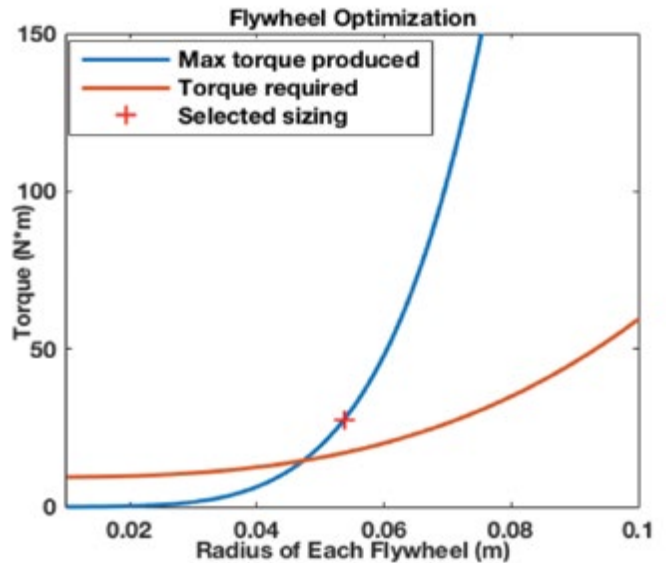


Figure 2: Scaled flywheel optimization

at the curve intersection would not be able to balance the pendulum from the desired maximum offset of 20° , and at the critical value, the system is marginally stable. Therefore, a radius higher than the critical value was found to be optimal.

The scaled flywheels were selected to have a radius of 5.37 cm and a height of 3.07 cm, weighing 2.18 kg each. The same process was performed for the full-scale device, resulting in a radius of 7 cm and a height of 0.4 cm, each weighing 4.83 kg.

The selection of the actuators for the gyroscopes was critical to the performance of the device. To maximize the torque, the maximum angular velocity and the maximum gimbal rate must be as high as possible. A DC motor was chosen to produce the steady-state angular velocity of the flywheels. The motor selected for this application had a maximum speed of approximately 10,000 RPM, and provided enough torque to achieve a spin-up time of less than two minutes, which would be appropriate for a full-scale device.

For the actuation about the gimbal axis, a high-torque servomotor was selected with a maximum speed of 7 rad/s, or about 400 deg/s. This is ideal for good performance, since $\dot{\beta}$ is the limiting variable for torque production and is constantly changing. These selections allowed the scaled model to produce a maximum torque of approximately 46 Nm, and the full-size device to generate a maximum torque of approximately 174 Nm.

2.1 Controller design

The response of the system is dependent on the torque output from the gyroscope, therefore this torque was the controlled variable in the system. Since the inertia and angular speed of the flywheels are constant, the limiting factor in torque production is the gimbal speed. A PID controller was implemented to set $\dot{\beta}$ depending on the torque required for the pendulum to return to the vertical position. The simplified system diagram is shown in Figure 3.

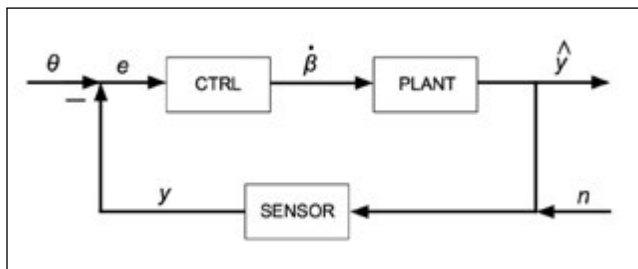


Figure 3: Complete system model

Here, θ is the desired angle, which is 0° for a vertical position. The variable e represents the error signal going into the controller, and $\dot{\beta}$ is the control signal going to the plant. The variable \hat{y} is the estimated position of the pendulum, and y is the actual position as measured by a sensor at the bottom of the pendulum. The variable n represents potential noise in the signals. The use of strictly a lead compensator (PD control) would cause the system to be faster but induce more error, and the use of just a PI controller would reduce error significantly, but would slow the system. A slower response could cause the subject to not be able to recover from an offset effectively, but increased overshoot could cause injury to the subject; thus, a PID controller was chosen for a balance between speed of response of the system and for reduction of overshoot.

3. Results

Simulations were performed in Simulink to study how quickly and effectively the system would respond to varying initial offset angles. Equation (2) was used as the plant for the system, and the torque input from the gyroscopes was modeled using equation (1).

3.1 Simulation results

The two focus metrics within the model were the recovery angle of the trunk, and the torque production of the gyroscope. The full-scale system recovered to within 10% of steady state in 0.95 seconds, with a maximum overshoot of 26.78%. For the scaled system, a rise time of 0.88 seconds was achieved from the same maximum angle of 20° . The slightly quicker response time was expected, as the inertia of the system is exponentially related to size and therefore was greatly reduced when the model was scaled. This also caused a higher overshoot, showing 48.07% at max offset. These results are shown in Figure 4.

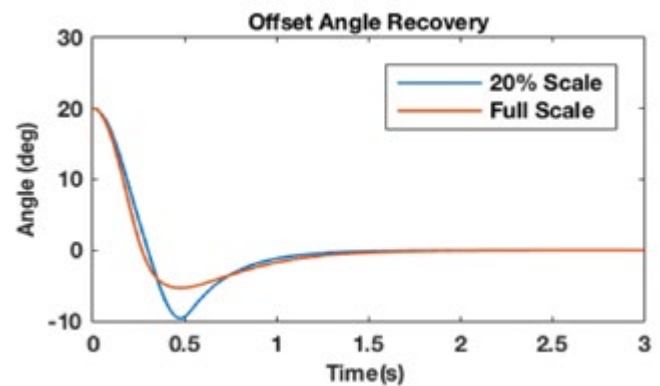


Figure 4: Offset angle of full and scale model

The placement of the device was found to be an important factor in the offset recovery results. If the full-scale device was placed on an actual exoskeleton, it would be placed such that the system was nominally balanced, which means either placing it to shift the center of mass into a desirable location, or aligning it with the center of mass of the exoskeleton. Mounting the device on the side of the pendulum to simulate how it would be mounted on an exoskeleton causes an offset torque, or a torque that has a nonzero value when the pendulum is in the vertical position.

Due to the nature of torque production from the gyroscopes, the cross product generates a cosine term, which goes to zero as θ approaches 90° . Here, the gyroscopes can no longer produce any torque in the plane of interest, and the pendulum becomes unstable. This means that the gyroscopes cannot hold an offset angle other than vertical. For this reason, the device was placed directly on top of the pendulum such that the center of mass of the gyroscopes aligned with that of the pendulum, and the offset torque was eliminated.

The key characteristic that affected how the system reacted was the torque produced by the gyroscopes, and its relation to the required torque to stabilize the trunk. The required torque was calculated using a static model at a certain offset angle θ , assuming that all accelerations are small enough to ignore. This assumption was made because on a human test subject, accelerations would be minimized to prevent the possibility of injury. Figure 5 shows the torque from the gyroscope vs. the required torque of the full-scale system, while Figure 6 represents the same comparison for the scaled model.

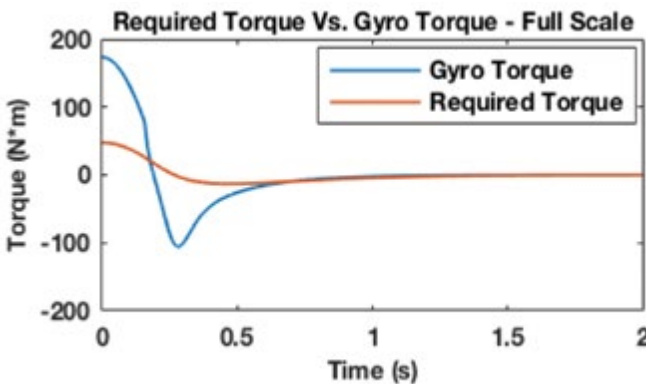


Figure 5: Torque plot for full scale model

4. Discussion

From the simulations, it can be seen that this device could steady both a full-scale model and a smaller model from the desired maximum offset angle. These devices generate enough torque for upper body balance, thus validating the stated hypothesis. However, since torque generation is directly related to the weight and inertia of the flywheel, the full-scale device quickly became heavy and cumbersome, making it improbable for actual human use. Additionally, the gyroscopes were incapable of holding an offset angle other than zero, which would hinder the effectiveness of the device in real-world applications. If a patient using an exoskeleton that utilized a gyroscopic balance system needed to bend over to perform a task, or simply wanted to lean slightly in one direction, the gyroscopes would be unable to produce a constant torque to hold that angle. This problem is also seen with the placement of the center of mass of the device.

As the gimbal angle approaches 90° , the torque decreases by a factor of $\cos(\beta)$. As the torque decreases, the controller attempts to compensate by increasing the gimbal velocity. As the gyroscopes approach the asymptote, the velocity sharply increases until it reaches the maximum. Once the angle hits 90° , the velocity of the gimbal is already maximized and the gyroscopes can no longer produce a torque in the plane of interest. Because of this, the system goes unstable.

4.1: Potential error

There were two possible sources of error within the developed model. Firstly, the required torque to return the pendulum to vertical was calculated at a given angle using the static model developed earlier. While this is

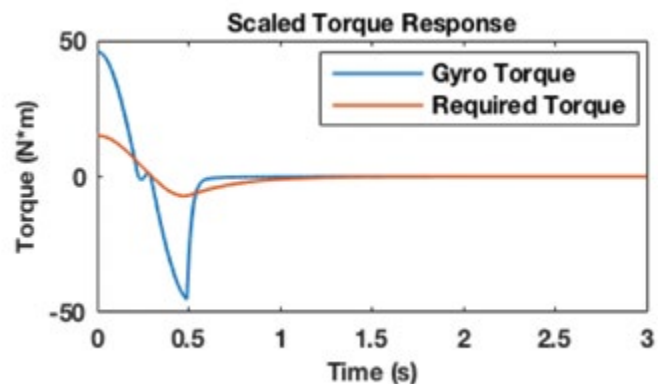


Figure 6: Torque plot for scaled down model

accurate enough for this application, it ignores accelerations of the pendulum occurring from the changing position. These accelerations were ignored because they were found to be small compared to the torques generated by the gyroscopes and the masses in the system.

Secondly, while a velocity limiter was imposed on the gyroscope model to represent the maximum speed of the servomotor controlling the gimbal speed $\dot{\beta}$, the acceleration stage of the servo was ignored. While there is an acceleration period for the servo when starting from zero velocity, it is very small for high-torque servomotors. This would only become a critical factor at offset angles resulting in balancing torques at the limits of the gyroscopes' torque range, which are angles larger than 20° . Thus, this small acceleration period was found to be negligible.

5. Conclusion

The design of the gyroscopic balance system was a success. The device could sufficiently return the trunk to vertical from the desired maximum offset angle. Additionally, both models had a rise time under one second. However, there were many issues that would prevent the device from being applied in real-world situations. Therefore, it was decided that this method of balance assistance was not the correct choice for a full-scale exoskeleton, as it would be too heavy for human use, and could not hold an offset angle other than vertical due to an asymptote in reaction torque at a gimbal angle of 90° . Other options to provide assistance, such as using high torque motors placed at the hip, will be explored and tested in the future.

6. References

- [1] Alibeji N, Kirsch N and Sharma N (2015) A Muscle Synergy-Inspired Adaptive Control Scheme for a Hybrid Walking Neuroprosthesis. *Front. Bioeng. Biotechnol.* 3:203.
- [2] Pons, J.l., J.c. Moreno, F.j. Brunetti, and E. Roco. "Lower-Limb Wearable Exoskeleton." *Rehabilitation Robotics* (2007): Web.
- [3] Sanz-Merodio, Daniel, Manuel Cestari, Juan Carlos Arevalo, and Elena Garcia. "A Lower-limb Exoskeleton for Gait Assistance in Quadriplegia." *2012 IEEE International Conference on Robotics and Biomimetics (ROBIO)* (2012): Web.
- [4] Colvin, Gregory R. "Development and Validation of Control Moment Gyroscopic Stabilization." *Diss. The Ohio State U*, 2014. Print.

7. Acknowledgments

I would like to thank Dr. Nitin Sharma, the Swanson School of Engineering, and the Office of the Provost for sponsoring this project. I also would like to thank Dr. Sharma, Naji Alibeji, and Dr. Kirsch for their guidance and support throughout my internship.

Electromyography Based Control for Lower Limb Assistive Therapy

Amanda Boyer and Dr. Nitin Sharma

*Neuromuscular Control and Robotics Laboratory, Swanson School of Engineering,
Department of Mechanical Engineering and Materials Science, University of Pittsburgh, Pittsburgh, PA, USA*

Abstract

The efficiency and impact of physical therapy techniques can be greatly increased by robotic systems. This project aims to test computational models that predict a patient's leg motion based off of the electromyographic signal. The model will then be used along with a motor to assist patients in leg exercises if they are unable to complete the movement. This paper covers three computational model approaches: an artificial neural network, a musculoskeletal model, and a combined artificial neural network/musculoskeletal model. The models did not produce useable results, but they indicated potential methods to use in the future to obtain more accurate results.

Keywords: electromyography, computational model, artificial neural network, musculoskeletal model, joint angle prediction

1. Introduction

Every year, approximately 9 million Americans use physical therapy services [1]. A large portion of the physical therapy process is repetitive exercises [2]. This can be tiring and time consuming for the physical therapist. The use of technology can assist patients in completing their exercises, which would benefit the physical therapists and allow the patients to perform these exercises at home. Robotics based neurorehabilitation is a promising technology. Recent research has shown that robotic therapy is as effective as traditional therapy [3].

In order to help patients regain leg mobility, this project aims to create a control system based on the surface electromyographic (EMG) signal. Muscles emit EMG signals as they contract [4]. This paper will discuss the first step toward EMG-based intent estimation. The objective was to create a computational model that predicts the position of the leg based on the EMG signal from the quadriceps muscles. To achieve this, three computational models were tested: 1) a sigmoid artificial neural network, 2) a musculoskeletal model, and 3) a combined musculoskeletal-neural network model.

There has been much research done on EMG signals and how they can be used. Artificial neural networks and musculoskeletal models are two of the most common methods of trying to predict variables based of the signal. For example, artificial neural networks have been used with EMG signals to identify hand forces based on forearm muscle contraction and for trunk torque estimation [5][6]. Musculoskeletal models have been used to predict elbow joint angles as well as wrist and finger movements [7][8].

2. Methods

In this study one adult participant's knee joint angle was estimated based on the EMG signals. The signal was measured with a Delsys surface EMG sensor. After the skin was cleaned with rubbing alcohol, a reference electrode was placed on the knee and an EMG sensor was placed on the skin above the vastus medialis. The participant was seated in a leg extension machine, as shown in Figure 1. An encoder was placed on the joint of the leg extension machine, providing a measurement of the knee angle. The participant was instructed to move his leg in random patterns for these experiments.

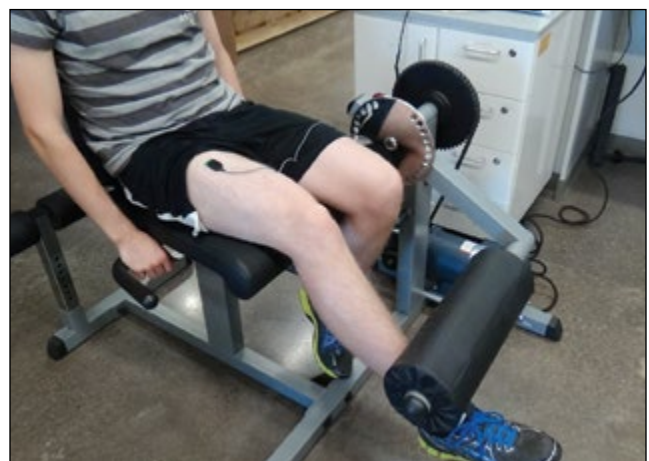


Figure 1: Leg extension machine with participant

3. Data Processing

The signal is filtered with a 20 to 450 Hz bandpass filter and a gain of 1k is applied with a Delsys Amplifier. The data was recorded at a frequency of 1000 Hz by a Quanser data acquisition device. The data was then digitally rectified and filtered with a root-mean square moving average filter of 50 steps. The square root of the signal was then taken as another filtering technique [9].

Artificial Neural Network

The first computational model used was a sigmoid artificial neural network. An artificial neural network is a computational model that relates the input to the output by putting weights on different nodes. These nodes are guided by the sigmoid function and the error of the predicted output vs. the actual output. Over time, the neural network learns the weights to predict the output, and can predict the output without using the error [10]. The neural network in this experiment uses one hidden layer with 30 nodes.

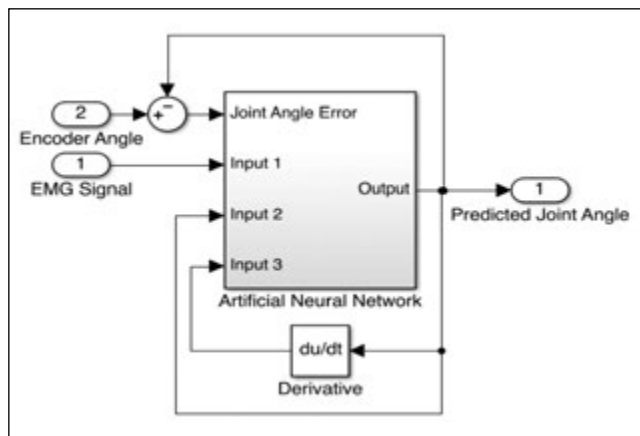


Figure 2: Caption

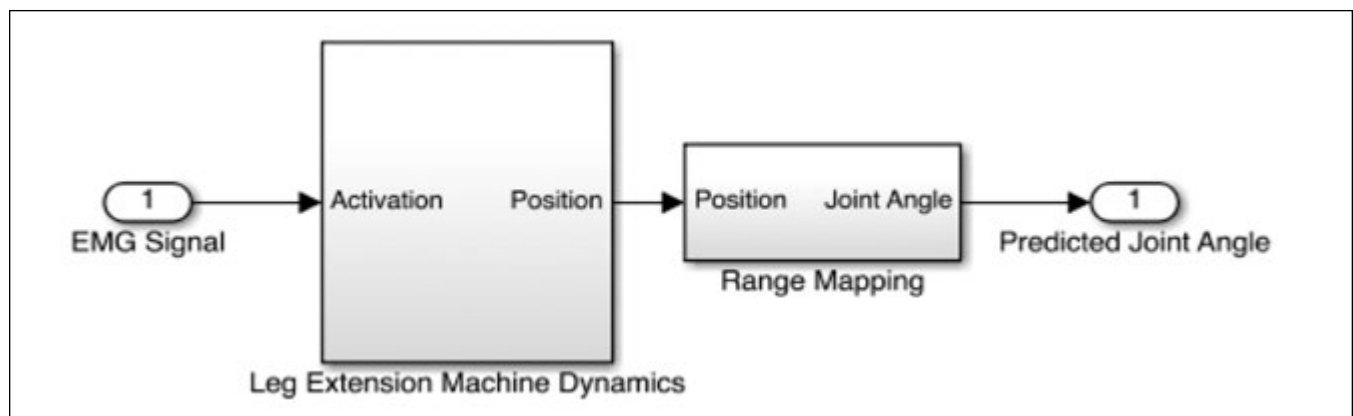


Figure 3: Block diagram of musculoskeletal model

This model was used first with a simulation of the leg extension machine dynamics. This was done to give the real time system starting weights. If the neural network has starting weights, it won't have to adjust the weights from zero and increases its chances of successfully converging on a solution. The leg extension machine dynamics were based off of work by Alibeji et al. [11]. The model uses the activation of the muscle and was modified so that this parameter is the EMG signal. The simulation uses muscle parameters of a subject that were taken from Popović et al. [12]. The system is modeled as a spring-mass-damper system, and inputs a sinusoidal joint angle and outputs the ideal activation potential of the EMG signal. For the simulation model, the input of the neural network was the ideal EMG signal and the model predicts the joint angle using the sinusoidal joint angle.

After the simulation, the neural network was used in experiments on the participant. The Simulink model was edited so that the neural network had three inputs: the EMG signal, the predicted joint angle from the neural network, and the filtered derivative of the predicted joint angle. The block diagram of this system is shown in Figure 2. The neural network was trained to output the joint angle of the leg extension machine.

Musculoskeletal Model

The second model used was the musculoskeletal model. The musculoskeletal model was the same as the simulation, except modified so that the system is reversed. This enables the model to input the EMG signal and output the position based on the leg extension machine dynamics. The output was then mapped to the range of the leg extension machine, 0-70 degrees. Figure 3 shows the block diagram of the model.

4. Results

The neural network simulations were run for 30,000 seconds with a real-time processor. During that time the neural network was learning the weights. Figure 4 shows the simulation being run again and after five seconds the learning was turned off. Here, the neural network is outputting the predicted joint angle without the assistance of the position feedback.

The root-mean square error (RMSE) before the learning was turned off is 3.94° and the RMSE after was 5.26° . This showed promising results for the experiments.

The neural network, with the weights from the simulations, was then used on the participant. The participant was sitting in the leg extension machine with the EMG signal being recorded and used as the neural network input. The joint angle was input for the error feedback. The learning for the neural network was turned on for at least 10 minutes, and then the network was run again with the same weights. In Figure 5 the learning was turned off after about 32 seconds.

The neural network experiments did not appear to be capable of learning in a feasible period of time with the

EMG input or with the EMG, angle, and velocity inputs. In Figure 5, shown on the next page, the predicted joint angle stays at zero when the learning was turned off.

The experimental model had an RMSE value of 6.40° during the learning phase and 10.14° RMSE during the non-learning phase.

The musculoskeletal model showed slightly better results, but with major limitations. For these experiments, the artificial neural network was swapped out for the musculoskeletal model. The results of this experiment are shown in Figure 6, which appears on the next page.

The model follows fast movements with an RMSE error of 9.08° , but when it attempts to predict slower movements the RMSE increases to 21.85° . The RMSE for the whole data set was 14.87° .

The third experiment was a combination of the neural network and musculoskeletal model. Instead of mapping the range for the musculoskeletal model, an artificial neural network was used to relate the musculoskeletal model output to the leg extension machine joint angle. A plot of these results is not shown, because the results were unstable and went to positive infinity.

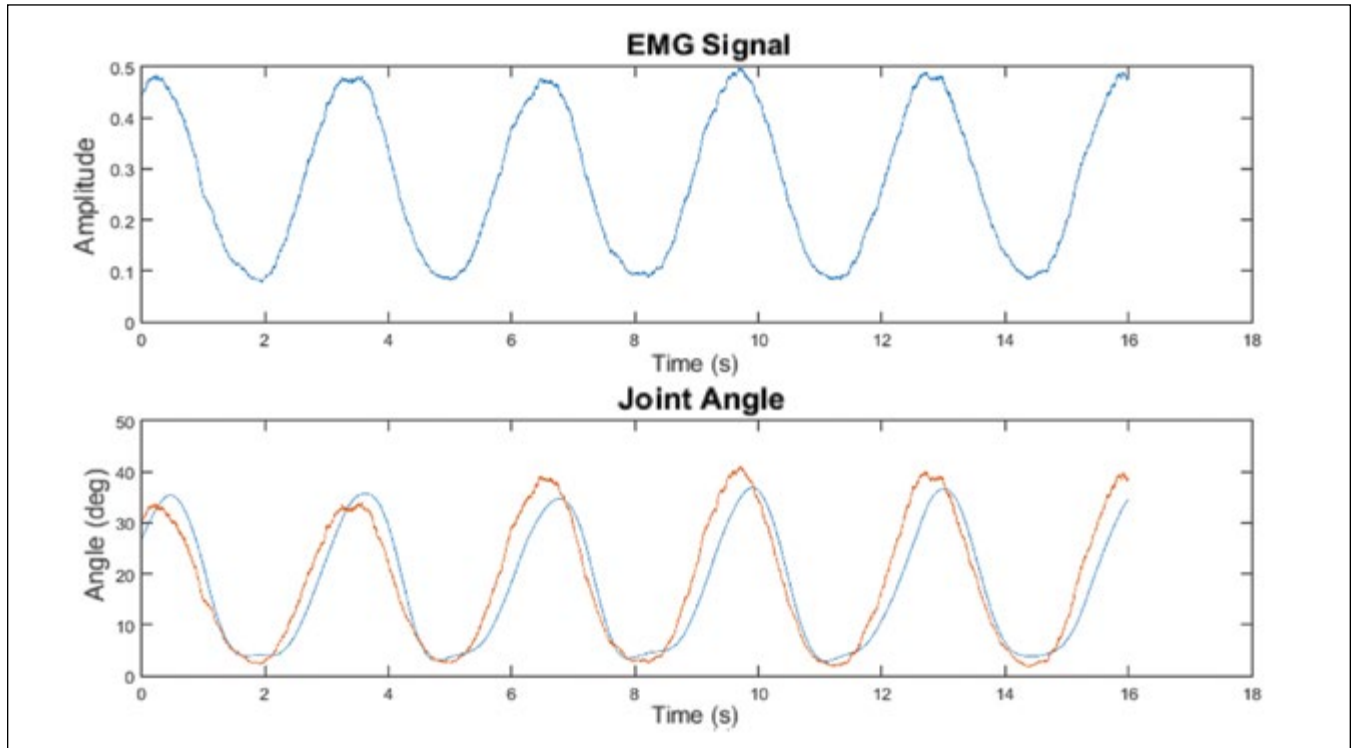


Figure 4: shows the EMG signal and position graph from neural network simulations. The red is the simulated position and the blue is the neural network's output.

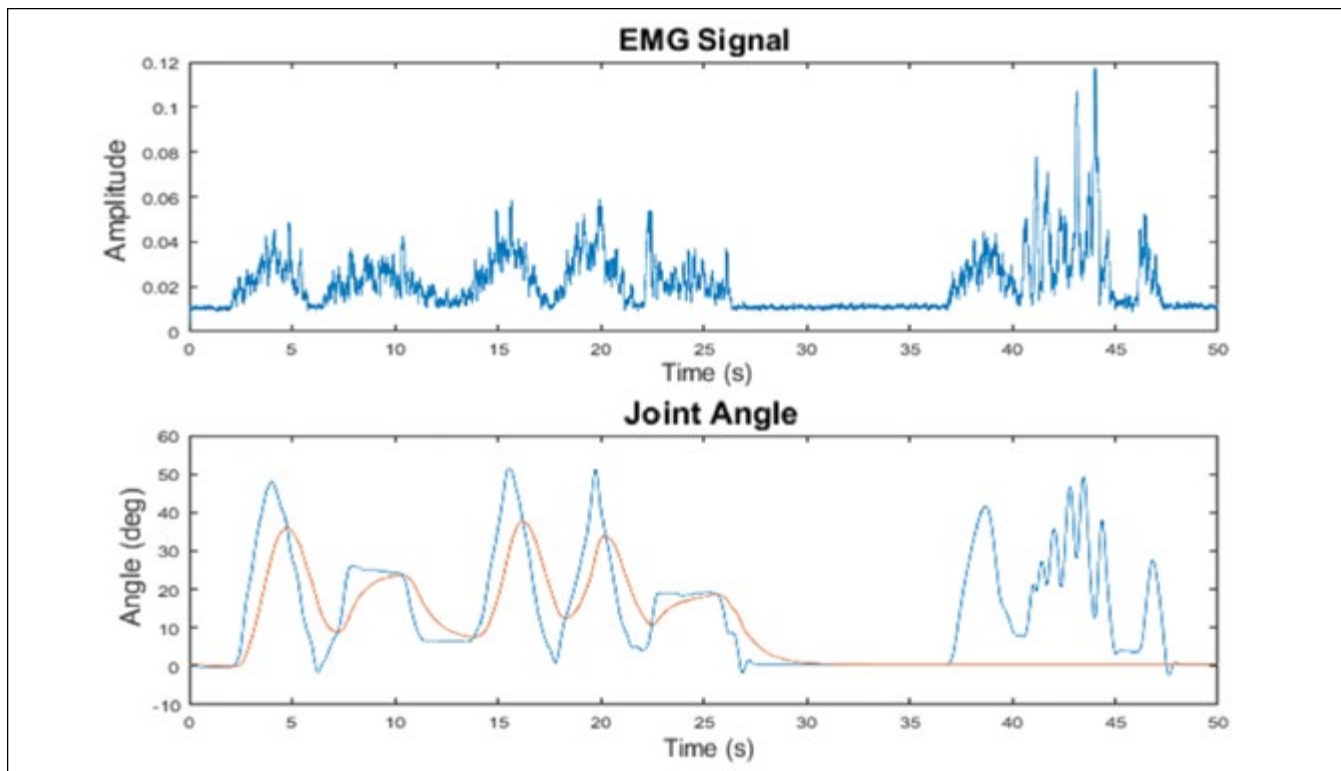


Figure 5: shows the EMG signal and position graph from neural network experiments. The blue is the position and the red is the neural network's output.

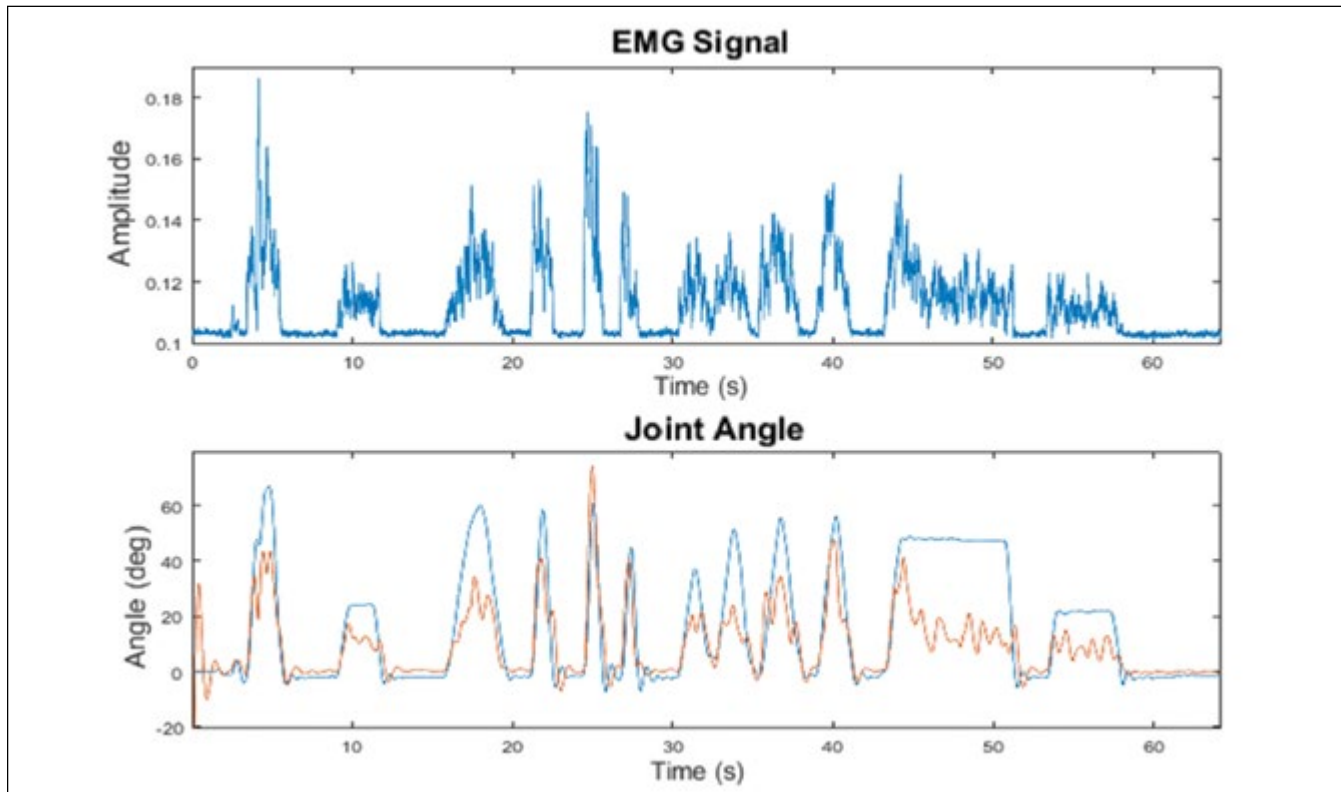


Figure 6: shows the EMG signal and position graph from musculoskeletal model experiments. The blue is the position and the red is the neural network's output.

5. Conclusion

The computational models used to predict the joint angle based on the EMG signal tested for this project were not sufficient. The artificial neural network had a RMSE of 10.14°, the musculoskeletal model had a RMSE of 14.87°, and the combined artificial neural network/musculoskeletal was unstable. The musculoskeletal model's results indicated that the system may be adjusted to create a more accurate model.

The artificial neural network could be structured in a way to make it more effective. This could be done by a different neural network method. An example of a possible method is batch processing. Batch processing would use previously acquired EMG and joint angle data to find more accurate weights to use in the experiments, without having to run the experiments in real time.

Support Vector Machine learning is another technique that could be used to predict the joint angle. Research done by Gutiérrez et al uses Support Vector Machine learning to predict forearm movement [13]. Additionally, the combined musculoskeletal and neural network model could be improved to make up for its shortcomings. After the position can be accurately estimated using the EMG signal, a motorized system can be created to make a robotic physical therapy machine for the lower limb.

6. References

1. Madden, Stacy. "Facts & Myths About Physical Therapy." *Health Net Pulse*. N.p., 21 Oct. 2014. Web. 28 Oct. 2016.
2. "Role of a Physical Therapist." *American Physical Therapy Association*. N.p., 15 Apr. 2016. Web. 28 Oct. 2016.
3. Hay, Timothy. "The Rise of Robotics for Physical Therapy." *The Wall Street Journal*. Wsj.com, 05 Aug. 2013. Web. 28 Oct. 2016.
4. Contessa, Paola, Carlo J. De Luca, and Joshua C. Kline. "EMG Sensor Placement." *Journal of Neurophysiology* 116.4 (2016): 1579-585. Delsys.com. Web.
5. Mobasser, Farid, and K. Hashtroodi-Zaad. "Rowing Stroke Force Estimation with EMG Signals Using Artificial Neural Networks." *Proceedings of 2005 IEEE Conference on Control Applications*, 2005. CCA 2005. (n.d.): n. pag. Web.
6. Szpala, Agnieszka, Alicja Rutkowska-Kucharska, Jarosław Drapała, and Krzysztof Brzostowski. "Choosing the Right Body Position for Assessing Trunk Flexors and Extensors Torque Output." *Human Movement* 12.1 (2011): n. pag. Print.
7. M. Pang and S. Guo, "A novel method for elbow joint continuous prediction using EMG and musculoskeletal model," 2013 IEEE International Conference on Robotics and Biomimetics (ROBIO), Shenzhen, 2013, pp. 1240-1245.
8. D. L. Crouch and H. Huang, "Musculoskeletal model predicts multi-joint wrist and hand movement from limited EMG control signals," 2015 37th Annual International Conference of the IEEE Engineering in Medicine and Biology Society (EMBC), Milan, 2015, pp. 1132-1135.
9. Gopura, R. A. R. C., D. S. V. Bandara, J. M. P. Gunasekara, and T. S. S. Jayawardane. "Chapter 12." *Recent Trends in EMG-Based Control Methods for Assistive Robots*. Electrodiagnosis in New Frontiers of Clinical Research, n.d. Web. 28 Oct. 2016.
10. ExtremeTech. "Artificial Neural Networks Are Changing the World." *ExtremeTech*. N.p., 11 Oct. 2015. Web. 28 Oct. 2016.
11. N. Alibeji, N. Kirsch and N. Sharma, "Dynamic surface control of neuromuscular electrical stimulation of a musculoskeletal system with activation dynamics and an input delay," 2015 American Control Conference (ACC), Chicago, IL, 2015, pp. 631-636.
12. D. Popovic, R. B. Stein, M. Namik Oguztoreli, M. Lebiedowska and S. Jonic, "Optimal control of walking with functional electrical stimulation: a computer simulation study," in *IEEE Transactions on Rehabilitation Engineering*, vol. 7, no. 1, pp. 69-79, Mar 1999.
13. Leon, M., J. M. Gutierrez, L. Leija, and R. Munoz. "EMG Pattern Recognition Using Support Vector Machines Classifier for Myoelectric Control Purposes." *2011 Pan American Health Care Exchanges* (2011): n. pag. Web.

7. Acknowledgments

Thanks to Dr. Sharma for his guidance and support. Thanks to Naji Albeji and Nicholas Kitsch for their advice and resources. Thank you to the Swanson School of Engineering, Dr. Sharma, and the Office of the Provost for funding this project.

Atomic Scale Topology Optimization Based on Finite Element Methods

Clement N. Ekaputra,^a Albert C. To, PhD^a

^a*Department of Mechanical Engineering and Materials Science,
Swanson School of Engineering, University of Pittsburgh, Pittsburgh, PA, USA*

Abstract

This work presents an atomic scale topology optimization MATLAB program. This program was developed from an existing finite element topology optimization model. Much of the original finite element program remains intact, but modifications were made to adjust for physical differences between the atomic and continuum scale, namely differences in interactions, surface effects, and long-range interactions. As a result of these modifications, optimal configurations obtained from the atomic scale program appear much more clustered, unlike the truss-like structures often seen and used at the continuum scale. However, it is unclear whether these differences in shape reflect actual physical differences between the two scales, or if they result from artificialities in the program; and future amendments to the program are discussed.

Keywords: topology optimization, atomic scale, finite element (FE) method

1. Introduction

Topology optimization is a useful method for finding efficient material configurations for a given design space, load, and support condition. By applying this method to the atomic scale, nanostructures may be designed with better mechanical properties than their bulk counterparts at the large, or continuum, scale. While continuum-scale topology optimization methods exist, similar methods are not complete at the atomic scale. It also cannot be assumed that ideal structures at continuum scale are ideal at atomic scale, since physical behaviors differ at the two scales. Surface effects and long-range interactions cause atoms to behave differently from elements in a continuum model. Therefore, atomic models must be developed, or existing continuum models modified. The primary aim of this project is to extend an existing finite-element topology optimization program to the atomic scale.

This atomic scale topology optimization program is based on top88, an 88-line finite element (FE) topology optimization MATLAB program by Andreassen et al. [1].

Much of this program remains intact. The original heuristic density updating algorithm for solving the problem of least compliance is also employed in the atomic program. More information on this method may be found in the paper regarding the 99-line topology optimization program by Sigmund [2]. In addition, modifications were made to account for atomistic behavior. First, the construction of the global stiffness matrix was revised to fit atomic interactions. Furthermore, surface effects are already considered in the program—fewer forces act on atoms near the boundary of a configuration. Lastly, long-range atomic interactions are accounted for in a further development by increasing the size of elements and amount of atoms in an element.

This paper is organized as follows. In section two, a brief overview of the atomic program will be given, with special attention given to the portions of code that have changed with respect to the FE program. In section three, the results obtained from the atomic program will be shown, and, in section four, will be analyzed in comparison with the original FE configurations. Lastly, further possible developments will be discussed.

2. Methods

2.1. Employing the Finite Element (FE) Method

Like the 88 and 99 line topology optimization programs, the design space in the atomic program consists of square elements. Then, the optimal configuration is found by heuristically modifying the density of each element to minimize the system's compliance. This process repeats until the change in the element densities is less than 1%. Thus, the final configuration is the stiffest one.

While the elements are identically implemented in each program, the physical meaning of an element differs between the atomic and FE cases. In the FE case, a design space is discretized into a number of square elements. Each element represents a space completely filled with material. The nodes at the four corners of the element are its degrees of freedom, and their displacement is

used to calculate the system's compliance. However, in the atomic case, a square lattice is assumed, so the elements that form are not a result of discretizing the design space, but rather arise naturally from the lattice structure. Furthermore, the material in each element is not at its center, but rather at its corners. The nodes of the element are not only its degrees of freedom, but are the atoms themselves. Also, the density of the element, on a scale from zero to one, represents the presence of atoms at its corners. If an atomic element has a density close to one, atoms exist at its corners. Conversely, if an atomic element has a density close to zero, atoms do not exist at its corners. Thus, this method avoids modifying most of the original FE algorithm, but at the cost of computational artificiality. Figure 1 below summarizes these differences.

Regarding the atomic interactions themselves, this model assumes that atoms behave like linear springs. The displacement of all atoms in the system is found using the matrix equation $F = KU$ (Eq. 1), where F is the force matrix containing the 2-D components of the force applied to each atom, K is the global stiffness matrix, and U is the displacement matrix containing the 2-D components of each atom's displacement. The global stiffness matrix is made up of many 8×8 element stiffness matrices, one for each element, which in turn is made up of 4×4 matrices that represent the stiffness between any two atoms in an element, given by

$$(Eq. 2) \quad K_e = k \begin{bmatrix} c^2 & sc & -c^2 & -sc \\ sc & s^2 & -sc & -s^2 \\ c^2 & -sc & c^2 & sc \\ -sc & s^2 & sc & s^2 \end{bmatrix}$$

where c, s are the direction cosines and sines of the atomic interaction. k is a constant for each pair of atoms depending on the distance between them, further addressed in Section 2.3. Additionally, the stiffness values in an element are proportional to the density of that element raised to a penalty, p (usually $p = 3$).

2.2. Surface Effects

Atoms at the boundary of a structure have fewer stiffness contributions than atoms at the center of a structure, since there are fewer atoms around it. At the continuum scale, this has little effect because a small fraction of atoms in the structure are at the boundary. However, at the atomic scale, where a larger fraction of atoms are at the boundary, surface effects play a greater role.

Recall from Section 2.1 that the stiffness of interactions between atoms is proportional to the density fraction raised to a penalty. Therefore, if an element is near the boundary and the density of that element is near zero, the stiffness of interactions between atoms in that element is also near zero, and it is like no atomic interaction occurs. Thus, surface effects are accounted for.

2.3. Long-range Interactions

At the atomic scale, atoms may interact with others beyond the nearest neighbor, even up to 10 or 20 atoms apart. For the sake of computational speed, the maximum distance of interaction is limited to three atoms apart. As seen in Section 3.3, while the compliance of the system decreases with greater interaction distance, the generated topologies change minimally, and it is expected that further increasing this distance would not significantly affect the configurations.

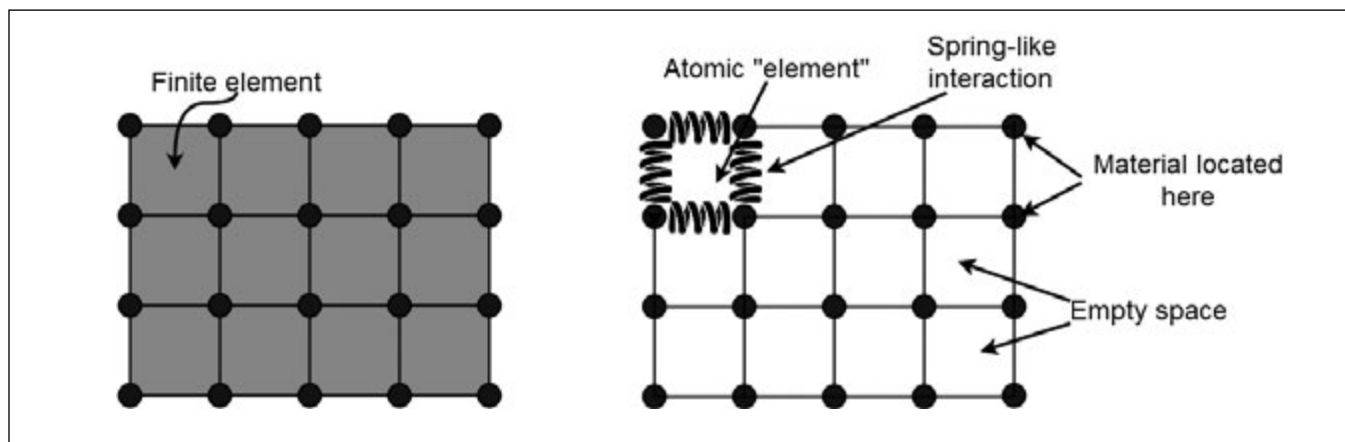


Figure 1. In the left FE diagram, the square elements are filled, with nodes at the corners. In contrast, the elements in the atomic program are mostly empty, with the material at the corners.

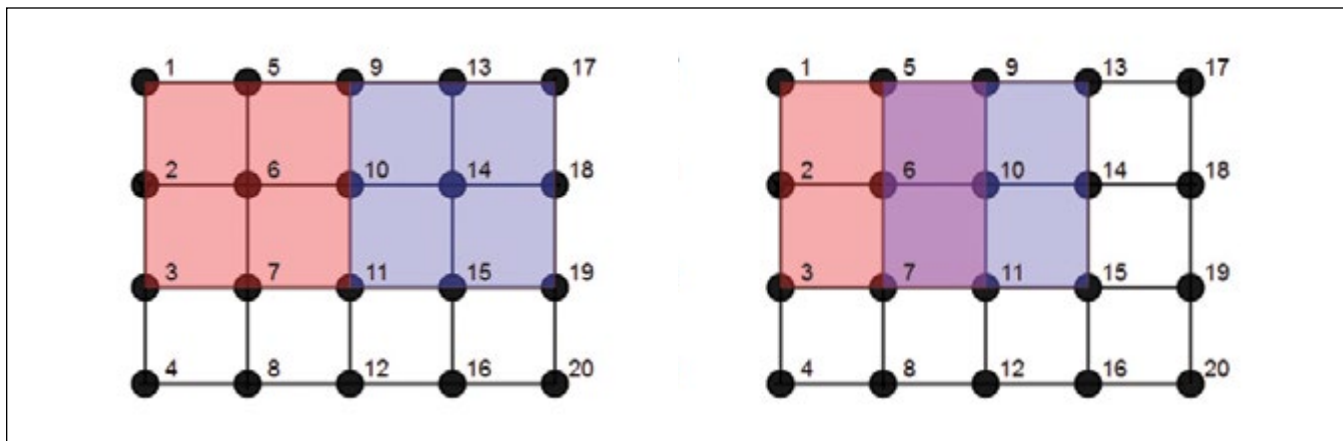


Figure 2. These lattice structures depict elements for a maximum distance of interaction of two atoms apart. The numbers next to each atom (black circle) are a numbering scheme for clarity.

To implement these long-range interactions, the size of the elements expands to include more than four atoms. For a maximum distance of interaction of two atoms apart, each element contains nine atoms, and the size of element stiffness matrix is 18x18. Similarly, for an interaction distance of three atoms apart, each element contains 16 atoms, with element stiffness matrix size 32x32. And in general, the element for a maximum distance of interaction of n atoms contains $(n+1)^2$ atoms with element stiffness matrix size $2(n+1)^2 \times 2(n+1)^2$. However, these elements must overlap in order to account for all possible atomic interactions. Figure 2 above illustrates this concept.

In this model, atomic interactions are considered if atoms are in the same element. If only the borders of elements touch, as in the left diagram, this leaves out interactions. For example, atoms 5 and 13 should interact, but since they are not in the same element, this is not considered. Therefore, elements must overlap, as depicted in the right diagram. The interaction between atom 5 and 13 is now included, and if this structure is applied to the whole design space, all possible interactions are now considered. Similar ideas may be applied for any interaction distance.

As stated earlier, the stiffness of the interaction, k , between two atoms is inversely proportional to the square of the distance between them, i.e. $k = 1/d^2$ (Eq. 3), where d is the distance between the atom. Note that values obtained for k do not reflect real-world values, but this should not affect the results. Now that the main physical differences between the continuum and atomic scale have been accounted for, the results of this study may now be presented.

3. Results

3.1. Initial Parameters

Here, the half MBB structure is used. Figure 3 shows the design space, loading points, and boundary conditions.



Figure 3. Half MBB structure: the lower right most atom is fixed vertically, while all atoms on the leftmost column are fixed horizontally. A downward force of 1 Newton is applied to the top rightmost atom. The design space is 150x50 atoms. The volume fraction of material (i.e. the initial density of each element) is 0.5.

3.2. Finite Element Configuration vs. Atomic Configuration

With the above parameters and design space, the following FE and atomic configurations are displayed in Figures 4 and 5, respectively. In all of the following configurations (Figures 4-7), the darker an element appears, the higher the density of that element. Therefore, the black spaces represent where atoms exist, and the white spaces

represent empty space. The compliance of the FE configuration (Figure 4) is 27.7525 Pa^{-1} , and that of the atomic configuration (Figure 5) is 22.0072 Pa^{-1} .



Figure 4. FE configuration. Compliance = 27.7525 Pa^{-1} .

A second program was written to calculate the compliance of FE configurations using atomic physical interactions, which is how the compliance of this structure was obtained.

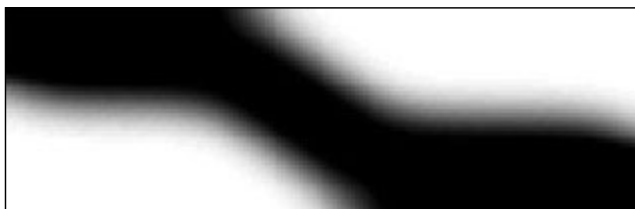


Figure 5 shows atomic configuration, interactions up to one atom apart. Compliance = 22.0072 Pa^{-1} .

Unlike the truss structures seen and used at the continuum scale with much empty space throughout the configuration, the atomic scale configurations tend to cluster, resembling a single beam. Material is concentrated near the top right corner and the bottom left corner. Note that the grey spaces near the boundary of the configuration in both the FE and atomic results occur because of density filter used in both programs to avoid checkerboard solutions [2].

3.3. Results from Studying Long-Range Interactions

Configurations for maximum range of interactions of two and three atoms apart also were obtained, shown in Figures 6 and 7 below. The compliance of the atomic configuration for an interaction distance of two (Figure 6) is 13.3564 Pa^{-1} , and that of an interaction distance of three (Figure 7) is 8.5662 Pa^{-1} .



Figure 6 shows atomic configuration, interactions up to two atoms apart. Compliance = 13.3564 Pa^{-1} .



Figure 7 shows atomic configuration, interactions up to three atoms apart. Compliance = 8.5662 Pa^{-1} .

As stated earlier in Section 2.3, the configurations obtained by extending the maximum interaction distance do not change much relative to the atomic configuration in Figure 5. The atoms also cluster, and do so around the same two corners. However, the compliance decreases, but this is expected. As more atoms act on each other, the more stiffness contributions there are on each atom, lowering the displacement of each atom and therefore the overall compliance.

4. Discussion

From Section 3.2, the atomic configurations cluster more than the FE configurations, with little empty space within the structure. One possible explanation for this is surface effects. Since atoms near the surface of a structure have fewer atoms acting on them, and therefore fewer stiffness contributions, their displacement will be higher. Conversely, atoms near the center of a structure are surrounded by more atoms, and therefore have more forces acting upon them, and have lower displacement. Therefore, since compliance decreases as displacement decreases, the fraction of atoms by the surface should be minimized. In the FE structure (Figure 4) more atoms border empty space, and the compliance is higher than in the atomic configuration (Figure 5), where the compliance is lower because more atoms are near the center of the structure.

A study conducted by Nanthakumar et al. demonstrates similar concepts, though not to the same extreme [3]. In their study, they demonstrated that without surface effects, nanoscale configurations tended to resemble a truss. With surface effects, configurations tended to conglomerate more, but still exhibited a truss structure, although still less dispersed.

Still, it is unclear if these results represent ideal atomic structures, or if they are the result of artificialities created by using the FE model. As described in Section 2, the program groups atoms into elements of four or more atoms each, and the density of the element is only representative of the “density” of the atom, “density” meaning whether or not atoms are present at the corners. A better way to approach this problem would be to modify the “density” of the atoms themselves. If the program pushes the densities toward either zero or one, similar solutions where either a location is occupied by an atom or is empty should arise. It is unclear if this will affect the results, but certainly more revisions and sources for comparison are required.

5. Conclusion

This paper presents the development of an atomic scale topology optimization program based on a finite element model. However, since atomic scale and continuum scale behaviors differ, modifications were made to the FE model to account for these physical differences. These differences in the program caused the atomic configurations

to cluster, compared to the dispersed structures obtained from the top88 program. However, it is unclear whether these discrepancies arise due to physical differences or because of incompatibility between the FE method and the atomic scale. Few sources for comparison are available, and more work is required to verify whether these results depict ideal atomic structures.

6. Acknowledgments

Many thanks to Dr. Albert To for his mentorship during this research. Also thanks to Dr. Qingcheng Yang for helping me to better understand the FE method. We gratefully acknowledge the University of Pittsburgh for sponsoring this research, and to the PPG Foundation for funding.

7. References

- [1] E. Andreassen et al., Efficient topology optimization in MATLAB using 88 lines of code. *Structural and Multidisciplinary Optimization* 43 (2010) 1-16.
- [2] O. Sigmund, A 99 line topology optimization code written in MATLAB. *Structural and Multidisciplinary Optimization* 21 (2001) 120-127.
- [3] S.S. Nanthakumar et al., Surface effects on shape and topology optimization of nanostructures, *Computational Mechanics* 56 (2015) 99-112.

Investigating Antibacterial Properties of Plasma Cleaned Polypropylene

Anthony Galante and Paul Leu

*Laboratory of Advanced Materials in Pittsburgh, Department of Industrial Engineering
Swanson School of Engineering, University of Pittsburgh, Pittsburgh, PA, USA*

Abstract

The cleanliness of plastics has become a priority in the modern age of technology, especially in the biomedical field. Preventing contamination of plastic surfaces is an absolute standard to prevent infections or ensure the effectiveness of a biomedical device. Plasma cleaning is a technique known for the unique physiochemical reactions that occur on a substrate's surface during cleaning. Changes of wettability and adhesion from these physiochemical modifications have been observed on various polymers. In this work, the changes in wettability and bacterial adhesion on polypropylene substrates caused by various plasma cleaning recipes were observed. This study aims to accommodate research toward creating self-cleaning surfaces for biomedical purposes.

Keywords: biomedical, polymer, plasma, clean

1. Introduction

Polypropylene (PP) is one of the most commonly used biomedical polymers for its unique properties such as rigidity and resistance to chemical solvents. Using this plastic for biomedical applications seems attractive, but the polymer is prone to infections when additional surface treatment is not viable [3]. Infection of biomedical polymers is one of the major hospital-induced complications that can occur during a patient's treatment. According to the American Association of Critical-Care Nurses, the most common infection from medical polymer devices is a catheter-associated urinary tract infection (CAUTI) [6]. In order to prevent the possibility of infections from hospital devices, antibacterial surface properties of treated polymers are desirable.

Approaches for creating antibacterial polymer surfaces include mixing antibacterial reagents in bulk polymers, copolymerization of antibacterial reagents and surface modification of polymer substrates [2]. Surface modification methods involve altering the physiochemical interactions between bacteria and the polymer surface

without damaging the bulk properties of the polymer [5]. Plasma surface modification is relatively expensive; however, advantageous for biomedical applications. Plasma immersion ion implantation (PIII), an extension to the plasma surface modification process, has been done on polyethylene and polyvinyl chloride with triclosan for effective antibacterial response [5]. Various gas plasmas were coupled with antibacterial agent deposition on polymer surfaces to enhance the surface antibacterial properties. This process is faster and possibly more efficient for mass production of biomedical products than other cleaning techniques.

Our research focused on how gas plasma alone can be used to alter the surface antibacterial properties for polymers, specifically PP. Polypropylene surfaces were characterized by Scanning Electron Microscopy (SEM), Atomic Force Microscopy (AFM), and contact angle measurements; also, bacterial adhesion properties were evaluated by plate-counting of *Staphylococcus Aureus* bacteria. Plasma cleaning was observed to significantly alter the surface wettability and roughness at the microscale. Additionally, plasma treatments altered the bacterial adhesion of *S. aureus*.

2. Methods

Polypropylene sheets with 0.0675-inch thickness were purchased from an online vendor and met ASTM D4101-0112 specifications regarding the chemical and structural integrity of the specimens. Polypropylene discs of equal 0.5-inch diameter were made by a custom hole punch supplied by the Swanson Center for Product Innovation. Afterward, disc samples were cleaned of all organics and solvents with acetone, methanol, and isopropyl alcohol.

Samples were plasma cleaned at the Gertrude E. and John M. Petersen Institute of NanoScience and Engineering at the University of Pittsburgh. Plasma cleaning or reactive ion etching (RIE) involves the bombardment of surfaces by activated ions from radio frequency gas plasma.

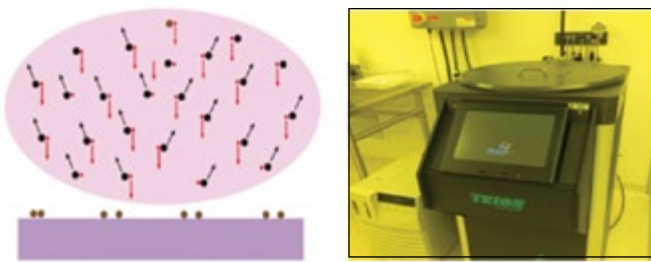


Figure 1: Schematic of ion exchanges between plasma and substrate during plasma cleaning and the RIE machine used at the Nanoscale Fabrication and Characterization Facility at Pitt

This process is favorable for fast, effective cleaning and etching of substrates. Experiments were made with different types of gas plasmas in order to observe the possible effects of plasma-cleaned polypropylene. Power, pressure, flow rate, and time are the parameters that control the plasma cleaning process.

In literature, hydrophilic polypropylene substrates were obtained by oxygenated surfaces with argon or oxygen gas plasma [1]. Our oxygen plasma treatment was performed at the optimal conditions based on many trial experiments: RF power = 100W, pressure = 75mTorr, flow rate = 25sccm and treatment time = five minutes. Under these conditions, super hydrophilicity was confirmed by measuring contact angles less than 30° for at least four hours. Moreover, super hydrophobicity (contact angle > 150°) was obtained on PP surfaces from fluorinating the surface with different fluorine present gas plasmas (CF₄, SF₆) [4]. The fluorinated gas plasma treatment was performed at the following processing parameters: RF power = 100W, pressure = 300mTorr, flow rate = 60sccm (CF₄) and 80sccm (SF₆).

3. Data Processing

The surface morphology and roughness of the modified polymer samples were measured by Atomic Force Microscopy (AFM) and Scanning Electron Microscopy (SEM). Surface wettability also was observed via contact angle from equal sized drops of water in a controlled environment.

Before testing surface bacterial adhesion, treated samples were confirmed to be super hydrophilic and super hydrophobic with contact angle measurements. Afterwards, the untreated sides were glued inside polystyrene 1-inch diameter circular wells with silicone gel. The wells were

placed in a vacuum chamber and then transported to the UPMC Ear & Eye Institute for bacterial adhesion testing. The tests involved exposing the treated surfaces to bacteria grown in a saline media solution. The non-adherent bacteria were detached from the samples in solution ultrasonically. After one hour, the samples were quantified in counting forming units (CFUs).

4. Results

AFM and SEM images demonstrated changes in surface roughness with varying treatments. These significant physical changes have potential to alter the adhesion properties of the surface material. SEM was used to confirm surface morphology changes and further explore the findings. The following 3-D plots and SEM images demonstrate the different physical features obtained by plasma cleaning.

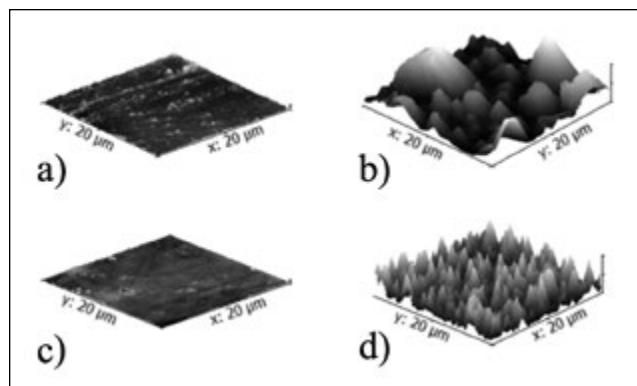


Figure 2: 3-D plots by AFM show physical surface at microscale of different recipes. Note: X-Y-Z Axes = 20μm-20μm-5μm
a) untreated b) Oxygen plasma
c) Argon plasma d) fluorinated plasma

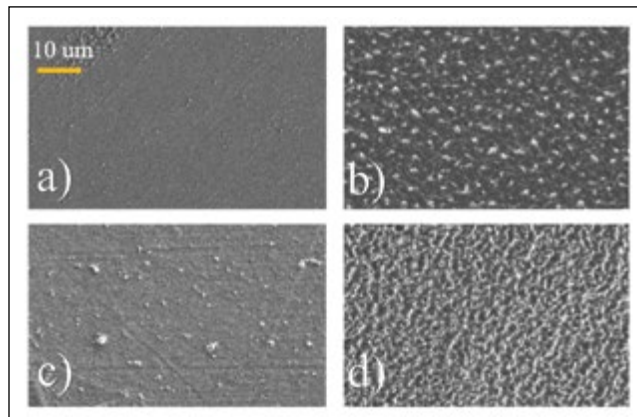


Figure 3: SEM images a) untreated b) fluorinated plasma
c) Oxygen plasma d) Pd deposition and Argon plasma

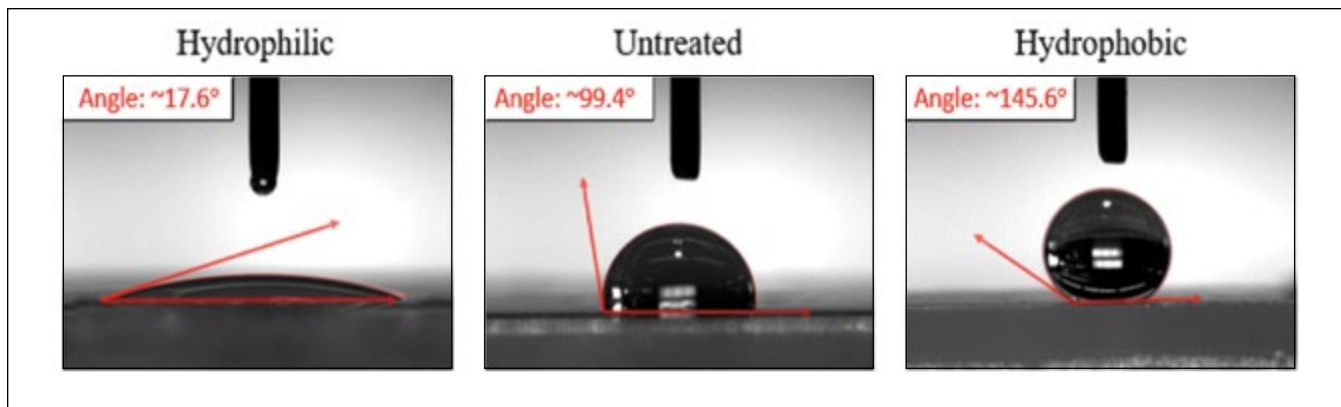


Figure 4: Range of wetting behavior obtained by plasma-treated polypropylene

Moreover, plasma cleaning significantly altered the wetting properties of polypropylene substrates. Treatment recipes were tailored in order to fully observe the different types of wetting behaviors on polypropylene surfaces. The full range of wettability obtained in plasma-cleaned polypropylene is demonstrated in Figure 4. The most hydrophilic sample (left, angle = 17.6°) is compared to an untreated sample (middle, angle = 99.4°) and the most hydrophobic sample (right, angle = 145.6 °) observed in experiments.

Figure 5 shows the bacterial adhesion of five different sample coupons. Results show an interesting difference between bacterial adhesion and plasma treatment recipes with *S. aureus* colonies. *S. aureus* appears to adhere less to treated polypropylene samples obtained from various plasma compared to untreated samples as shown

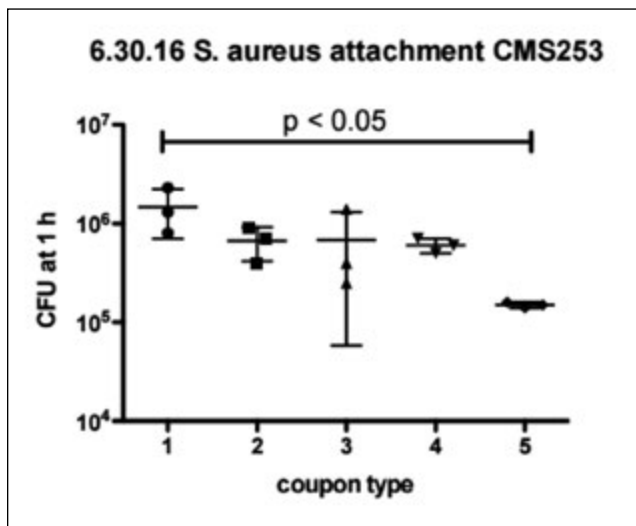


Figure 5: Colony forming unit (CFU) counts of *S. aureus* bacterial adhesion for different surface treatments

in Figure 5. The coupons consisted of polypropylene samples under a different plasma-cleaning recipe, except coupon 1 being the control.

Future work is to be conducted testing the adhesion of different bacteria, specifically *E. Coli*, under the same plasma cleaning recipes. Furthermore, XPS must be conducted to observe the surface chemistry of the samples. Surface chemistry is known to be a key factor for bacterial adhesion on polymers [3]. Certain bacterial species may adhere less to plasma cleaning recipes on polypropylene; therefore, it is important to continue investigating this cleaning process for? biomedical material.

5. Conclusion

Research for obtaining antibacterial polymer surfaces alternative to the use of biocide releasing or antibiotic agents is a positive step for finding more sustainable anti-infecting methods. Biocides and other antibiotic agents kill mutualistic bacteria in the human body and in the environment. Furthermore, these methods increase the overall tolerance of bacteria survival, resulting in the constant need to accommodate for the intelligent evolution of bacteria. Exploring alternative surface anti-infecting methods that may reduce the initial adhesion of bacteria potentiates a sustainable practice to prevent bacterial infections.

6. References

- [1] V. Švorčík, K. Kolářová, P. Slepčík, A. Macková, M. Novotná, and V. Hnatowicz, "Modification of surface properties of high and low density polyethylene by Ar plasma discharge," *Polym. Degrad. Stab.*, vol. 91, no. 6, pp. 1219–1225, Jun. 2006.

[2] F. Siedenbiedel and J. C. Tiller, “Antimicrobial Polymers in Solution and on Surfaces: Overview and Functional Principles,” *Polymers*, vol. 4, no. 4, pp. 46–71, Jan. 2012.

[3] A. Popelka, I. Novák, M. Lehocký, I. Chodák, J. Sedliačik, M. Gajtanska, M. Sedliačiková, A. Vesel, I. Junkar, A. Kleinová, M. Špírková, and F. Bílek, “Antibacterial Treatment of Polyethylene by Cold Plasma for Medical Purposes,” *Molecules*, vol. 17, no. 12, pp. 762–785, Jan. 2012.

[4] M. Strobel, S. Corn, C. S. Lyons, and G. A. Korba, “Plasma fluorination of polyolefins,” *J. Polym. Sci. Part Polym. Chem.*, vol. 25, no. 5, pp. 1295–1307, 1987.

[5] D. J. Balazs, K. Triandafillu, Y. Chevolut, B.-O. Aronsson, H. Harms, P. Descouts, and H. J. Mathieu, “Surface modification of PVC endotracheal tubes by oxygen glow discharge to reduce bacterial adhesion,” *Surf. Interface Anal.*, vol. 35, no. 3, pp. 301–309, Mar. 2003.

[6] D. Hegemann, H. Brunner, and C. Oehr, “Plasma treatment of polymers for surface and adhesion improvement,” *Nucl. Instrum. Methods Phys. Res. Sect. B Beam Interact. Mater. At.*, vol. 208, pp. 281–286, Aug. 2003.

[7] “home:whyx:proj:thick_oil:wettability.jpg[home].” [Online]. Available: http://phylab.fudan.edu.cn/lib/exe/detail.php?id=home%3Awhyx%3Aproj%3Alotus_leaf&media=home:whyx:proj:thick_oil:wettability.jpg. [Accessed: 21-Jul-2016].

[8] T. Jacobs, R. Morent, N. Geyter, P. Dubruel, and C. Leys, “Plasma Surface Modification of Biomedical Polymers: Influence on Cell-Material Interaction,” *Plasma Chem. Plasma Process.*, vol. 32, no. 5, pp. 1039–1073, Jul. 2012.

7. Acknowledgments

Thank you to the Mascaro Center for Sustainable Innovation for facilitating our research experience and the Swanson School of Engineering’s Office of Diversity for the opportunity to be a part of the INVESTING NOW program. Thanks to Dr. Paul Leu, Imrul Kayes, and Tongchuan Gao for their mentoring and suggestions that were provided over the time spent under their advisement. We offer additional thanks to Dr. Robert Shanks, Nick, and Jake at the UPMC Ear & Eye Institute.

Cell Recoverability After Exposure to Complex Engineered Nanoparticles

Julie Hartz, Sharlee Mahoney, Thomas Richardson, Ipsita Banerjee, and Götz Veser

Department of Chemical and Petroleum Engineering, Swanson School of Engineering, University of Pittsburgh, Pittsburgh, PA, USA

Abstract

Over the past decade, the use of nanoparticles (NPs) and complex engineered nanomaterials (CENs) in both consumer products and industrial applications has been significantly increasing because of their unique physical and chemical properties which differ from their bulk forms. However, despite their promise, NPs could have unforeseen, detrimental health effects on humans and the environment due to their unique properties, which motivates our lab to study toxicity of CENs.

In this study, our lab investigates the toxic effects of Ni/SiO₂ CENs on 3T3 fibroblasts because they are widely used catalysts composed of a toxic metal (Ni) and nontoxic support (SiO₂). We are specifically interested in cell recoverability, i.e., what happens when cells are exposed to CENs followed by a period without exposure? To assess toxicity, cell metabolism and intracellular Ni²⁺ ion concentration were measured. Results showed that while cells exposed to NiCl₂ experienced nearly full recovery, those exposed to the CENs experienced a continuous decrease in metabolism even after the recovery period. We hypothesize a Trojan horse toxicity mechanism is taking place in cells exposed to the CENs which prevents the cells from expelling CENs and causes the long term toxicity.

Key Words: complex engineered nanomaterials, toxicity, recoverability

1. Introduction

Over the past decade, the applications of nanotechnology in industry and consumer products have drastically increased. Medicine, catalysis, and many more fields have been completely revolutionized by nanoparticles (NPs) [1]. They are being employed in promising new applications in these fields because NPs possess different physical and chemical properties than the same material in their analogous bulk forms [2]. For example, nickel NPs display favorable catalytic properties, which allow

them to be used in petroleum refining, hydrogen production via methane reforming, and even high performance lithium ion batteries [3-5].

However, despite their significant promise, increasing evidence suggests that NPs could have unforeseen, detrimental health effects on humans and the environment due to their unique properties [6, 7]. Current environmental and health regulations regarding NPs treat them essentially identically to their bulk substances, neglecting the significant differences between the two [8, 9]. This absence of an appropriate regulatory framework is largely due to a lack of understanding of the toxic effects of NPs, which could guide such regulations. The ultimate goal of our research is to establish an improved understanding of nanotoxicity based on identification of correlations between NP structural elements and toxicity so that regulations can be improved.

Our work focuses specifically on complex engineered nanomaterials (CENs) composed of Ni NPs embedded in an amorphous, porous SiO₂ support. Ni/SiO₂ CENs are commonly used in the catalysis industry because SiO₂ functions as an inert support that prevents the metal NPs from aggregating, which can cause deactivation [4]. However, Ni NPs are known to be toxic [10]. Therefore, it is necessary to understand the long-term toxicity of these materials in order to determine any health ramifications they could pose to those who encounter them.

Many studies regarding nanotoxicity investigate the effects of exposure to a nanomaterial over time. However, nonstop exposure to a nanomaterial is unrealistic. For the present study, we were interested in recoverability and long-term toxicity, i.e., what happens when the cells are exposed to the CENs for some time followed by a period of no exposure? A 3T3 fibroblast - mouse skin cell—*in vitro* toxicity model was employed since these cells are cheap, robust, and widely available [11]. To determine long-term toxicity, cells were exposed to either non-hollow Ni on SiO₂ (“nhNi@SiO₂”) CENs or NiCl₂ for 24 hours

followed by a 24-hour “recovery period” of no exposure. Cell metabolism and intracellular Ni²⁺ ion concentration were measured both directly after exposure, as well as after the recovery period to determine if the cells could expel the toxin and restore their metabolism.

2. Methods

2.1 3T3 Fibroblast Cell Culture

Mouse-derived NIH 3T3 cells were used to evaluate recoverability after exposure to nhNi@SiO₂. Cells were cultured in Dulbecco’s Modified Eagle Medium (DMEM, Life Technologies) supplemented with 10% fetal bovine serum (FBS, Atlanta Biologicals) and 1% penicillin streptomycin (P/S, Life technologies), referred to as 3T3 media. The cells were cultured at 37°C in a 5% CO₂ environment. Cells were passaged at 70% confluence (every 2-4 days). They were seeded at 125,000 cells/well in 12-well plates.

2.2 CEN Synthesis

NhNi@SiO₂ CENs were synthesized using a one pot reverse micro emulsion that was developed and reported previously by the Veser lab [12]. The CENs are composed of Ni NPs embedded in an amorphous, porous SiO₂ support. CEN size and morphology were characterized with transition electron microscopy (TEM, JEOL-2000FX electron microscope). To sterilize the CENs for the nhNi@SiO₂ media solutions, they were exposed to UV light for one hour. Subsequently, the CENs were sonicated for 15 minutes at a concentration of 800 mg Ni/L in 3T3 media supplemented with 20 mM HEPES buffer. All nhNi@SiO₂ solutions were loaded into 12-mm diameter Transwell Permeable Supports (Corning), which were then placed in wells that had already been seeded with cells and contained 1.5 mL of 3T3 media.

2.3 MTS Cell Metabolism

To determine cell metabolism, a CellTiter 96® Aqueous One Solution Cell Proliferation Assay MTS assay (Promega) was used according to manufacturers instructions. The assay measures cells’ ability to reduce [3-(4,5-dimethylthiazol-2-yl)-5-(3-carboxymethoxyphenyl)-2-(4-sulfophenyl)-2H-tetrazolium; MTS] into a formazan product. Twenty-four hours after seeding the cells, 0.5 mL of 800 mg Ni/L solution nhNi@SiO₂ solution was added to two Transwells, which were placed inside the wells. The cells were exposed for 24 hours, after which the CEN-containing Transwells were removed, and the

CEN-containing media was aspirated out of the wells. For one well, 480 µL of DMEM/FBS+20% MTS was added to determine cell metabolism immediately after exposure. The cells were incubated for one hour, and the absorbance at 490 nm was measured with a Synergy 2 multimode Microplate Reader. The other well, however, was given 1.5 mL of fresh media and incubated for a 24-hour “recovery period.” These cells were then subjected to the MTS assay to determine metabolism after the exposure had been removed.

This cell metabolism recovery experiment was repeated using a 200 mg Ni/L solution of NiCl₂ instead of the nhNi@SiO₂. We chose a 200 mg Ni/L solution because in the previous study, there was 0.5 mL of 800 mg Ni/L CEN solution and 1.5 mL of 3T3 media in each well. Thus, the effective exposure was calculated to be 200 mg Ni/L of nhNi@SiO₂. The analogous NiCl₂ concentration was therefore 200 mg Ni/L. Cells were exposed 24 hours after seeding and incubated for 24 hours. Subsequently, one well was analyzed via MTS, while the other well was given fresh 3T3 media and a 24-hour “recovery period” of incubation, immediately followed by MTS.

2.4 Newport Green Intracellular Ni²⁺ Concentration

To analyze intracellular Ni²⁺ ion concentration, Newport Green™ DCF indicator (NPG, Life Technologies) was used. The dye’s fluorescence is magnified by the presence of Ni²⁺ ions, so it can be used to study the intracellular Ni²⁺ ion concentration [13]. Twenty-four hours after seeding, 0.5 mL of 800 mg Ni/L nhNi@SiO₂ solution was added to two Transwells and placed inside the wells. The cells were exposed for 24 hours, after which the CEN-containing Transwell was removed, and the media was aspirated out of the well. For one well, cells were incubated for 20 minutes in 0.5 mL of 10 µM NPG solution. After the incubation period, the cells were washed with PBS, collected using trypsin, centrifuged, rinsed, and resuspended in PBS. Finally, an Accuri C6 flow cytometer was used to quantify the Newport Green fluorescent intensity. At least 10,000 events were collected per sample to obtain a viable histogram. In parallel, the other well was given 1.5 mL of fresh 3T3 media and incubated for a 24-hour “recovery period.” The cells were subsequently run through the same Newport Green assay to determine intracellular Ni²⁺ concentration after exposure was removed.

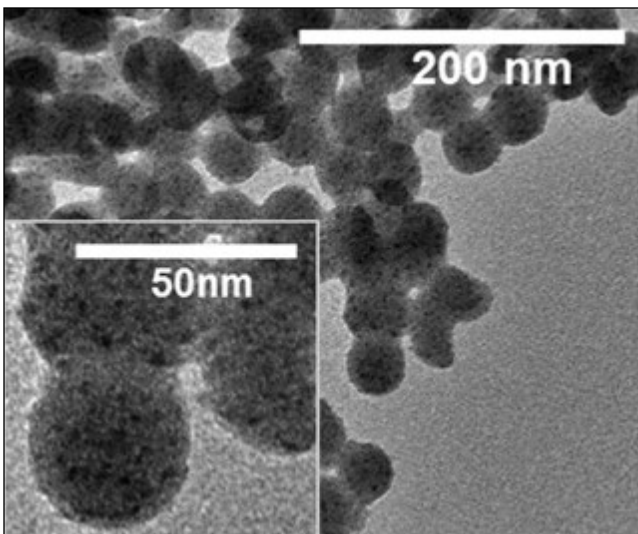


Figure 1. TEM image of nhNi@SiO₂ depicting the Ni NPs (small, black spheres) embedded within the SiO₂ shell (large, lighter spheres)

3. Results

3.1 CEN Synthesis

The structures of all synthesized nhNi@SiO₂ CENs were thoroughly observed using TEM. Figure 1 shows the resulting CENs. The CENs themselves are ~50 nm in diameter, while the embedded Ni NPs are ~2 nm in diameter.

3.2 MTS Cell Metabolism

After exposure to nhNi@SiO₂, cell metabolism decreased by 23%, while cells exposed to NiCl₂ experienced a decrease of 54%. However, when granted a recovery period with no exposure, the cells that had been exposed to nhNi@SiO₂ experienced an additional 10% decrease in metabolic function. Alternatively, cells that had been exposed to NiCl₂ exhibited almost full recovery after the 24 hours of no exposure, returning metabolism back to 98% of its original functionality. The results of the MTS assay can be seen in Figure 2.

3.3 Newport Green Intracellular Ni²⁺ Ion Concentration

After exposure to nhNi@SiO₂, the intracellular Ni²⁺ concentration increased to 1.35 times the control value. Cells that were exposed to nhNi@SiO₂ and granted the 24-hour recovery period displayed almost identical intracellular Ni²⁺ concentrations as those that had no recovery time, exhibiting 1.37 times as much Ni²⁺ as the control cells. The results of the Newport Green assay can be seen in Figure 3.

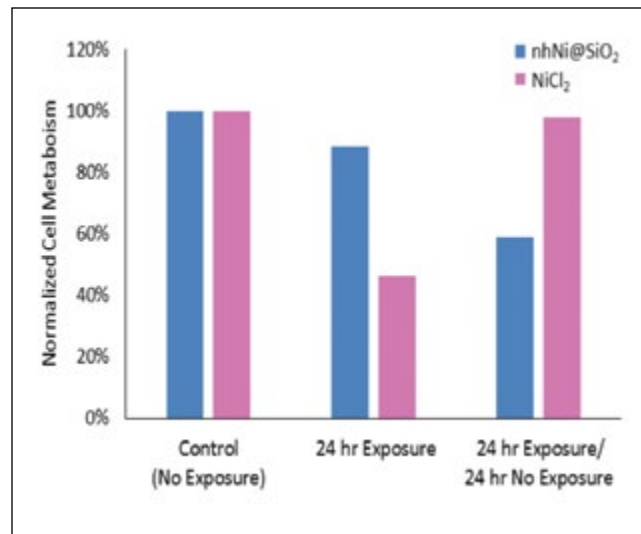


Figure 2. Normalized cell metabolism of cells exposed to either 800 mg/L nhNi@SiO₂ solution via Transwell or 200 mg/L NiCl₂ solution for 24 hours followed by a 24-hour “recovery period” of no exposure. Data was normalized to the control cells which were incubated in regular 3T3 media for 24 hours. The recovery data suggests that cells have a clearance mechanism for Ni²⁺ ions but not CENs.

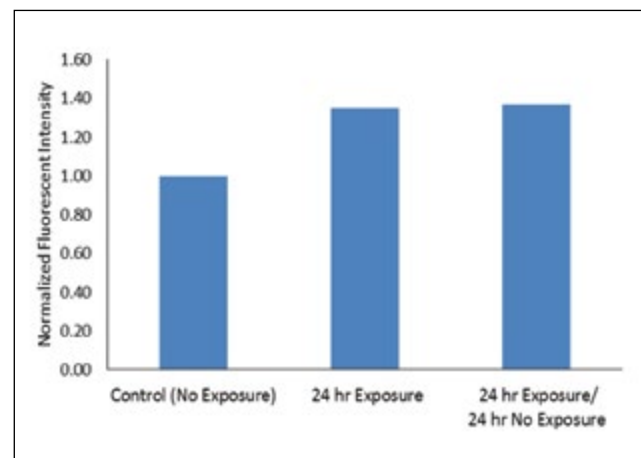


Figure 3. Intracellular Ni²⁺ ion concentration of cells exposed to 800 mg/L nhNi@SiO₂ solution via Transwell for 24 hours followed by a 24-hour “recovery period” of no exposure. Fluorescent intensity was normalized to the control cells which were incubated for 24 hours in CEN-free 3T3 media. The results indicate that the cells do take up the CENs, after which they cannot expel them.

4. Discussion

4.1 MTS Cell Metabolism

Because cell metabolism decreased after the cells were exposed to both nhNi@SiO₂ and NiCl₂, it is apparent that both materials elicit a toxic response in the fibroblasts. The more significant decrease in metabolism from the cells exposed to NiCl₂ indicates that NiCl₂ is initially more toxic than the CEN. However, the fact that cell metabolism recovers to nearly full functionality after exposure was removed implies that the cells have some kind of clearance mechanism to expel the toxic Ni²⁺ ions within the cell. Cells exposed to nhNi@SiO₂ did not experience a recovery in cell metabolism after the exposure was removed. This indicates that once the CENs enter a cell, the cell cannot expel them, causing long-term toxicity.

4.2 Newport Green Intracellular Ni²⁺ Ion Concentration

The increase in fluorescent intensity after 24 hours of exposure can be correlated to an increase in intracellular Ni²⁺ concentration, which confirms that the CENs are being taken up by the cells. Also, the fact that intracellular ion concentration effectively stays constant after the 24 hour period of no exposure further validates the hypothesis that once inside, the cells cannot expel the CENs.

We hypothesize that the following Trojan horse mechanism of toxicity is occurring within the cells that have been exposed to nhNi@SiO₂: Cells take up the CENs during the 24 hour exposure period. Once inside, the CENs cannot be ejected. They are transported to the lysosomes—organelles that are responsible for eliminating waste in the cell. Inside the lysosome, toxic Ni²⁺ ions are given off by the Ni NPs. Because they are contained within the lysosome, some toxic response is elicited, but it is mitigated. However, over time, the lysosome begins to fail, and the toxic Ni²⁺ ions leak out and affect the other organelles, causing more toxicity. This hypothesis accounts for the fact that intracellular Ni²⁺ concentration stays constant after the recovery period, while cell metabolism continues to decrease. The CEN initially produces a finite amount of Ni²⁺ ions which harms the cell, and when they leak out of the lysosome, the cell is damaged more severely.

A previous study in our lab used confocal microscopy to determine the location of Ni²⁺ ions and lysosomes in cells that had been exposed to nhNi@SiO₂ or NiCl₂ in order to validate the Trojan horse mechanism [14]. The

results showed that in the cells exposed to the CEN, the Ni²⁺ ions are often colocalized with lysosomes. This explains why the CENs exhibited a less toxic response than the NiCl₂ after the 24-hour exposure. Because the toxic ions were contained in the lysosome, damage was mitigated. However, in the cells that were exposed to NiCl₂, there was less colocalization, i.e., the Ni²⁺ ions were present throughout the entire cell. Hence, why NiCl₂ initially exhibited a more toxic effect on metabolism after the 24-hour exposure. Because the toxic ions were not contained in the lysosomes, they were free to damage the entire cell. Additionally, since the ions were floating freely throughout the cell, they could diffuse out of the cell when the exposure was removed, which is demonstrated by the cells' metabolic recovery. The confocal microscopy data further validates the Trojan horse mechanism hypothesis.

5. Conclusions

Results from the recoverability studies demonstrate that a Trojan horse mechanism occurs within cells that have been exposed to Ni/SiO₂ CENs. Confocal microscopy data from previous studies show that in cells exposed to the CENs, Ni²⁺ ions are often located within lysosomes, which we believe initially, partially shields the cell from the toxic effects. Once compromised, however, the ions may leak out of the lysosome harming the rest of the cell. However, those exposed to NiCl₂ had less localization of ions in the lysosomes. These phenomena explain the results of the recoverability studies well. Because the CENs initially remain in the lysosomes while Ni²⁺ ions from the NiCl₂ are spread throughout the cell, metabolism in cells exposed to the CEN only decreased by 23% while those exposed to NiCl₂ decreased by 54%. While, it is evident that the cells have some form of clearance mechanism for free Ni²⁺, which accounts for the NiCl₂ recovery, it is the fact that cells cannot eject the Ni/SiO₂ CENs once inside, and the Trojan horse mechanism, that prevents cells from being able to recover even after exposure is removed.

In addition to nhNi@SiO₂, we intend to rerun this same study with other Ni/SiO₂ CENs that are structured in different conformations. This will allow us to determine if the Trojan horse mechanism holds true regardless of structure. It will also give insight into correlations between structure and toxicity which can ultimately aid in proper regulation of these nanomaterials.

6. Acknowledgments

I would like to show my immense gratitude to PPG Industries and the Swanson School of Engineering for supporting this research. My thanks also are extended to my research mentors Dr. Götz Veser and Dr. Ipsita Banerjee, as well as Thomas Richardson, Jason Ferree, and Sharlee Mahoney, for their guidance, patience, and wisdom.

7. References

- [1] Roco, M.C., *The long view of nanotechnology development: the National Nanotechnology Initiative at 10 years, in Nanotechnology Research Directions for Societal Needs in 2020*. 2011, Springer. p. 1-28.
- [2] Love, Sara A., Melissa A. Maurer-Jones, John W. Thompson, Yu-Shen Lin, and Christy L. Haynes. "Assessing Nanoparticle Toxicity." *Annual Review of Analytical Chemistry* 5.1 (2012): 181-205. Web.
- [3] Group, T.W., *The importance of nickel compounds: catalysts*. 2007, European Nickel Institute.
- [4] Prakasham, R.S., et al., *Nickel-impregnated silica nanoparticle synthesis and their evaluation for biocatalyst immobilization*. *Applied biochemistry and biotechnology*, 2010. 160(7): p. 1888-1895.
- [5] Mai, Y.J., et al., *Graphene anchored with nickel nanoparticles as a high-performance anode material for lithium ion batteries*. *Journal of Power Sources*, 2012. 209: p.1-6.
- [6] Nel, A., et al., *Toxic potential of materials at the nanolevel*. *Science*, 2006. 311(5761): p. 622-627.
- [7] Oberdoester, G., *Nanotoxicology: An Emerging Discipline Evolving from Studies of Ultrafine Particles* (vol 113, pg 823, 2005). *Environmental Health Perspectives*, 2010. 118(9): p. A380-A380.
- [8] "Control of Nanoscale Materials under the Toxic Substances Control Act." EPA. Environmental Protection Agency, 8 Sept. 2016. Web.
- [9] "FDA's Approach to Regulation of Nanotechnology Products." *U.S. Food and Drug Administration*. 5 Aug. 2015. Web.
- [10] Zhao, J., et al., *Occupational toxicology of nickel and nickel compounds*. *Journal of Environmental Pathology, Toxicology and Oncology*, 2009. 28(3).
- [11] Nel, A., et al., *Nanomaterial Toxicity Testing in the 21st Century: Use of a Predictive Toxicological Approach and High-Throughput Screening*. *Accounts of Chemical Research*, 2013. 46(3): p. 607-621.
- [12] Mahoney, et al., *The Developmental Toxicity of Complex Silica-Embedded Nickel Nanoparticles Is Determined by Their Physicochemical Properties*, PLOS ONE, 2016. 11(3): p.e0152010.
- [13] Zhao, J., et al., *The interaction of biological and noxious transition metals with the zinc probes FluoZin-3 and Newport Green*. *Analytical biochemistry*, 2009. 384(1): p. 34-41.
- [14] Mahoney, S. (2016). Evaluation of the Toxicity Associated with Complex Engineered Nanomaterials Utilizing *In Vivo* And *In Vitro* Models. (PhD), University of Pittsburgh.

Modeling Amplifiers in Linear Stages

Gabriel Hinding, Tim Ryan, and Dr. Jeffrey Vipperman

*Department of Mechanical Engineering and Materials Science, Swanson School of Engineering,
University of Pittsburgh, Pittsburgh, PA, USA*

Abstract

Precision motion is essential in a variety of applications, and improvements can be made by redesigning the hardware, but it is more cost effective to upgrade the software instead. Two Aerotech Inc. stages were examined with intentions of eventually developing a systematic way to virtually design and test any stage for explicit precision requirements. To do this, it was necessary to investigate various aspects of system dynamics, evaluating the increase in model accuracy achieved with each increased step of model complexity. By using a black-box model, it is possible to focus strictly on the relationship between the input and output of the system. Thus, part of the investigation was to determine an input signal that excites the correct parameters. The stage behavior was collected using an Aerotech program, and the input and output currents of the amplifiers in each stage were recorded. Frequency domain data was used to create models, which were then validated using time domain step data. It was first necessary to determine the point at which increasing the order of the transfer function model stopped resulting in significant improvements in the model's accuracy. After considerable testing, it was concluded that transfer function models that were higher than third order had diminishing return on the level of complexity. After settling on a third order transfer function model with high ($> 90\%$) fit percentage, the data was run through unit gain and time delay models to determine if the complexity of the transfer model, versus the simpler unit gain and time delay models, greatly improved the quality of the model.

The amplifier in the Aerotech Inc. stages is closed loop, thus it is not surprising that the unit gain models resulted in the best time domain fit percentages. Although only two stages are examined, a successful model framework could be used for any linear stage as well as a variety of the components in a stage.

Keywords: precision motion, linear stages, frequency domain, time domain, amplifier, transfer function, time delay

Abbreviations

Autoregressive moving-average – ARMA, Autoregressive-moving-average model with exogenous inputs – ARMAX, Hertz – Hz

1. Introduction

Precision motion is essential in a wide variety of applications, including materials science, physics, and even biology [1, 2, 3, 4, 5]. Improvements can be made by redesigning the hardware, but it is significantly more cost effective to upgrade the software instead. Regardless of the approach, it is advantageous for both a vendor and a consumer to have a better understanding of the equipment. A consumer who thoroughly understands the demands of his or her project can better select equipment without overpaying for unnecessarily high quality. A manufacturer can ensure that it is getting the best performance possible out of its products, identify gaps or overlap in its product lines, and better serve the customer. This project focuses on linear stages, which represent just one kind of precision motion equipment. However, linear



Figure 1. ABL1500, an Aerotech Inc. linear stage



Figure 2. ALS130H, an Aerotech Inc. linear stage

stages are widely used in manufacturing and in projects like semiconductor production, hard drive development, and precision machining.

The overarching goal of the project is to build a framework for modeling linear stages. Specifically, two Aerotech Inc. stages (ABL1500 and ALS130H, pictured in Figure 1 and Figure 2, respectively) are examined with the intention of eventually developing a systematic way for manufacturers to virtually design and test any linear stage for explicit precision requirements.

To do this, it is necessary to investigate various aspects of system dynamics, evaluating the increase in model accuracy achieved with each increased step of model complexity. Often in the literature, a single aspect of a model is examined at a time. Less often is the system modeled as a whole as did Villegas, Hecker, Peña, Vicente, and Flores in the paper “Modeling of a linear motor feed drive including pre-rolling friction and aperiodic cogging and ripple” [6]. Similar to the motor feed project, this project started with the simplest, autoregressive moving-average model. More complex parts will be added and the tradeoff for model complexity and accuracy will be quantified. The difference between this project and previous work is the intention to establish a methodical way to evaluate the expected accuracy of any linear stage, not just a model for a particular one. To summarize, the end goal is to provide manufacturers with a systematic way to determine how many modeling steps they can take, how accurate each one is, and what the simplest order required is for the level of accuracy they desire.

2. Methods

Over the course of the summer, an NDrive ML amplifier was modeled using ARMA, ARMAX, and various black box models [7]. Black box modeling only examines the inputs and outputs of a system, without any previous knowledge or examination of its inner workings; black box modeling makes it possible to focus on the relationship between the input and output of the system. Thus, a wide frequency range (from 1 to 2000Hz) in order to determine what frequencies had the biggest impact on the behavior of the amplifier and excited the correct parameters. Stage behavior was collected using an Aerotech Inc. program called A3200 Motion Composer (5.04.003), and the command and output currents of the amplifiers in each individual stage were recorded. MATLAB’s System Identification tool was used to create transfer function,

state space, polynomial, spectral, and correlation models using frequency-domain data. The models were validated in both the frequency and time domains. A good model was one that had a high degree of fit for every recorded step size in the time domain while also not being unreasonably complex.

$$\text{fit \%} = 100 \left(1 - \frac{\|y - \hat{y}\|}{\|y - \text{mean}(y)\|} \right)$$

The data was next run through a unit gain model (white box) and a unit gain model with a time delay (grey box). A white box model is one that is completely theoretical and a grey box model uses some physical understanding of the system to choose a model structure before identifying parameters [8]. Specifically, a unit gain model is one where the output feedback is equal to the input command, meaning the signal does not change. A time delay model applies a time shift in the signal’s unit gain without affecting its other characteristics. For this experiment, amplifier’s input current is compared to its output current, and in the unit gain model the two currents are equal. The fit percentages of each model output were compared.

3. Results

After a comparison of several different ARMAX models (transfer function, state space, correlation, etc.), it was determined that transfer function models were the best way to describe the frequency-domain data. It is possible to get a fit percent upwards of 93% with a third order transfer function and the models did not improve significantly as the order of the model increased. Table one describes how the transfer function models (defined below) fit the frequency-domain data of the ABL and ALS stages when fed current command data.

$$\text{ABL Transfer Function Model} \quad \frac{.3783z^{-1} + .6092z^{-2}}{1 - .158z^{-1} + .01512z^{-2} + .1137z^{-3}}$$

$$\text{ALS Transfer Function Model} \quad \frac{.4032z^{-1} + .7584z^{-2}}{1 - .1386z^{-1} + .01788z^{-2} + .1164z^{-3}}$$

Note that the variable in the models is z^{-1} , rather than the more traditional ‘s’ variable used in Laplace transforms. The variable ‘z’ describes a function in discrete time, and it is convention in most digital signal processing to represent functions in terms of z^{-1} , as is done in this paper.

Table 1. The fit percentages of the models fit to frequency-domain data from both the ALB and ALS stages

Stage	Model Fit Percentage
ABL	92.1
ALS	92.69

Next, the transfer function models were validated using time-domain step data for each stage. Plots of the responses are represented in Figure 3–Figure 7. For simplicity, only plots of the ABL data have been included because the ALS are almost identical in shape. The fit percentages differ, and are presented in Table 2 (ABL) and Table 3 (ALS).

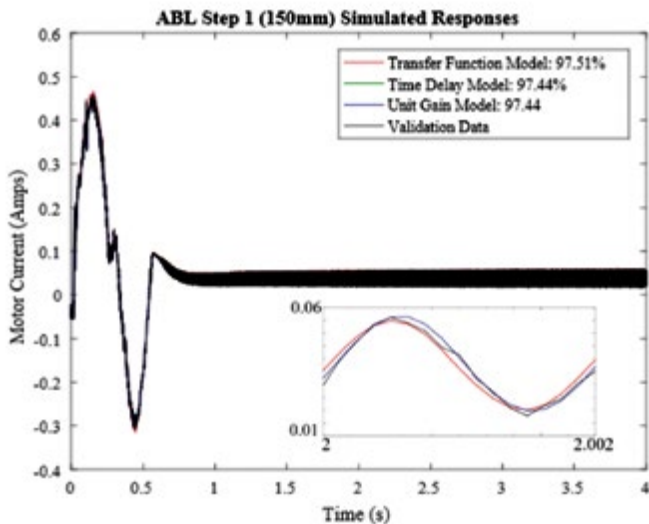


Figure 3. Simulated responses of each model with time-domain ABL data (150mm step size) used as validation

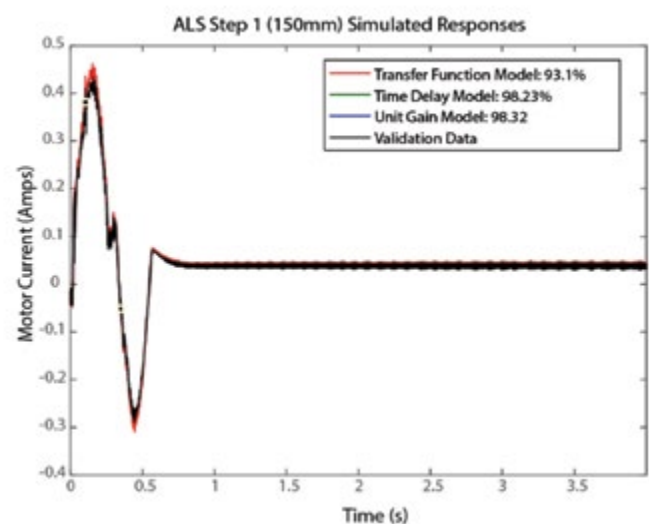


Figure 4: Simulated responses of each model with time-domain ABL data (150mm step size) used as validation; serves as confirmation that the shape of the ALS and ABL responses are extremely similar

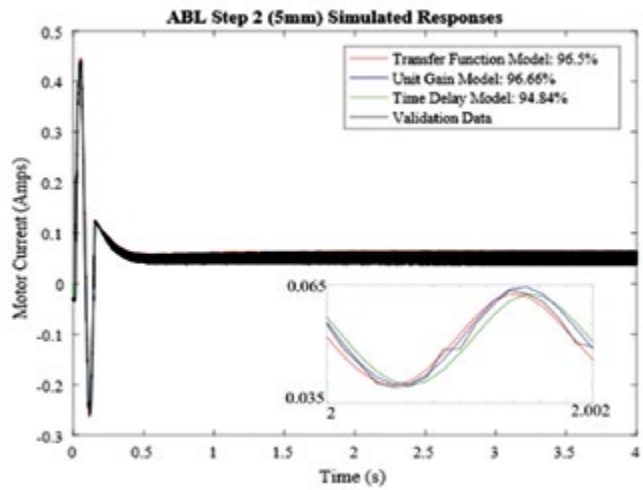


Figure 5. Simulated responses of each model with time-domain ABL data (5mm step size) used as validation

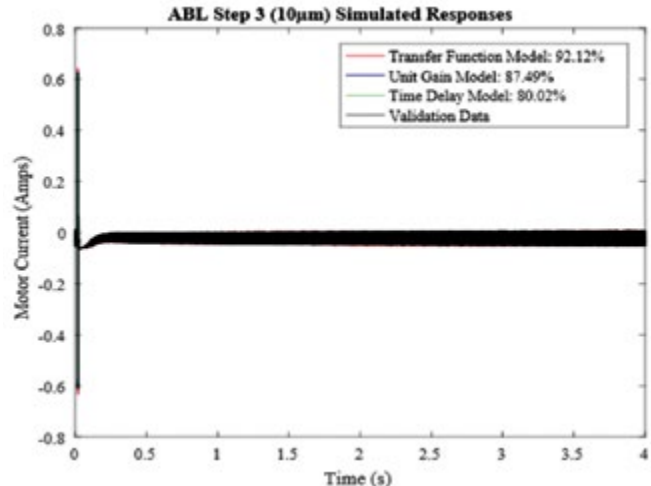


Figure 6. Simulated responses of each model with time-domain ABL data (10μm step size) used as validation

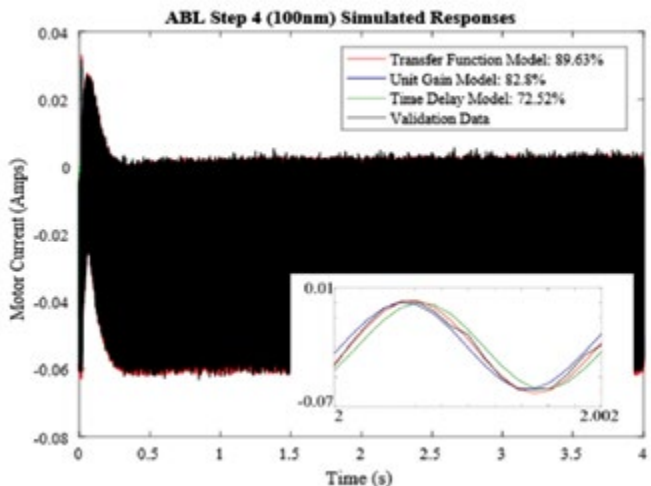


Figure 7. Simulated responses of each model with time-domain ABL data (100nm step size) used as validation

Table 2. Models' fit percentages when validated with ABL time-domain, current feedback data

Step Size	Fit Percent by Model		
	Transfer Function Model	Unit Gain	Time Delay
150mm	97.51	97.44	97.44
5mm	96.5	96.66	94.84
10μm	92.12	87.49	80.02
100nm	89.63	82.8	72.52

Table 3. Models' fit percentages when validated with ALS time-domain, current feedback data

Step Size	Fit Percent by Model		
	Transfer Function Model	Unit Gain	Time Delay
75mm	93.1	98.32	98.23
5mm	93.05	97.18	95.78
10μm	89.32	87.25	80.69
100nm	86.76	82.51	72.14

Consistently, at every step size, the unit gain model (white box) fit the data better than the time delay model (grey box). At large step sizes, the in the time domain, the fit of the unit gain model was similar to that of the transfer function model, and was even a better fit in some cases. The quality of the unit gain model begins to diminish as the step sizes get smaller, but remain comparable to the transfer function model. With minimal filtering, the fit of the time-delay model improves for the smaller steps.

4. Discussion

The amplifier in the Aerotech Inc. stages is closed loop, thus it is not a surprise that the unit gain and time delay models resulted in reasonable time-domain fits, although the unit gain was superior. The fit of the transfer function models was consistently better, but the model itself is more complex. The main difference between the high order, transfer function model and the simpler, unit model is the fit at high frequencies, as indicated by the limited filtering analysis.

5. Conclusion

The amplifier was successfully modeled at multiple different step sizes for two different stages. Next, it would be advantageous to continue modeling components of the stage in a similar manor, with the goal of predicting the behavior of multiple components at the same time. During the system identification process, a MATLAB script was written that allows the user to select input

and output datasets and the order of the desired transfer function model. The program prints the fit percentages and a graph displaying the validation data and the model output. It is possible to evaluate other parts of the stages using the same methods and MATLAB scripts. One of the most revealing models, and a goal for future work, would be one that effectively predicted the relationship between current command versus position output, including the stage as a whole. This model would make systematic design and testing significantly easier. In the long term, the processes used in this project can be applied to the modeling of any linear stage.

6. Acknowledgments

Special thanks to the University of Pittsburgh for such a wonderful summer research opportunity. Additionally, thanks go to Dr. Jeffery Vipperman and Tim Ryan for assistance throughout the project. Funding was provided by the Swanson School of Engineering and the Office of the Provost.

7. References

- [1] S. Devasia, E. Eleftherious, and S. R. Moheimani, "A survey of control issues in nanopositioning," *Control Systems Technology, IEEE Transactions on*, vol. 15, no. 5, pp. 802–823, 2007.
- [2] K. K. Tan, T. H. Lee, and S. Huang, *Precision motion control: design and implementation*. Springer Science & Business Media, 2007.
- [3] L. R. Harriott, "Limits of lithography," *Proceedings of the IEEE*, vol. 89, no. 3, pp. 366–374, 2001.
- [4] Q. Zou, K. Leang, E. Sadoun, M. Reed, and S. Devasia, "Control issues in high-speed afm for biological applications: Collagen imaging example," *Asian Journal of Control*, vol. 6, no. 2, pp. 1159–1167, 2005.
- [5] R. M. Schmidt, G. Schitter, and A. Rankers, *The Design of High Performance Mechatronics: High-Tech Functionality by Multidisciplinary System Integration*. IOS Press, 2014.
- [6] F. Villegas, R. Hecker, M. Peña, D. Vicente, G. Flores, "Modeling of a linear motor feed drive including pre-rolling friction and aperiodic cogging and ripple," *International Journal of Advanced Manufacturing Technology* 73 (2014).
- [7] Box, George EP, et al. *Time series analysis: forecasting and control*. John Wiley & Sons, 2015.
- [8] M.E. Khan and F. Khan. "A comparative study of white box, black box and grey box testing techniques." *Int. J. Adv. Comput. Sci. Appl* 3, no. 6 (2012).

Additive Manufacturing of Magnetocaloric Material for High-Efficiency Cooling

Katerina Kimes, Erica Stevens, Jakub Toman, Amir Mostafaei, and Markus Chmielus

*Department of Mechanical Engineering and Materials Science, Swanson School of Engineering,
University of Pittsburgh, Pittsburgh, PA, USA*

Abstract

Magnetocaloric materials have been studied extensively within the past few decades in an effort to find alloys that exhibit a large temperature change when magnetized. These materials are used in magnetic refrigeration, which is a more sustainable and efficient alternative to traditional refrigeration methods. This study focuses on the characterization of the Direct Laser Deposition (DLD) of NiCoMnSn powder. Powder size distribution analysis and microscopy were performed on the powder before printing. The distribution was found to be varied over a wide range of sizes. Printed samples were characterized using various methods. Vibrating sample magnetometer results showed a small hysteresis and a saturation magnetization around 50 emu/g for both samples. Differential scanning calorimetry tests gave wide phase transformation peaks between 50 °C and 150 °C. Scanning electron microscopy showed microstructural characteristics such as grains, twinning, dendrites, and segregation. The microstructure varied from bottom to top in all samples. Energy dispersive x-ray spectrometry analysis resulted in nominal composition in the twinned regions and enriched/depleted areas outside of the twins.

Keywords: magnetocaloric, Heusler alloy, additive manufacturing, direct laser deposition, characterization

1. Introduction

The magnetocaloric effect (MCE) is a phenomenon that occurs in many conventional magnetic materials where upon adiabatic magnetization, the material heats up and upon adiabatic demagnetization, it cools down [1]. The MCE was first observed in 1881 and since then, has been widely studied in an attempt to develop alloys that exhibit a large temperature change in an effort to find a viable material for magnetic refrigeration. This urge to advance the magnetic cooling technology is driven by its environmental benefits and energy savings of up to 30% [2,3]. Most magnetic materials exhibit the conventional, or positive, MCE. The MCE arises from two contributions in the

material (Figure 1). The first is the coupling between the martensitic variants and the magnetic domains due to the uniaxial magnetic anisotropy of the martensite [4–6]. The martensitic variants of the pseudo-tetragonal martensitic phase have magnetic spins, which orient along the easy axis of orientation along the shortest axis of the structure, as shown in Figure 2. When a magnetic field is applied, the magnetic spins within the variants align with the field. As they align, the variant with the more parallel magnetic spin consumes the other variant [7]. As this reorientation occurs, the material simultaneously goes through a phase transformation into the variant-less cubic austenite phase in which all the sides are the same length and there are no easy axes for the spins to align with (Figure 3). Instead, they align to the axis parallel to the magnetic field. Now that the magnetic spins in the austenitic phase are more ordered than they were in the martensitic phase, with respect to

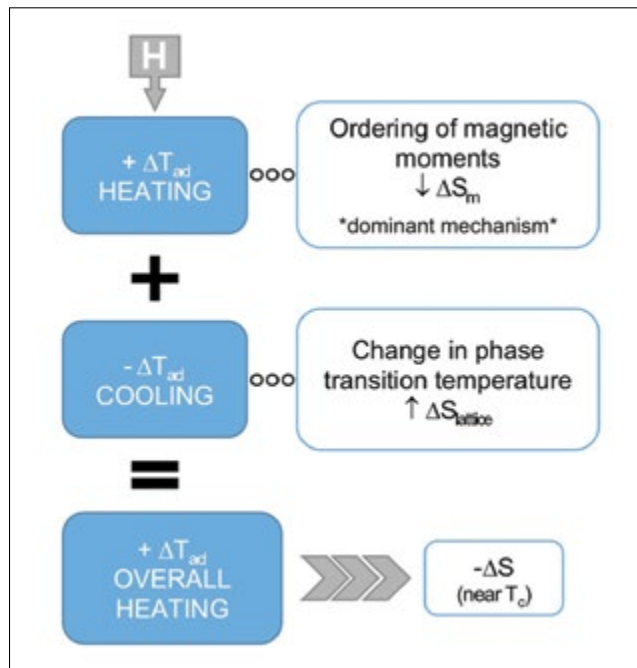


Figure 1. The two contributions to the magnetocaloric effect are opposite in sign and since the first contribution dominates over the second, an overall heating effect occurs.

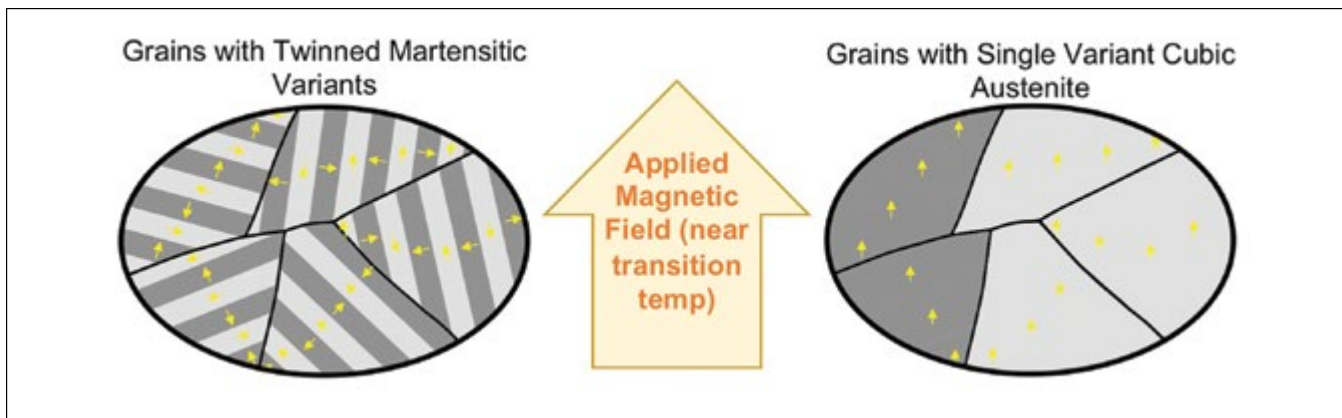


Figure 2. Growth of twin variants during magnetization and resulting magnetic spin orientations

the magnetic field, there is a negative change in magnetic entropy (ΔS_m) and an increase in temperature [4,6].

The second contribution arises from the shift of the martensitic transformation temperature during the phase transformation temperature (Figure 3), which causes a positive ΔS_m and an increase in temperature [5]. For a positive MCE, the second contribution is dominant, resulting in a negative ΔS_m and a temperature increase upon adiabatic magnetization. On the other hand, when ΔS_m is dominated by the coupling mechanism, a decrease in temperature upon adiabatic magnetization occurs. This is known as the inverse, or negative MCE.

One important aspect in the application of these materials to magnetic refrigeration is that they must exhibit a reversible MCE so that the material can be repeatedly used in the refrigeration cycle. Figure 4 shows the way a typical magnetic refrigeration cycle would operate. The material starts in equilibrium. When an electromagnetic field is applied, the MCE occurs and the material

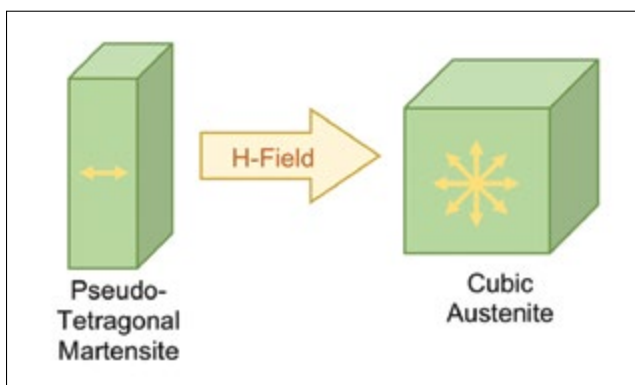


Figure 3. Phase transformation due to shift of martensitic transformation temperature including direction of easy axis of magnetization

increases in temperature as the magnetic spins align. The heat is then removed from the material while it is still in the magnetic field to return it to its starting temperature. When the field is removed, the material wants to return to its initial microstructure and spin state, so to compensate for this increase in entropy, it cools down. At this point, the heat expelled from the refrigerator is absorbed by the magnetic material and it returns once again to its initial temperature. The cycle is repeated to continue the refrigeration cycle.

In 1997, a giant MCE was discovered in $Gd_5(Si_2Ge_2)$ [2] and has since been experimentally shown to exhibit $-\Delta S_m = \sim 14 \text{ Jkg}^{-1}\text{K}^{-1}$ in a magnetic field of 2 T and at a

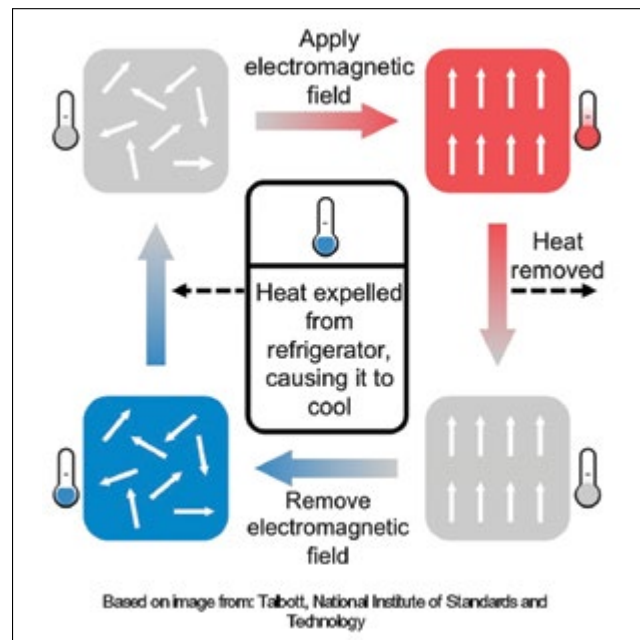


Figure 4. Diagram of generalized refrigeration cycle for MC materials.

temperature of ~ 277 K [8]. Since this discovery, many other alloys composed of magnetic elements have been studied. One class of materials that has gained a lot of attention is Heusler alloys that are based on the X_2YZ formula [9]. More specifically, Ni-Mn-Ga Heusler alloys have been extensively studied due to their additional magnetic shape memory functionality. These alloys curiously exhibit both negative and positive MCEs in low and high magnetic fields, respectively [10]. ΔS_m values as large as $20.7 \pm 1.5 \text{ J kg}^{-1}\text{K}^{-1}$ have been reported for $\text{Ni}_{2.18}\text{Mn}_{0.82}\text{Ga}$ in a magnetic field of 1.8 T and at a temperature of 333.2 K [3]. This is promising for the development of a more inexpensive, readily available alloy for magnetic refrigeration.

Although progress has been made in finding magnetic alloys that exhibit a large MCE near room temperature and in low magnetic fields, there have not been any studies regarding the additive manufacturing (AM) of magnetocaloric materials. As a result, there are still challenges that arise in the various methods of the AM of these materials. Direct Laser Deposition is one process of AM in which powder particles are sprayed towards a melt pool created by a laser which adds to the volume of the specimen, causing it to grow. Characterization of samples printed with DLD is important in understanding the functionality of MC materials.

2. Materials and Methods

2.1 Powder Analysis

$\text{Ni}_{43}\text{Co}_7\text{Mn}_{39}\text{Sn}_{11}$ was obtained from collaborators in Poland and Spain. Powder size distribution analysis was performed using ImageJ software [11] on both optical microscope images at various magnifications. Conglomerated powder was eliminated from the sample set so data was not skewed and size range was adjusted based on magnification and kept consistent through images of the same magnification. Images were run through a threshold filter to get the clearest boundaries as possible.

2.2 Additive Manufacturing

Samples were previously printed using an Optomec LENS (Laser Engineered Net Shaping) 450 3D printer using varying laser power, hatch distance, layer height, and powder feed rate (Table 1). After printing, they were cut off the substrate and cut in half lengthwise. Half was kept as-is and the other half was mounted in epoxy.

2.3 Sample Preparation

Sample preparation on mounted samples was done based on the ASTM standard for Ni based alloys. The last

Table 1. Printing parameters for NCMS samples. The parameters for the 200 W and 300 W samples reported in the results are bolded.

Short name	Laser power [W]	Layer height [mm]	Powder feed rate [rpm]	Hatch spacing [mm]
200 W	200	0.25	5	0.25
250 W	250	0.25	5	0.25
300 W	300	0.25	5	0.25
Sample 1	200	0.25	4	0.5
Sample 2	200	0.25	5	0.25
Sample 3	200	0.25	5	0.25
Sample 4	200	0.5	6	0.5
Sample 5	250	0.25	5	0.25
Sample 6	200	0.5	4	0.5

step in the polishing process lightly etched the samples. Following polishing and cleaning, mounts were sputter coated in gold palladium.

2.4 Characterization Methods

A Zeiss Sigma 500 VP scanning electron microscope (SEM) equipped with energy dispersive x-ray spectroscopy (EDS) software was used to analyze microstructure, porosity, and composition.

Optical microscopy on a Keyence VHX-600K was performed on unmounted samples followed by vibrating sample magnetometer (VSM) measurements on a Lake-shore VSM-7404 to find saturation magnetization and hysteresis and differential scanning calorimetry (DSC) using a TA Instruments Q10 DSC to determine phase transformation temperatures and Curie temperature.

3. Results

Samples identified as 200 W and 300 W printed as expected but all other samples overbuilt and printing results were unpredictable. Therefore, although all samples went through the same characterizations, only the 200 W and 300 W sample results will be reported.

3.1 Powder Analysis

A histogram distribution of powder diameters for 35 images at various magnifications is shown in Figure 5. Diameters were calculated from ImageJ area measurements under the assumption that the particles were spherical. The distribution range is very wide with a majority of diameters between 10 and 30 μm . 16% of the particles were removed due to conglomeration.

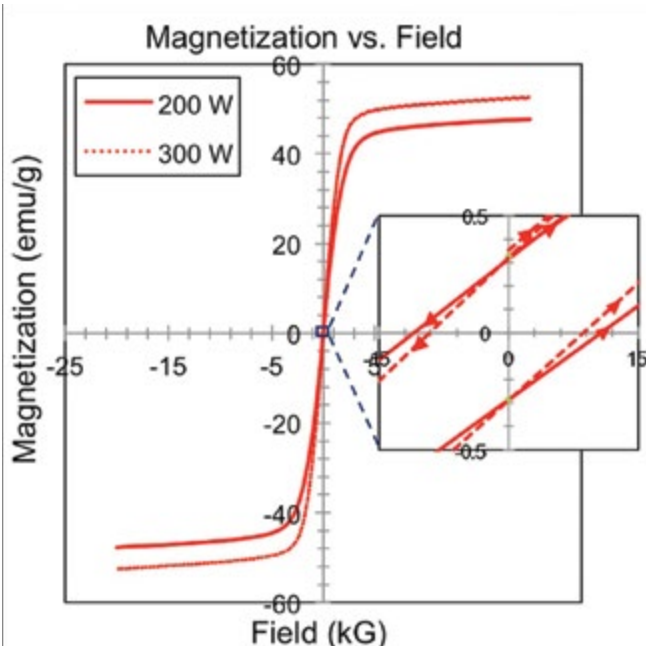


Figure 5. Magnetization plot for 200 W and 300 W sample; Hysteresis is shown in magnified inset plot.

3.2 Vibrating Sample Magnetometry

VSM hysteresis tests were done up to 20,000 Gauss. The results showed relatively consistent saturation magnetization between the two samples of approximately 47 emu/g for the 200 W sample and 52 emu/g for the 300 W sample. A very small hysteresis is also present in the alloy, confirming its ferromagnetism. (Figure 6)

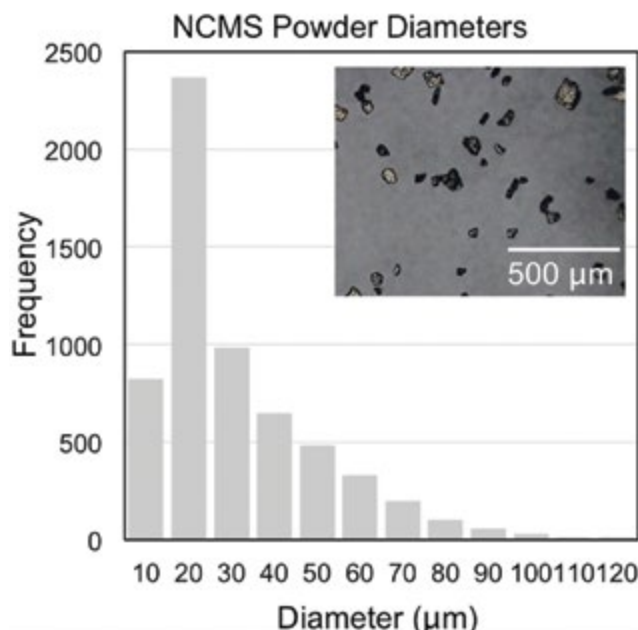


Figure 6. Histogram of powder size distribution; Both mounted and unmounted powder were analyzed.

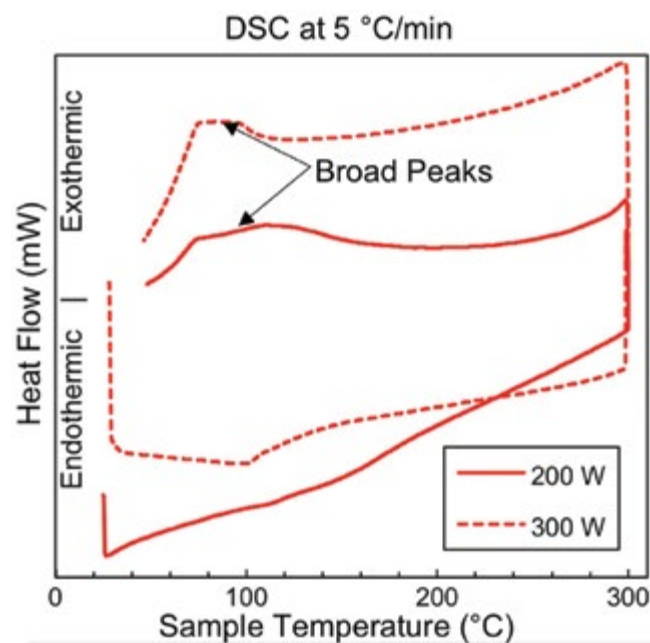


Figure 7. DSC plot with endothermic (positive) heat flow values down

3.3 Differential Scanning Calorimetry

DSC tests were run using a heating/cooling rate of 5 °C/min. For both samples, the temperature was allowed to equilibrate at the initial temperature set at 25 °C and then it was held isothermally at 300 °C before ramping back to 25 °C. The results shown in Figure 7 are far from what was expected. Rather than sharp peaks to identify phase transition temperatures, the peaks appeared very wide and ranged from 50 °C to 150 °C.

3.4 Scanning Electron Microscopy

SEM was performed on all samples in various locations as well as on mounted powder. There are many fractures throughout the powder particles. Also visible in the powder is twinning as shown in Figure 8. Images were taken throughout the samples. The same variations were observed in all samples. Images from the lower middle portion of the 300 W sample are shown in Figure 9. The dark grey regions are most likely dendrite borders. The enlarged image clearly shows twinning visible in many sizes: larger in higher regions and decreasing in size in lower regions. Because the material is a functional martensite, twinning is expected in these samples. Figure 10 shows images from the top region of the 200 W sample. The microstructure appears very different at the top of the sample than in the middle. The dark regions in the magnified image seem to make up a grain.

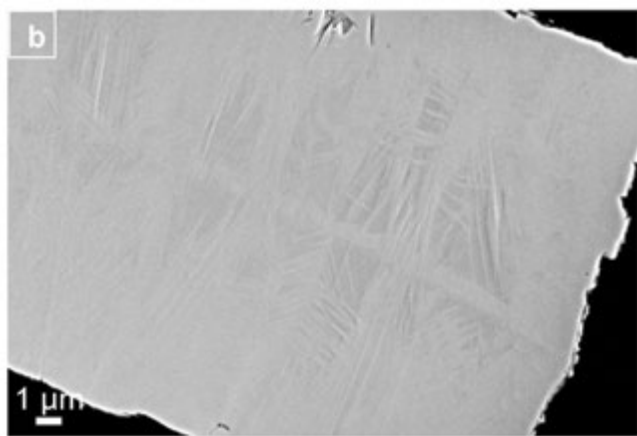
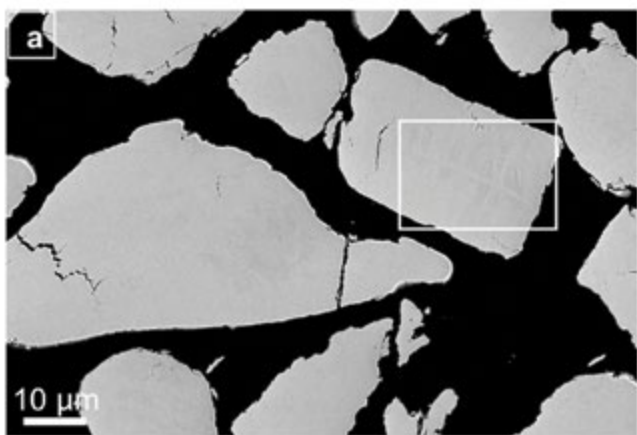


Figure 8. SEM image of mounted and cross-sectioned powder; Cracks appear throughout powder (a) and twinning also is visible (b).

EDS analysis was done on all samples to get compositions of various areas. There were four main areas that had similar characteristics in all samples: twinning, pores, dark grey, and light grey (Figure 11). Point and area scans were performed on these areas and averaged results are shown in Table 2. Overall, the twinned regions had the expected nominal composition of Ni₄₃Co₇Mn₃₉Sn₁₁. However, in the light grey areas, dark grey areas, and pores, compositions are enriched and depleted in certain elements. This is due to segregation of the elements during solidification.

4. Discussion

During printing, many of the samples not reported in this work overbuilt. One cause of this could be having an insufficient amount of powder to keep the powder flow continuous during printing. Another likely cause of overbuilding is the wide range of particle sizes. This could cause inconsistent powder flow, resulting in inconsistent printing.

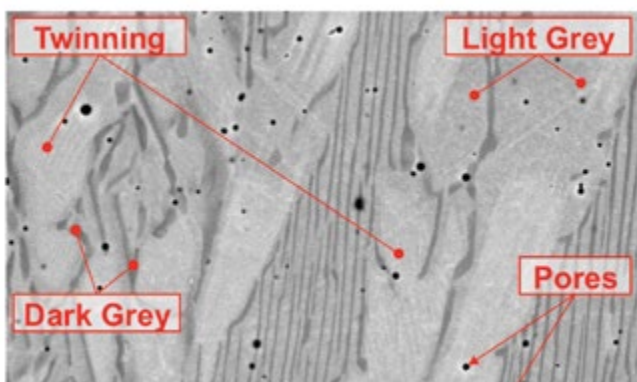


Figure 9. Image from the bottom of the 300 W sample showing areas identified for EDS; Stripes not identified as twins in this image are due to segregation.

Although the magnetization curves did give good results, only one angle was tested. The samples are still in the martensite phase, so it is expected that there is an easy axis of alignment. Various orientation angles have not yet been tested to confirm the direction of the easy axis. This could give a larger saturation magnetization value than reported here.

Based on the DSC results, there is no definitive peak for the transformation temperature. The transition is occurring throughout the material at different temperatures due to the composition inhomogeneity throughout the samples, causing a flat, wide peak rather than one peak. This being said, the martensitic phase transformation temperature can be approximated by averaging the transition start and finish points of the wide peak. Unfortunately, no distinct peak appeared on the lower portion of the plot so austenitic phase transformation temperature cannot be estimated at this time. More methods will need to be explored to determine phase transformation temperature.

Table 2. EDS analysis results averaged based on similar characteristics (Lt=Light and Dk=Dark)

Element	Twins	Pores	Dk Grey	Lt Grey
Ni	43.8	28.2	42.9	45.6
Co	7.2	5.8	11.8	7.3
Mn	38.5	55.7	39.4	34.4
Sn	10.4	10.3	5.8	12.7

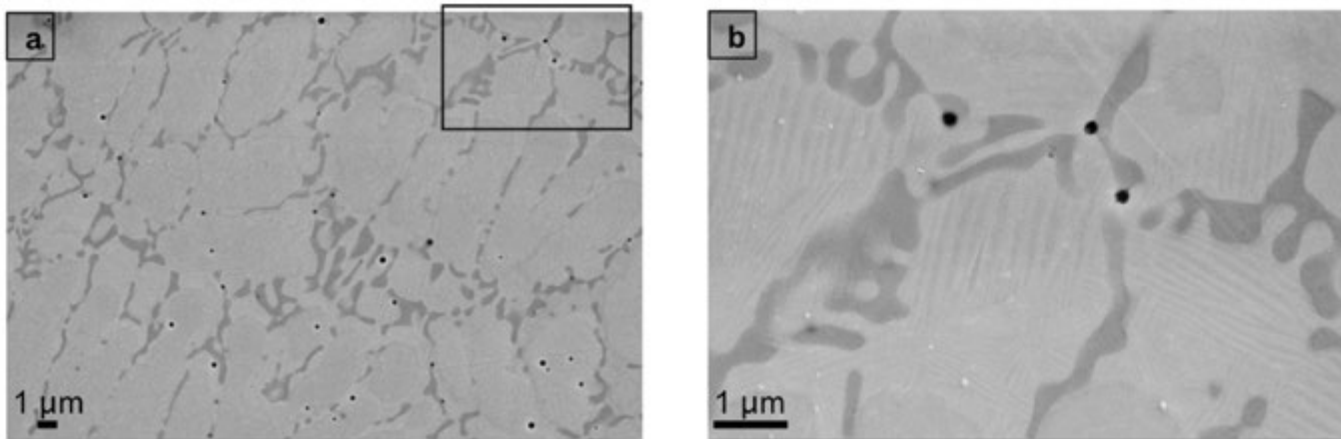


Figure 10. Image from 300 W lower middle section; twinning is very clearly seen as light and dark parallel stripes (b) as well as dendrite borders as dark grey regions bordering twinned regions (a)

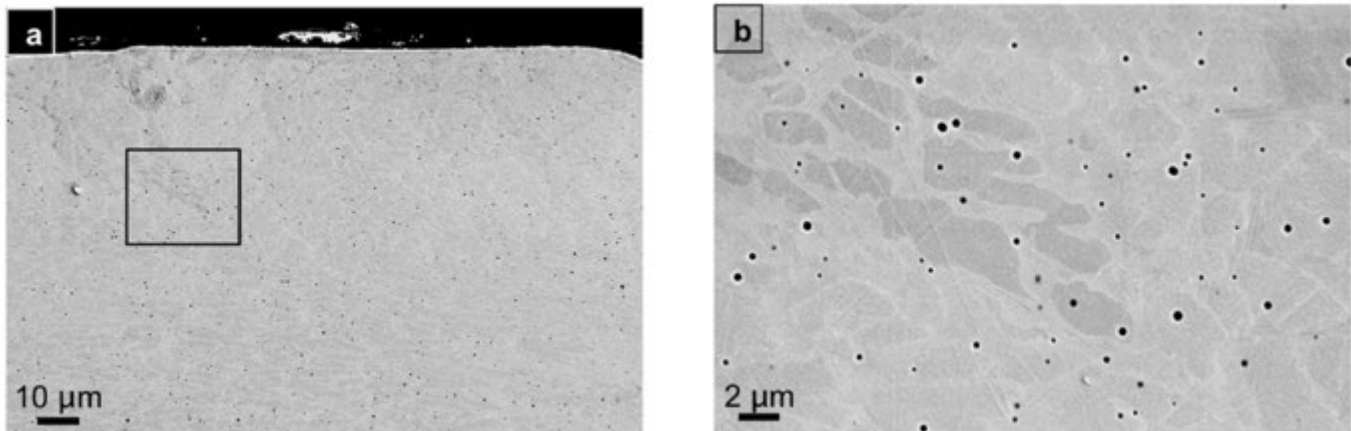


Figure 11. Top of 200 W sample (a) showing dark regions that make up a grain (b)

SEM imaging showed both dendritic structures and grain structures throughout all samples. There was a gradient of microstructure from bottom to top due to solidification rate. The EDS results demonstrate the lack of homogeneity within the samples. EDS showed that manganese segregated to the dark regions at the edges of the dendrites and the light grey regions were depleted in Mn. The pores have compositions that are very different from nominal. Since the pores are not a flat surface, the electron beam is not able to easily escape so EDS results are most likely not very accurate.

5. Conclusion

Overall, many characterization techniques were performed on AM NiCoMnSn. Most methods gave good insight into the effect of the printing method on the MCE

and the microstructure of the material. More tests need to be done to determine phase transformation temperatures and other characterization methods such as Differential Interference Contrast (DIC) microscopy, mechanical testing, and heated VSM can be performed to greater understand AM MC material.

6. Acknowledgments

This project was funded by the Mascaro Center for Sustainable Innovation. I would like to thank all members of the Chmielus Lab, especially Erica Steven, Jakub Toman, Amir Mostafaei, and my advisor Dr. Markus Chmielus. For materials, I would like to thank our collaborators in Poland and Spain: V. K. Chernenko, Anna Wojcik, and Wojciech Maziarz.

References

- [1] J. Liu, T. Gottschall, K.P. Skokov, J.D. Moore, O. Gutfleisch, Giant magnetocaloric effect driven by structural transitions., *Nat. Mater.* 11 (2012) 620–6. doi:10.1038/nmat3334.
- [2] K.A. Gschneider Jr., V.K. Pecharsky, A.O. Tsokol, Recent developments in magnetocaloric materials, *Reports Prog. Phys.* 68 (2005) 1479–1539. doi:10.1088/0034-4885/68/6/R04.
- [3] A.A. Cherechukin, T. Takagi, M. Matsumoto, V.D. Buchel'Nikov, Magnetocaloric effect in $\text{Ni}_{2+x}\text{Mn}_{1-x}\text{Ga}$ Heusler alloys, *Phys. Lett. Sect. A Gen. At. Solid State Phys.* 326 (2004) 146–151. doi:10.1016/j.physleta.2004.03.072.
- [4] A. Planes, L. Mañosa, A. Saxena, *Magnetism and Structure in Functional Materials*, Springer Series in Materials Science, 2005. doi:10.1007/3-540-31631-0.
- [5] I.D. Rodionov, Y.S. Koshkid'ko, J. Cwik, A. Quetz, S. Pandey, A. Aryal, I.S. Dubenko, S. Stadler, N. Ali, I.S. Titov, M. Blinov, M. V. Prudnikova, V.N. Prudnikov, E. Lähderanta, A.B. Granovski, Magnetocaloric effect in $\text{Ni}_{50}\text{Mn}_{35}\text{In}_{15}$ Heusler alloy in low and high magnetic fields, *JETP Lett.* 101 (2015) 385–389. doi:10.1134/S0021364015060107.
- [6] A. Planes, L. Mañosa, M. Acet, Magnetocaloric effect and its relation to shape-memory properties in ferromagnetic Heusler alloys., *J. Phys. Condens. Matter.* 21 (2009) 233201. doi:10.1088/0953-8984/21/23/233201.
- [7] P. Müllner, V.A. Chernenko, G. Kostorz, Large cyclic magnetic-field-induced deformation in orthorhombic (14M) Ni-Mn-Ga martensite, *J. Appl. Phys.* 95 (2004) 1531–1536. doi:10.1063/1.1639144.
- [8] V.K. Pecharsky, K.A. Gschneidner, Jr., Giant Magnetocaloric Effect in $\text{Gd}_5(\text{Si}_2\text{Ge}_2)$, *Phys. Rev. Lett.* 78 (1997) 4494–4497. doi:10.1103/PhysRevLett.78.4494.
- [9] I. Dubenko, T. Samanta, A.K. Pathak, A. Kazakov, V. Prudnikov, S. Stadler, A. Granovsky, A. Zhukov, N. Ali, Magnetocaloric effect and multifunctional properties of Ni-Mn-based Heusler alloys, *J. Magn. Magn. Mater.* 324 (2012) 3530–3534. doi:10.1016/j.jmmm.2012.02.082.
- [10] L. Mañosa, A. Planes, M. Acet, Advanced materials for solid-state refrigeration, *J. Mater. Chem. A.* 1 (2013) 4925. doi:10.1039/c3ta01289a.
- [11] C. a Schneider, W.S. Rasband, K.W. Eliceiri, NIH Image to ImageJ: 25 years of image analysis, *Nat. Methods.* 9 (2012) 671–675. doi:10.1038/nmeth.2089.

Addressing Infusion Pump Management Challenges Through Implementation of a PAR Stock System

Kelly R. Larson and Dr. Bryan A. Norman

*Department of Industrial Engineering, Swanson School of Engineering,
University of Pittsburgh, Pittsburgh, PA, USA*

Abstract

This paper focuses on a study of infusion pump management at the University of Pittsburgh Medical Center at Montefiore (MUH) and Presbyterian (PUH) hospitals. In this study, challenges with infusion pump management were identified, solutions were generated, and a new system was implemented. To identify specific challenges and solutions, a root cause analysis, interviews with stakeholders, and literature reviews were conducted. One of the biggest concerns found in the process was that in response to low infusion pump availability, some infusion pump handling practices led to further issues, including reduced preventative maintenance and cleaning of infusion pumps. This could potentially pose a risk to patient safety—further motivating the search for solutions to these challenges for this study. A Periodic Automated Replenishment (PAR) stock system was piloted in two units at MUH. The pilot successfully increased the availability of infusion pumps and there are future plans to implement it across both MUH and PUH.

Key Words: PAR Stock System, infusion pump management, asset management, healthcare

1. Introduction

Infusion pumps are used in hospitals in order to deliver medications, fluids, and blood to patients in a controlled manner. The infusion pump consists of a PC Unit (PCU) and channels. The PCU controls customization of infusion delivery, while the channels control specific infusions. Infusion pumps are crucial to the care of patients. Consequently, ensuring that PCUs and channels are available for patients when needed is vital to patient safety.

1.1 Literature Review

Infusion pump management can be challenging for many reasons. Major drivers of these challenges are that infusion pumps must be cleaned between patients and undergo preventative maintenance and repair. Ensuring

proper cleaning and maintenance is critical from a patient safety perspective, but can pose challenges, as it requires additional travel and handling to bring the equipment to the proper department and location. When this is considered along with the variability of demand and potential lack of adherence to established practices, management of infusion pumps becomes extremely challenging.

One common practice that causes infusion pump management challenges is infusion pump hoarding. This refers to the practice of keeping infusion pumps on a unit between patients, rather than returning the equipment to be cleaned and maintained. In one study it was found that “nurses respond to technology system problems by solving the immediate problem using whatever strategy works” [1]. That is, practices such as infusion pump hoarding are representative of nurses trying to solve immediate infusion pump availability issues when larger system problems are at the root of the problem. This highlights the importance of finding the root causes of systems issues, as well as choosing an appropriate system solution.

Because of the common difficulties associated with managing infusion pumps, various system solutions have been implemented in the industry. The common thread among the systems is that infusion pumps need to be cleaned, maintained, and stored. The changing factor is primarily who will be responsible for meeting each of these needs, and the location in which these needs are met. A literature review was conducted of potential system solutions, in order to gain an understanding of the advantages and disadvantages of the various systems. Centralized, decentralized, and PAR stock systems have all been used with varying degrees of success [2, 3]. Real-time locating systems (RTLS) have also been used to help address asset management challenges [4]. Because these various types of systems have had a range of results, it is crucial to consider each system’s strengths and weaknesses relative to the site of interest.

1.1.1 Centralized Systems

In a centralized infusion pump management system, equipment is shared across the various units. When an infusion pump is done being used, it is returned to the system to be cleaned or maintained, and returned to central inventory. When a unit needs new equipment, a request is made and it is brought directly to the unit. Because inventory is shared in this system, it requires less inventory (as the safety stock is able to be shared across units). However, a major disadvantage is that more logistical coordination is needed for the system to run successfully.

1.1.2 Decentralized Systems

Decentralized systems are characterized by ownership of infusion pumps by individual units. In this case, infusion pumps are cleaned at each individual unit. This system requires a greater amount of inventory, because a safety stock is needed at each unit in order to handle demand variation. Decentralized systems also require additional resources at each unit such as storage space and cleaning materials, making this model potentially costly. However, this system is logically simpler and addresses equipment availability challenges well.

1.1.3 Periodic Automated Replenishment (PAR) Stock Systems

PAR stock systems can be seen as a hybrid between the centralized and decentralized models. In this model infusion pumps are centrally owned, but a set amount of inventory is kept at each unit. When inventory falls below the set level, a request is made for more equipment. Since requests are made to fill inventory rather than direct patient requests, this addresses the issue of infusion pump availability well. Furthermore, this requires less equipment than the decentralized model, thereby mitigating inventory costs. However, this system requires consideration of how to meet demand when it is much lower or higher than expected.

1.2 Study Motivation

As with asset management of many types of equipment in the healthcare industry, there can be many challenges in ensuring that the correct number of PCUs and channels are in good condition (clean and having received preventative maintenance when appropriate) and available to patients when needed. Due to the expensive nature of the equipment, availability cannot always be handled by simply purchasing more equipment. However, by changing the infusion pump management system, these chal-

lenges can be addressed. There are different benefits and drawbacks to the various system types, making selection of the appropriate system crucial.

2. Methods

After a literature review of similar studies was completed, a root cause analysis of the infusion pump management system was conducted at MUH and PUH—two connected hospitals that used a centralized infusion pump management system. The root causes of their management challenges were determined to be resource requirements of a centralized model, lack of adherence to established practices, and demand variation. After defining the root causes of the current infusion pump management challenges at PUH and MUH, the effectiveness of different systems for addressing the root causes at these hospitals was considered.

In order to decide which infusion pump management system would be best for PUH and MUH, each of the systems being considered was evaluated in terms of its ability to solve the root causes of the infusion pump management problems, as well as additional benefits and challenges. After considering these various system types, project stakeholders were interviewed. These interviews helped to identify further potential challenges both with the different systems in theory as well as in implementation. After considering the project stakeholder consultations and literature regarding previously mentioned related studies, the PAR stock system was determined to be the best system for PUH and MUH.

This system was piloted in two units at MUH. Nurse surveys were conducted before and after pilot implementation, in order to provide metrics to evaluate the success of the pilot. These surveys asked 11 questions related to infusion pump availability and care for patients. The percentage of survey respondents to select each option was compared before and after the pilot, and had promising results. Furthermore, the success of the pilot was evaluated through analyzing the service levels—which were found to be high. Higher service levels translate to equipment being available to patients, and increased patient safety. Through the results of the surveys and the service level analysis, the PAR stock system was found to be successful. The pilot implementation is planned to roll out to the remainder of the units in MUH and PUH, with the goal of having the PAR stock system successfully running throughout the hospitals.

3. Implementation

Unit walkthroughs were completed to determine PAR stock levels (pre-pilot phase) and service levels (throughout pilot phase). Admissions data and nurse expertise were also used to collect data for the parameters that were used in calculating PAR stock levels. This includes percentage of admits who need an infusion pump, percentage of admits who need two PCUs, average number of channels needed per patient, and 98% and 99% confidence levels of the number of patients admitted across four-hour time slots throughout the day. These parameters were used to develop optimistic and pessimistic PAR stock levels for each unit. Further considerations needed to be made before implementing the pilot, such as PAR stock storage space requirements and impacts on labor in Central Supply.

4. Results

Analyzing the various potential infusion pump management systems resulted in discovering major advantages to the PAR stock system and its desirability for MUH and PUH. PAR stock systems follow just-in-time practices, which enable providing patients with the correct amount of equipment when needed. Receiving infusion pumps in a timely fashion can have tremendous safety implications, making high service levels an important measure of a successful system. The PAR stock system is able to provide higher service levels than the centralized system. The centralized system fails to provide equipment in a

timely fashion, and the fully decentralized system requires an infeasible amount of equipment to run appropriately. The PAR stock system (Figure 1) was determined to be the best approach for PUH and MUH.

In the PAR stock system, infusion pumps are kept in the clean equipment room of units. Central Supply then replenishes the PAR stock to the appropriate level at specific times throughout the day. This system requires little change to the projected overall labor effort, yet allows equipment to be pulled immediately when needed for patients, providing them with the correct amount of infusion pumps in a timely fashion.

4.1 System Performance

A pilot of the PAR stock system was rolled out to two units at MUH. The goal of these pilots was to determine the potential for success of the PAR stock system at MUH and PUH, and to identify potential challenges with the system. The pilots showed that the PAR stock system could consistently provide infusion pumps in a timely manner. Data analysis of the PAR stock levels in the pilot units showed service rates to be within one percent of 100% service rates, as indicated in Table 1. Almost all instances where items did stock out occurred during the first few days of the trial, as personnel were adjusting to the new system. Overall, this data shows the positive effect that the PAR stock system had on infusion pump availability.

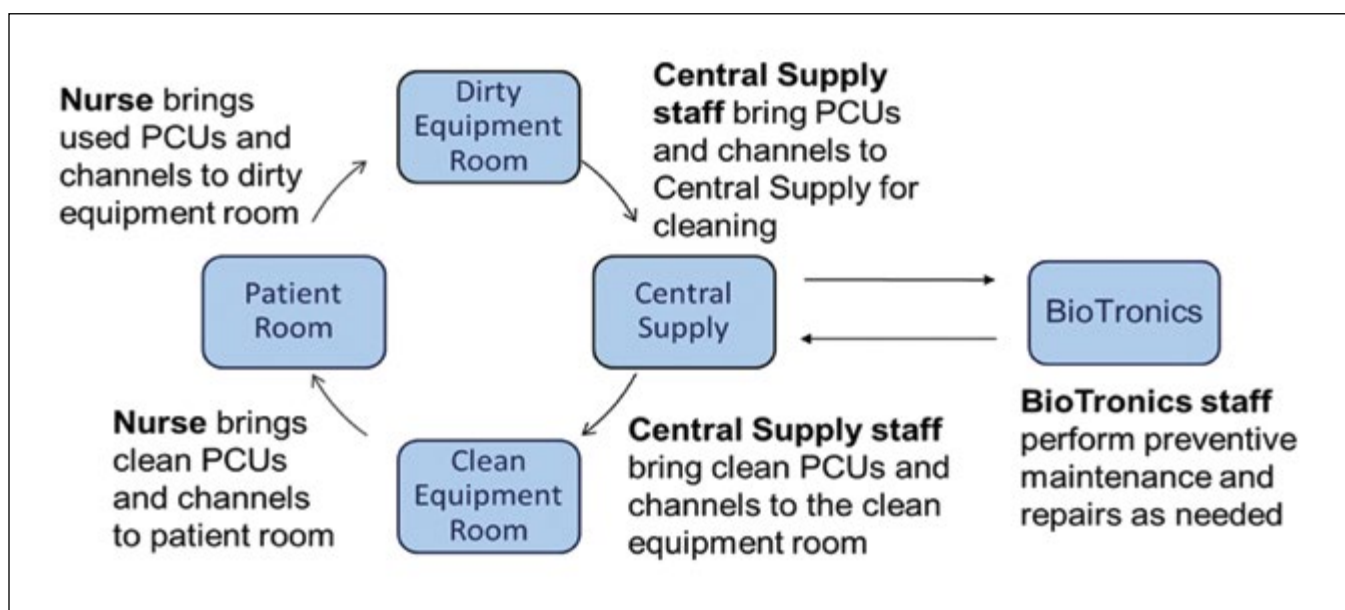


Figure 1: The illustration of the PAR stock system is distinct from other systems in the usage of the clean room as an intermediate storage location for PAR stock.

Table 1: Pilot unit service rates were found to be nearly 100% for both channels and PCUs.

Pilot Unit	Channel Service Rate	PCU Service Rate
1	100.0%	99.6%
2	99.8%	99.1%

4.1.1 Nurse Surveys

Nurses were surveyed before and after the PAR stock system pilot was implemented, in order to measure success. These surveys prompted nurses to evaluate the infusion pump management system using a Likert-type scale (Always, Sometimes, Rarely, Never). Two examples of statements evaluated are “IV Pumps are available when I need them” and “IV Channels are available when I need them”. (Note: IV Pumps are PCUs). These surveys had striking results. The evaluation of the two aforementioned statements yielded a 2.1% “Always” rating on the pre-pilot surveys, and then a 94.7% “Always” response rating on the post-pilot surveys. These results illustrate how implementing a PAR stock system can increase equipment availability for patients. Additionally, other than a few calls for expedited deliveries in the beginning of the pilot due to procedural errors, the PAR stocks have not stocked out of PCUs or channels, indicating the PAR stock system’s ability to increase infusion pump availability.

5. Discussion

The results of this study have implications for asset management using a PAR stock system in hospitals. The system’s usage of just-in-time (JIT) principles allows equipment to be provided immediately. Other systems that utilize JIT have also been used in the healthcare industry. For instance, in the Two Bin system, a bin of inventory is kept on a shelf and replaced with the second bin when empty, and the empty bin triggers ordering equipment. However, this system is ideal for low-cost, high-velocity equipment [5]. A major advantage of the PAR stock system over the decentralized model is that it requires less equipment and space. Compared to a centralized model, the PAR stock system requires less travel by Central Supply staff, and provides equipment immediately when needed. The PAR stock system

is expected to decrease infusion pump hoarding, as the system is designed to work effectively to increase nurses’ trust in equipment availability. Pre- and post-pilot nurse surveys were consistent with this expectation.

6. Conclusions

Infusion pump management can be a challenge in many hospitals due to the expensive nature of the equipment and the implications that the condition and availability of the equipment have on patient safety. When a patient is in critical condition, having the correct amount of properly cleaned and maintained equipment available is extremely important for treatment. This study led to the decision that a PAR stock system would be best for PUH and MUH.

One notable limitation of this study is the ability to apply the results to other hospital locations. Although the PAR stock system was found to be the most appropriate system for PUH and MUH, the root cause analysis of the hospitals’ management problems was a crucial step to determining this and should also be done when considering similar problems at other locations. Another limitation of this study is regarding limited access to data. If concrete infusion pump usage data were available, this could have been used in order to determine PAR stock levels. Due to the lack of certain types of data, some data estimates were used.

The results of the pilot showed the PAR stock system to be an effective way to address infusion pump management challenges, based on nurse surveys and service levels. These survey results and high service levels have significant implications on the potential to increase patient safety through changing infusion pump management systems in hospitals. As a result of this study, the PAR stock system is planned to continue to be rolled out throughout PUH and MUH.

7. Acknowledgments

This work was supported with funding provided by Bryan Norman, the Swanson School of Engineering, and UPMC. Additional contributors to this project include University of Pittsburgh students Chris Jambor, Stephen Teacher, and Saurabh Jha.

8. References

- [1] Zuzelo et al. "Describing the Influence of Technologies on Registered Nurses' Work." *Clinical Nurse Specialist* 22.3 (2008): 132-40. Web
- [2] Kaczmarek. "Reducing Labor on Inventory PAR for the Course." *Healthcare Purchasing News*. 44, 2015. <<http://digital.hpnonline.com/editions/A39ika/1501-HPN/resources/46.htm>>.
- [3] Krupansky et al. "University of Michigan Health Systems Alaris Infusion Pump Analysis." 2007. <http://www.umich.edu/~ioe481/ioe481_past_reports/w0706.pdf>.
- [4] Buchsteiner. ACHIEVING 'JUST-IN-TIME' PAR LEVEL ASSET MANAGEMENT WITH RTLS. Versus, 2015. <<http://www.versustech.com/pdf/107.pdf>>
- [5] Jump Technologies. "Industry Report: Inventory Management v. PAR Replenishment?" (n.d.): n. pag. *Jump Technologies*. Jump Technologies. Web. 16 July 2016.

Chemical Looping for Syngas Production

Isaac Mastalski, Amey More, and Götz Veser

Department of Chemical and Petroleum Engineering, Swanson School of Engineering, University of Pittsburgh, Pittsburgh, PA, USA

Abstract

The rapidly increasing global population is expected to result in a concomitant rise in demand for commodity chemicals. Natural gas has recently emerged as a cheap, abundant, and locally available feedstock for bulk chemical production. However, most commercial processes for natural gas upgrading require conversion of methane (the main component in natural gas) to syngas (a mixture of H₂ and CO) as a first step, which can be subsequently converted to specific end chemicals depending on the H₂:CO ratio. In this work, we utilize the “chemical looping principle”—the coupling of two independent reactions via a “carrier”—to produce inherently separated streams of H₂ and CO from CH₄ and CO₂. To this end, we discuss the development of a core-shell Ni@CeO₂ carrier; proof of concept testing for the proposed process indicates that it will result in 95% conversion of CH₄, 90% conversion of CO₂, and ~99% purity in both the H₂ and CO effluent streams.

Keywords: chemical looping, syngas, methane, catalysis

1. Introduction

The anticipated rise in global population and the rapidly growing economies of the developing world will result in a corresponding increase in demand for consumer products [1]. Consumer products encompass all aspects of modern life, including fuels, pharmaceuticals, foods, fertilizers, paints, and plastics, and they are primarily derived from commodity chemicals (methanol, olefins, ammonia, etc.) [2]. Most commercial chemical processes produce large CO₂ emissions, and thus the expected increase in demand for chemicals is likely to exacerbate the already critical levels of atmospheric CO₂ [2]. Current industrial infrastructure and abundant global reserves of natural gas (typically 80–95% CH₄) together motivate the need to develop methane-based chemical processes for end-chemicals, preferably with net negative CO₂ emissions.

In the absence of viable industrial processes to upgrade natural gas directly to end chemicals, the conversion of methane to syngas—a mixture of H₂ and CO—is required

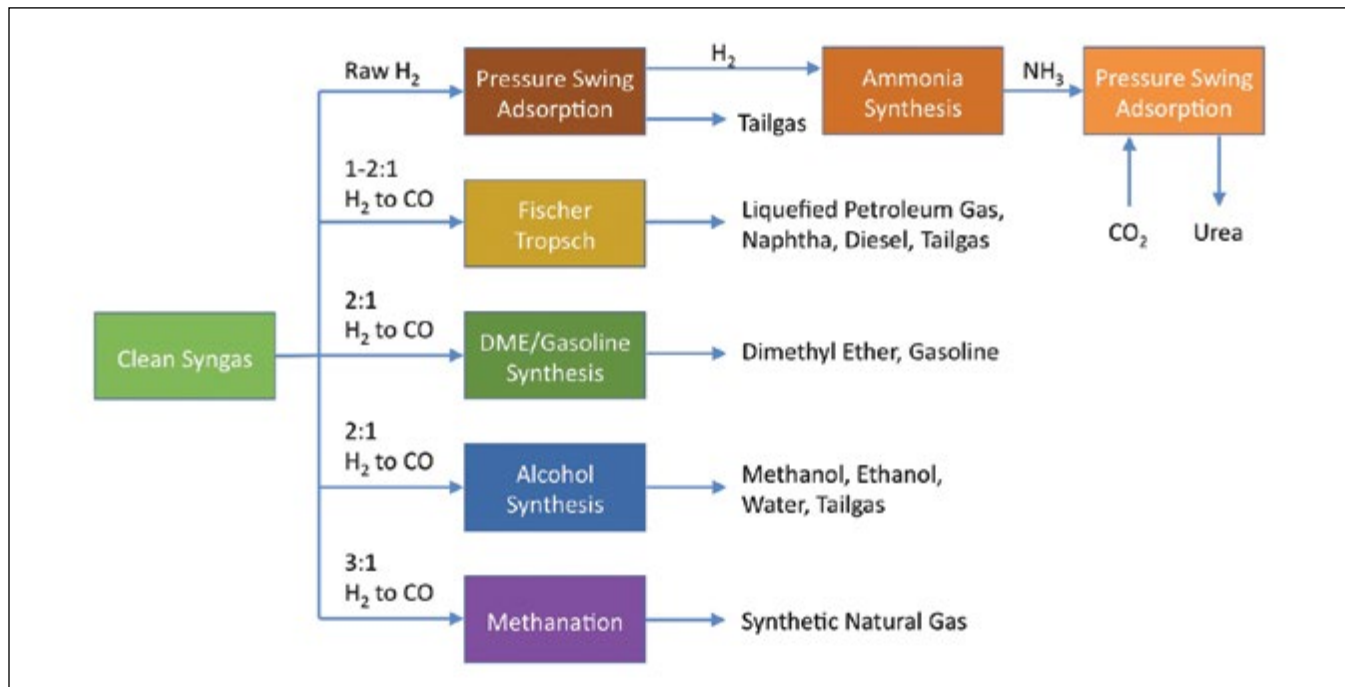


Figure 1 Schematic illustrating various end chemicals that can be produced from a syngas feed

as the first step. Subsequently, depending on the H₂:CO ratio, syngas can be further processed in a number of different processes to produce a variety of end chemicals, as seen in Figure 1. However, current processes (e.g., steam reforming of methane, dry reforming of methane, partial oxidation, etc.) can only produce syngas in very specific H₂:CO ratios (e.g., 1:1, 3:1, etc.), which need to be further adjusted downstream, thereby increasing the overall processing time, cost, and energy requirements [2]. Hence, as a potential alternative, we propose applying the chemical looping concept—the coupling of two independent reactions via a “carrier”—to produce separate streams of H₂ and CO that can be blended together as required, while consuming an abundant resource (natural gas) and a greenhouse gas (CO₂).

1.1 Proposed Chemical Looping Process

Chemical looping combustion (CLC) has been widely demonstrated as a promising combustion technology enabling inherent CO₂ capture [3, 4]. In CLC, a fuel is combusted in a “reducer” reactor in contact with an oxygen carrier (typically a transition metal oxide). The reduced metal oxide is transferred to an “oxidizer” reactor, where it is re-oxidized in contact with air. The oxidized metal is circulated back to the reducer, closing the material “loop.” In the reducer, ideally a pure mixture of CO₂ and H₂O is formed as combustion gases, from which high-concentration, high-pressure (i.e., sequestration ready) CO₂ streams can be readily obtained via condensation of steam. Thus, the overall process offers efficient combustion of fossil fuels with inherent CO₂ capture. In the proposed process (Figure 2), we demonstrate the application of the chemical looping concept beyond

combustion, that is, for syngas production. A suitable metal (typically Ni) “cracks” CH₄, forming solid carbon deposits and a gaseous stream of H₂ in the “cracker.” The deposited carbon is then oxidized by CO₂ in the “oxidizer,” producing a stream of pure CO. The metal is cycled between the two reactors as a “carbon carrier” (as opposed to an “oxygen carrier” in CLC), thus producing entirely separate streams of syngas components. In addition to significantly reducing the downstream processing, the proposed process also consumes CO₂, so it enables net carbon-negative chemicals production.

The primary challenge for the proposed process is developing a robust metal/support structure. While the metal nanoparticles are the active catalysts for CH₄ cracking, a support is needed to prevent metal sintering at the high reaction temperatures (>700°C). However, conventional metal nanoparticle deposition on a support is not stable, since carbon deposits form nanotubes that lift the metal from the support (Figure 3) during the cracking process. During oxidation, the carbon “burn-off” can detach the metal particle completely from the support, resulting in blow-out and thus metal loss (and deactivation) over just a few cycles.

Hence, we propose synthesizing a “core-shell” structure (Ni@support), with metal encapsulated (and accessible) within a porous support, thereby preventing metal “lift-off” and loss. Prior studies in our lab have shown the suitability of CeO₂ over conventional support materials (MgAl₂O₄ and SiO₂) in facilitating the methane cracking reaction, motivating the choice of ceria as support and thus the focus on development of Ni@CeO₂ structures.

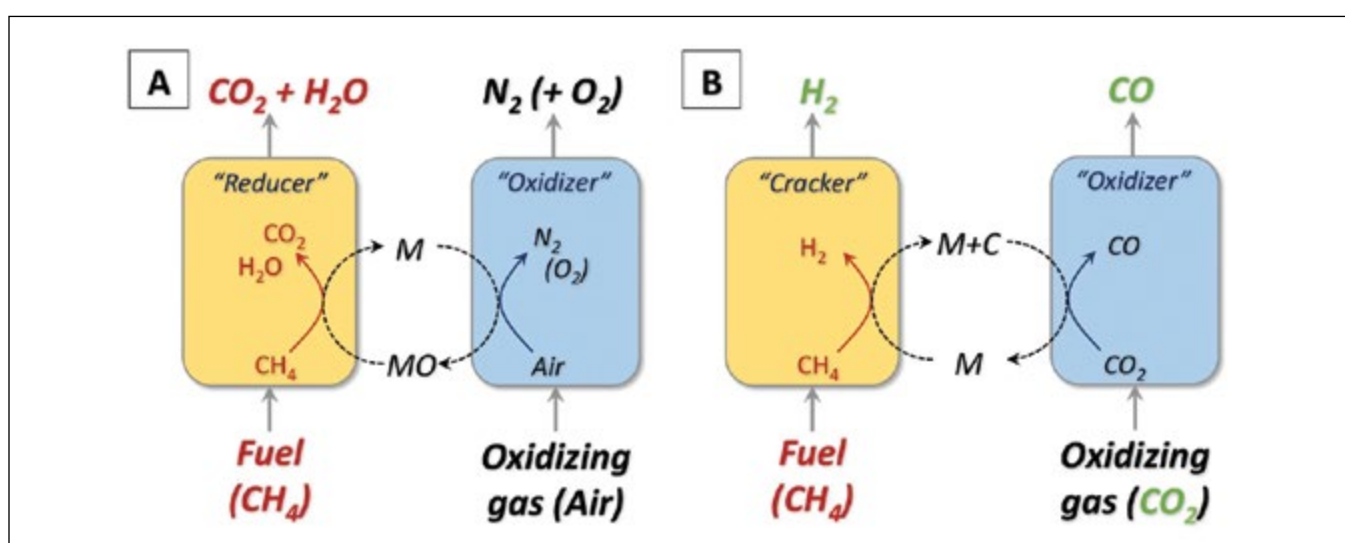


Figure 2 (A) Chemical looping combustion; (B) Proposed chemical looping process

2. Methods

To produce our Ni@CeO₂ structures, we followed the outline illustrated in Figure 4. Moreover, to simplify our initial syntheses, we eliminated the Ni at first; that is, we aimed to synthesize only ceria shells over silica templates. The first synthesis approach was adapted from work by Zhang et al [5]. As a first step, we synthesized monodisperse silica using the well-established Stöber method. Next, we dispersed silica (100 mg) in a pH-controlled buffer solution of MOPS (Sigma-Aldrich, 99.5%; 0.5232 g in 50 mL H₂O) and sodium hydroxide (Sigma-Aldrich, 98%; added until pH = 7.35). After heating to 70°C, cerium(III)sulfate (Sigma-Aldrich, 99.99%; 240 mg) was added to the buffer solution under N₂ atmosphere. The mixture was allowed to react for 2 h under vigorous stirring, at which point it was washed with DI water and centrifuged three times (Hermle Labnet Z206A; 6000 rpm, 6 min.). The product was dried in a vacuum oven (Fisher Scientific Isotemp Model 282A) overnight at 120°C and analyzed by transmission electron microscopy (“TEM”; JEOL 2000 operating at 200 kV).

A second synthesis protocol was based on work by Strandwitz and Stucky [6]. Again, Stöber silica was synthesized first. This silica (300 mg) was dispersed in ethylene glycol (Sigma-Aldrich, 99.8%; 21.5 mL) in a ~42 mL Teflon-lined autoclave, and then cerium(III) nitrate (Sigma-Aldrich, 99.99%; 1 M, 1.13 mL) was

added. At this point, the vessel was sealed and placed in the hydrothermal oven (Columbia International Series MBF-T1700) at 130°C for 15 h. Again, the product was washed with DI water and centrifuged three times, then dried overnight in the vacuum oven.

Finally, after initial results with both protocols proved unsuccessful, reaction conditions were altered to hopefully obtain the desired products. For the initial synthesis, we dissolved the cerium(III)sulfate in DI water (20 mL and 40 mL) and added that solution dropwise. For the hydrothermal synthesis, we (i) doubled the amount of cerium(III)nitrate (2 M, 1.13 mL), (ii) doubled the cerium(III)nitrate and water (1 M, 2.25 mL), (iii) used a custom beaker setup with an impeller instead of the hydrothermal reactor, and (iv) removed the silica template from the synthesis pathway.

To test the etching process, samples were dispersed in 5 M sodium hydroxide (NaOH) and stirred for 1, 3, or 5 h. They were then washed, centrifuged, dried, and characterized as before.

We also performed preliminary reactivity tests using a fixed bed reactor setup coupled with a mass spectrometer (Pfeiffer Vacuum Prisma), to confirm that our process would work. For this, we used Ni nanoparticles deposited on ceria spheres, as opposed to our targeted ceria shells with Ni on the inside. These tests aimed to establish

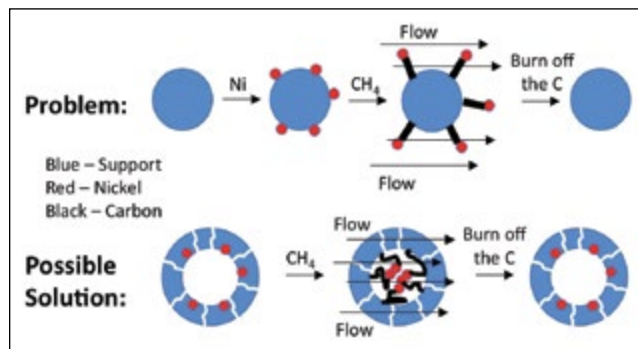


Figure 3 Problem with standard structures and possible solution using core-shell structures

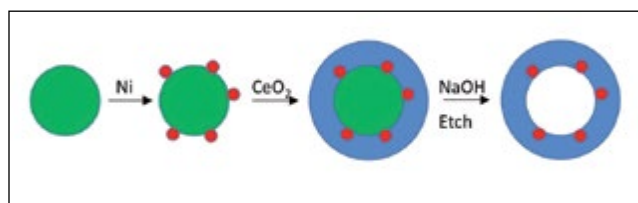


Figure 4 Core-shell structure synthesis outline

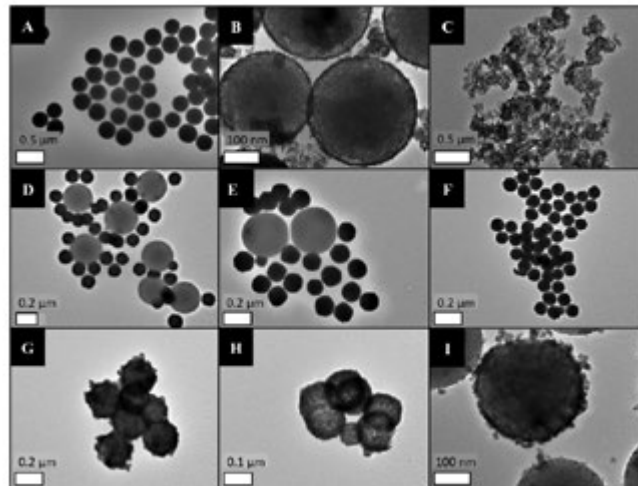


Figure 5 (A) Typical silica as prepared by Stöber method; (B) Ceria shell formation from initial synthesis; (C) Product of B after etching 1 h with 5 M NaOH; (D, E) Samples prepared using the hydrothermal method; (F) Product of D after etching 5 h with 5 M NaOH; (G, H, I) Recent results from tweaking the hydrothermal synthesis protocols

proof-of-concept for our looping process, and the use of a conventional (and thus likely unstable) Ni-ceria material instead of the core@shell configuration was not a concern, as we only needed few cycles of cracking/oxidation, over which degradation of the catalyst would not affect the results significantly. Tests were conducted at 700°C under pure streams of CH₄ and CO₂.

3. Results

Early results using syntheses as described in the literature were largely unsuccessful. Figure 5 shows TEM images of various samples from our syntheses. First (Figure 5A) is an image of the result of a typical silica synthesis. Figure 5B shows one of our early partial successes in depositing a ceria shell on the silica, but the shells were measured to be just 7-8 nm thick. Thus, when the silica was etched with 5 M NaOH, the shells were not strong enough to support their own weight and broke apart, as seen in Figure 5C. Figures 5D and 5E both show results from our second synthesis using the hydrothermal reactors. Unexpectedly, we observed (dense) spherical ceria particles instead of coated SiO₂, as reported in the literature. Figure 5F shows the results of etching the samples from Figures 5D and 5E. As expected, etching removed the silica nanoparticles and left the ceria nanoparticles unaffected. Finally, Figures 5G-I show results from our more recent tweaked hydrothermal syntheses. Here we observed a mixture of ceria shells on SiO₂ as well as spontaneously formed (silica-free) hollow ceria nanoparticles.

The results from an initial proof-of-concept fixed bed reactor test can be seen in the mass spectrometer readout

in Figure 6. In both graphs, the blue line corresponds to the right-side y-axis to represent the conversion of CH₄. For the cracking half cycle (left graph), this blue line represents the conversion of CH₄, which is well over 95%, and for the oxidation half cycle (right graph), it represents the conversion of CO₂, which is well over 90%. During the cracking half cycle, the effluent stream is comprised of ~99% H₂, with ~1% CO and negligible CO₂. During the oxidation half cycle, we see an effluent of ~99% pure CO, with the remainder being a small amount of unconverted CO₂. At around t=14 min., the CO₂ concentration increases while the CO concentration sharply decreases. This indicates complete C burn-off at this point and hence CO₂ breaking through (i.e. the reaction has gone to completion).

4. Discussion

While other studies in the literature specifically report syntheses of our desired hollow ceria structures under conditions *similar* to ours, our results suggest that attaining a specific nanostructure is highly dependent on the *exact* reaction conditions (especially pressure in the hydrothermal reactors, critical information which was omitted in the published reports) [4, 5]. Hence, we believe our unexpected results (i.e., the inability to reliably produce uniform CeO₂-coated SiO₂ structures) are, at least in part, due to incomplete information available about certain aspects of the overall synthesis. However, one take-away from our syntheses is the fact that etching with concentrated NaOH does not significantly affect ceria structure (see Figure 5F), reaffirming that the etching process works as intended. Our TEM images from more recent syntheses (Figures 5G-I) show our protocols are

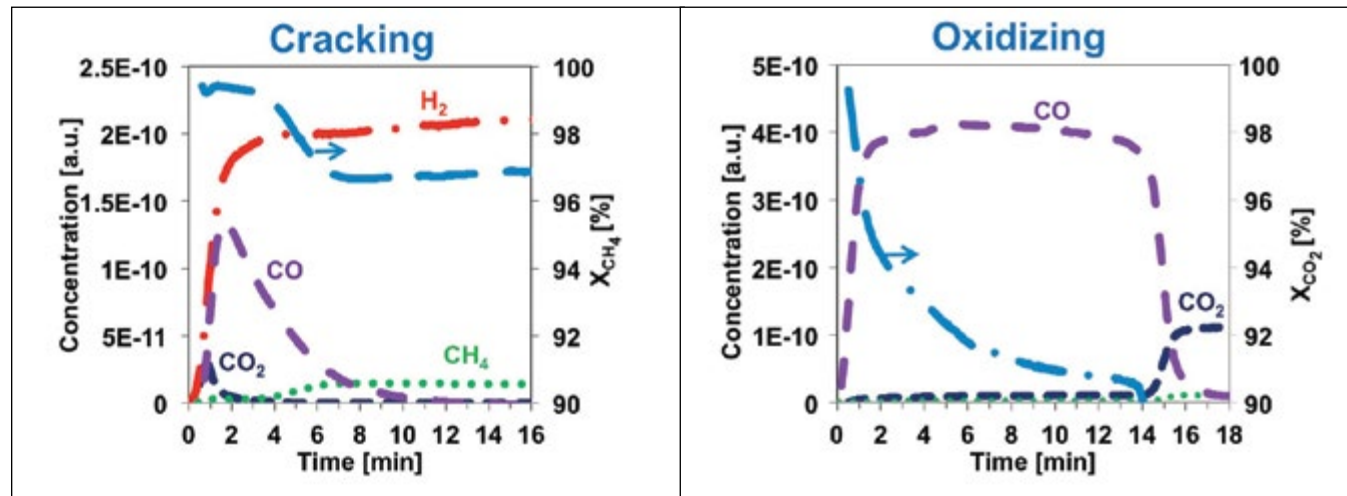


Figure 6 Mass spectrometer readout from preliminary fixed bed reactor tests using nickel nanoparticles deposited on commercially available ceria spheres

moving in the right direction to produce ceria shells. Our current efforts are hence directed toward understanding the formation mechanism in order to better control the material synthesis.

The fixed bed reactor tests were conducted with (solid) ceria spheres coated with Ni nanoparticles, as opposed to the desired Ni@CeO_2 core@shell structures. These structures are expected to be unstable over multiple cycles in industrial operation due to Ni loss from the reactor (as discussed in the Introduction). However, for our simple proof-of-concept test, the structures worked sufficiently well and demonstrated the intended process goal: cracking methane over a Ni-CeO_2 material indeed yields a high-purity stream of H_2 while depositing solid carbon on the Ni. In both halves of the cycle, high reactant conversions (95% for cracking and 90% for oxidizing), combined with high-purity effluent streams (~99% in both), prove that our proposed chemical looping process should be able to produce inherently separated streams of pure syngas components.

5. Conclusions

Though our ceria shell syntheses have not been wholly successful as of yet, we are confident that we are moving in the right direction, as evidenced by TEM images from our more recent syntheses. Continued optimization will give us better insights into the synthesis mechanism, shells with improved quality, and a more robust synthesis protocol; therefore, future studies will first be targeted toward understanding the formation mechanism. Moreover, first fixed bed reactor tests using conventional samples show that our Ni-CeO_2 carbon-carrier structures will crack methane efficiently (95% conversion) and produce high-purity (~99% pure), separate streams of H_2 and CO. Those effluent streams can then be utilized individually or combined in any desired ratio to produce a range of targeted end chemicals. Finally, despite using a fossil fuel (natural gas), the proposed chemical looping process has a negative carbon footprint since it consumes CO_2 in the carbon burn-off step. Hence, in terms of sustainability, this chemical looping process is superior to any current method of syngas production and indicates a path toward reconciling use of abundant natural gas reserves with the need to drastically reduce anthropogenic carbon emissions.

6. Acknowledgments

We gratefully acknowledge the Mascaro Center for Sustainable Innovation and the Swanson School of Engineering for their funding of this project.

7. References

- [1] A. Kiersz, The world may have another billion people in thirteen years, *Business Insider*. (2015). <http://www.businessinsider.com/un-world-population-projections-2015-7>
- [2] V. Nguyen, L. Blum, Syngas and Synfuels from H₂O and CO₂: Current Status, *Chemical Engineering Technology*. 87 (2015) 354-375.
- [3] J. Adanez, et al, Progress in Chemical-Looping Combustion and Reforming Technologies, *Progress in Energy and Combustion Science*. 38 (2012) 215-282.
- [4] M. Hossain, H. de Lasa, Chemical-looping combustion (CLC) for inherent CO₂ separations – a review, *Chemical Engineering Science*. 63 (2008) 4433-4451.
- [5] W. Zhang, et al, Controlled formation of uniform CeO₂ nanoshells in a buffer solution, *Chemical Communications*. 52 (2016) 1420-1423.
- [6] N. Strandwitz, G. Stucky, Hollow microporous cerium oxide spheres templated by colloidal silica, *Chemistry of Materials*. 21 (2009) 4577-4582.

Anti-tumor (M1) Macrophages Secrete Cytokines that Prime Breast Cancer Cells for Apoptosis

Maya McKeown^A; Jennifer Guerriero, PhD^B; and Anthony Letai, MD, PhD^B

^ADepartment of Bioengineering, Swanson School of Engineering, University of Pittsburgh, Pittsburgh, PA, USA

^BDepartment of Medical Oncology, Dana-Farber Cancer Institute, Boston, MA, USA

Abstract

Tumor associated macrophages modulate many aspects of breast cancer progression and tumor microenvironment. M1 anti-tumor macrophages are currently being explored for potential uses in novel immunotherapies, since they release cytokines that activate anti-tumor adaptive immunity and initiate tumor killing via apoptosis. This study utilizes BH3 profiling, a unique assay that measures mitochondrial outer membrane permeabilization (MOMP) as an indication of how “primed” a cell is for apoptosis.

We first validate past work showing that a breast cancer cell line, BT20, is in fact primed in response to treatment of conditioned media from M1 macrophages (“CM M1”). BT20 cells also are treated with a caspase-8 inhibitor (“CM M1 + Cas8inh”) and BH3 profiled to assess priming with and without death ligand-mediated mitochondrial apoptosis. Results suggest that a veritable degree of mitochondrial apoptotic priming is due to death ligand signaling. Additionally, cell viability and caspase levels, in response to CM M1 media with and without caspase-8 inhibition, are compared between three responding cell lines (BT20, MCF7, and HCC202) and three nonresponding cell lines (MD-MBA-453, T47D, and MD-MBA-436). Viability assays show key differences between the two groups, but more research is needed to discern why. Further evaluation of cell viability along with BH3 profiling after inhibition of caspase-8, the link between extrinsic apoptosis and the mitochondrial pathway, may clarify whether this route is indeed the preferred apoptosis pathway in sensitive breast cancer cell lines. Understanding such mechanistic preferences may help discriminate if a patient’s tumor would be susceptible to certain macrophage based immunotherapies.

Keywords: M1 macrophages, immunotherapy, apoptosis, BH3 profiling

Abbreviations: M1—anti-tumor macrophages; M2—pro-tumor macrophages; TAM—Tumor associated macrophages; Bcl-2–B cell lymphoma 2; BH3—BCL2 protein Homology domain 3; MOMP—mitochondrial outer membrane permeabilization; LPS—lipopolysaccharide;

IFNg— Interferon gamma; CM M1—conditioned media of M1 macrophages; CM M1 + Cas8inh—conditioned media of M1 macrophages with caspase-8 inhibitor; CTG—CellTiter Glo

1. Introduction

1.1 Tumor associated macrophages in breast cancer

Acquired resistance to chemotherapy is a persistent challenge in oncology. The goal of cancer immunotherapy is to break away from cytotoxic treatments and focus on harnessing the power of the immune system to eliminate tumors. In addition to manipulating the adaptive immune system (as in T-cell reprogramming and checkpoint blockade inhibition), there is increasing appreciation for the innate immune system in facilitating an effective anti-tumor response. Tumor associated macrophages (TAMs) can represent up to 50% of breast tumor mass as the most abundant immune cell population [1-2]. They release soluble factors that modulate many aspects of tumor progression, invasion, metastasis, and angiogenesis. They are traditionally classified into two phenotypes: the anti-tumor phenotype (M1) or the pro-tumor (M2) [3]. Clinically, high tumor density of TAMs has been associated with chemoresistance and a worse clinical outcome [4].

There are two main strategies to target macrophages in immunotherapy: depletion or inhibition of TAMs or redirection of phenotype from M2 to M1. Use of an antagonist to block the signaling of the myeloid growth factor receptor CSF1R on the surface of macrophages has shown a decrease in the number of TAMs and a bolstered T cell activation [5]. Additionally, Trabectedin (Yondelis®) is an FDA approved alkylating agent

indicated for soft tissue sarcomas that has been shown to inhibit the cytokine production of M2 TAMs [6]. Research into reprogramming macrophage phenotype is a relatively new concept, however initial studies of CD40 agonists, Toll Like Receptor agonists, and Class IIa histone deacetylase inhibitors show promising results [7-10]. Unlike previous research, this study focuses more narrowly on the specific mechanism of apoptosis induced by cytokines released by M1 macrophages in attempt to discern why certain cell lines may be more susceptible or resistant to macrophage mediated immunotherapy approaches.

1.2 Mechanisms of apoptosis

Prevention of apoptosis is one mechanism that cancer cells utilize to prolong development and survival. Macrophages are known to secrete cytokines that modulate apoptosis [11]. As demonstrated in Figure 1, there are two main pathways of apoptosis. The intrinsic pathway triggered in response to intracellular stress, such as DNA damage, activates the pro-apoptotic BCL-2 family proteins of the mitochondria causing mitochondrial outer membrane permeabilization (MOMP), cytochrome c release, and a caspase cascade, ultimately resulting in apoptosis [12]. The extrinsic pathway is triggered by

death ligands, such as cytokines in the TNF super family, TRAIL, and FasL, external to a cell and may proceed either by a direct caspase cascade or via the mitochondrial route, as the two are linked after cleavage of Procaspsase-8 in the cytoplasm [12].

1.3 BH3 profiling measures apoptotic priming

BH3 profiling is a tool developed in the Letai Lab that measures MOMP by cytochrome c release as an indication of how close cells are to the threshold of mitochondrial apoptosis, categorizing cells as either “primed” or “unprimed.” A cell is considered “primed” if, upon treatment, there is a statistically significant increase in the percentage of MOMP above baseline as detected by BH3 assays, often correlating with greater cell death. The priming of cancer cells is a predictor of clinical response to conventional chemotherapy [14]. Unpublished BH3 profiling from the Letai Lab shows that macrophage phenotype can enhance apoptotic priming of tumor cells, inducing chemosensitivity. In earlier unpublished studies, comparison of the percentage of apoptotic priming in response to conditioned media of M1 macrophage treatment among 16 breast cancer cell lines identified the three most highly primed cell lines qualitatively considered “responders,” and the three most

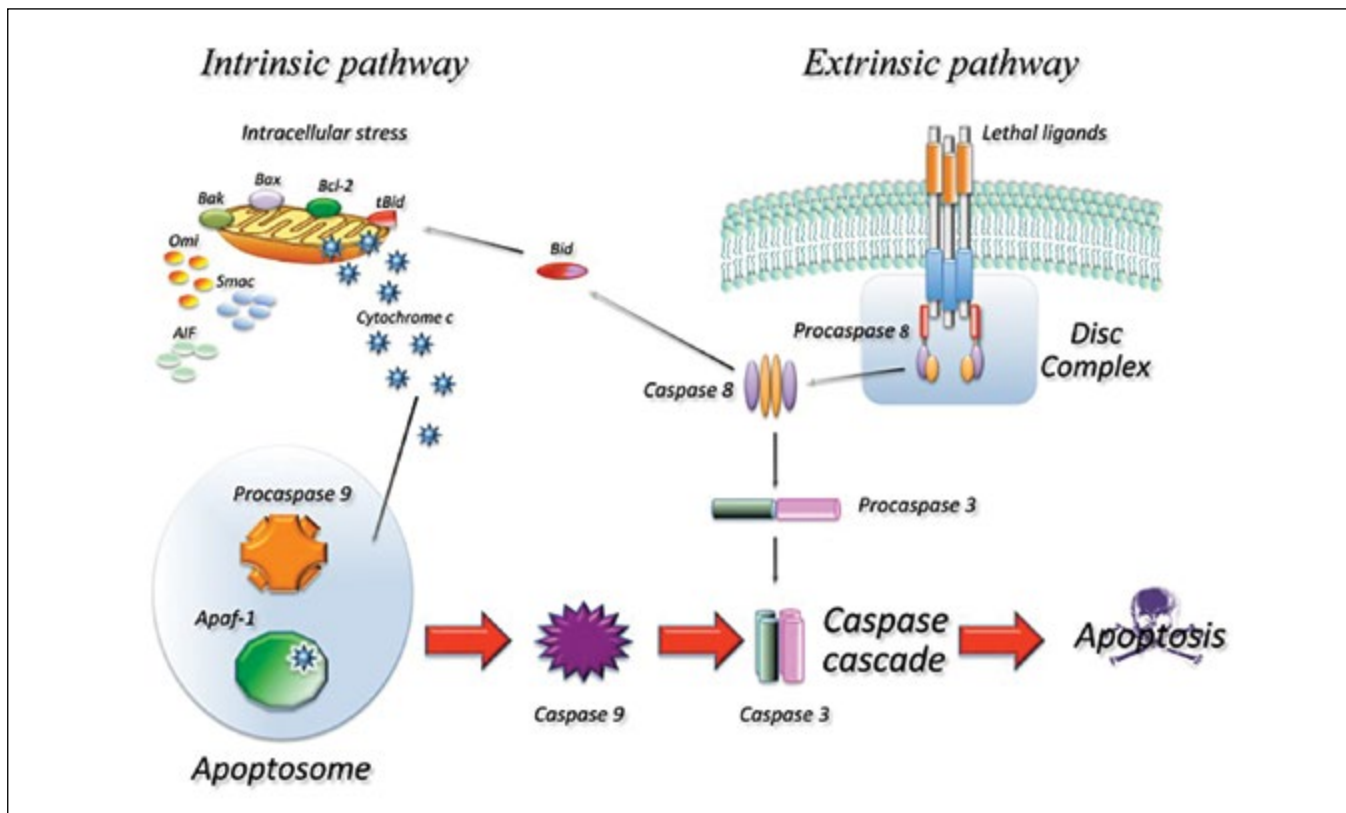


Figure 1. The pathways of apoptosis are linked at the cleavage of Procaspsase-8 [13].

weakly primed cell lines suggesting resistance to conditioned media treatment, referred to as “non-responders.”

We hypothesize that BH3 profiling will show a reduction in priming in responding cell lines when caspase-8 is inhibited, blocking apoptosis from proceeding via extrinsic death ligands to the mitochondrial pathway. Additionally, caspase activity and cell viability assays will be compared between responding and nonresponding cell lines after CM M1 treatment with and without inhibition of caspase-8. This study aims to evaluate potential mechanistic differences in apoptosis of responding cell lines versus nonresponding cell lines, in the hopes of contributing to a body of knowledge that will help discriminate which patients’ tumors may be susceptible to macrophage based immunotherapies in the future.

2. Methods

2.1 Treatment groups

To study how M1-secreted cytokines may alter a tumor cell’s apoptotic priming, we stimulated a murine macrophage cell line with Interferon gamma (IFNg) and lipopolysaccharide (LPS) to induce an M1 anti-tumor phenotype. We then collected media cultured by these M1-stimulated cells (“CM M1”) and added a caspase-8 inhibitor (“CM M1 + Cas8inh”) (R&D Systems Inc., Minneapolis, MN). The three treatment groups thus included control (LPS + IFNg), CM M1, and CM M1 + Cas8inh.

2.2 BH3 profiling of BT20 cells

BH3 profiling was used to assess the apoptotic priming of sensitive BT20 cells in response to the conditioned media treatment with and without caspase-8 inhibition. Cells were pretreated for four hours with 40uM Cas8inh in RPMI media (Thermo Fisher) for the CM M1 + Cas8inh group, while the control and CM M1 groups were pretreated with 40uM DMSO (Thermo Fisher) in RPMI media for four hours. After pretreatment, BT20 cells in the CM M1 + Cas8inh group were treated with 40uM Cas8inh in CM M1 for 24 hours, while BT20 cells in the other groups (LPS + IFNg and CM M1) were also treated separately for 24 hours.

As detailed in Ryan and Letai [15], single cell suspensions are permeabilized with detergents and reducing agents to expose the mitochondrial matrix to the treatment of various pro-apoptotic BH3 only peptides and control peptides. Staining with JC-1 dye (Thermo Fisher) allows for automated fluorescence readings of MOMP by the Safire2 microplate spectrophotometer (Tecan, Medford, MA). The detection of MOMP is reported as the percentage of mitochondrial priming and is normal-

ized to positive control DMSO and negative control Alamethicin peptide.

2.3 Cell viability and caspase activity assays

CellTiter-Glo (CTG), caspase-Glo 3/7, and caspase-Glo 8 luminescent assays (Promega, Madison, WI) assessed ATP levels as a marker of cell viability, caspase-3/7 activity, and caspase-8 activity, respectively, of cells in response to CM M1 and CM M1 + Cas8inh treatments. The assays were performed on cell lines previously identified as responders (BT20, MCF7, HCC202) or nonresponders (MDA-MB-453, T47D, MDA-MB-436) to CM M1 treatment.

Relative luminescence for all Glo assays was read by the Safire2 microplate spectrophotometer after 8-, 24-, and 48-hour incubation time points, following the initial 4-hour pretreatment and treatment scheme identical to the BH3 profiling procedure. For the CTG study, the 20th minute of the luminescent read was compared across all time points, cell lines, and treatment groups. For the caspase-Glo studies, the area under the curve was calculated at each time point and compared across cell lines and treatment groups. All results were normalized to the control treatment group (LPS + IFNg).

Results

BH3 profiling of BT20 cells confirmed that CM M1 treatment increases depolarization, priming BT20 cells for apoptosis; however, addition of a caspase-8 inhibitor rescues priming to levels similar to control, shown in Figure 2.

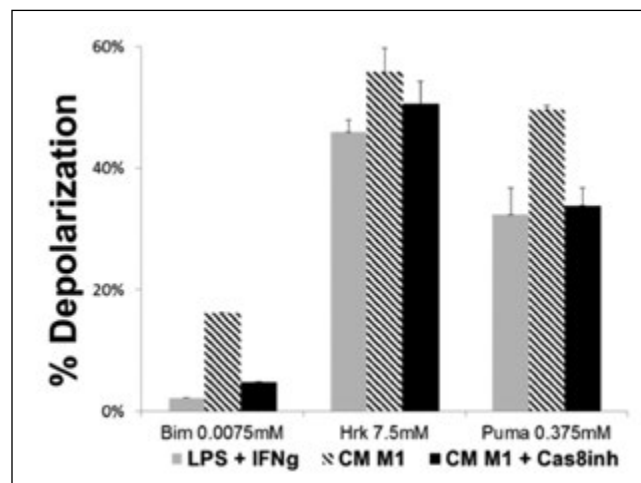


Figure 2. BH3 profile of positively responding BT20 cells showing mitochondrial depolarization upon specific dilutions in DMSO of pro-apoptotic BH3 only peptides Bim, Hrk, and Puma. Addition of the Caspase-8 inhibitor during 24-hour CM M1 treatment rescues priming to levels similar to the control group, LPS + IFNg. Standard error bars show consistency among triplicate samples.

Results from the CTG and caspase-Glo assays in Figure 3 show that in all cell lines, caspase-8 activity, as well as downstream caspase-3 activity was indeed extremely inhibited upon addition of caspase-8 inhibitor to the conditioned media treatment. Not only are BT20 cells less primed for mitochondrial apoptosis as evident in the BH3 profile, but the results together confirm that lack of functional caspase-8 leads to a reduction in BT20 cell death. In non-responding cell lines, at the 48-hour time point the inhibitor rescued less cells relative to responders, except in MD-MBA-453 which had notably increased cell viability.

Discussion

The caspase-8 inhibitor blocks apoptosis from proceeding via extrinsic death ligands to the mitochondrial pathway. Since caspase-8 inhibition which causes a reduction in priming can be measured by BH3 profiling (which specifically measures priming in the mitochondrial pathway), the results suggest that, as hypothesized, in BT20 cells apoptosis depends on caspase-8 activation triggered by death ligands secreted by M1 macrophages. Although such a result for BH3 profiling is only shown for BT20 cells, in the future we hope to more clearly compare the priming levels of responding cell lines to nonresponding cell lines, with and without caspase-8 inhibition.

Caspase-Glo 3/7 and caspase-Glo 8 assays were used to verify that the caspase-inhibitor was indeed reducing levels of caspase-8 and downstream caspase-3 and -7.

The CTG data shows that caspase-8 inhibition not only causes a reduction in priming in BT20 cells, but also causes an increase in cell viability. Considering inhibition of caspase-8 stunts extrinsic apoptosis, these results are consistent and suggest that in BT20 cells, cell death is largely due to apoptosis triggered by death ligands from M1 macrophages. HCC202 cells, also previously identified as sensitive, show a large increase in cell viability after caspase-8 inhibition, though not to the extent of the BT20s. Although repeated trials are necessary, in general the sensitive cell lines showed greater cell rescue after caspase-8 inhibition, suggesting a larger reliance on death ligands to trigger apoptosis through the mitochondrial pathway.

Since the CTG assay is only evaluating viability, we cannot conclude why specifically cell death occurs in some cell lines and not others based solely on the varying dependence on caspase-8. Performing BH3 profiles of all the cell lines in response to CM M1 with and without caspase-8 inhibitor would be helpful to discriminate which cell lines carry out apoptosis mostly due to death ligands, versus those which rely more so on intracellular stress signals and the intrinsic apoptosis pathway. In addition, we hope to utilize RNA sequencing to assess the potential transcriptomic basis for such mechanistic differences between responders and nonresponders. Determining these differences in M1 macrophage mediated apoptosis could eventually affect drug selection, depending on tumor cell type.

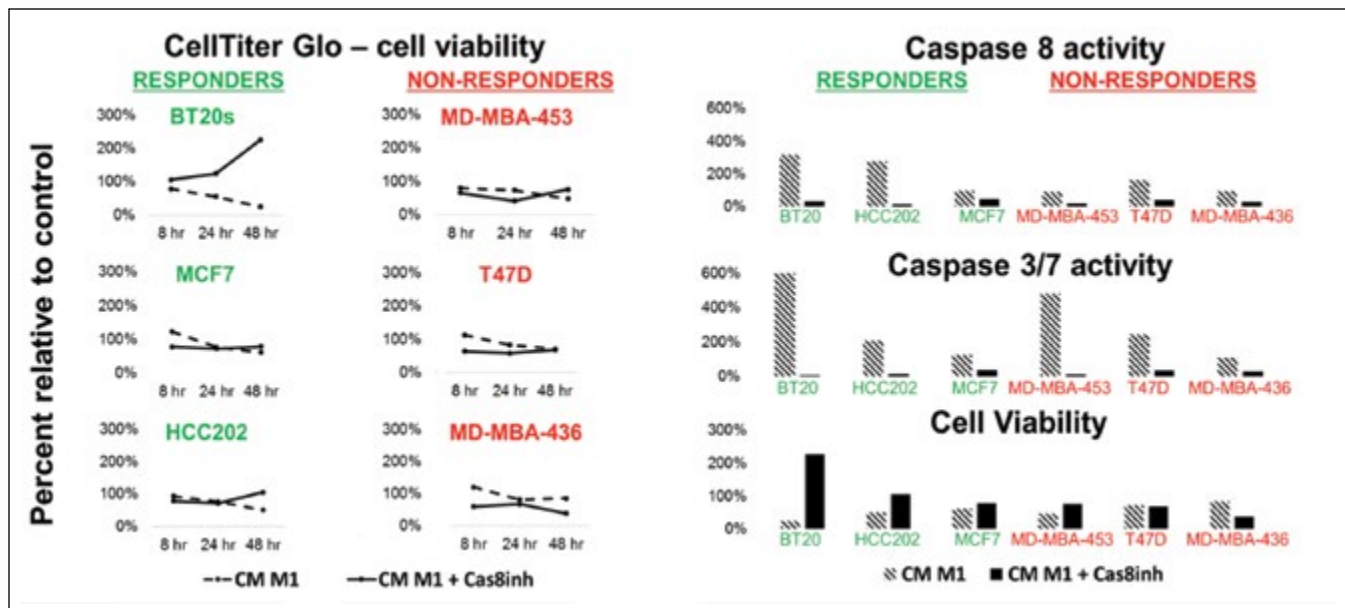


Figure 3. The left panels show three time points of CTG levels (relative ATP concentration) as an indication for cell viability. The right panels show the 48-hour data for CTG, as well as Caspase-8 and Caspase-3/7 activity levels. All results compare CM M1 to CM M1 with Caspase-8 inhibitor, both normalized to control, LPS + IFNg.

Conclusion

M1 anti-tumor macrophages modulate many aspects of apoptosis in various breast cancer cell lines. BH3 profiling coupled with cell viability assays with and without caspase-8 inhibition can be used to determine the reliance of apoptosis initiation on death ligands released by M1 macrophages. This study suggests that in responding breast cancer cell lines like BT20s, a large degree of mitochondrial priming is due to death ligand signaling. As the cell viability assay results show, there are noticeable differences in responding cell lines versus non-responding cell lines after blocking death-ligand mediated mitochondrial apoptosis through use of the caspase-8 inhibitor. To better understand the mechanistic differences in apoptosis between responding and nonresponding cell lines, more studies are necessary. Understanding such differences as well as the cellular signaling may help discriminate if a patient's tumor would be reasonably sensitive to certain macrophage based immunotherapies.

Acknowledgments

Funding was provided by the University of Pittsburgh Swanson School of Engineering and the Office of the Provost. An additional thank-you goes to the members of the Letai Lab for welcoming me at Dana-Farber and helping me to learn and optimize assays and cell culture.

References

- [1] P.M. Kelly, R.S. Davison, E. Bliss, J.O. McGee, Macrophages in human breast disease: a quantitative immunohistochemical study, *Br. J. Cancer* 57 (1988) 174-177.
- [2] R.D. Leek, A.L. Harris, C.E. Lewis, Cytokine networks in solid human tumors: regulation of angiogenesis, *J. Leukoc. Biol.* 56 (1994) 423-435.
- [3] A. Mantovani, S. Sozzani, M. Locati, P. Allavena, A. Sica, Macrophage polarization: tumor-associated macrophages as a paradigm for polarized M2 mononuclear phagocytes, *Trends. Immunol.* 23 (2002), 549-555.
- [4] R.Z. Panni, D.C. Linehan, D.G. DeNardo, Targeting tumor-infiltrating macrophages to combat cancer, *Immunotherapy* 5 (2013), 1075-1087.
- [5] Y. Zhu, B.L. Knolhoff, M.A. Meyer, T.M. Nywening, B.L. West, J. Luo, A. Wang-Gillam, S.P. Goedegebuure, D.C. Linehan, D.G. DeNardo, CSF1/CSF1R Blockade Reprograms Tumor-Infiltrating Macrophages and Improves Response to T Cell Checkpoint Immunotherapy in Pancreatic Cancer Models. *Cancer Research*, 74(18) (2014), 5057-5069.
- [6] M. D'Incalci, & C.M. Galmarini, A review of trabectedin (ET-743): a unique mechanism of action. *Molecular cancer therapeutics*, 9(8) (2010) 2157-2163.
- [7] G.L. Beatty, E.G. Chioorean, M.P. Fishman, B. Saboury, U.R. Teitelbaum, W. Sun, R.D. Huhn, W. Song, D. Li, L.L. Sharp, D.A. Torigian, P.J. O'Dwyer, R.H. Vonderheide, CD40 agonists alter tumor stroma and show efficacy against pancreatic carcinoma in mice and humans. *Science*, 331(6024), (2011) 1612-1616.
- [8] T.S. Kapellos, & A.J. Iqbal, Epigenetic Control of Macrophage Polarisation and Soluble Mediator Gene Expression during Inflammation. *Mediators of inflammation*, 2016.
- [9] M.R. Shakespear, D.M. Hohenhaus, G.M. Kelly, N.A. Kamal, P. Gupta, L.I. Labzin, K. Schroder, V. Garceau, S. Barbero, A. Iyer, D.A. Hume, R.C. Reid, K.M. Irvine, D.P. Fairlie, M. J. Sweet, Histone deacetylase 7 promotes Toll-like receptor 4-dependent proinflammatory gene expression in macrophages. *J. Biol. Chem.*, 288(35) (2013), 25362-25374.
- [10] Q. Cao, S. Rong, J.J. Repa, R. St Clair, J.S. Parks, N. Mishra, Histone deacetylase 9 represses cholesterol efflux and alternatively activated macrophages in atherosclerosis development. *Arterioscler. Thromb. Vasc. Biol.* 34(9) (2014), 1871-1879.
- [11] A. Eichten, K.E. de Visser, L. Coussens, Macrophages in tumor development and metastasis, in: H.E. Kaiser, A. Nasir (Eds.), *Selected Aspects of Cancer Progression: Metastasis, Apoptosis, and Immune Response* (Vol. 11), Springer Science and Business Media, New York, 2008, pp. 115-137.
- [12] D.R. Green, *Apoptosis: physiology and pathology*. Cambridge University Press, New York, 2011.
- [13] B. Favaloro, N. Allocati, V. Graziani, C. Di Ilio, V. De Laurenzi, Role of apoptosis in disease, *Aging* 4 (2012), 330-349.
- [14] T. Ni Chonghaile, K.A. Sarosiek, T.T. Vo, J.A. Ryan, A. Tammareddi, V.D.G. Moore, J. Deng, K.C. Anderson, P. Richardson, Y.T. Tai, C.S. Mitsiades, Pretreatment mitochondrial priming correlates with clinical response to cytotoxic chemotherapy, *Science* 334 (2011), 1129-1133.
- [15] J. Ryan and A. Letai. BH3 profiling in whole cells by fluorimeter or FACS. *Methods* 61 (2013) 156-164.

Creating an Osteochondral Bioreactor for the Screening of Treatments for Osteoarthritis

Derek A. Nichols¹, Inderbir S. Sondh², Paolo Zunino^{1,4}, and Riccardo Gottardi^{3,5}

¹*Department of Mechanical Engineering and Materials Science, ²Department of Bioengineering, Swanson School of Engineering, University of Pittsburgh, Pittsburgh, PA, USA*

³*Department of Orthopedic Surgery, University of Pittsburgh, Pittsburgh, PA, USA*

⁴*Department of Mathematics, Politecnico di Milano, Milano, Italy; ⁵Ri.MED Foundation, Palermo, Italy*

Abstract

Bioreactors are systems that can be used to monitor the response of tissues and cells to candidate drugs. Building on the experience developed in the creation of an osteochondral bioreactor at the University of Pittsburgh, we designed a new system that will allow constant optical access to the cells throughout testing unlike our previous model, which limited observations to end-point testing. This new design was optimized in order to achieve the maximum possible fluid transport through the central chamber, which corresponds to the maximum possible drug exposure. This was achieved by minimizing the channel diameter while maximizing the step height, outer ring diameter, pore diameter, and number of pores. A model with maximized drug exposure was then created and tested in a laboratory setting.

Keywords: bioreactor, osteoarthritis, computational fluid dynamics, ANSYS CFX

Abbreviations: osteoarthritis (OA), osteochondral (OC)

1. Introduction

Osteoarthritis (OA) is characterized by the breakdown of the cartilage lining the ends of long bones [1]. When studying the mechanism of OA progression to identify possible therapies, it is crucial to consider both bone and cartilage simultaneously as there is growing evidence suggesting interplay between them [1, 2].

Currently, there is no pharmacological treatment to arrest or cure cartilage degeneration during OA [1]. In order to screen drug candidates to identify potential treatments for OA while excluding potentially harmful compounds, it would be beneficial to possess systems of medium to high throughput screening that recapitulate the three-dimensional organization of cells within a tissue and that are thus more biosimilar to human physiology than cells in a dish [3]. Such systems would be used prior

or in parallel to animal testing to decrease the need of animal use and increase the safety profile of the screen candidate drugs [4]. Appropriate bioreactors for this purpose are then necessary, i.e., apparatuses in which to place and maintain native tissues or cells in a 3-D scaffold environment whose response to a candidate drug can be monitored. Some of our recent work has resulted in one such device for the study of osteochondral (OC) tissues or engineered constructs, that is, a physiological unit composed of cartilage and its subchondral bone [1, 5, 6]. This osteochondral system bioreactor is unique as it can be used to generate engineered OC constructs comparable in size to native tissues, and it also can be used to culture native tissue over several weeks (unpublished results). The current bioreactor system (Figure 1) which consists of a 3-D printed part filled with an OC construct which is hooked up to a pump containing drugs and other nutrients, relies heavily on end-point testing, i.e., assessment of the effects of treatment by destructive tests such as PCR and histology, since it does not allow for direct optical access

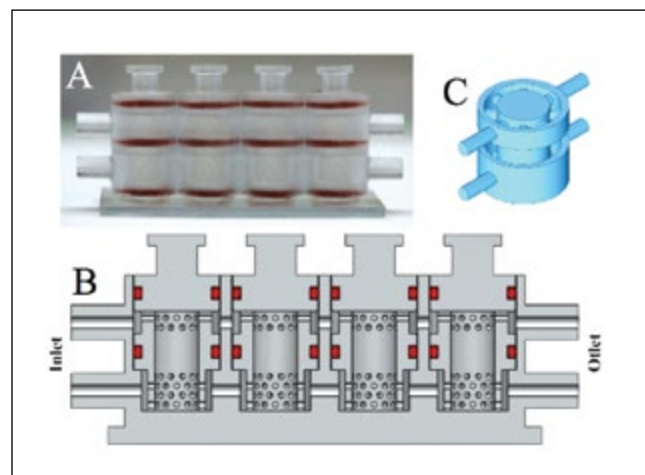


Figure 1: A) Osteochondral bioreactor system (4 wells), B) its cross section, and C) “negative” of one well of the bioreactor highlighting the volume occupied by fluid and constructs

to the cells. Having such an optical access would allow the periodic, non-destructive monitoring of cell behavior, using, for instance, fluorescently labeled cells or cells transduced with gene reporters, which keep the cells and construct intact for future observations and tests.

To address this issue, the aim of this project was to design and optimize a new bioreactor system that would allow optical access to cells within 3-D engineered constructs. We have achieved this objective by optimizing via finite element modeling a design that meets the required design parameters (small unit to host constructs to allow complete volumetric imaging, sufficient flow through the constructs to allow nutrients and waste exchange, size and fluidic channels compatible with a 96-well plate format), followed by 3-D printing of the bioreactor and its testing.

2. Methods

2.1 Finite Element Modeling

Models of the flow path were created using the CAD software SolidWorks (Waltham, MA) and tested using the finite element analysis software ANSYS Fluid Flow (CFX) (Canonsburg, PA). A volume flow rate of 1 mL/day was imposed at the inlet, and the outlet was open to the environment. The chamber hosting the cells (central chamber) was considered as filled with photocross-linked methacrylated gelatin (GelMA), a hydrogel with a permeability of 1×10^{-16} m² and a porosity of 0.8 [7]. Velocities through the central chamber were measured in CFX Post, the data resulting from the ANSYS simulation, and plotted against each specific design change in the bioreactor schematics to determine any relationships between design features and central velocity. Each model was assessed based on the velocity of the fluid through the middle of the central chamber, as this is a fair representation of drug exposure throughout.

2.2 3-D Printing

The bioreactor was printed by stereolithography (SLA) using a 3Dsystems Viper si2 (Rock Hill, SC) printer and Somos WaterShed XC 11122 (Elgin, IL) resin. The resolution of the printer is 50 µm and the smallest possible void able to be printed is 0.60 mm [8, 9].

2.3 Fluidic Validation

Once the bioreactor was printed and assembled, the central chamber was filled with GelMA. The inlet was then hooked up to a syringe filled with water which, in turn, was hooked up to a Kiyatec FC230 (Greenville,

SC) pump that forced the water through the bioreactor at a rate of 1 mL/day [10]. Food dye was added to the water in order to better observe the flow through the central chamber. Pictures were then taken in 15-minute intervals in order to observe the flow of the fluid through the bioreactor.

3. Results

3.1 Bioreactor Design

In order to allow for optical access to the cells, the thickness of the cell construct could not exceed 1 mm in height, as this is the focal range of a standard microscope. The main block of the bioreactor (Figure 2a), which houses the GelMA in the central chamber and contains the path for the fluidics (Figure 2b), is assembled with the addition of other components (Figure 3).

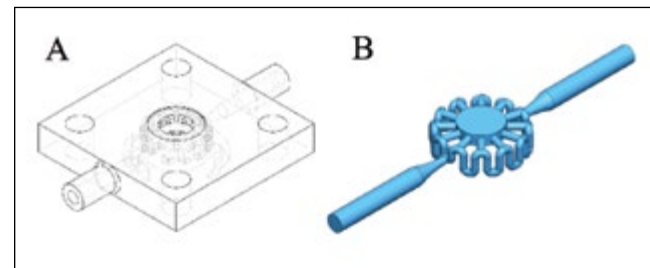


Figure 2: A) The physical bioreactor, B) volume occupied by fluid and constructs

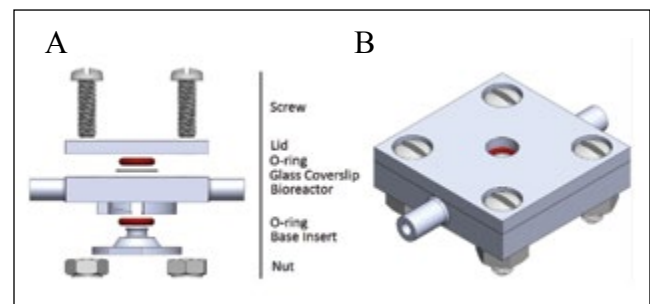


Figure 3: A) Exploded view of the bioreactor, B) assembled bioreactor model

Cells are hosted in the central chamber within a scaffold with low permeability, resulting in a relatively low amount of drug exposure, since most of the fluid will travel through the surrounding channel [1]. The specific goal for this research was to define the optimal fluidic design of an individual bioreactor chamber, such as the one seen in Figure 2b, that allows complete permeation of the engineered constructs with nutrients and other factors. The medium flow can be controlled by changing

the geometric properties of the flow channels to control local pressure differences and the effectiveness of the model can be quantified by measuring the velocity of the fluid through the central chamber. In fact, since the volume flow rate at the inlet is fixed, the higher the velocity through the central chamber, the greater the amount of total mass flow, and more mass flow equates to higher drug and nutrient exposure for the cells over time.

3.2 Design Optimization

Optimization of the bioreactor can be achieved by altering the dimensions of the features found in Figure 4, as these dimensions are what control the flow through the model.

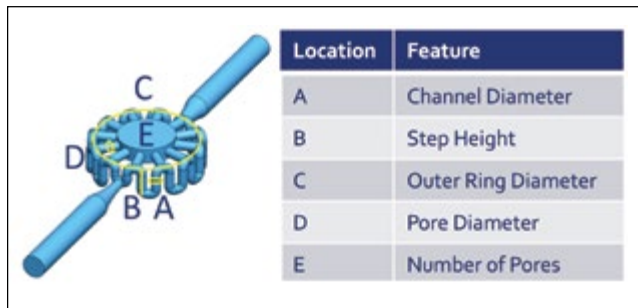


Figure 4: Defining the features of the bioreactor

One dimension can be increased in 0.05 mm increments while all other dimensions remain constant. The fluid velocity in the central chamber can then be plotted against the dimension of the design parameter of interest. Doing so for all dimensions results in the plots shown in Figure 5.

Fluid velocity is linearly dependent on the step height, outer ring diameter, pore diameter, and number of pores whereas the correlation with the channel diameter is logarithmic and becomes linear when both variables are plotted on a log scale. Once parameter constraints are defined, it is possible to identify the maximum flux through the central chamber hosting the engineered constructs by simply using these linear relationships for each design feature.

Using these relationships, an optimized bioreactor was created, and the ANSYS results could be compared to a simple circular ring model in order to determine how the design was improved by optimizing the features from Figure 4. The results from the simulation are seen in Figure 6.

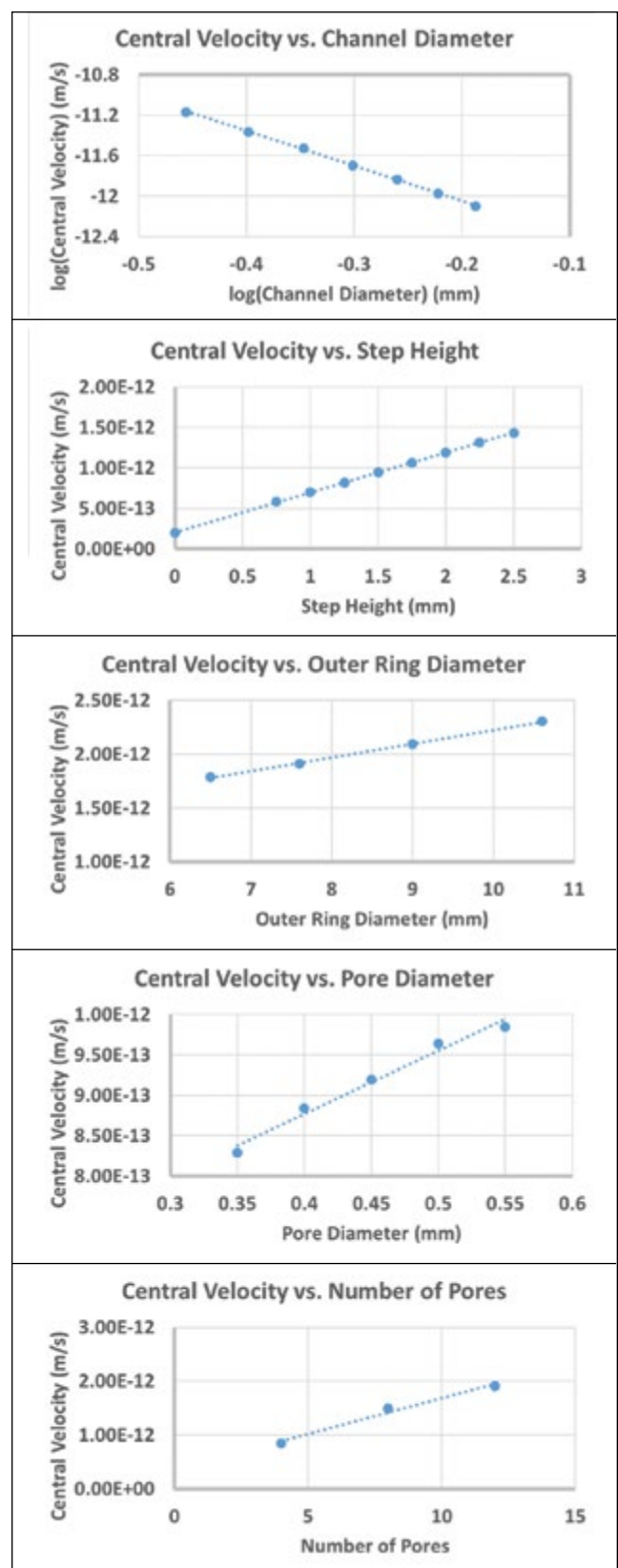


Figure 5: Plots of the central velocity versus various dimensions

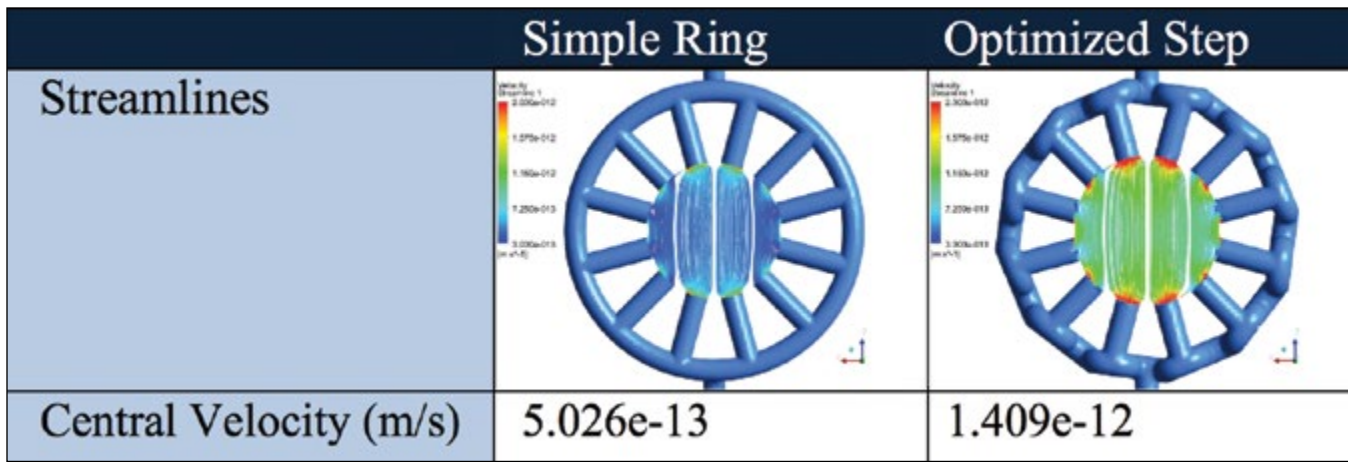


Figure 6: ANSYS results comparing the simple ring model to the optimized step model

It is evident that the step model is more effective than the ring model, offering a central fluid velocity that is nearly two times greater. These two models were 3-D printed and tested by flowing dyed water through the systems at a rate of 1 mL/day and making observations every 15 minutes. The results from the laboratory tests are seen in Figure 7, which confirm the simulation results. It is apparent that the step bioreactor achieves more drug

exposure than the ring bioreactor, as evidenced by more dye flowing through the central chamber over the same period of time.

4. Discussion

As shown in the previous section, by simply altering the geometry, the flux through the central chamber can be controlled. These findings agree with similar simulations done at the University of Pittsburgh in which a dual fluidic bioreactor was used for high throughput screening [11]. The results indicate that maximization of fluid velocity, and therefore the total drug/nutrients exposure, can be achieved by minimizing the channel diameter and maximizing all other design features. These relationships develop as a result of a rise in the hydraulic resistance of the model. In fact, lengthening the path the fluid has to move through in the surrounding ring or decreasing its channel diameter, the hydraulic resistance is increased and consequently more fluid will move through the central chamber [12]. The sole constraints then are determined by the resolution of the 3-D printer and by the overall design considerations of the model.

The step height can be extended only a certain amount before it runs into other portions of the model; therefore, the maximum size for the step height is 1.75 mm. In order to eventually be used in a 96-well plate, the entire ring of the design must fit within a 6.8 mm cylinder. The pore diameter can be only as large as the channel diameter, and, because the channel diameter relationship is logarithmic versus the linear pore diameter relationship, it was determined that the model benefits more from a

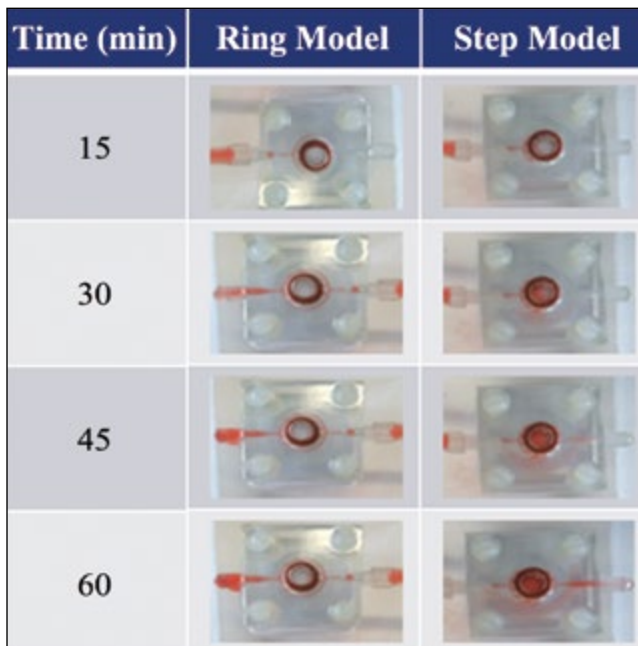


Figure 7: Results from laboratory testing proving that the step model attains more drug exposure through the central chamber

small channel than large pores. To satisfy these requirements, the following dimensions were chosen:

Table 1: Chosen dimensions for the optimized model

Feature	Dimension
Channel Diameter	0.60 mm
Step Height	1.75 mm
Outer Ring Diameter	6.75 mm
Pore Diameter	0.60 mm
Number of Pores	12

5. Conclusions

This optimized step bioreactor maximizes the drug exposure to the cells under test while minimizing the dimensions of the model while allowing for optical access within the 3-D construct and maintaining dimensions compatible with a standard 96-well plate.

Having confirmed the predictive value of the simulations, in future research different and unique models can be created and tested in ANSYS to account for specific experimental needs in engineering multiphasic constructs or for delivering drug candidates to specific construct locations. For instance, a dual inlet model can be used to engineer bone on one side of the central chamber with cartilage on the other, and to deliver a compound to only one tissue to assess cartilage-bone interaction, while simultaneously accounting for the possible difference in densities between the two components of the OC construct. Some of these activities are currently being pursued in the laboratory. Furthermore, based on these studies with a single chamber, a bioreactor comprised of an array of identical units is currently being implemented to allow for medium to high throughput screening.

6. Acknowledgements

Funding to DN was kindly provided by the Swanson School of Engineering and the Office of the Provost, and to RG by the Ri.MED Foundation.

7. References

- [1] Lozito T.P., Alexander P.G., Lin H, Gottardi R, Cheng A, Tuan R.S. (2013) *Stem Cell Research & Therapy* 4(Suppl 1):S6.
- [2] Goldring S.R., Goldring M.B. (2016) *Nature Reviews Rheumatology* 12:632-44.
- [3] Sutherland M.L., Fabre K.M., Tagle D.A., (2013) *Stem Cell Research & Therapy* 4(Suppl 1):I1
- [4] Wikswo J.P. (2014) *Experimental Biology and Medicine* 239(9):1061-72.
- [5] Iannetti L, D'Urso G, Conoscenti G, Cutrì E, Tuan RS, Raimondi MT, Gottardi R, Zunino P. (2016) *PLoS ONE* 11(9): e0162774.
- [6] Lin H., Lozito T.P., Alexander P.G., Gottardi R., Tuan R.S. (2014) *Molecular Pharmaceutics* 11(7):2203-12
- [7] Taffetani M, Gottardi R, Gastaldi D, Raiteri R, Vena P. (2014) *Medical Engineering and Physics* 36(7):850–8.
- [8] http://www.3dsystems.com/products/datafiles/viper/datasheets/International/viper_si2_uk.qxd.pdf
- [9] http://www.dsm.com/products/somos/en_US/products/offerings-somos-water-shed.html
- [10] <http://www.shop.kiyatec.com/Multi-syringe-Pump-Infuse-Withdraw-FC230.htm>
- [11] G. Conoscenti, G. D'Urso, L. Iannetti, V. La Carrubba, V. Brucato, R.S. Tuan, P. Zunino, R. Gottardi. *Lab on a Chip*. Submitted.
- [12] Hsu Y., Moya M., Hughes C., George S., Lee A. (2013) *Lab on a Chip*. 10.1039/c3lc50424g

Microphysiological Model to Study Transport Across the Osteochondral Junction

Kalon J. Overholt^{a,b}, Riccardo Gottardi^{b,c}, and Rocky S. Tuan^{a,b}

^a*Department of Bioengineering, Swanson School of Engineering,
University of Pittsburgh, Pittsburgh, PA, USA*

^b*Center for Cellular and Molecular Engineering, Department of Orthopaedic Surgery,
University of Pittsburgh, Pittsburgh, PA, USA*

^c*Fondazione Ri.MED, Palermo, Italy*

Abstract

Microphysiological systems are devices that contain small systems of living tissue that replicate a specific component of the human body. These systems enable *in vitro* modeling of normal tissue function and are mostly aimed at high-throughput screening. The current study aimed to evaluate the efficacy of a previously designed microphysiological bioreactor containing osseous (bone) and chondral (cartilage) tissue together as an osteochondral (OC) complex. This bioreactor was designed to study biochemical communication between bone and cartilage across their interface, a phenomenon that is only beginning to be understood and plays a key role in the pathogenesis of osteoarthritis (OA) [1]. The main objectives of this investigation were to evaluate the system's capacity to host native tissue and to verify that the system can be used to study biochemical transport. To test the first objective, OC explants were cultured in the 4-chambered bioreactor using separately circulated media streams specific to bone and cartilage. Live/dead viability assays demonstrated 14 days of viability, indicating that the bioreactor is suitable for culture of native tissues. To study transport at the OC junction, fluorescein, a small fluorescent molecule, was introduced into the chondrogenic flow stream and its diffusion through the interface was quantified by measuring fluorescence in the osteogenic stream. There was measurable fluorescent perfusion (diffusivity = $0.0188 \pm 0.00752 \mu\text{m}^2/\text{s}$), confirming that the OC interface is a permeable barrier that may allow transport of inflammatory cytokines relevant in the progression of OA.

Keywords: osteochondral engineering, diffusion, osteoarthritis, microphysiological system

1. Introduction

Osteoarthritis is a debilitating joint disease characterized by the degradation of articular cartilage and subchondral bone [1]. Millions of people worldwide are affected by the disease and suffer from symptoms including joint pain, stiffness, and decreased mobility. While palliative treatments can relieve these symptoms, no curative treatment for OA currently exists and most patients eventually require total joint replacement surgery. A better definition of the mechanism of OA pathogenesis is essential for the identification of therapeutic targets and the subsequent screening of disease-modifying drugs. A locus of the disease has been identified at the OC junction, indicating that biochemical communication between bone and cartilage tissues may play a crucial role in the overall mechanism of OA [1]. Although the OC interface was previously believed to be impermeable to transport of solutes and gases [2,3,4], evidence is mounting that the OC junction does in fact allow transport [5,6]. OC permeability is an important parameter to investigate because it may facilitate bone-cartilage crosstalk, especially as the interface breaks down due to OA. A sufficient understanding of the interactions between these tissues requires that they be studied as a single unit, introducing the need for an *in vitro* osteochondral model.

Despite their proximity, bone and cartilage occupy extremely different environments *in vivo*. Cartilage is avascular, aneural, and alymphatic; chondrocytes (cartilage cells) thrive in a hypoxic environment low in glucose, whereas osteoblasts (bone cells) are best suited to a normoxic, glucose-rich medium [7]. Hence, the ideal conditions for cartilage are undesirable and potentially toxic for bone, and vice-versa. Therefore, *in vitro* models have primarily focused on either bone or cartilage studied in isolation. The present study used a previously developed bioreactor which ensures two adjacent but

separate microphysiological environments, allowing the culture of bone and cartilage together as an OC complex [8,9,10,11]. The primary objective was to show that the system can be used to study small molecule transport across the OC junction. It was hypothesized that diffusion would be detected and that a calculated diffusivity value would align with values found in recent studies [5,12]. Furthermore, it was relevant to show that the system is suitable for long-term culture of native tissue. A tissue viability period at least seven days was chosen as a success criterion, since experiments simulating the effects of OA can be completed within this time [8].

2. Methods

2.1 Tissue Samples

Native osteochondral tissue was explanted from both juvenile and adult donors. Human tissue was sourced from the waste materials of patients undergoing total joint replacement surgery (with IRB approval, University of Washington/University of Pittsburgh). Adult human donors ($n=8$) were females between 60 and 80 years of age. Due to the lack of juvenile human donors, porcine tissue cores ($n=4$) were obtained from juvenile farmed pigs. All tissue cores were extracted from macroscopically asymptomatic regions of the femoral condyle and trochlea using a biopsy punch (3.5 mm).

2.2 *In Vitro* Culture of Native Osteochondral Tissue

The dual-chambered bioreactor (Figure 1) allows the separate perfusion of two media streams through an osteochondral core. The setup consists of a row of wells, each with a central insert containing a tissue sample and input and output flow canals. Native OC explants were fitted tightly into the inserts, which were then loaded into the 4-well microfluidic row as shown. Chondrogenic medium (CM) was supplied through the upper conduit, while osteogenic medium (OM) was supplied through the bottom conduit. The following formulations were used: for OM, Dulbecco's Modified Eagle's Medium (DMEM), 10% fetal bovine serum (FBS), 5% penicillin/streptomycin/fungizone (PSF), supplemented with 10 nM dexamethasone, 0.1 mM L-ascorbic acid 2-phosphate (AsA2-P), and 10 mM beta-glycerophosphate (β -GP); for CM, DMEM, 5% PSF, supplemented with 10 ng/mL TGF- β 3, 1% ITS+, 50 μ M AsA2-P, 55 μ M sodium pyruvate, and 23 μ M L-proline. Media was stored in 20 mL syringes and allowed to perfuse through the tissue at a rate of 0.083 mL/h. Effluent media from each stream was collected in collection bags. Syringes and media were replaced every 5 days. The entire apparatus was stored in a tissue culture incubator at 37°C. At 3, 5, 7, 14, and 28 day time points, OC cores were collected to assess viability using live/dead assays with calcein AM and EthD-1.

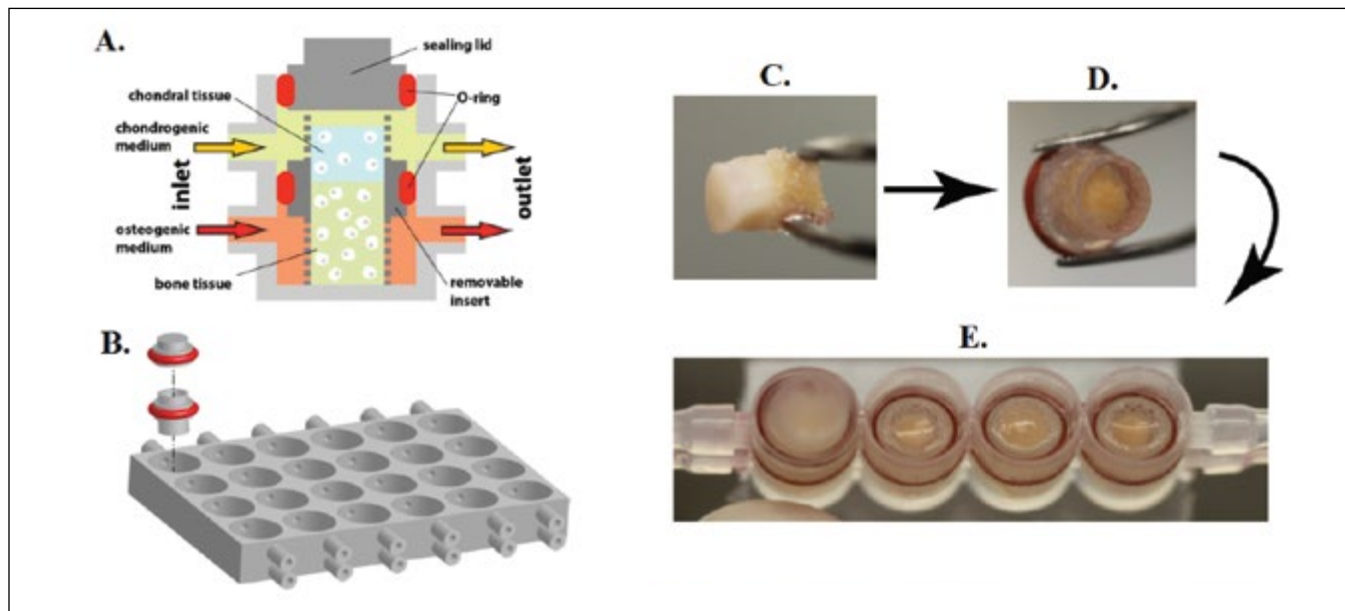


Figure 1. Schematic of the bioreactor for *in vitro* osteochondral study. (A) An individual bioreactor composed of the removable insert (dark gray) within a chamber (light gray) and sealed in place with 4 mm O-rings. The OC tissue sample within the insert separates the upper and lower media streams. Small pores in the wall of the insert assist in perfusion of media through the tissue. (B) A single bioreactor formed by the insert and lid in the context of a 24-well plate. (C,D,E) Loading procedure. An OC core is loaded into the insert, which is then placed into the 4-well row.

2.3 Fluorescein Transport Test

Fluorescein sodium salt, a small fluorescent molecule (376 Da), is a useful marker to study the communication of bone and cartilage at their interface because it can indicate the presence of transport pathways including microfissures, invasive vascular channels, and structural defects [5]. In order to quantitatively measure molecular perfusion through native tissue in the bioreactor environment, fluorescein (Sigma Aldrich) was introduced to the bottom (bone) stream (concentration = 0.6 mg/mL in FluoroBrite DMEM, flow rate = 0.125 mL/h). Again, human (n=3) and porcine (n=4) tissue cores were used. Fluorescein diffusion into the upper (cartilage) stream was measured by collecting the effluent media at 12-hour intervals and measuring fluorescence intensity with a microplate reader (200 μ L/well, Synergy HT, BioTek, Winooski, VT). A standard curve was then prepared using a series of fluorescein dilutions of known concentrations and used to map spectrophotometer intensity units to concentration values. Using the parameters of the system and the integrated concentration at 12-hour intervals, the approximate diffusivity of the bone-cartilage complex was calculated according to Fick's first law of diffusion (Equation 1) [13].

$$J = -D \frac{\partial(C)}{\partial x} \quad \text{Eq. 1}$$

Here, C denotes fluorescein concentration (mg/mL), D denotes diffusivity ($\mu\text{m}^2/\text{s}$) of fluorescein through the OC junction, J denotes flux (mg/A*s), and x denotes distance (mm) from the midpoint of the cartilage segment to the midpoint of the bone segment. For this system, the parameters were $x=5.5$ mm and $C=0.6$ mg/mL. In the calculation of diffusivity, diffusion of fluorescein was assumed to occur in the vertical direction with no lateral diffusion through pores in the insert. A single diffusivity value D was assumed to apply to the osteochondral complex. Although bone and calcified cartilage each have individual diffusivities ($D_{\text{bone}}= 0.024 \mu\text{m}^2/\text{s}$, $D_{\text{cartilage}}= 0.007 \mu\text{m}^2/\text{s}$) [5], we preliminarily assumed a value governing diffusion through the OC composite as an overall resultant diffusivity. To verify that fluorescein presence in the top stream was due only to diffusion through the tissue, inserts were filled with paraffin and fluorescein was induced at the same flow rate. Fluorescence spectroscopy was used to test for leaking, and none was found.

3. Results

3.1 Viability of Native OC Tissue

Live/Dead staining demonstrated that human tissues remain viable in the bioreactor environment throughout at least a 14-day window. In Figure 2, representative images centered on the OC interface show preserved viability from day 5 to day 14 in human samples. Between the 14- and 28-day time points, significant dieback occurred in both the cartilage and bone segments in preliminary tests. No difference was observed between the viability periods of human and porcine tissue. The analysis is purely qualitative; no attempt was made to quantify live/dead results.

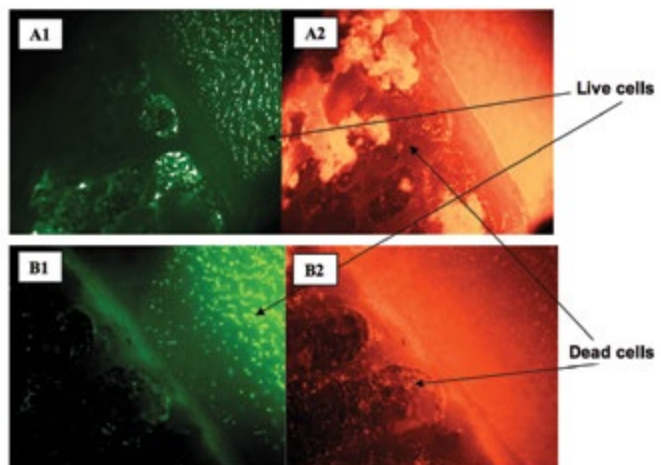


Figure 2. Results of live/dead cell viability assays on day 5 (A1, A2) and day 14 (B1, B2) of tissue culture in the bioreactor. A cross section of the tissue sample is shown in each image, with cartilage in the top right segment and bone in the bottom left. Green fluorescence indicates live cells and red fluorescence indicates dead cells.

3.2 Fluorescein Perfusion Across the OC Junction

The bioreactor allowed the diffusion of fluorescein through the osteochondral tissue. The concentration profiles as measured in the top (cartilage) stream for human and porcine tissue are indicated in Figure 3 (see page 76). As shown, the concentration diffused through juvenile pig tissue began at zero after 5 minutes (0 hours) and steadily increased within a 3-day time period. In human tissue, no 5-minute time point was taken. At 12 hours, the concentration diffused through the human samples was approximately 50 times greater than that of juvenile porcine samples. Only the values from porcine tissue were used to find diffusivity, since the graph is a typical diffusion model, whereas the graph of transport in human tissue does not have enough points for modeling. Using Eq. 1, the diffusivity value for the osteochondral interface was calculated to be $0.0188 \pm 0.00752 \mu\text{m}^2/\text{s}$.

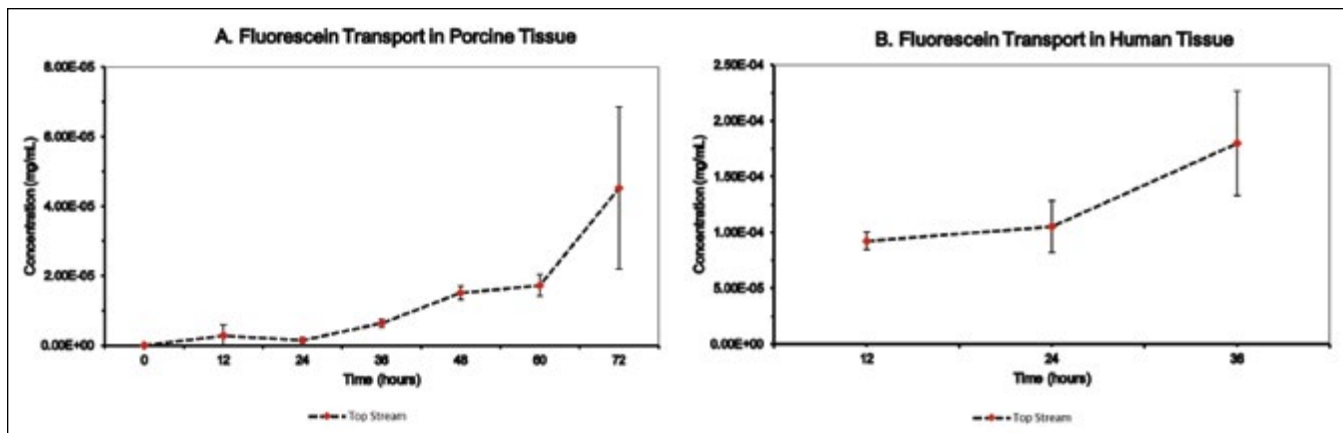


Figure 3. Comparison of fluorescein concentration profiles during transport through native porcine (A) and human (B) OC tissue in the bioreactor environment. Note that the two graphs use different axes. The error bars indicate one standard deviation.

4. Discussion

The quantified fluorescein diffusion has shown that the osteochondral interface is permeable to transport of small molecules. To establish a valid comparison between diffusion in juvenile porcine and adult human tissue, further experimentation is needed. It was necessary to use a cross-species comparison in these tests since juvenile human and adult porcine tissues are difficult to obtain. If possible, these tissues should be acquired for later studies. To account for the 50-fold difference in initial concentration found between juvenile and adult tissues, early time points should be acquired more frequently than every 12 hours. It is possible, however, that the higher concentration diffused through adult human samples is a result of increased permeability due to osteoarthritic degradation. The fluorescein diffusivity of the porcine OC measured using the bioreactor agrees with values calculated in recent studies using fluorescence loss induced by photobleaching (FLIP) for healthy calcified cartilage and subchondral bone ($D_{bone} = 0.024 \mu\text{m}^2/\text{s}$, $D_{cartilage} = 0.007 \mu\text{m}^2/\text{s}$) [5,13]. Given these values, diffusion is expected to be rate-limited by cartilage. The overall osteochondral diffusivity value ($0.0188 \pm 0.00752 \mu\text{m}^2/\text{s}$) lies between the diffusivities of cartilage and bone and therefore agrees with expectations. These tests confirm the hypothesis that the bioreactor is an accurate tool to study molecular transport at meso- to macroscopic scales and can usefully complement other approaches such as FLIP.

The data presented in section 3.1 suggest that the bioreactor system can maintain tissue viability for at least 14 days, a sufficient period to model some degenerative effects of osteoarthritis *in vitro* [8]. During this time interval, the bioreactor will be suitable to host both native and engineered tissue complexes. However, it is possible that longer viability can be achieved, especially since the observed tissue dieback may have been a result of the high-impact load delivered when extracting the OC tissue cores. Further studies to examine these effects are underway.

5. Conclusions

This investigation of fluorescein transport has shown that the osteochondral interface is a permeable barrier, one that as suggested in the literature may allow transport of cytokines that cause OA inflammation and degradation [1]. While the specific permeability of the interface to cytokines is still unknown, it has been shown that the bioreactor can be used to study transport of OA cytokines in the future. The results validate use of the bioreactor for long-term culture, meaning that in later studies the system can be used to simulate the effects of OA in engineered OC constructs over a two-week span. This project shows great promise for creating a realistic microphysiological model for osteoarthritis progression, a necessary first step in developing new OA treatments.

6. Acknowledgments

This work was generously supported by the Swanson School of Engineering at the University of Pittsburgh, the Ri.MED Foundation, and CASIS GA-2016-236.

7. References

- [1] Goldring, S. R., & Goldring, M. B. (2016). Changes in the osteochondral unit during osteoarthritis: structure, function and cartilage–bone crosstalk. *Nature Reviews Rheumatology*, 12(11), 632–644.
- [2] Ogata, K., & Whiteside, L. A. (1979). Barrier to material transfer at the bone-cartilage interface: measurement with hydrogen gas in vivo. *Clinical Orthopaedics and Related Research*, 273–276.
- [3] Maroudas, A., Bullough, P., Swanson, S. A., & Freeman, M. A. (1968). The permeability of articular cartilage. *J Bone Joint Surg Br*, 50.
- [4] Brower TD, Akahoshi Y, Orlic P. (1962). The Diffusion of Dyes Through Articular Cartilage in Vivo. *The Journal of Bone and Joint Surgery. American Volume*, 44:456–463.
- [5] Pan, J., Zhou, X., Li, W., Novotny, J. E., Doty, S. B., & Wang, L. (2009). In situ measurement of transport between subchondral bone and articular cartilage. *J Orthop Res*, 27.
- [6] Arkill, K. P., & Winlove, C. P. (2008). Solute transport in the deep and calcified zones of articular cartilage. *Osteoarthritis Cartilage*, 16.
- [7] Honner, R., & Thompson, R. C. (1971). The nutritional pathways of articular cartilage. *The Journal of Bone and Joint Surgery. American Volume*, 53(4), 742–8.
- [8] Lin, H., Lozito, T. P., Alexander, P. G., Gottardi, R., & Tuan, R. S. (2014). Stem Cell-Based Microphysiological Osteochondral System to Model Tissue Response to Interleukin-1 β . *Mol. Pharmaceutics*, 11 (7), pp 2203–2212.
- [9] Gottardi, R., Lin, H., D’urso, G., Iannetti, L., Zunino, P., Lozito, T. P., Tuan, R. S. (2016). Validation of an Osteochondral Microphysiological System Applied to Study the Protective Role of Sex Hormones. *Orthopaedic Research Society Annual Meeting*, 5.
- [10] Alexander, P. G., Gottardi, R., Lin, H., Lozito, T. P., & Tuan, R. S. (2014). Three-dimensional osteogenic and chondrogenic systems to model osteochondral physiology and degenerative joint diseases. *Experimental Biology and Medicine (Maywood, N.J.)*, 1080–1095.
- [11] Lozito, T. P., Alexander, P. G., Lin, H., Gottardi, R., Cheng, A., & Tuan, R. S. (2013). Three-dimensional osteochondral microtissue to model pathogenesis of osteoarthritis. *Stem Cell Research & Therapy*, 4(Suppl 1), S6.
- [12] Lee, J. I., Sato, M., Ushida, K., & Mochida, J. (2011). Measurement of diffusion in articular cartilage using fluorescence correlation spectroscopy. *BMC Biotechnology*, 11(1), 19.
- [13] Fick, A. (1855). On liquid diffusion. *Journal of Membrane Science*, 100, 33–38.

Assessment of Schwann Cell Migration After Peripheral Nerve Injury and Treatment with Tissue-Specific Extracellular Matrix Hydrogel

Mara C. Palmer¹, Travis A. Prest^{1,2}, and Bryan N. Brown^{1,2,3}

¹Department of Bioengineering, Swanson School of Engineering, University of Pittsburgh, Pittsburgh, PA, USA

²McGowan Institute for Regenerative Medicine, University of Pittsburgh, Pittsburgh, PA, USA

³Department of Obstetrics, Gynecology, and Reproductive Sciences, University of Pittsburgh, Pittsburgh, PA, USA

Abstract

Peripheral nerve injuries resulting in a gap are particularly difficult to repair, and even the gold standard, a healthy nerve autograft, only produces moderate return to function. As an alternative to an autologous nerve graft, the present study analyzes decellularized porcine peripheral nerve-specific extracellular matrix (PNS-ECM) hydrogel as a nerve conduit (NC) luminal filler to treat peripheral nerve gap defects in a rodent model. The study proposes that with hydrogel degradation, the distribution of PNS growth factors will result in amplified Schwann cell (SC) migration, as measured by positive identification of SC nuclei, contributing to axonal outgrowth, resulting in a more effective nerve gap defect treatment. A modified Boyden chamber assay quantitatively compared *in vitro* SC migration using varying concentrations of decellularized, porcine-derived PNS-ECM (n=6), non-nerve specific small intestine submucosa (SIS) ECM (n=4), and non-nerve specific urinary bladder matrix (UBM) ECM hydrogels (n=5). SIS-ECM and UBM-ECM testing was used as a comparative standard, as SIS-ECM and UBM-ECM are commonly studied ECM matrices for tissue regeneration and wound healing. *In vivo* migration was evaluated in a rodent model using a 15mm sciatic nerve gap defect repaired with a NC and filler (PNS-ECM or saline). Nerve explant cross-sections were taken at controlled intervals following repair and SC migration was measured along the gap length. CellProfiler analysis identified and counted positively stained SC nuclei in both experiments. Compared to other experimental conditions, *in vitro* and preliminary *in vivo* analysis show amplified SC migration with PNS-ECM hydrogel use. A significant increase in *in vitro* SC migration was observed with the use of 1000 μ g/mL and 500 μ g/mL PNS-ECM hydrogel ($p<0.05$). Improved SC migration demonstrates the capability of PNS-ECM hydrogel to produce more favorable regenerative outcomes when paired with a NC as treatment for peripheral nerve gap defects.

Keywords: peripheral nerve, extracellular matrix, nerve transection repair, Schwann cells

1. Introduction

A multitude of traumatic occurrences, including car collisions, crush injuries, and lacerations, cause peripheral nerve damage, resulting in over 900,000 peripheral nerve reconstruction surgeries of the upper extremities per year in the United States [1, 2]. The more severe cases of injury involve partially or fully transected peripheral nerves, which leave many patients with permanent motor deficits, significantly impacting quality of life [3]. Sensory nerve autografts are the current gold standard treatment for severe peripheral nerve transections, yet autograft retrieval contributes to donor site morbidity and potential sensory loss at the donor site location. Moreover, the autograft only provides moderate recovery at the gap site.

Peripheral nerves have the inherent ability to recover after injury. However, nerve regeneration is often slow and recovery incomplete, especially in large gap injuries [4]. This is due in part to limitations associated with the local injury microenvironment during the repair process. Manipulating factors of this local microenvironment including recruitment of supporting cell populations (i.e., Schwann cells) and the nature of the early host macrophage response (M1, pro-inflammatory vs. M2, anti-inflammatory) provide an opportunity to improve downstream outcomes.

Existing as an alternative to autograft repair, natural and synthetic hollow nerve conduits (NCs) can be used as in the repair procedure, but are rarely chosen as a treatment method as outcomes seldom match the use of the autograft [5]. Recent advancements pair NCs with lumen fillers to influence this local microenvironment and to increase the efficacy of regeneration; the lumen filler provides growth factors and biochemical cues for cellular growth, function, and differentiation, creating a more natural microenvironment for regeneration [5]. Yet these procedures often do not produce recovery results exceeding those of autograft procedures [5]. The introduction of NCs in conjunction with lumen fillers has shown deficiencies in multiple aspects of use, including

impediment of neuron growth due to luminal filler matrix density in fillers engineered to last the length of recovery, in addition to Schwann cell death within weeks of the introduction of the NCs to the body [5].

Alternatively, newer branches of research are pursuing the use of decellularized biologic scaffolds derived from extracellular matrix (ECM) material. ECM scaffolds have been successfully used in reconstruction in a number of tissues, including the heart, kidney, esophagus, lower urinary tract, and skeletal muscle [6]. As characterized by Zilic et al., porcine peripheral nerve tissue exhibits anatomical and biological similarities to human peripheral nerve tissue, making it a viable and promising option for use in clinical applications [7]. This study investigates the use of an injectable hydrogel derived from porcine peripheral nerve-specific ECM (PNS-ECM).

Through decellularization, xenogeneic nerve tissue is processed to remove cellular and other immunogenic material making human use possible while maintaining important structural and functional components of the extracellular environment. This tissue-specific ECM provides adequate structural support for cellular growth and contains similar functional molecules to those found in autologous nerve grafts. The ability for these functional molecules and biochemical cues to be expressed at the site of regeneration establishes a more hospitable microenvironment, which has been shown to enhance nerve regeneration [3]. Critical elements for growth such as laminin, fibronectin, and collagen are contained within peripheral nerve ECM, and when combined, these components have been found to enhance Schwann cell response to the largest degree [8]. Furthermore, laminin has been shown to influence the degree of neurite growth. When present in the co-culture of Schwann and NG108-15 cells, laminin activates transcription factors, which bolster the growth of longer neurites by neuronal cells [8]. Previous studies have also shown the use of ECM scaffolds triggers a promotion of anti-inflammatory M2 macrophages, which perform a neuroprotective role, and this could potentially be a crucial immune-therapeutic strategy during neurodegeneration and recovery [9].

The present study analyzes the use of decellularized porcine-derived PNS-ECM hydrogel as a NC luminal filler to treat peripheral nerve gap defects in a rodent model. As the PNS-ECM hydrogel degrades, biochemical components of the filler will be released into the local microenvironment. It is proposed this distribution will amplify Schwann cell (SC) migration as compared to other ECM hydrogels and control conditions, contributing to axonal outgrowth and positive functional outcomes,

resulting in a more effective treatment for critical gap nerve defects.

2. Methods

In vitro and *in vivo* analyses of SC migration in response to the use of experimental ECM hydrogels (PNS, SIS, UBM) and control conditions served to assess the chemotactic ability of PNS-ECM, as compared to non-nerve specific tissue derived ECM hydrogels. *In vitro* analysis was performed using a modified Boyden chamber assay to assess directional chemotactic migration of SCs [10]. ECM hydrogels were created through the decellularization of each respective nerve- and non-nerve specific tissue. The decellularized material was then used to create an ECM digest solution for each tissue, which was then modified to form a hydrogel used for completion of the assay. In parallel, SCs (RT4-D6P2T cell line) were cultured to confluence and starved in serum-free media for 24 hours prior to use. Starvation served to eliminate added serum growth factors, which may interfere with SC movement, and therefore, the accuracy of the Boyden assay. DAPI staining and imaging techniques were implemented to identify SC nuclei and quantify SC migration. An overview of experimental procedures used to assess and quantify *in vitro* SC migration is shown below (Figure 1).

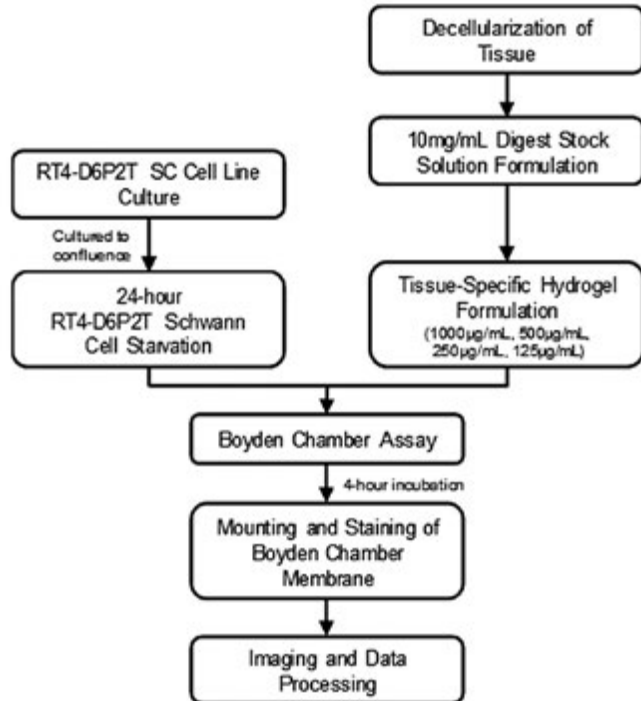


Figure 1. Flowchart overview of methods used to assess *in vitro* SC migration. SC cell culture and hydrogel preparatory stages performed in parallel.

A Lewis rat model was used to assess *in vivo* SC migration. After surgical transection of the sciatic nerve, gap defects were repaired with a NC coupled with PNS-ECM or saline. Nerve explants were sectioned and stained for SC nuclei at controlled time intervals post-surgical repair. Imaging techniques identified and quantified SC migration.

***In vitro* SC Migration**

Modified from Agrawal, et al., a Boyden chamber assay evaluated *in vitro* SC migration [10]. Decellularized porcine-derived PNS-ECM (n=6), non-nerve specific small intestine submucosa ECM (SIS-ECM) (n=4), and non-nerve specific urinary bladder matrix ECM (UBM-ECM) (n=5) hydrogels were utilized as comparative attractant solutions. Batch-made concentrated tissue-specific ECM digest stock solutions were used to produce ECM hydrogel. Prior to each assay, final hydrogel solutions were prepared, and the cells to be used in the assay were cultured.

Decellularization of Porcine Peripheral Nerve Tissue

Porcine nerve decellularization was completed as follows. Porcine sciatic nerves were harvested following euthanasia of healthy adult animals for reasons unrelated to neurological injury or disease. The tissue was then frozen for ≥ 16 hours at -80°C . After frozen, tissue was quartered longitudinally and cut into segments 5mm in length. Decellularization was performed as detailed in Agrawal, et al [10]. In brief, the decellularization process consists of a series of agitated washes: type I water (ultrapure, Milli-Q® purified water; 14 hours at 4°C); 0.02% trypsin (HyClone, Marlborough, MA, USA)/0.05% EDTA (Invitrogen, Waltham, MA, USA) (60 minutes at 37°C); 3.0% Triton X-100 (Sigma-Aldrich, St. Louis, MO, USA; 60 minutes); type I water rinse (repeated until agitation no longer produces bubbles); 1M sucrose (ThermoFisher, Waltham, MA, USA; 15 minutes); 4.0% sodium deoxycholate (Sigma-Aldrich, St. Louis, MO, USA; 60 minutes); 0.1% peracetic acid/4% ethanol (Sigma-Aldrich, St. Louis, MO, USA; 120 minutes); 1X PBS (15 minutes); water (15 minutes); water (15 minutes); 1X PBS (15 minutes). If not otherwise indicated, agitated wash treatments occurred at room temperature. Following treatment, samples were frozen (-80°C) and then lyophilized.

Decellularization of Porcine Small Intestine Submucosa Tissue

The decellularization process for porcine SIS tissue was completed as detailed in Brown, et al. [11]. In brief, the process was completed as follows. The porcine intestine

was removed. Water was used to rinse the jejunum. Mesenteric tissue was removed prior to creating a longitudinal incision along the intestines. The tunica serosa, tunica muscularis externa, and the luminal portion of the tunica mucosa including the majority of the lamina propria were removed from the intestines via mechanical delamination. Remaining tissue was comprised of the tunica submucosa and the basal layer of the tunica mucosa including the muscularis mucosa and the stratum compactum of the lamina propria. Following mechanical delamination, the remaining tissue was subjected to a series of washes including 0.1% (v/v) peracetic acid (Rochester Midland Corporation, Rochester, NY, USA) and multiple rinses with saline and deionized water.

Decellularization of Porcine Urinary Bladder Matrix Tissue

The decellularization process consists of a combination of washes and mechanical removal of layers of bladder tissue previously detailed in Brown, et al. [11]. Urinary bladders were harvested from market weight pigs following sacrifice of the animal. After removal, the urinary bladder was trimmed to remove external connective tissue and adipose tissue, and repeated washes with tap water removed residual urine contents. Soaking in 1N saline was used to remove the urothelial layer. Removal of the tunica serosa, tunica muscularis externa, tunica submucosa, and most of the muscularis mucosa from the bladder tissue was completed manually, using mechanical methods to remove each layer of tissue. UBM tissue, consisting of the basement membrane of the tunica epithelialis mucosa and the subjacent tunica propria, remained. Immersion in 0.1% (v/v) peracetic acid, 4% (v/v) ethanol, and 96% (v/v) deionized water (2 hours) was used to decellularize the remaining UBM tissue. The UBM-ECM material was then washed with phosphate-buffered saline (PBS) (pH 7.4, 15 minutes, repeated twice) and deionized water (15 minutes, repeated twice). UBM-ECM tissue was subsequently frozen (-80°C) and lyophilized.

ECM Digest Stock Solution Preparation

Tissue-specific ECM digest solution was used in hydrogel creation. Stock digest solutions were made by combining the appropriate quantity of milled lyophilized tissue-specific ECM (PNS-ECM, SIS-ECM, or UBM-ECM) in a solution containing 2mg/mL (w/v) pepsin derived from porcine gastric mucosa (≥ 2500 units/mg protein units, Sigma LifeSciences, St. Louis, MO, USA) and 0.1N HCl (Acros Organics, New Jersey, USA) to obtain a 10mg/mL ECM digest stock solution. The digest solution was mixed at 250 RPM for 48 hours. After 48 hours,

pH was tested to confirm acidity, and the solution was aliquoted into 1mL Eppendorf microcentrifuge tubes (Sigma-Aldrich, St. Louis, MO, USA) for freezer storage at -20°C. The process was repeated for each tissue type to create PNS-ECM, SIS-ECM, and UBM-ECM digest stock solutions.

ECM Hydrogel Preparation

Tissue-specific ECM hydrogel was prepared for each individual assay. ECM digest solution (10mg/mL) was modified with 0.1M NaOH (Acros Organics, New Jersey, USA), 10x phosphate-buffered saline (PBS), and Dulbecco's Modified Eagle's Medium (DMEM) with 4.5g/L glucose, L-glutamine, and sodium pyruvate (Mediatech, Inc., Manassas, VA, USA) to produce 1mL of tissue-specific ECM hydrogel at 1mg/mL.

Half-wise step dilution with DMEM in Eppendorf microcentrifuge tubes generated working assay hydrogel concentrations of 1000 μ g/mL, 500 μ g/mL, 250 μ g/mL, 250 μ g/mL.

The procedure was followed for each tissue-specific ECM digest (PNS-ECM, SIS-ECM, UBM-ECM).

Schwann Cell Culture

RT4-D6P2T Schwann cell line was cultured to confluence in T-25 flasks (Sigma-Aldrich, St. Louis, MO, USA) in DMEM with 10% fetal bovine serum and 1% Penicillin/Streptomycin per the protocol specified by Agrawal, et al. [10]. Cells were then passaged to a secondary T-25 flask and starved in serum-free DMEM for 24 hours. Prior to use, serum-starved cells were counted, and the appropriate volume for the Boyden chamber assay (see below) was calculated (target 30,000 cells/well).

The cell culture and starvation process was repeated for each Boyden chamber assay performed.

Boyden Chamber Assay [10]

The hydrogel concentrations noted above (1000, 500, 250, and 125 μ g/mL) were tested for each tissue-specific ECM assay; a lower well volume of 25 μ L was used (Figure 2). The assays evaluated three controls: a positive, negative, and chemokinetic condition. DMEM with 10% fetal bovine serum (Mediatech, Inc., Manassas, VA, USA) and 1% Penicillin/Streptomycin (Mediatech, Inc., Manassas, VA, USA) served as the positive control; serum-free DMEM as the negative control; and 15 μ L of 1000 μ g/mL tissue-specific hydrogel on the cell side of the chamber (upper well) as the chemokinetic condition (Figure 2). A chemokinetic condition was tested to

monitor non-directional chemotaxis of SC facilitated by the biochemical molecules within the hydrogel.

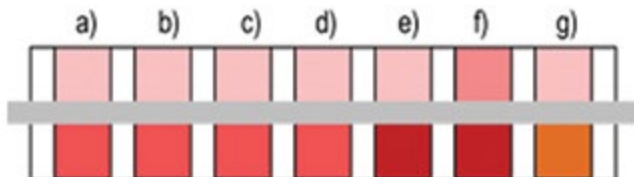


Figure 2. Schematic of modified Boyden chamber assay detailing experimental conditions. Conditions tested with PNS-, SIS-, and UBM-ECM hydrogels:
Lower well (25 μ L): a) ECM hydrogel, 1000 μ g/mL; b) ECM hydrogel, 500 μ g/mL; c) ECM hydrogel, 250 μ g/mL; d) ECM hydrogel, 125 μ g/mL; e) DMEM; f) DMEM; g) DMEM, 1% penicillin streptomycin, 10% FBS.
Upper well (target: 30,000 cells): a-e, g) Schwann cells (DMEM); f) Schwann cells (DMEM) and 15 μ L ECM hydrogel, 1000 μ g/mL.

Assays underwent incubation for four hours at 37°C in a ThermoForma Series II Water Jacketed CO₂ Incubator (ThermoFisher Scientific, Waltham, MA, USA). Membranes were mounted using VectaShield mounting medium with DAPI (Vector Laboratories, Burlingame, CA, USA) between two slides for fixation and imaging purposes, and DAPI staining of the microporous membrane identified SC nuclei. Images of the DAPI stained membrane were taken (510 nm, 4X) using Nuance multispectral imaging system (ThermoFisher Scientific, Caliper Life Sciences). For calculation purposes, images were grouped by chemotactic or chemical condition. Nuclei were counted using CellProfiler (Broad Institute).

In vivo SC Migration

A 15mm gap defect of the sciatic nerve in adult Lewis rats (n=2) was used to assess *in vivo* SC migration. Rodents underwent surgical procedures to create a gap defect of the sciatic nerve and subsequent surgical repair using a NC and lumen filler (PNS-ECM hydrogel, 10mg/mL, or saline solution). Rodents were monitored, and cross-sections of the rodent nerve explant were taken at controlled time intervals after surgery (7 days, 28 days). Cross-sections were stained with S100 antibody (ab868, donkey anti-s100, Abcam, Cambridge, MA, USA) and a corresponding secondary antibody (Alexa Fluor donkey anti-rabbit 488, Abcam, Cambridge, MA, USA). *In vivo* migration was measured along the length of the gap (1, 5, 10, 15mm), with respect to the proximal stump. Immunofluorescent stains were imaged using a Nuance multispectral imaging system (4X).

3. Data Processing

CellProfiler analysis was used to evaluate both *in vitro* and *in vivo* SC migration images. Nuclei detection specifications were optimized for each image set to omit extraneous object detection. CellProfiler analysis identified and counted nuclei (Figure 3).

Average cell counts within each chemical condition were calculated for each assay performed and used for statistical analysis. GraphPad Prism (GraphPad Software, Inc.) was used to perform a two-way ANOVA ($\alpha=0.05$) with multiple comparisons for *in vitro* SC migration data. Statistical analysis was not performed for *in vivo* findings due to the small sample size of the study.

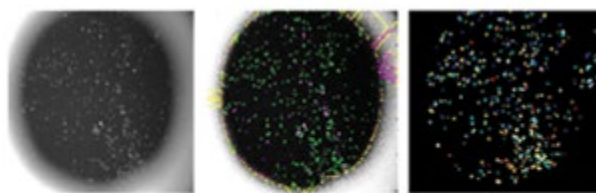


Figure 3. Image of Boyden chamber microporous membrane from UBM-ECM assay, 1000 μ g/mL (left). White dots represent SC nuclei. Initial CellProfiler identification of SC nuclei (middle), where green nuclei colored green fit optimization parameters. Final CellProfiler evaluation depicting positively identified nuclei (right).

4. Results

Analysis of *in vitro* migration revealed increased SC movement with the use of higher concentrations (1000, 500 μ g/mL) of PNS-ECM hydrogel. Figure 4 depicts the average number of SCs identified through CellProfiler analysis for each condition across all nerve-specific and non-nerve specific *in vitro* hydrogel assays. For all directional ECM chemotactic conditions, except the hydrogel concentration of 125 μ g/mL, SC migration was amplified by the use of PNS-ECM hydrogel, with significant differences ($p<0.05$) between groups at 1000 μ g/mL and 500 μ g/mL. Quantitatively, PNS-ECM attracted 153% and 76% more SC, as compared to SIS-ECM and UBM-ECM at 1000 μ g/mL, respectively. Similarly, SC migration increased by 151% with the use of 500 μ g/mL PNS-ECM when compared with the use of SIS-ECM at the same concentration. A positive control was not tested with the use of SIS-ECM hydrogel.

In vivo SC migration was measured across the length of the nerve explant, with respect to the proximal stump,

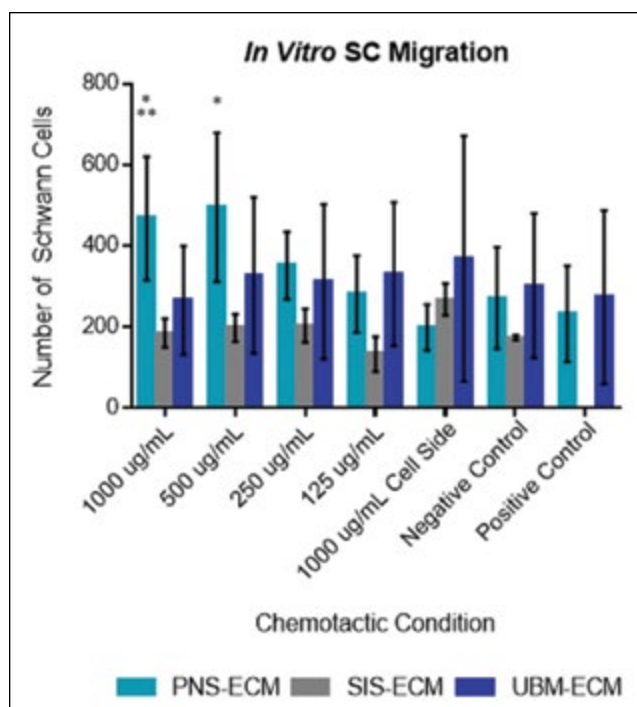


Figure 4. Experimental and control *in vitro* SC migration cell counts. Results referring to PNS-ECM use are in light blue, SIS-ECM in grey, and UBM-ECM in dark blue. Error bars depict standard deviation within the group. PNS-ECM increased SC migration to a significant degree as compared to 1000 μ g/mL SIS(*), UBM-ECM(**), and 500 μ g/mL SIS-ECM(*), at each respective concentration.

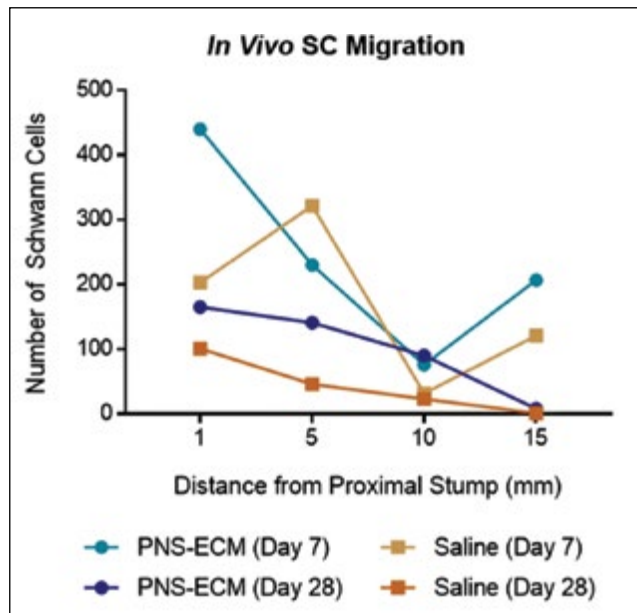


Figure 5. *In vivo* nerve explant SC migration count from post-operative day 7 and day 28. *In vivo* migration measured along the length of the gap with respect to the proximal stump. Statistical analysis was not performed on this data set due to the small sample size.

at 7 days and 28 days post-surgical repair for both the PNS-ECM hydrogel and saline luminal filler conditions (Figure 5). Preliminary analysis of *in vivo* SC migration showed a larger presence of SC with the use of PNS-ECM hydrogel at all time points and distances except at 5mm, 7 days post-operation.

5. Discussion

Data obtained from both *in vitro* and initial *in vivo* analyses supports the proposed hypothesis of an increase in SC migration when using PNS-ECM hydrogel as a treatment for peripheral nerve repair. Evaluating SC migration *in vitro* through the use of a Boyden chamber assay allowed for the assessment of the chemotactic capability of the PNS-ECM hydrogel at various concentrations. With the use of higher concentrations of PNS-ECM, a significant increase in SC migration was observed as compared to SIS-ECM at 1000 μ g/mL and 500 μ g/mL and UBM-ECM at 500 μ g/mL. Though the mechanism for response is not fully understood, it has been shown the breakdown products of ECM hydrogels act as chemoattractants for numerous cell types, including the directional migration of SC to the site of ECM deposition [10]. The results of this study corroborate the findings of prior research, and furthermore, indicate the nerve-specific biomolecules contained within and released from the PNS-ECM hydrogel create a nerve-specific local microenvironment, which promotes SC migration to the gap site in greater quantities than SIS-ECM and UBM-ECM.

Though non-nerve specific UBM-ECM hydrogel exhibited comparable SC migration to PNS-ECM at lower concentrations, the degree to which the UBM-ECM hydrogel solution gels over the incubation period is not known, and increased gelation may contribute to uneven concentrations within the bottom well of the Boyden chamber. Furthermore, when evaluating the addition of 1000 μ g/mL hydrogel on the cell side of the chamber, SCs demonstrated chemokinesis in response to the 1000 μ g/mL UBM-ECM hydrogel, whereas SC exposed to the PNS-ECM hydrogel did not. The PNS-ECM hydrogel exhibited a directed attraction for SCs across the microporous membrane, indicating a PNS-ECM hydrogel is a more advantageous NC lumen filler for clinical use.

Preliminary *in vivo* testing in a rodent model supports the theory that the use of PNS-ECM as a NC luminal filler will demonstrate chemotactic abilities *in vivo* and

promote the recruitment of SC to the gap site. As prior testing by Pabari, et al. exhibited SC death within weeks of repair with the use of NCs coupled with non-nerve specific luminal fillers, the results of initial *in vivo* animal model testing show promise for early migration of SC to the gap site [5]. This *in vivo* migration supports a hospitable local microenvironment for nerve regeneration and shows the biomolecular components and growth factors within the PNS-ECM hydrogel aid in the movement of SC to the gap site *in vivo* as well.

As this testing focused on the recruitment of supporting cell populations, it reasonable to deduce the microenvironment created as a result of the migration of SC to the gap site and the biochemical molecules released within the PNS-ECM hydrogel will facilitate favorable nerve regeneration and improve post-operative functional outcomes. This premise serves as the basis for continuing animal model testing to evaluate post-surgical functional outcomes through over-ground gait analysis following nerve gap repair with PNS-ECM. Functional analysis will evaluate potential for the use of PNS-ECM as a treatment for peripheral nerve gap defects in the clinical setting.

6. Conclusion

Results of the research thus far show potential for the development of an alternative treatment for peripheral nerve gap defects that spare the patient from the undesired secondary outcomes associated with autograft retrieval. Coupling a NC with the PNS-ECM hydrogel offers structural support to stabilize the gap defect and luminal filler and provides the biological chemoattractant compounds and proteins to enhance the local environment supporting nerve regeneration.

Schwann cells are crucial for the regeneration of nerve tissue in peripheral nerve gap defects. Moreover, amplified SC migration with the use of PNS-ECM hydrogel demonstrates the PNS-ECM hydrogel and nerve-specific functional molecules are capable of producing advantageous regenerative outcomes when paired with a NC in the surgical repair of a peripheral nerve gap defect. This course of treatment, if deemed equivalent to the current gold standard, can provide clinicians with an encouraging alternative treatment for peripheral nerve gap repair and possibly provide patients with equal, if not improved, functional outcomes and eliminate graft site morbidity due to omission of sensory nerve autograft retrieval.

References

- [1] Brattain, K. Analysis of the peripheral nerve repair market in the United States. Minneapolis, Minnesota: Magellan Medical Technology Consultants, Inc., 2013.
- [2] Menorca RMG, Fussell TS, Elfar JC. Peripheral Nerve Trauma: Mechanisms of Injury and Recovery. *Hand clinics*. 2013;29(3):317-330. doi:10.1016/j.hcl.2013.04.002.
- [3] Brown BN, Badylak SF. Extracellular matrix as an inductive scaffold for functional tissue reconstruction. *Transl Res* 163, 268, 2014.
- [4] Xu Jiang, Shawn H. Lim, Hai-Quan Mao, Sing Yian Chew, Current applications and future perspectives of artificial nerve conduits, *Experimental Neurology*, Volume 223, Issue 1, May 2010, Pages 86-101, ISSN 0014-4886, <http://dx.doi.org/10.1016/j.expneurol.2009.09.009>.
- [5] Pabari, A., Yang, SY., Mosahebi, A., Seifalian, AM. Recent advances in artificial nerve conduit design: strategies for the delivery of luminal fillers. *Journal of controlled release: official journal of the Controlled Release Society*. 2011;156(1):2-10. Epub 2011/07/19. doi: 10.1016/j.jconrel.2011.07.001. PubMed PMID: 2176337.
- [6] Crapo PM, Medberry CJ, Reing JE, Tottey S, van der Merwe Y, Jones KE, Badylak SF. Biologic scaffolds composed of central nervous system extracellular matrix. *Biomaterials*. 2012;33(13):3539-47. Epub 2012/02/22. doi: 10.1016/j.biomaterials.2012.01.044. PubMed PMID: 22341938; PubMed Central PMCID: PMCPmc3516286.
- [7] Zilic L, Garner PE, Yu T, Roman S, Haycock JW, Wilshaw SP. An anatomical study of porcine peripheral nerve and its potential use in nerve tissue engineering. *J Anat*. 2015;227(3):302-314. doi:10.1111/joa.12341.
- [8] Armstrong SJ, Wiberg M, Terenghi G, Kingham PJ. ECM molecules mediate both Schwann cell proliferation and activation to enhance neurite outgrowth. *Tissue Eng*. 2007;13(12):2863-70. Epub 2007/08/31. doi: 10.1089/ten.2007.0055. PubMed PMID: 17727337.
- [9] Brown BN, Valentin JE, Stewart-Akers AM, McCabe GP, Badylak SF. Macrophage phenotype and remodeling outcomes in response to biologic scaffolds with and without a cellular component. *Biomaterials*. 2009;30(8):1482-91. Epub 2009/01/06. doi: 10.1016/j.biomaterials.2008.11.040. PubMed PMID: 19121538; PubMed Central PMCID: PMCPmc2805023.
- [10] Agrawal V, Brown BN, Beattie AJ, Gilbert TW, Badylak SF. Evidence of innervation following extracellular matrix scaffold-mediated remodelling of muscular tissues. *Journal of tissue engineering and regenerative medicine*. 2009;3(8):590-600. Epub 2009/08/25. doi: 10.1002/term.200. PubMed PMID: 19701935; PubMed Central PMCID: PMCPmc2787980.
- [11] Brown B., Lindberg K., Reing J., et al. The basement membrane component of biologic scaffolds derived from extracellular matrix. *Tissue Eng* 2006; 12:519.

Acknowledgments

This research was jointly funded by the University of Pittsburgh's Swanson School of Engineering, the Office of the Provost, and the Brown Lab at the McGowan Institute for Regenerative Medicine. Additionally, I would like to thank Dr. Bryan Brown and Travis Prest for their continued support.

Analysing the Porosity of Low-Cost Ceramic Water Filters through X-Ray Microtomography

Rafael Rodriguez^a, Qinghao Zang^a, and Ian Nettleship^a

^a*Department of Mechanical Engineering and Materials Science,
Swanson School of Engineering, University of Pittsburgh, Pittsburgh, PA, USA*

Abstract

The lack of access to safe drinking water causes millions of deaths every year worldwide. Many technologies have been developed to address this problem and among these, low-cost ceramic water filters (CWFs) have proved to be one of the best. Even though investigation of CWFs began more than 20 years ago, there are still many questions regarding the effect of the internal microstructure on filter efficacy.

In this study, 3-D imaging of the internal structure of low-cost ceramic filters was accomplished for the first time by X-ray microtomography. Filter samples were obtained from Potters Water Action Group, a Pittsburgh based non-governmental organization. This investigation was able to image these filters' inner structure reporting the presence and size of a network of small pore channels spread throughout the entire volume. This is the first time this type of pores is directly imaged.

Almost all of the porosity in the filter samples was open and connected. Nearly all (89.6%) of the total porosity of the filters was below 100 µm while almost half of the pores (45.8%) were smaller than 10 µm. The latter being the size range that should be most effective at removing bacteria from water by size selection

Keywords: 3-D imaging, ceramic water filters, x-ray micro-tomography

1. Introduction

Access to drinking water is a major problem for many countries. According to the World Health Organization, 748 million people in the world lack access to safe drinking water [1]. Contaminated water is the main cause of spreading sicknesses like diarrhea, dysentery, poliomyelitis, etc., which causes many deaths, mainly in developing countries.

Ceramics have been used to filter and store water since ancient times. However, the low-cost ceramic water filters that can reliably remove bacteria from drinking

water are a more recent invention. The sustainability of ceramic water filters (CWFs) and their effectiveness in removing microorganisms from drinking water have been exhaustively tested, both in field and in laboratory environments. [2, 3]. Different tests showed a logarithmic reduction values of E. coli between 2-4 [3, 4, 5], and some others registered even higher values, between 5-7 [6] for other types of bacteria.

The CWFs are made of a mixture of clay, water and some combustible organic material such as sawdust. The mix is pressed into shape, then allowed to dry for about a week before being fired to temperatures near 900 °C in a kiln. During heating the organic material is combusted, leaving connected porosity in the filter that is instrumental in removing bacteria from the water while allowing adequate flow rate. Finally, after flow rate testing, the filter is coated with a dilute, aqueous suspension of antibacterial silver nanoparticles (AgNPs) that enhance the efficacy of the filters [7]. Figure 1 shows how the ceramic filter has been designed to fit into a commonly available 5-gallon plastic bucket to provide safe water treatment and storage. The addition of the nanoparticle coating takes advantage of the ability of silver to provide safe drinking water, which has been known from ancient

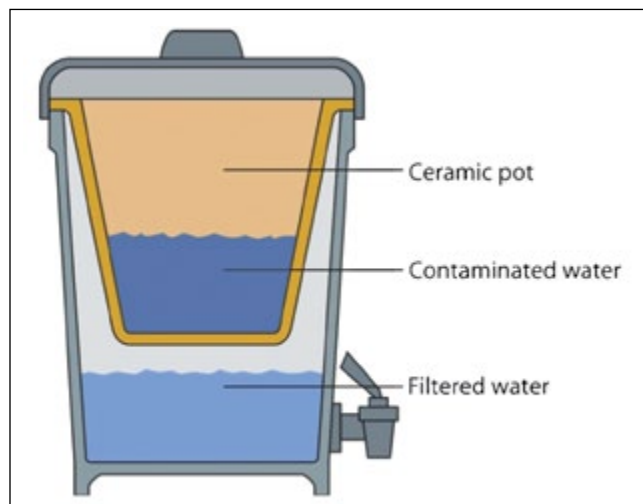


Figure 1. Scheme of a Ceramic Water Filter [3]

times. In recent years, many studies have evaluated the role of silver in antibacterial efficacy, particularly in the form of nanoparticles. While the exact mechanism is still not known, it is clear that metallic silver acts as a durable source of antibacterial silver ions by oxidation and silver nanoparticles are much less effective against aerobic bacteria in more anaerobic conditions [8].

Numerous investigations had proved the antibacterial effectiveness of the CWFs, however, at present, there is no complete microstructural description that fully explains how the filtration process works. Preliminary approaches have referred to the pore space between the fine clay particles or the holes left by combustion of the sawdust to explain both flow rate and bacteria retention. [7]. However, based on the known size of bacteria, neither pore type can explain both effects. The porosity between clay particles ($\sim 1 \mu\text{m}$) is too small to explain the observed water flow rates and sawdust holes (millimeters to hundreds of micron) are too large for bacteria retention (e.g. *E. coli* is between 1-3 μm and *Cryptosporidium parvum* around 4-7 μm). Therefore, a third type of pore population, smaller than the sawdust particles but bigger than the space between clay particles, is hypothesized to exist in the filters to explain flow rate and bacteria retention.

In the last 10 years, several investigations have focused on measuring this third type of pores and they have successfully reported it using indirect techniques such as mercury porosimetry. Their results have shown the prevalence of pores sized of about a few microns [9] which represents pore sizes that are at least two orders of magnitude smaller than the sawdust particles [4, 5, 6]. However, until present day, no one has been able to accurately observe this pore structure. A new technique, able to accurately measure internal structure of materials, has been developed. X-ray microtomography (Micro-CT) has proved to be an efficient means of measuring 3-D microstructure parameters such as connectivity and spatial distribution of the pore networks, porosity and pore size distribution [10]. Moreover, there are several studies that, have shown how Micro-CT can overcome the limitations and associated errors of conventional indirect methods such as the mercury porosimetry technique (e.g. MIP) [11].

Therefore, the objective of this investigation was to use x-ray microtomography to reconstruct the microstructure of CWFs in the form of 3-D images, to detect the above mentioned third pore population and measure the pore

volume fraction and pore size distribution in CWFs. In this way, the origin of the third pore population in CWFs could be identified.

2. Experimental Procedure

The experiments were conducted using x-ray Micro-CT. This technique involved the physics of x-ray absorption and the mathematics related to the tomography reconstruction.

2.1 Principles

X-ray radiography is based on the extent of absorption from transmitted X-rays when they pass through a material and result in a back projection of the internal structure. However, a single radiograph does not lead to an accurate description of a material's structure. Tomographic reconstruction from many X-ray radiographs solves this limitation. A series of radiographs of the object is obtained while the object is rotated about a perpendicular axis to the incident beams. Specific algorithms are then used to construct a 3-D image from the 2-D "slices" radiographs. The reconstructed picture is digitized into volume step units called voxels (the 3-D analog of a pixel), which describes the local attenuation (μ).

2.2 Sample preparation and experimental settings

Two types of sample were used. Both were obtained from the PWAG, Pittsburgh, PA. The first sample type was a square filter plate cut from the flat base of a filter. The second sample type was a square clay plate made with the same procedure for making the filters but without the addition of any sawdust. These plates were pressed into molds and not pressed. This second sample type acts as a negative control that did not go through burn out. The composition of both samples are described in Table 1.

Table 1. Mix Composition of the samples

Sample	Filter	Just-Clay
Diameter (mm)	4.47 \pm 0.01	4.48 \pm 0.01
Height (mm)	9.65 \pm 0.01	9.67 \pm 0.01
Weight (g)	0.1700 \pm 0.0001	0.2775 \pm 0.0001
Sawdust (Wt %)	16	0
Sand added (Wt %)	10	0
Sawdust Sieved size	16-60 (1190-250 μm)	0
Flow rate (L/h)	2.4	N/D

The x-ray microtomography scanning requires small size samples; therefore, small cylinders were cut from the plates, sanded and placed in the SkyScan 1272 x-ray machine (version 1.1.2 ©Bruker Corporation) for 3-D imaging.

Knowing that most of the pathogens filtered by these ceramic units are about 1-10 μm , the x-ray micro-tomography scan was set up to give high-resolution (HR) level of pixel size equal to 1.0 μm . A second scan with medium resolution (MR) level of 2.5 μm was taken in order to save time and for qualitative comparison purposes.

Setting the energy of the x-ray source to 90 kV and 111 μA (Al 0.5 mm + Cu 0.038 mm filter), the sample was mounted on a translating/rotating positioning support. For the MR scan the sample was placed at a distance of 58.24 mm from the x-ray source with a rotation step of 0.3° until a total rotation of 180° was achieved. Five hundred 2-D pictures were obtained using a cone-beam CDD detector of 4904 x 3280 pixels. The imaging process lasted eight hours.

For the HR scan, the sample was positioned 45.07 mm from the source and the total rotation was 180° with a 0.1° steps. One thousand and one 2-D slices were acquired using the cone-beam CDD detector with a 4904 x 3280 pixels. This second imaging process lasts more than 15 hours.

The reconstruction procedure of the cross section images was completed using the ®NRecon software (version 1.6.10.4 ©Bruker Corporation). To eliminate, as much as possible, the surface cracks induced by sample prepara-

Table 2: Pore Volume Fraction

% Pore sizes $\geq 250\mu\text{m}$	0
% Pore sizes $\leq 100\mu\text{m}$	89.6
% Pore sizes $\leq 50\mu\text{m}$	83.7
% Pore sizes $\leq 10\mu\text{m}$	45.8
% Pore sizes = 1-5 μm	8.4
% Closed Pores	0.9
% Open Pores	38.9

tion, a smaller region of interest (a circular section of 3.57 mm in diameter) was used. A total sample' volume of 3.2 mm³ was analyzed with ®CT Analyser (version 1.15.4.0 ©Bruker Corporation) and 3-D images were acquired using ®CTvox software (version 3.1.0 ©Bruker Corporation)

3. Results

3.1 Pore Size Distribution

The quantitative results obtained from the high resolution (HR 1.0 μm) scanning of the filter sample are described in Figure 2 and Table 2.

No pores were detected in the filter with a size greater than the sawdust particles used in the processing. All the reported pores are smaller than 250 μm and nearly all (83.7%) the pores detected have a size smaller than 50 μm . Moreover, almost half (45.8%) of the total pores have a size less than 10 μm , this is two orders of magnitude smaller than the sawdust size used and smaller enough

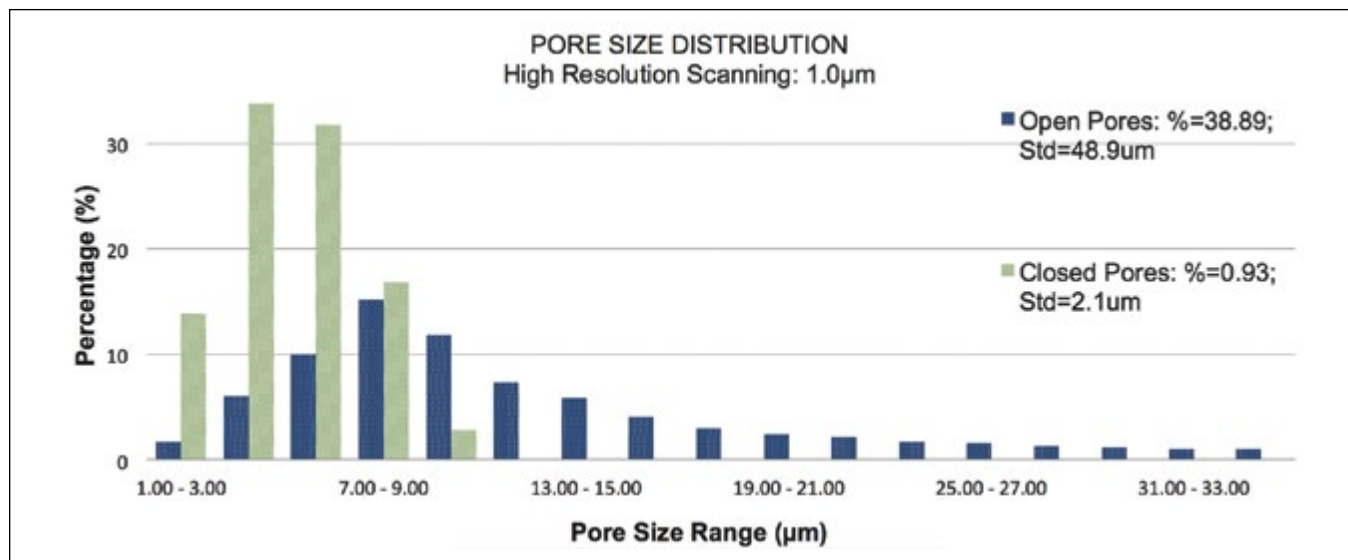


Figure 2: Pore size distribution from the HR scan Size: Largest diameter of a sphere fully enclosed by the pore

to block the passage of bacteria by size exclusion. Most of the pores are open. The closed pores (green distribution) in Figure 2 account for a very small fraction of the volume of the sample (0.9%) and were limited to pores less than 10 μm . In contrast the open connected porosity (purple distribution) accounts for 38.9% of the volume of the sample and extends over a much wider range of sizes from 1 μm all the way to 35 μm .

3.2 Qualitative Results

Figure 3 shows images were obtained from the medium resolution scan of both the filter' sample and the just-clay sample.

The left column of images in Figure 3 show fewer large isolated pores, in the internal structure of the material. These are large air pockets that were incorporated into the clay during mixing and were not eliminated when the clay was pressed into the molds. Many of the smaller black dots are image noise, not actual pores. Equivalent images of the filter material are shown in the right column. This structure contains large anisotropic cavities that are similar in size and shape to the sawdust particles added to

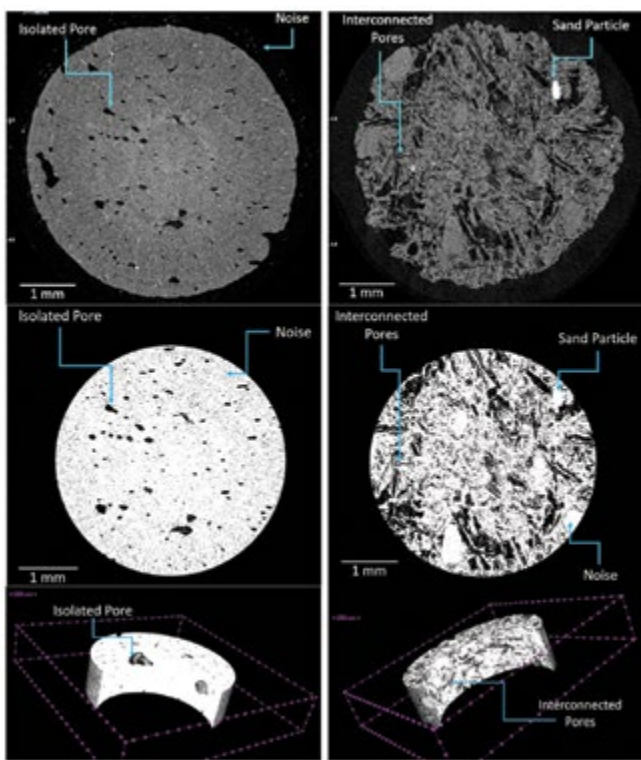


Figure 3: The images on the left are from the control sample formed without sawdust. The images of the right are from the filter materials.

the clay mix. These are thought to directly result from the burnout on heating to the maximum firing temperature. There is also a population of smaller pore channels that connect the large cavities to each other and also connect them to the external surface of the sample.

4. Discussion

The total porosity of the sample from the high resolution scan was 38.89%. 98.56% of the total porosity corresponded to open pores, which constitute an interconnected network spread throughout the entire volume and would facilitate the flow of water through the sample.

Pore-size between 250-1190 μm was expected to be observed, since that was the size range of the sawdust particles used in the mix for making the filter, however no pore was reported having that size in the high-resolution scan. Therefore, there were no cavities from the sawdust in the sample. This was not unexpected, given the small volume of material used in the high-resolution scan. Nearly half of the entire population in this sample are open pores smaller than 10 μm in diameter, which is two orders of magnitude smaller than the sawdust particle used in processing and they are small enough to filter common bacteria by size exclusion. Both the 2-D and 3-D images of the filter from the medium resolution scans in Figure 3 clearly shows that these small pores channels, quantified in the HR scan, are a major microstructural feature of the filter and connect the large anisotropic cavities produced by the burnout of the sawdust. These pore channels are entirely absent in the control samples that were made without sawdust.

This Micro-CT observation of the internal structure of low-cost ceramic water filters confirmed the importance of the addition of the sawdust particles (or any other organic combustible material) to the filter formulation. However, the direct observation of the pore structure showed the presence of a network of finer pore channels that connect the large cavities produced by burnout of the sawdust. These pore channels are in the size range that could retain bacteria by size exclusion. The images also suggest an explanation for these pore channels.

It is not unusual for polymeric materials to be used in the processing of ceramics from powders. The polymers then burn out during heating of the ceramic to the firing temperature. The resulting gases, such as carbon dioxide, have difficulty in escaping from between the ceramic powder particles and the gas pressure can rise. If the gas

pressure reaches a critical value, it can crack the ceramic during burnout. This provides an explanation for the observed internal pore structure of the ceramic filters. The gas buildup from the combustion of the sawdust is thought to create cracks (pore channels) that link the large cavities created by the sawdust. Hence there is a third pore population, not created directly by the sawdust or thought to be due to the pores space between the individual clay particles. The third pore population quantitatively analyzed in the HR images and qualitatively observed in the MR images is thought to be caused by the buildup of gas pressure as the sawdust burns out.

5. Conclusion

Imaging of low-cost ceramic filters using Micro-CT has detected a large fraction (45.8%) of open pore channels less than 10 μm in diameter. These pores are too large to be the pores between individual clay particles and they are absent in control samples processed without sawdust. In addition, the pore channels in the filters are too small to the cavities that remain after the burnout of sawdust particles. The imaging comparison in this study suggest this open pore population and its interconnectivity is caused by cracking of the clay between the sawdust particles due to the buildup of gas pressure in the burnout of the sawdust.

6. Acknowledgments

The authors would like to thank Michael Stubna of Potters Water Action Group for providing the samples for this study.

References

- [1] WHO/UNICEF, "Progress on Drinking Water and Sanitation. Update," Geneva, 2014.
- [2] A. K. Plappally, I. Yakub, and L. C. Brown, "Theoretical and Experimental Investigation of Water Flow through Porous Ceramic Clay Composite Water Filter," *Fluid Dyn. Mater. Process.*, vol. 5, no. 4, pp. 373–398, 2009.
- [3] D. Van Halem, H. Van Der Laan, S. G. J. Heijman, J. C. Van Dijk, and G. L. Amy, "Assessing the sustainability of the silver-impregnated ceramic pot filter for low-cost household drinking water treatment," *Phys. Chem. Earth*, vol. 34, no. 1–2, pp. 36–42, 2009.
- [4] E. N. Kallman, V. A. Oyanedel-craver, A. M. Asce, J. A. Smith, and M. Asce, "Ceramic Filters Impregnated with Silver Nanoparticles for Point-of-Use Water Treatment in Rural Guatemala," *J. Environ. Eng.*, vol. 137, no. 6, pp. 407–415, 2011.
- [5] J.A. Oyanedel-Craver, Vinka A; Smith, "Sustainable Colloidal-Silver-Impregnated Ceramic Filter for Point-of-Use Water Treatment," *Environ. Sci. Technol.*, vol. 42, no. 3, pp. 927–933, 2008.
- [6] I. Yakub, D. Ph, A. Plappally, D. Ph, M. Leftwich, D. Ph, K. Malatesta, D. Ph, K. C. Friedman, S. Obwoya, D. Ph, F. Nyongesa, D. Ph, A. H. Maiga, D. Ph, M. Asce, A. B. O. Soboyejo, D. Ph, S. Logothetis, W. Soboyejo, and D. Ph, "Porosity , Flow , and Filtration Characteristics of Frustum-Shaped Ceramic Water Filters," *J. Environ. Eng.*, vol. 139, no. 7, pp. 986–994, 2013.
- [7] Potters For Peace. (n.d.). About Us. [Online] Available: http://pottersforpeace.com/?page_id=8 [Accessed: 15-Aug-2016].
- [8] Z. Xiu, Q. Zhang, H. L. Puppala, V. L. Colvin, and P. J. J. Alvarez, "Negligible Particle-Specific Antibacterial Activity of Silver Nanoparticles," *Nano Lett.*, vol. 12, pp. 4271–4275, 2012.
- [9] J. J. Simonis and A. K. Basson, "Evaluation of a low-cost ceramic micro-porous filter for elimination of common disease microorganisms," *Phys. Chem. Earth*, vol. 36, no. 14–15, pp. 1129–1134, 2011.
- [10] B. E. Maire, J. Buffi, L. Salvo, J. J. Blandin, W. Ludwig, and J. M. Løtang, "On the Application of X-Ray Microtomography in the Field of Materials Science," *Adv. Eng. Mater.*, vol. 3, no. 8, pp. 539–546, 2001.
- [11] R. C. Atwood, J. R. Jones, P. D. Lee, and L. L. Hench, "Analysis of pore interconnectivity in bioactive glass foams using X-ray microtomography," *Scr. Mater.*, vol. 51, pp. 1029–1033, 2004.

Glutaraldehyde Efficacy Against Microbial Species Found in Produced Water

Cassandra Valcourt^{1*}, Daniel Lipus^{1,3}, and Kyle Bibby^{1,2}

¹*Department of Civil and Environmental Engineering, Swanson School of Engineering,
University of Pittsburgh, Pittsburgh, PA, USA*

²*Department of Computational and Systems Biology, Swanson School of Engineering, University of Pittsburgh,
Pittsburgh, PA, USA*

³*National Energy Technology Laboratory (NETL), Pittsburgh, PA, USA*

Abstract

Hydraulic fracturing is a commonly used process in the United States to extract natural gas from underground shale formations. In hydraulic fracturing, millions of liters of fracturing fluid are pumped into a well-bore at high pressures to expand the previously made cracks, maximizing the amount of gas extracted. Fracturing fluid is mostly water and proppant, but it also contains a small amount of chemicals, including biocide. Biocide is supposed to limit bacterial growth and kill the microbes found in the wastewater that results from this process. However, very little is currently known on the efficacy of biocide utilized during hydraulic fracturing. In this study, we isolated six produced water microorganisms and subsequently evaluated their growth under a range of glutaraldehyde conditions, one of the most commonly used hydraulic fracturing biocides, with the goal to determine the minimum inhibitory concentration (MIC) for each isolate. Results showed that although MIC ranges varied for different isolates, increasing the concentration of glutaraldehyde did not completely inhibit growth; the biocide only suppressed growth, resulting in an extended lag phase at higher concentrations. Finding the glutaraldehyde MIC for native produced water microorganisms will lead to more efficient biocide application strategies and improve produced water management.

Keywords: hydraulic fracturing, produced water, glutaraldehyde, minimum inhibitory concentration (MIC)

1. Introduction

Hydraulic fracturing (also known as “fracking”) enables the extraction of fossil fuel resources from previously unrecoverable shale formations. The fracturing process begins with the drilling of a well several miles long vertically downward then horizontally underground to where shale formations are located. After drilling, the well-bore is lined tightly with layers of steel casing and cement,

protecting the surrounding environment from leakage and contamination [1]. 15-20 million liters of fracturing fluid are then pumped down the well at high pressures, creating and expanding cracks in the rock. This fluid consists of 90% water, 9% sand, and 1% chemical additives, including biocides [2]. After the hydraulic fracturing process is completed, approximately 10-50% of the original fluid returns to the surface [3], equating to several million gallons of wastewater. Unlike regular wastewater, which can be treated and reused or disposed, wastewater from hydraulic fracturing, called “produced water,” can be difficult to manage and can cause several problems. Produced water consists of hydraulic fracturing fluids and subsurface brines, and is often characterized by high total dissolved solids (TDS) concentrations and radioactivity [4]. It is also a suitable environment for specific types of bacteria that produce acids and sulfides, which leads to corrosion of fracturing equipment and gas souring [4].

1.1 Produced Water Microbiology

Bacteria can be introduced to hydraulic fracturing produced water through hydraulic fracturing fluid, the hydraulic fracturing infrastructure, or may be native to the site [3]. Once the hydraulic fracturing process has begun, microorganisms are more likely to grow and reproduce due to an introduction of nutrients from the fracturing fluid and the release of nutrients from the surrounding areas. Bacteria can return to the surface in the produced water, however, the microbial communities associated with a hydraulic fracturing environment have been found to change over time. Early flowback water microbial populations have been reported to be mainly aerobic and similar to those found in fracturing fluid, while later staged produced water microbial populations are less diverse and dominated by anaerobic taxa [5].

The fluids returning to the surface during hydraulic fracturing are changing in both chemical and micro-

bial composition as time goes on. A long-term study on produced water from the Marcellus Shale exemplified these changes. A produced water sample taken on day 1 following fracturing closely resembled prefracturing fluid, with Alphaproteobacteria and Gammaproteobacteria as the dominant species among a diverse microbial community [3,6]. However, a sample taken seven days later already showed significant changes. The abundances of both the Alphaproteobacteria and the Gammaproteobacteria had decreased, along with the amount of diversity that had previously been observed. The chemical composition of the produced water also changes over time. Later stage produced water was found to have higher ionic concentrations, salinity, and radioactivity than produced water sampled within a few days of fracturing [3]. A sample of produced water taken on day 187 showed even greater change, with the majority of all species found being of the *Halanaerobium* genus [3]. This genus is composed of species that are both anaerobic and halophilic, which allows them to flourish in the high salinity environment [3].

Although it is unclear exactly where these microbes come from, bacterial growth is known to cause several problems during and after hydraulic fracturing. Bacterial growth can lead to acid production, sulfide release, and biofilm formation causing fouling, gas souring, clogging of the cracks, corrosion, and equipment damages [7]. This creates a produced water management challenge, potentially interfering with hydraulic fracturing operations, making wells less effective, resulting in loss of profits for extraction companies and even environmental damage. To minimize bacterial growth, operators use biocides, which are added to the fracturing fluids.

1.2 Produced Water Biocides

There are two types of biocides that are used in an attempt to kill the bacteria found in produced water: lytic and electrophilic [8]. Lytic biocides weaken and disrupt the cell wall. Electrophilic biocides damage the cell wall or interfere with cellular processes in the cytoplasm that are critical to regulating cell function [8]. Glutaraldehyde, which is electrophilic, is the most commonly used biocide in hydraulic fracturing, but has limited effectiveness [8]. Microbes found in produced water have shown an increased resistance towards glutaraldehyde and other biocides [2]. Researchers have discovered that hypersaline produced water exposure induces a stress response, consisting of genes involved in cellular processes protecting the cell such as chaperones

or cell membrane stability, and found this response to lead to an increased resistance to the biocides glutaraldehyde and sodium hypochlorite [2]. Increasing biocide concentration could possibly combat bacterial resistance but is more expensive and leads to greater environmental concerns [8]. Testing the minimum inhibitory concentration (MIC) of each microbe found is one method that can be used to try and prevent bacterial resistance, and find a more resourceful amount of glutaraldehyde to be used in fracturing fluid. MIC testing is commonly used to test how a chemical affects bacteria growth, but this has not yet been done for bacteria exposed to glutaraldehyde. Finding the minimum inhibitory concentrations (MICs) of the biocide glutaraldehyde for native produced water organisms will optimize application strategies, leading to improved biocide efficacy and greater encouragement of produced water reuse.

2. Materials and Methods

Produced water was sampled from various fracturing sites around Pennsylvania and Ohio in the summers of 2014, 2015, and 2016. Samples were taken in sterile 1L bottles and kept on ice during transportation and stored at -20°C until being used for experiments. Bakken shale produced water samples were collected in 2L glass bottles and shipped to the Pittsburgh lab overnight.

2.1 Plate Preparation

Three types of growth media were used for culture maintenance and MIC assays. Media A was a mixture of Mueller Hinton (MH) broth with 20,000 mg/L of NaCl salt. Media B was a mixture of MH broth and salts characteristic of produced water (PW salts) as previously described [7]. These salts were 3.4 g/L NaHCO₃, .048 g/L MgSO₄, .035 g/L K₂NPO₄, and 2.0 g/L NH₄Cl. Media C was a minimum media, based on a previously described media for biocide assessment [9] and consisted of 6.4 g NaCl, 1.5 g CaCl, 0.75 g peptone, 0.75 g dextrose/glucose mixture, and PW salts, which were filter sterilized and added after autoclaving. All media were prepared as broth for culture maintenance, MIC assays, and 1% bacteriological agar plates for organism isolation.

2.2 Plate Inoculation

100 µL of hydraulic fracturing produced water was pipetted onto one of the three types of agar plates. Sterile loops or beads were then used to evenly distribute the produced water around the plate surface. Plates were incubated for three days at 25°C or until bacteria growth was observed.



Figure 1: Bacteria growth after the incubation period. A colony has been selected before isolation.

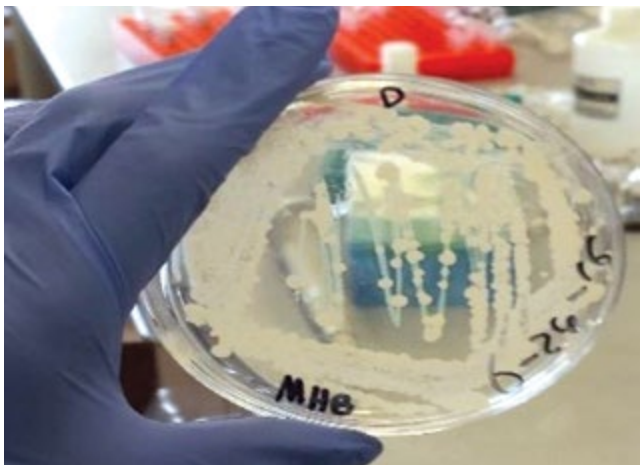


Figure 2: A streak plate after incubation. Bacteria growth is heavier around the sides and lighter down the middle. All bacteria on the plate look the same therefore the colony that was isolated was purely cultured.

Table 1: Individual bacterial isolate sample locations and media types

Isolate	Sample Location	Media
A	Marcellus Shale, Greene County, PA	A
B	Marcellus Shale, Greene County, PA	B
D	Marcellus Shale, Greene County, PA	B
E	Marcellus Shale, Greene County, PA	B
H	Bakken Shale, MO	C
H1	Bakken Shale, MO	C

An example of an agar plate with a produced water isolate can be seen in Figure 1.

2.3 Colony Isolation

After inoculation, bacteria colonies were picked and used to inoculate 15 mL of fresh media. The mixture was incubated at 25°C for several days. Bacterial isolates were maintained by starting a fresh culture every two days. 100 µL of culture were transferred into a new tube and grown in fresh media. Overall, six bacterial strains were isolated. The media used and the sample location for each isolate are listed in Table 1.

2.4 Streak Plate Inoculation

To verify pure culturing techniques, bacteria strains that were isolated were re-grown using a streak plate. 200 µL of the isolated culture in the salt supplemented MH Broth was pipetted onto an agar plate and streaked out, allowing for the observation of individual colonies (Figure 2). The plates were then incubated for three days at 25°C.

2.5 MIC Testing

Cultures that confirmed to contain pure isolates were used for MIC testing. Growth was assessed by measuring optical densities at 600nm (OD₆₀₀) for a 200 µL volume of each sample in triplicate reactions, using a plate reader. For each measurement, a blank was included which consisted of the corresponding broth solution without any added culture.

MIC testing was performed at a range of concentrations between 0 mg/L and 1100 mg/L glutaraldehyde, with a starting OD₆₀₀ of 0.1. Briefly, calculated amounts of glutaraldehyde and seed culture were added to 800 µL of salt supplemented MH broth in 1.5 mL micro centrifuge tubes. Three samples were tested at a time along with controls. Control samples contained the varying amounts of glutaraldehyde but had no added bacteria.

200 µL of the control and the three samples were taken from each tube and pipetted into a well on a microtiter plate, in biological triplicates, with glutaraldehyde concentrations ranged between 0 mg/L and 1100 mg/L (Figure 3). The 96 well plate was sealed with parafilm, inserted into the plate reader, and optical density at 600nm was measured over a 48 hour period at 30 minute intervals. The resulting data was collected and analyzed in Excel to determine lag times and growth rates for each isolate and glutaraldehyde concentration. Based on initial observation, glutaraldehyde concentrations were modified and experiments repeated until a concentration at which no bacterial growth was observed was found or

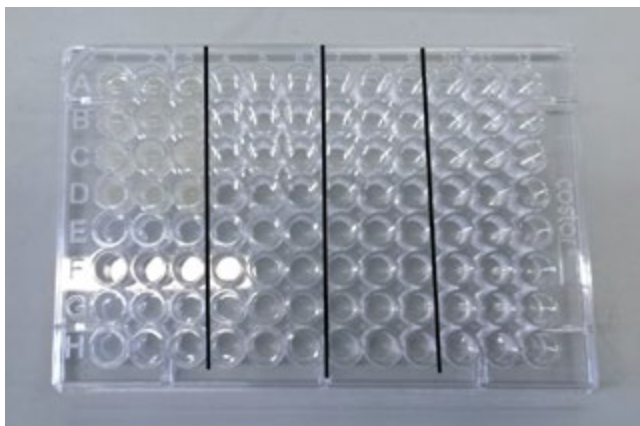


Figure 3: Microtiter plate setup for MIC testing. Lowest glutaraldehyde concentrations (0mg/L) were in row A, while highest glutaraldehyde concentrations were in row H. The black lines indicate the separation between different samples; samples were run in triplicates

until growth patterns were seen in the data as concentration changed.

2.6 DNA Extraction and Sequencing

DNA was extracted using a PowerSoil DNA Isolation Kit (MoBio, Carlsbad, CA), according to manufacturer's instructions. DNA was amplified using polymerase chain reaction (PCR). Briefly, 1 μ L of DNA was added to 12.5 μ L of PCR master mix, 0.5 μ L of 16S rRNA universal forward primer, 0.5 μ L of 16S rRNA universal reverse primer, and 11 μ L of molecular water. Reactions were run in a thermocycler using the following protocol: 3 minutes initial denaturation at 96°C, 40 cycles of 45 seconds denaturation at 96°C, 45 seconds primer annealing, 60 seconds elongation at 72°C; 10 minutes final elongation at 72°C and hold at 4°C. PCR products were cleaned up using AMPure beads. Briefly, AMPure beads were added to each sample incubated at room temperature for five minutes, placed on a magnetic stand, and supernatant removed. Bead pellets were washed with 80% ethanol, air dried, and resuspended in TE buffer. Cleaned up products were run on an agarose gel for cleanup verification. Cleaned up 16S rRNA product concentration was assessed using Qubit technology, and submitted to the University of Pittsburgh Genomics Research Core for rRNA sanger sequencing. 16S rRNA sequences were annotated against the nr NCBI database using BLAST [10].

3. Results and Discussion

After multiple 48-hour time periods, MIC tests were completed and all data was collected and exported to an Excel spreadsheet. Data contained OD values taken at 30-minute intervals for each sample at different glutar-

aldehyde concentrations. These values were then plotted, creating a series of growth curves for each sample. To determine how the concentration of glutaraldehyde affected bacteria growth and get an estimate of MIC range, growth curves at each sample at each respective concentration were analyzed.

Bacteria grows in four main stages: lag time, exponential phase, deceleration phase, and saturation phase. Bacteria growth starts in the exponential phase, slows down during deceleration, and then the bacteria die throughout the saturation phase. Since the glutaraldehyde was expected to slow and limit bacteria growth, only the lag time and exponential phase were evaluated in this research.

Growth curves of all isolates showed similar patterns. As the concentration of glutaraldehyde used increased, bacteria in all samples tested started growing at later times, but there was no concentration at which any bacteria sample completely stopped growing. At 1000 mg/L of glutaraldehyde bacteria growth was delayed about 24 hours in samples H and H1, 32 hours in sample D, and about 48 hours in samples A, B, and E (Table 2). In addition to this, higher concentrations of glutaraldehyde had no effect on the growth rate of the bacteria. Even though the lag time became longer and the exponential phase was delayed as concentration increased, once the bacteria started growing, it grew at about the same rate across all concentrations. This was observed in the slope of the OD values during the exponential phase, as seen in Figure 4. To determine the slope, for each concentration of each sample, the OD value and time at the beginning and end of the exponential phase was used. Since each concentration was tested in triplicates, the average slope of each well was taken and plotted (Figure 4). This was then fitted using linear regression in Excel. If glutaraldehyde concentration had an effect on the growth rate, as concentration increased, the growth rate of the bacteria should have decreased and eventually stopped. However, the slope of the line of best fit through all the points is 0, indicating that this relationship does not exist, and growth rate did not change as the bacteria was exposed to higher concentrations of glutaraldehyde. This suggests that glutaraldehyde does not completely inhibit bacteria growth as was previously believed [2], but serves to extend the lag growth time.

16S rRNA sequencing allowed for the phylogenetic identification of two of the isolated colonies. BLAST analysis suggested Isolate B to be closely related to the *Bacillus* genus and Isolate E to belong to the *Enterococcus* genus. Sequencing products were not long enough to assess phylogeny at the species level. 16S rRNA sequencing

Table 2: Lag times (in hours) for each isolate at the various concentrations of glutaraldehyde tested. N/A indicates that the isolate was not tested at that concentration level while a dash indicates that no observable growth occurred during the 48-hour testing period. Lag times for all isolates increased with increasing glutaraldehyde concentrations.

Glutaraldehyde Concentration (mg/L)	A	B	D	E	H	H1
0	1.5	3.5	3	5	8	5.5
10	2	4	6.5	5.5	8.5	6
20	2.5	4.5	6.5	6	9.5	6.5
50	2.5	5	7.5	7.5	10	6.5
75	3	5	8.5	8.5	11.5	8.5
100	4.5	7.5	9.5	10	12.5	10.5
200	7.5	12.5	16	13	16.5	13
350	12.5	N/A	N/A	17.5	N/A	N/A
400	12.5	N/A	18	28.5	N/A	N/A
500	21.5	24	19.5	30	22	16.5
1000	40	48	32.5	48	23	24.5
1100	48	N/A	-	-	N/A	N/A

data for the remaining samples could not be analyzed due to poor quality.

Although phylogeny could only be assessed at the genus level both samples were characterized as types of bacteria that have qualities of those previously found in produced water. The *Bacillaceae* family contains a diverse range of bacteria that are abundant in the environment. *Bacillus* species can be found anywhere from soil to bodies of water [11]. These species contain bacteria that are able to survive and grow in harsh environments, similar to the conditions found in produced water.

4. Conclusion

In this study, six microbial cultures taken from produced water samples were isolated, grown, and tested for their ability to grow over a range of glutaraldehyde concentrations. Results suggested that increasing the concentration of glutaraldehyde only increases the duration of the lag time while having no significant effect on the growth rate in the exponential phase. In hydraulic fracturing glutaraldehyde concentrations of around 150 mg/L to 500 mg/L are used [12]. According to the results obtained in this study, bacteria continue to grow at these and even higher concentrations. Our results suggest that at a concentration of 150 mg/L to 500 mg/L, glutaraldehyde delays bacteria growth for only up to 24 hours, a timeframe shorter than the fracturing process [12]. Based on the findings in

this study, we therefore do not recommend the usage of glutaraldehyde as a biocide during the hydraulic fracturing process. Although glutaraldehyde may not be as toxic as other potential biocides, it still can cause environmental contamination as well as breathing problems and irritation in workers that are exposed to it [13]. In addition, inefficient use of the biocide glutaraldehyde may lead to increased operational costs. As our data suggests, glutaraldehyde does not serve its ultimate purpose so we believe the usage of glutaraldehyde in hydraulic fracturing should be questioned and re-evaluated.

More research should be done in the subject area of both biocides and produced water microbiology. Further work in this study could include observing if glutaraldehyde has any effect on bacteria growth over a longer time period, testing glutaraldehyde on other types of microbes found in produced water, or finding biocide alternatives that are more efficient. A possible alternative biocide could be NaClO, which is known to work quickly and kill bacteria efficiently [2].

Acknowledgments

Thanks to Dr. Bibby for mentoring, teaching, and allowing me to work in his lab, along with Daniel Lipus, who guided me throughout my research project. Also, thanks to the Pitt Excel staff for providing me with the opportunity to do research under SRI this summer and for their support.

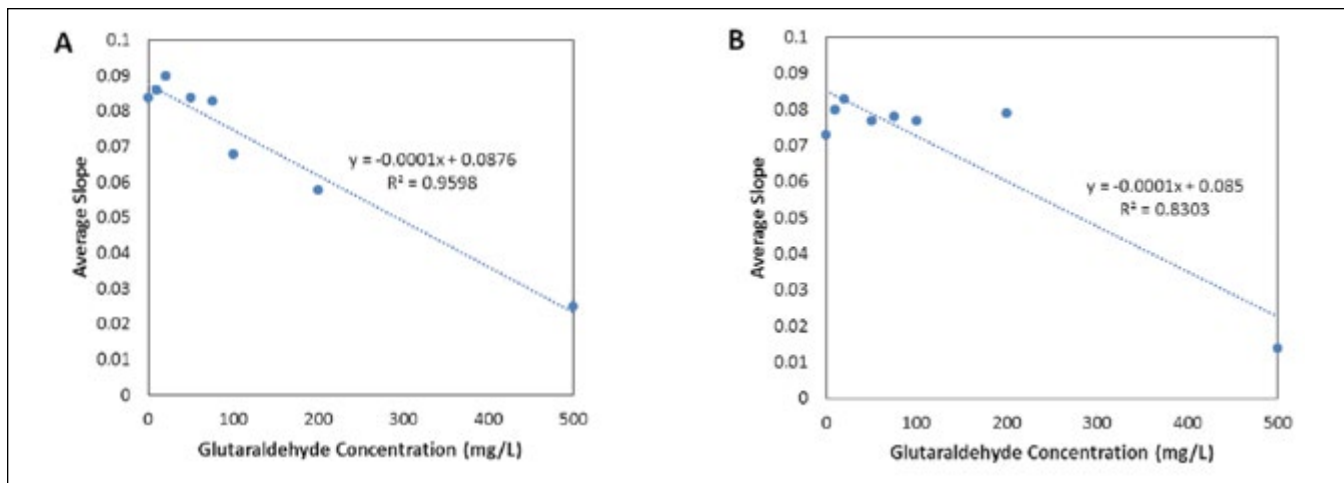


Figure 4: Average growth rate of samples A (Graph A) and sample D (Graph B) during the exponential phase. Although a higher concentration of glutaraldehyde is needed to have a significant effect on lag times in sample D than sample A, both experienced no change in growth rate despite the increasing concentrations of glutaraldehyde. This was found to be true for all tested samples.

References

- [1] Norris, J. Q, Turcotte, D, L, Moores, E, M, Brodsky, E, E, Rundle, J, B, “Fracking in Tight Shales: What Is It, What Does It Accomplish, and What Are Its Consequences,” Annual Review of Earth & Planetary Sciences, 44, (2016), 321-351
- [2] Vikram, A, Lipus, D, Bibby, K, “Produced Water Exposure Alters Bacterial Responses to Biocides,” Environmental Science & Technology, 48, (2014), 13001-13009
- [3] Mohan, M, M, Hartsock, A, Bibby, K, J, Hammack, R, W, Vidic, R, D, Gregory, K, B, “Microbial Community Changes in Hydraulic Fracturing Fluids and Produced Water from Shale Gas Extraction,” Environmental Science & Technology, 47, (2013), 13141-13150
- [4] Ahearn, A, “Managing Wastewater from Fracking, with Robert B. Jackson,” Environmental Health Perspectives, 120, (2012), 1-8
- [5] Akob, D, Cozzarelli, I, Dunlap, D, Rowan, E, Lorah, M, “Organic and Inorganic Composition and Microbiology of Produced Waters from Pennsylvania Shale Gas Wells,” Applied Geochemistry, 60, (2015), 116-125
- [6] Cluff, Maryam, A, Hartsock, Angela, MacRae, Jean, D, Carter, Kimberly, Mouser , Paula, J, “Temporal Changes in Microbial Ecology and Geochemistry in Produced Water from Hydraulically Fractured Marcellus Shale Gas Wells,” Environmental Science & Technology, 48, (2014), 6508-6517
- [7] Santillan, E, U, Choi, W, Bennett, P, C, Leyris, J, D, “The Effects of Biocide Use on the Microbiology and Geochemistry of Produced Water in the Eagle Ford Formation, Texas, U.S.A,” Journal of Petroleum Science and Engineering, 135, (2015), 1-9
- [8] Kahrlas, G, A, Blotevogel, J, Stewart, P, S, Borch, T, “Biocides in Hydraulic Fracturing Fluids: A Critical Review of Their Usage, Mobility, Degradation, and Toxicity,” Environmental Science & Technology, 49, (2014), 16-32
- [9] Oh, S, Tandukar, M, Pavlostathis, S, Chain, P, Konstantinidis, K, T, “Microbial Community Adaptation to Quaternary Ammonium Biocides as Revealed by Metagenomics,” Environmental Microbiology, 15, (2013), 2850-2864
- [10] Acland, Abigail et al., “Database Resources of the National Center for Biotechnology Information,” US National Library of Medicine National Institutes of Health, 42, (2013), 7-17
- [11] Fajardo-Cavazos, P, Maughan, H, Nicholoson, W, “Evolution in the Baciliaceae,” Microbiology Spectrum, 2, (2015), 1-32
- [12] Sianawati, E, Yin, B, Williams, T, McGinley, H, The Dow Chemical Company-USA, Nair, S, The Dow Chemical Company-UAE, “Microbial Control Management for Oil and Gas Recovery Operations,” Society of Petroleum Engineers, (2013), 819-829
- [13] United States Department of Labor, “Best Practices for the Safe Use of Glutaraldehyde in Health Care Practices,” Occupational Safety and Health Administration, (2006), 1-43

Design of Highly Efficient Bifunctional Metal-Organic Framework Catalysts for Tandem Catalysis by Shortening the Reaction Pathway

Benjamin Yeh¹, Zhigang Hu², and Dan Zhao²

¹ Department of Chemical and Petroleum Engineering, Swanson School of Engineering, University of Pittsburgh, Pittsburgh, PA, USA

² Department of Chemical and Biomolecular Engineering, National University of Singapore, Singapore

Abstract:

Tandem reactions are important in the scientific community because they reduce time and money to carry out a reaction as well as chemical waste. However, tandem reactions are two consecutive reactions with each step of the reaction requiring a different catalyst. Metal organic frameworks (MOFs) have the capability to catalyze reactions; more specifically, the UiO-66 can be functionalized with two different moieties, making it a good candidate for the tandem deacetalization–Knoevenagel reaction, which is an acid-base tandem reaction. The modulated hydrothermal (MHT) synthesis of UiO-66-type MOF is used to create the catalyst used. Since the MHT synthesis method is relatively new, powder X-ray diffraction (PXRD) and Brunauer-Emmett-Teller (BET) analysis were used to show that the structures of the UiO-66 derivatives using the MHT method and the actual UiO-66 were similar. The UiO-66 type MOFs can be functionalized with both an acidic and basic site at varying amounts which affects reaction progress. To analyze these effects, a kinetic study using ¹H NMR was used to calculate the conversion of benzaldehyde dimethyl acetal (BADA) to benzalmalonitrile. Overall, the bifunctional UiO-66 MOFs were able to convert BADA into benzalmalonitrile within 10 minutes while a biphasic mixture of UiO-66 MOFs converted BADA into benzalmalonitrile in 1 hour.

Keywords: tandem reactions, acid-base catalysis, bifunctional catalysts, UiO-66

Abbreviations: metal organic framework (MOF), modulated hydrothermal (MHT), nuclear magnetic resonance (NMR), sodium sulfoterephthalate (SSBDC), aminoterephthalate (ATC), powder x-ray diffraction (PXRD), Brunauer-Emmett-Teller (BET), benzaldehyde dimethyl acetal (BADA), dimethyl sulfoxide (DMSO), porous aromatic framework (PAF)

1. Introduction

Tandem reactions are consecutive organic reactions that proceed from a reactive intermediate. Most often, each step in a tandem reaction requires a catalyst, and therefore, the reaction requires different active sites. Research of tandem reactions is important due to their inherent nature where there is no isolation of intermediates, offering a huge economic and environmental advantage. Most often, tandem reactions are one pot reactions, reducing the need for a solvent and the extra space required for reactors.

Metal organic frameworks (MOFs) are high porous materials containing metal ions and organic ligands and can serve as catalysts [1]. Multi-functional metal organic frameworks (MOFs) have shown promising results when carrying out tandem reactions, as they can be functionalized antagonistically to carry out redox or acid/base reactions [1, 2, 3]. Thus, they eliminate the need for multiple catalysts for a reaction, and the reaction can be carried out in a single reaction flask. UiO derivatives are a family of MOFs that have face centered cubic structures, contributing to their high thermal stability [1]. Specifically, the UiO-66 MOF was shown to show high hydro and thermal stability, which most MOFs lack. Research has shown that the UiO-66 has the ability contain many different moieties, which varies its functionalities [2]. Using the modulated hydrothermal synthesis (MHT) method, the amount of organic ligands are varied and added to the zirconium complex, creating different ratios of acidic and basic active sites in for the UiO-66 MOF [4].

The purpose of this research is to use the UiO-66 MOF with different acidic and basic functionalities synthesized using the MHT method for tandem reactions. This project attempts to explore how the ratios of acidic and basic sites will affect the progress of the deacetalization–Knoevenagel reaction using the toluene and water solvent system

proposed in the literature and a proposed safer solvent system of water and ethanol at a lower temperature. The reaction progress is measured with ^1H Nuclear Magnetic Spectroscopy (NMR) to show how much of the initial reactant was converted to the final product.

2. Methods

2.1 Synthesis

The UiO-66 was synthesized using the modulated hydro-thermal synthesis method, which is generally safer and more environmentally-friendly than traditional methods of making UiO-66 MOFs. First, 1.8g of $\text{Zr}(\text{NO}_3)_4$ was dissolved in 20 mL of water and 30 mL of acetic acid. To vary the acidity and basicity of the UiO-66 MOF, sodium sulfoterephthalate (SSBDC) and aminoterephthalate (ATC) were used as ligands and varied by molar ratio (total 5 mmol), respectively [4]. Figure 1 below shows a schematic of how the organic ligands are linked to the inorganic metal ion.

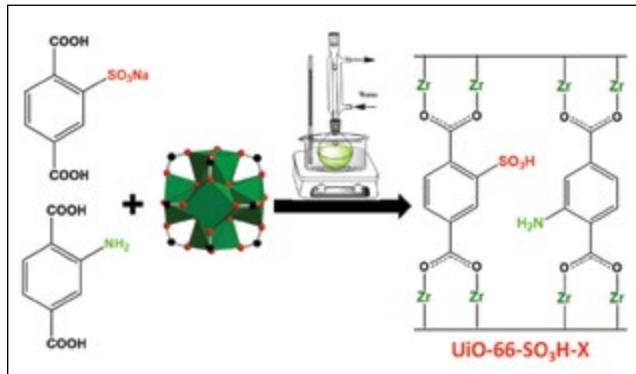


Figure 1: Simplified synthesis scheme of UiO-66 MOFs using MHT method

The mixture was refluxed at 90°C for 24 hours. The product was washed every 24 hours for 96 hours. The sample was washed with water for the first two 24 hour rotations and then ethanol for the last two 24 hour rotations. Finally, the sample was dried in a vacuum oven at 120°C for 24 hours to yield the dried product. Table 1 below shows the varying molar ratios used in the MHT synthesis method to make the UiO-66 MOF derivatives.

2.2 Characterization

Powder X-ray diffraction (PXRD) analysis was used to compare the actual UiO-66 structure with the compounds synthesized in lab. Theoretically, PXRD analyzes a crystalline structure by observing X-ray diffraction that

Table 1: Summary of UiO-66-X MOFs with their molar ratios

Sample	SSBDC added (mmol)	Expected -SO ₃ H molar ratio	ATC added (mmol)	Expected -NH ₂ molar ratio
UiO-66-NH ₂	0.00	0.00	5.00	1.00
UiO-66-SO ₃ H-25	1.25	0.25	3.75	0.75
UiO-66-SO ₃ H-50	2.50	0.50	2.50	0.50
UiO-66-SO ₃ H-75	3.75	0.75	1.25	0.25
NUS-6	5.00	1.00	0.00	0.00

occurs when an X-ray comes in contact with a three dimensional crystal lattice. Therefore, by comparing PXRD data from the samples synthesized in lab and the PXRD data for UiO-66, it is possible to see if the samples synthesized using the MHT method are UiO-66 derivatives. The PXRD characterization test was done by grinding a small amount of each sample onto a sample holder with each sample analyzed with a Bruker D8 Advanced X-Ray diffractometer.

Brunauer-Emmett-Teller (BET) analysis was also used to compare the synthesized samples with the UiO-66 structure by measuring surface area and pore size. This analysis is important because smaller pore sizes can affect the diffusion of the substrate and sterically hindering the reaction to the final product. For BET analysis, about 100mg of each sample was cleansed of any gas in the sample at 150°C and 0.01 Pa for 24 hours. Then the sample was put into a Micromeritics ASAP 2020 surface area and pore size analyzer for nitrogen sorption tests using a liquid nitrogen bath at 77K.

2.3 Tandem Reaction

The tandem reaction to test the efficiency of the MOF catalysts is shown below in Figure 2. Two solvent systems were initially used: water and toluene, and water and ethanol (2.5 mL for each solvent, 5 mL for each system) using only the UiO-66-SO₃H-50 MOF. Water and ethanol was later used as the primary solvent for the rest of the tandem reactions because it is safer and more environmentally friendly compared to toluene. Thirty microliters of benzaldehyde dimethyl acetal (BADA) was added to the solvent system. Then, malonitrile (30 mg) was added to the solution. Finally, the MOF catalyst (10 mg) was added to each system, and then heated for 24 hours. Initially, the tests were done at 50°C and then 60°C , both stirred at 800 RPM.

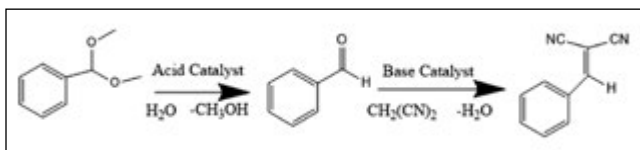


Figure 2: Tandem deacetalization–Knoevenagel reaction scheme to test bifunctional catalyst properties

To analyze the reaction progress kinetics of the tandem reaction for each reaction, ^1H NMR samples were taken. Thirty microliters of the reaction solution was pipetted into a NMR tube and dissolved with 400 microliters of dimethyl sulfoxide (DMSO). Samples were initially taken after 10, 20, 30, 40, and 50 minutes, as well as 1, 2, 3, 4, 5, 6, 7, and 24 hours for the $\text{UiO-66-SO}_3^-\text{H-50}$ MOF with the toluene and water system and ethanol and water system. These ^1H NMR samples were analyzed using Bruker's 600 MHz Nuclear Magnetic Resonance (NMR) spectrometer. After analyzing these results, ^1H NMR samples were taken after 10 minutes, 30 minutes, 1 hour, 3 hours, 6 hours, and 24 hours when the solvent system was just water and ethanol for the rest of the MOFs.

These ^1H NMR samples were analyzed using the Spin-solve spectrometer. Using MestNova, the relative peak areas of the tertiary hydrogen (~ 5.5 ppm) on BADA, the aldehyde hydrogen (~ 9.9 ppm) on benzaldehyde, and the alkanyl hydrogen (~ 8.0 ppm) on benzalmalonitrile were measured and compared to calculate the conversion of the substrate to the intermediate and final product. The conversion of the overall tandem reaction is reported as,

$$\frac{B + C}{A + B + C} \quad (1)$$

where A, B, and C are the relative peak heights of BADA, benzaldehyde, and benzalmalonitrile, respectively.

3. Results and Discussion

3.1 Characterization

The PXRD and BET analysis results are plotted in Figure 3. Figure 3a shows the UiO-66 MOF derivatives plotted with the simulated UiO-66 MOF along with the simulated NUS-6 . The simulated UiO-66 has two significant peaks at around 7.4° and 8.4° . The PXRD data show that all synthesized UiO-66 MOF derivatives made in

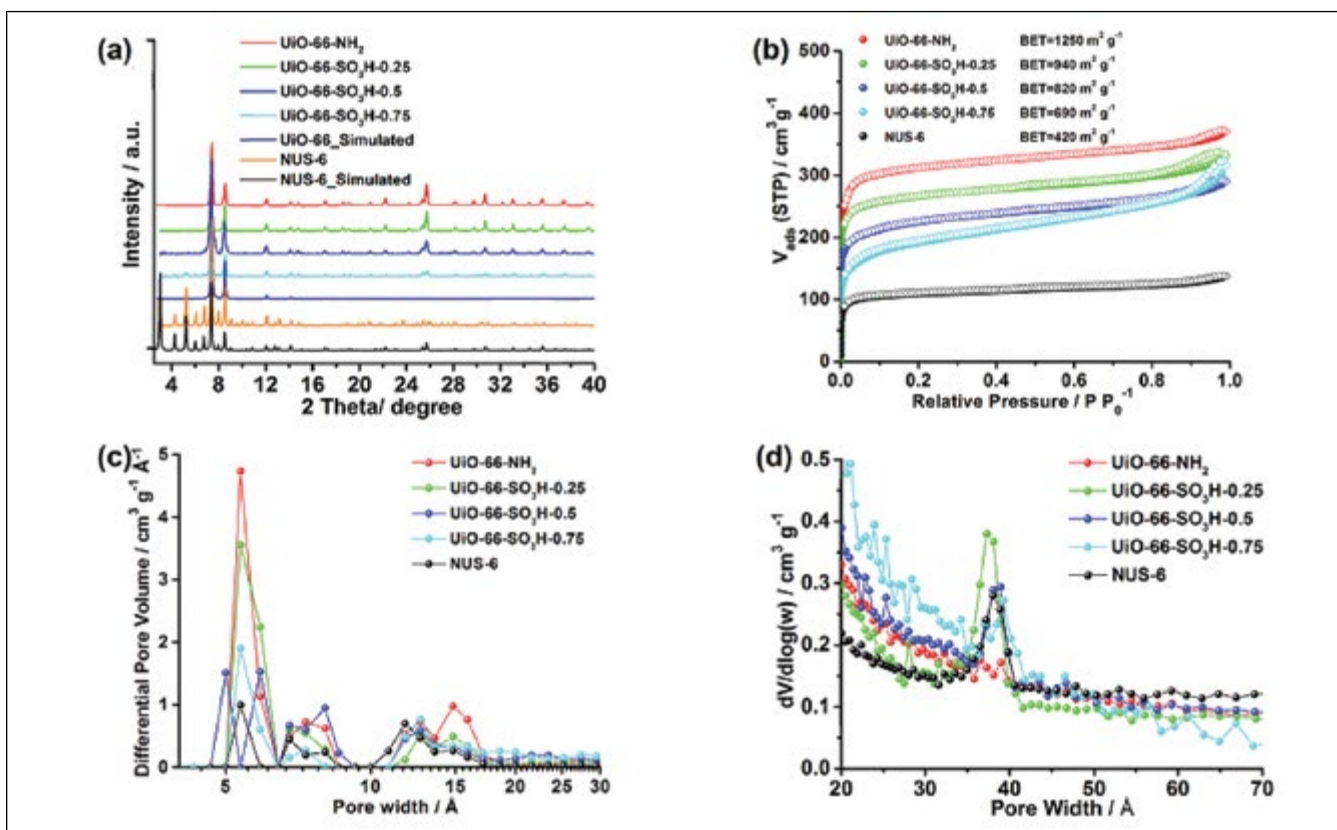


Figure 3: (a) PXRD data of synthesized UiO-66 derivatives and simulated UiO-66 MOFs. (b) Nitrogen isotherm of MOF derivatives at 77K. (c) Pore distribution of synthesized MOF derivatives. (d) Logarithmic scaled graph of pore distribution of synthesized MOF derivatives.

lab have those two significant peaks, indicating that they have a similar crystal structure to the simulated UiO-66 MOF. The smaller peaks after 15° indicate impurities in the crystal structure, like acetic acid which may have been trapped in the crystalline structure. Nevertheless, there is evidence the UiO-66 type MOFs were synthesized successfully.

BET surface area analysis (Figure 3b) indicates a hybrid of type I and type IV isotherms, which is present in the majority of MOFs. Type I isotherms are representative of a microporous structure (pore size < 2 nm), which the UiO-66 has. Type IV isotherms are representative of mesoporous structures (~2-50 nm), indicative of mesopore that exists in the MOF [4]. This larger pore width could be due to the MHT synthesis method of the UiO-66 derivatives. The simulated UiO-66 surface area is around 1500 m²/g [4]. The synthesized UiO-66 MOF derivatives all have surface areas less than the simulated UiO-66. This could be due to the functional groups that were incorporated into the UiO-66 that would provide more steric hindrance. This would result in a lower surface area compared to the literature value. Because -NH₂ is a smaller functional group compared to -SO₃H, the UiO-66-NH₂ has the largest surface area while the surface area of the UiO-66 MOF derivatives decreases with an increase in molar ratio of the larger sulfonic acid groups. Also, when adding functional groups to the UiO-66, the crystal lattice structure can be damaged, reducing its surface area. The synthesized UiO-66-NH₂ has a BET surface area of 1250 m²/g, suggesting its high crystallinity in our MHT synthesis.

The pore size distribution graph is reported in Figure 3c. Pore size is essential in catalysis because it can affect how efficiently the substrate can move through the MOF. The majority of the synthesized UiO-66 MOF derivatives have pore sizes around 6 Å, 9 Å and 11-13 Å. These all coincide with the reported literature value of the simulated UiO-66 MOFs [4]. A general trend which is seen is that the pore size decreases as the amount of the acidic moiety is increased. This is observed because the sulfonic acid moiety is significantly larger than the basic amino moiety, decreasing the pore sizes.

3.2 Catalysis and Kinetic Curves

First, ¹H NMR tests with the UiO-66-SO₃H-50 MOF in the toluene and water system and the ethanol and water system were performed. The kinetic curves are recorded below in Figure 4. For the toluene and water system, it was seen that there was 100% conversion of BADA to

benzalmalonitrile. A previous study, where this tandem catalysis study is based off of, used a porous aromatic framework (PAF) with the same moieties and reported almost complete conversion after 3 hours [5]. With the synthesized UiO-66-SO₃H-50 MOF, it was also found almost complete conversion (~84%) after 3 hours. The PAF and MOF are similar in time for the catalysis reaction given the same parameters [5]. However, the synthesis of the UiO-66 MOF is cheaper and more environmentally friendly using the MHT synthesis method, making MOFs more advantageous for industrial uses. Furthermore, the reaction was carried out at 50°C, instead of literature temperature of 90°C. This means that the reaction can be carried out at a lower temperature using the UiO-66 MOF, saving energy and prohibiting possible side reactions.

For the ethanol and water system, it is seen that the conversion of BADA to benzalmalonitrile occurs almost instantly, and complete conversion occurs much faster than the toluene and water system. This can be explained by the solvent system because water, a reagent for the tandem reaction, is insoluble in toluene. Water is soluble in ethanol, allowing water to react more favorably with BADA in a homogeneous solution. Furthermore, in comparison with the initial study, ethanol is more environmentally friendly and safer than toluene, making the water and ethanol solvent system better industrially.

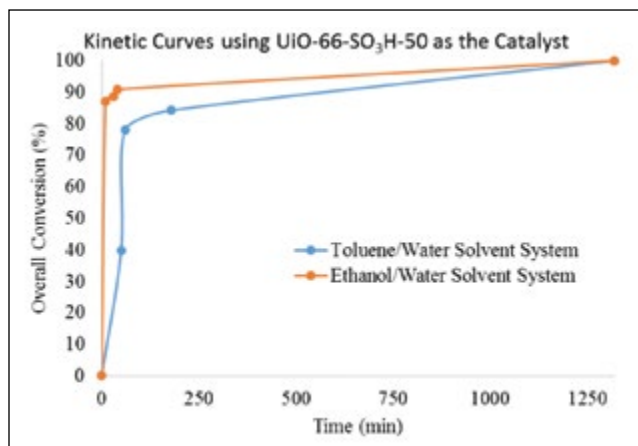


Figure 4: Kinetic curve of the toluene/water solvent system and the ethanol/water solvent system for the UiO-66-SO₃H-50 MOF

Because the ethanol and water system seemed more promising than the toluene and water system, the ethanol and water system was used as the primary solvent system when performing the tandem reaction with all six UiO-66 MOFs. Due to time constraints, the rest of the ¹H NMR

samples were analyzed using the SpinSolve spectrometer which is less sensitive than the Bruker 600 MHz NMR spectrometer. For example, none of the ^1H NMR spectra reported a peak for the intermediate, benzaldehyde. As a result, it was difficult to quantitatively report the relative peak heights of the samples and the overall conversion could not be calculated. However, some general conclusions could be made about the bifunctional UiO-66 MOFs and are summarized below in Table 2.

Table 2: Results showing when the benzalmalonitrile peak appeared in the ^1H NMR spectra.

Catalyst	Time for Final Product Peak to Appear
UiO-66-NH ₂	10 minutes
UiO-66-SO ₃ H-25	10 minutes
UiO-66-SO ₃ H-50	10 minutes
UiO-66-SO ₃ H-75	Minimal peak after 24 hours
NUS-6	None
Biphasic Mixture of UiO-66-NH ₂ and NUS-6	1 hour

For the NUS-6 MOF, the alkenyl hydrogen peak for benzalmalonitrile is not present in the ^1H NMR spectra. This makes sense for the NUS-6 because the tandem reaction requires both an acid and base catalyst. NUS-6 is not bifunctional and only contains the sulfonic acid moiety, catalyzing BADA to benzaldehyde only. The UiO-66-SO₃H-75 did not show the hydrogen peak for benzalmalonitrile until about 24 hours but the peak was minimal. This can be explained by the large sulfonic acid groups. Once BADA is catalyzed into benzaldehyde, it is possible that the sulfonic acid groups sterically hinder the benzaldehyde from reacting with the amine groups in the MOF. UiO-66-NH₂, which only has basic ligands, surprisingly showed the presence of the final product. There is no Brønsted-Lowry acid to catalyze the reaction, but the UiO-66-NH₂ may have contained acid as an impurity because its synthesis involved acetic acid. This

is why the hydrogen peak for the product is relatively prominent, as the intermediate product was able to form for the reaction to proceed. Lastly, it is important to show that the bifunctional UiO-66-SO₃H-50 MOF can catalyze the reaction faster than a biphasic mixture of UiO-66-NH₂ and NUS-6. According to the ^1H NMR spectra, the peak for benzalmalonitrile was prominent just after 10 minutes when the UiO-66-SO₃H-50 MOF was used as the catalyst. In comparison, the peak for benzalmalonitrile appeared after 60 minutes when the biphasic mixture of MOFs were used as the catalyst. When the catalyst system is a biphasic mixture, the substrate has to move through two MOFs which can be hundreds of nanometers apart. This will cause a longer reaction time for BADA to be converted into benzalmalonitrile.

Conclusion

The UiO-66 MOF can be functionalized with multiple moieties and therefore becomes a promising material for catalysis. In this study, it was found that the UiO-66 MOF can be bifunctionalized with both acidic and basic moieties to catalyze a tandem reaction at almost 100% conversion within 10 minutes with a 50-50 acid-base bifunctional MOF in an ethanol/water solvent system. We can also prove that a bifunctional MOF is a more efficient catalyst for acid-base tandem catalysis than a biphasic mixture of MOFs as the reaction was catalyzed in 10 minutes and 1 hour, respectively. Bifunctional UiO-66 MOFs are advantageous for this reason, as they save energy and money in a one pot tandem reaction. Furthermore, the tandem reaction presented in this study could be performed at a lower temperature and with safer solvent than what was previously reported, showing the efficiency of the UiO-66 MOF system as it saves energy and money. More testing with other tandem reactions needs to be done with bifunctional UiO-66 MOFs to analyze the efficiency of this catalytic material. Nevertheless, this study provided insight into the capability of bifunctional MOFs to catalyze two different reactions in one pot efficiently due to the short distance between the organic ligands in the MOF.

References

- [1] A. Dhakshinamoorthy, A. M. Asiri, Catalysis by metal-organic frameworks in water, *Chem. Commun.* 50 (2014) 12800-12814.
- [2] A. Dhakshinamoorthy, H. Garcia, Cascade reactions catalyzed by metal organic frameworks, *ChemSusChem*, 7 (2014) 2392-2410.
- [3] P. G. Garcia, M. Muller, MOF catalysis in relation to their homogeneous counterparts and conventional solid catalysts, *Chem. Sci.* 5 (2014) 2979-3007.
- [4] Z. G. Hu, Y. W. Peng, A modulated hydrothermal (MHT) approach for the facile synthesis of the UiO-66-type MOFs, *Inorg. Chem.* 54 (2015) 4862-4868.
- [5] Y. M. Zhang, B. Y. Li, Dual functionalization of porous aromatic frameworks as a new platform for heterogeneous cascade catalysis, *Chem. Commun.* 50 (2014) 8507-8510.

Acknowledgments

I would like to thank Hu Zhigang and Dr. Dan Zhao at the National University of Singapore for mentoring me on my first experimental project as well as Jingyun Ye and Dr. Karl Johnson for supporting me at the University of Pittsburgh. I would also like to thank the Swanson School of Engineering and the Office of the Provost for giving me this opportunity and funding me on this project to allow me to do research in Singapore.

Development of Computational Tools for 3-D *In Vivo* Morphometry and Analysis of Deformations of Monkey Optic Nerve Head

Ziyi Zhu^a, Huong Tran^{b,c}, Andrew P. Voorhees^c, Jacob Wallace^c, Andrew Moore^d, Matthew A. Smith^{b,c}, Gadi Wollstein^c, and Ian A. Sigal^{b,c}

^aDepartment of Mechanical Engineering and Materials Science, Swanson School of Engineering,
University of Pittsburgh, Pittsburgh, PA, USA

^bDepartment of Bioengineering, Swanson School of Engineering,
University of Pittsburgh, Pittsburgh, PA, USA

^cDepartment of Ophthalmology, University of Pittsburgh Medical Center, Pittsburgh, PA, USA

^dDepartment of Biological Sciences, Kenneth P. Dietrich School of Arts and Sciences,
University of Pittsburgh, Pittsburgh, PA, USA

Abstract

Elevated intraocular pressure (IOP) is the main risk factor for glaucoma, which is characterized by neural tissue loss in the optic nerve head (ONH). The cause of the tissue loss and its relation to IOP is not well understood, although it is widely believed to be, at least in part, due to IOP-related biomechanical insult on the ONH. Our long-term goal is to characterize the deformations of the ONH caused by IOP changes and how these lead to neural tissue loss. This requires precise and robust measurement of ONH morphology. Specifically, in this project we developed Matlab tools to analyze morphology of ONH structures from *in vivo* optical coherence tomography (OCT) images. Specifically, these tools analyzed the dimensions and positions of 4 important ONH structures: inner limiting membrane (ILM), Bruch membrane (BM), BM opening (BMO), and anterior lamina cribrosa (ALC). From these, ALC, BM and ILM surfaces, the BMO planarity, the minimum rim width (MRW) and the minimum rim area (MRA) were computed. The tools were tested using monkey data acquired under three IOP conditions: normal, low, and high. The ALC depth, BMO planarity, MRW, and MRA under these three IOP conditions were determined. Increase in BMO planarity, as well as decreases in MRA and MRW were observed under high IOP, while the opposite was observed under low IOP. An anterior shift of the ALC depth was also observed under low IOP. Compared to literature values, our measurements of average ALC depth, BMO planarity, MRW, and MRA under normal IOP conditions deviated by 2.3%, 11.4%, 35.8% and 5.9%, respectively, showing consistency with the literature. The program allowed efficient and comprehensive analysis of ONH structures.

This, in turn, will facilitate the study of the role of ONH anatomy and biomechanics on susceptibility to glaucoma and of techniques to prevent vision loss.

Keywords: glaucoma, optic nerve head, biomechanics, Matlab

Abbreviations: ONH-Optic Nerve Head, IOP-Intraocular Pressure, ALC-Anterior Lamina Cribrosa, ILM-Inner Limiting Membrane, BM-Bruch Membrane, BMO-Bruch Membrane Opening, OCT-Optical Coherence Tomography, Minimal Rim Width-MRW, Minimal Rim Area-MRA.

1. Introduction

Glaucoma is the second most prevalent cause of blindness worldwide [1]. It is a progressive and irreversible loss of retinal ganglion cell axons, which carry the visual information from the eye to the brain. This axon loss is initiated in the region in the back of the eye called the optic nerve head (ONH), where the retinal ganglion cell axons converge and exit the eye through a collagenous structure called the lamina cribrosa (Figure 1). An elevated intraocular pressure (IOP) of 21 mmHg or higher is considered as a high risk for glaucoma [2], but patients vary in their sensitivities to the elevated IOP. The mechanisms of the neural tissue loss and the origin of the differences in sensitivity to IOP remain unclear, in part because of the challenges in imaging the ONH *in vivo* and in extracting from these images information on the effects of IOP [3]. These challenges and current efforts to overcome them are discussed in detail in two recent review manuscripts [3], [4]. Our group has recently started imaging rhesus macaque *in vivo* utilizing optical coherence tomography

(OCT), a noninvasive imaging modality that provides real time, 3-D, and high resolution images of the ONH region. We aim to quantify in these images the pressure-induced displacements and deformations of the neural tissue (at the inner limiting membrane-ILM), the Bruch membrane (BM), the scleral canal opening (measured at the Bruch membrane opening-BMO), and the anterior lamina cribrosa (ALC), which are commonly studied structures of the ONH (**Figure 1**) [5]. However, there are a number of challenges in extracting information from the OCT images. First is the ability to compare multiple ONH structures under a given pressure condition or one structure across multiple pressures conditions. Second is the difficulty in acquiring quantitative results to describe these ONH deformations [4]. The purpose of this work was to develop an easy to use set of Matlab tools to resolve these issues and to provide meaningful data of ONH deformation under changing pressures. The program was evaluated by comparing measured outcome parameters from a set of monkey data to the literature.

2. Methods

ONH regions of one monkey eye were imaged *in vivo* with OCT while controlling for IOP, following methods described elsewhere [6]. Motion artifacts due to breathing and heart rate, identified as a periodic pattern in

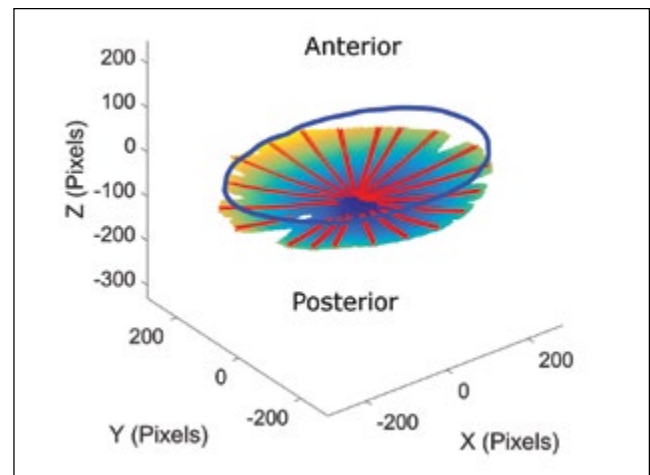


Figure 2: ALC surface reconstructed using the radial markings (red). Blue denotes the outline of the BMO plane used as reference. The surface color represents a heat map of the surface depth.

the known smooth structure of the BM on the slow-scan direction, were removed by translating images in anterior-posterior direction. Manual markings were made on radially resliced images [7] and were reconstructed, using scattered data interpolation, into 3-D surfaces by custom Matlab tools that were previously developed in the laboratory (**Figure 2**). When reconstructing a surface,

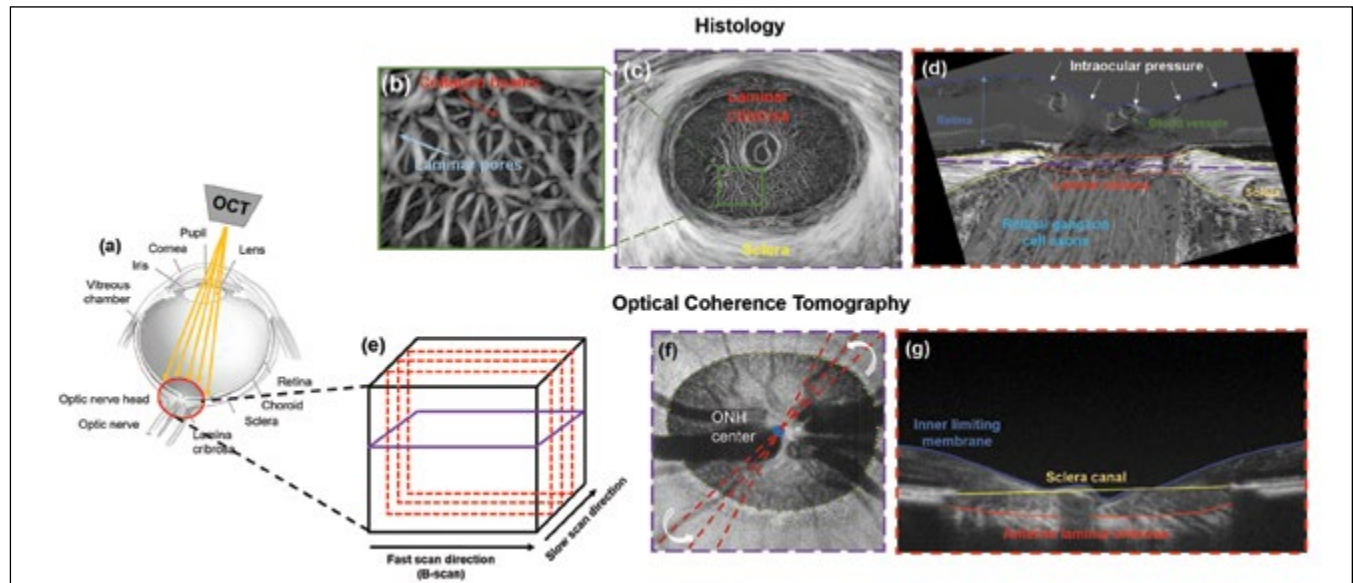


Figure 1: (a) Diagram of the eye, showing the ONH in the back of the eye, which is imaged non-invasively and in 3D with OCT. Top row: (b and c) Coronal sections through the LC shows the microstructures of collagenous beams and pores. (d) An example sagittal histological ONH section. Bottom row: (e) Schematic of a 3D OCT volume of the posterior pole, showing the fast scan direction and the slow scan direction, which may be affected by motion artifacts. (f) Motion artifacts in the slow scan direction are removed, before the volume is resliced radially to obtain virtual radial resliced images for delineations. Shown is a coronal digital section through the OCT volume. (g) Virtual radial resliced image. Colored lines are examples of manual markings

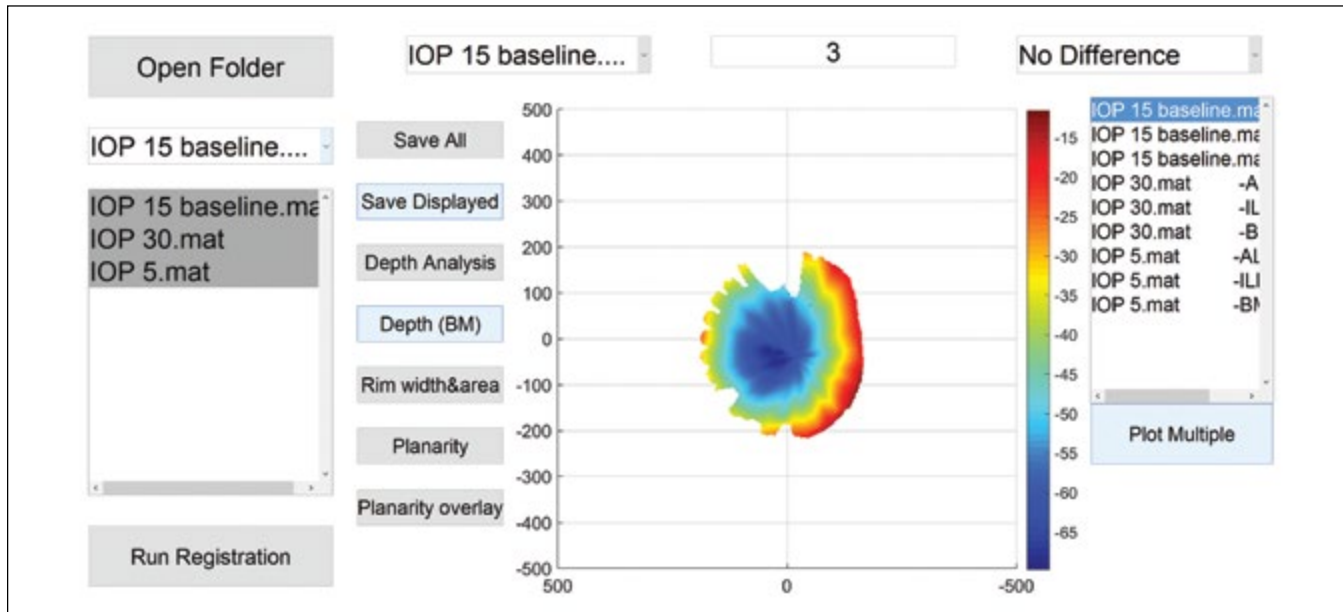


Figure 3: Graphical user interface of the program. Showed in the graphic window was the anterior-posterior view of a ALC surface, colored by the heatmap of the depth.

the program computed a confidence map to determine regions where the interpolated surface was reliable. The program reconstructed and visualized the ALC, BM, and ILM surfaces based on their depth with respect to the best-fit plane of the BMO markings, also known as the BMO plane. The BMO plane was selected because it is a commonly used reference plane in the literature [5], [8], simplifying comparisons. Experimental methods and animal care procedures adhered to the Association for Research in Vision and Ophthalmology (ARVO) Statement for the Use of Animals in Ophthalmic and Vision Research, and were approved by the local Institutional Animal Care and Use Committee (IACUC).

2.1 Surface Depth- ALC, BM, ILM

To analyze the displacement of a surface, the program calculated the mean, median, and standard deviation of its depth. Surfaces across different IOPs were registered using BMO and only differences within overlapping regions were compared as a measure of displacement. However, it is possible that two surfaces with similar mean and median will differ significantly in shape. Thus, to better represent the surface, our program was designed to output the depth distribution curves, using Matlab “histcounts” function, and box plots. The distribution curves provide a general view of how a surface deformed and the box plots simplify discerning quantitatively the amount of displacement. We define the sign of the depth

by the relative position with respect to the BMO plane, with anterior to the BMO as positive direction and vice versa. In the surface depth computation, the program used the confidence map to ensure that only reliable regions present in all images were compared to avoid bias. The threshold to define that a region was reliable was determined empirically by identifying the value that maximized surface continuity while avoiding bridging gaps in regions that were not visible.

2.2 BMO Planarity

BMO planarity is a measure of the extent to which the scleral canal, measured at BMO, deviated from a plane. The BMO planarity function applied principal component analysis to the BMO marking to find the best-fit plane and its normal vector, thus allowing calculation of the projection error: the perpendicular distances from the BMO points to the fitted plane. The function generated a plot that visualized the BMOs and the projection, also outputting the normal vector of the plane and the mean of the distances, namely, the BMO planarity. Since several measures are taken with respect to the best-fit BMO plane, it was important to test how well this plane fits the BMO. Small deviations from a plane (small planarities) indicate that the BMO plane is a good representation of the BMO location. Conversely, large deviations (large planarities) suggest that measurements with respect to this plane should be interpreted with caution.

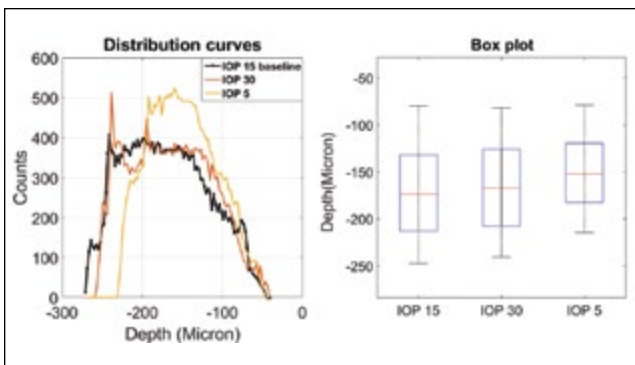


Figure 4: Depth distribution curves (left) and box plot (right) of ALC depth.

2.3 Rim Width and Area

A decrease in the neuroretinal rim tissue thickness has been shown to be an indicator of glaucoma progression [8], and is therefore an important parameter to determine from our images. The 2-D minimum rim width (MRW) segments were first measured in each radial slice as the shortest distance from the BMO to the ILM surface. These were then used to compute the minimum rim area (MRA) by the triangulation of the end points of the MRW segments.

2.4 Application and Evaluation

All the functions were incorporated into a graphical user interface (**Figure 3**) and were tested on a set of monkey eye data from three OCT images under baseline (15 mmHg [9]), low (5 mmHg), and high (30 mmHg) IOP, respectively. The baseline results were compared with the literature data also at baseline.

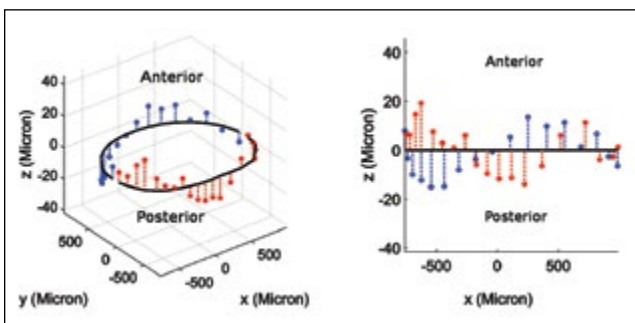


Figure 5: (left) 3D view and (right) side view of the BMO planarity under baseline condition. BMO markings (nasal-temporal side: red-blue dots) were plotted with respect to the outline of the BMO plane (black lines). The z axis was normal to the BMO plane and was stretched 20 times for illustration.

Table 1: ONH parameters of the three test cases and baseline values reported in other studies

Condition	Mean ALC depth (μm)	BMO Planarity (μm)	Minimum rim width (μm)	Minimum rim area (mm ²)
Low IOP (5 mmHg)	-150.0	7.12	195.5	0.987
High IOP (30 mmHg)	-165.8	9.98	187.2	0.938
Baseline (15 mmHg)	-171.0	7.80	192.5	0.941
Baseline in literature	~ -175 [8]	~7 [5]	~300 [8]	1.00±0.19 [10]

3. Results

3.1 ALC Surface Depth

Distribution of the ALC surface depths in the test cases is presented in **Figure 4**. Under 5 mmHg IOP, the ALC depth distribution curve shifted anteriorly, with the median depth decreasing by 12.5% from -174 μm to -152 μm. Under 30 mmHg IOP, the ALC median depth decreased by 4%, from -174 μm to -167 μm. Although the median depth decreased slightly under high IOP, the distribution curve remained close to the baseline case, while under low IOP the curve shifted noticeably as a whole to the anterior.

3.2 BMO Planarity

The BMO planarity is illustrated in **Figure 5** using the case with baseline IOP as an example. The BMOs under three IOP conditions were plotted with respect to the baseline BMO plane in **Figure 6**. BMO planarity was 7.8 μm under baseline condition. Planarity increased by 28% to 9.98 μm at 30 mmHg IOP and decreased by 9.8% to 7.12 μm at 5 mmHg IOP (**Table 1**). Our test

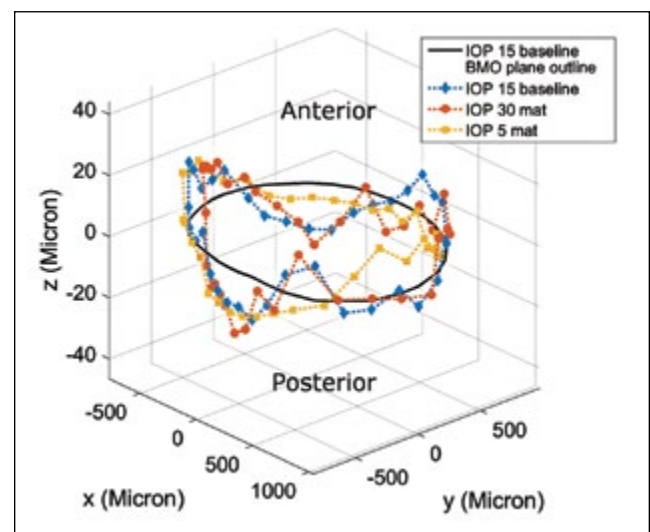


Figure 6: BMO of the three cases. Black is the BMO plane outline under baseline condition. Blue is the baseline, Red is under high IOP, Orange is under low IOP. Note that the Z axis was stretched by 20 times for the purpose of illustration.

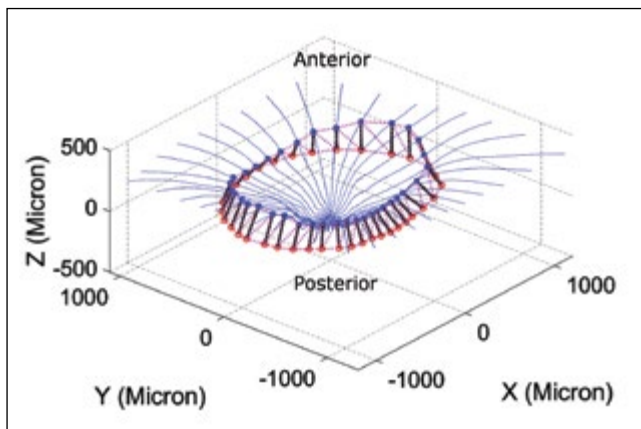


Figure 7: Example minimum rim width and minimum rim area. Figure showing minimum rim width (black) and area (magenta), plotted with BMO markings (red) and ILM surface (blue).

cases showed that increasing IOP led to increased BMO planarity whereas low IOP led to decreased planarity, indicating flattening of the scleral canal opening under low IOP and vice versa.

3.3 Rim Width and Area

Both MRW and MRA (**Figure 7**) decreased with increasing IOP, and increased with decreasing IOP (**Table 1**), reflecting a reduction of the neural tissue thickness under elevated IOP. In this data set, the baseline MRW was 192.5 μm , which decreased by 2.8% to 187.2 μm under high IOP and increased by 1.5% percent to 195.5 μm under low IOP. The MRA was 0.941 mm^2 under the baseline condition, which decreased by 0.3% to 0.938 mm^2 under high IOP and increased by 4.9% to 0.987 mm^2 under low IOP. The percent change in the MRA and MRW were smaller than changes in other ONH measurements.

3.4 Evaluation

All four parameters computed by the program for the three test cases were compared with results from three previous studies in **Table 1** [5], [8], [10]. Compared to the literature, the mean ALC depth, the BMO planarity, the MRW and MRA were 2.3%, 11.4%, 35.8% and 5.9% different, respectively. Although, the MRW computed in the test case showed a 35.8% deviation from the previous study, all other results were comparable with literature, showing less than 15% deviation.

4. Discussion

Our program allows 3-D quantitative analysis of *in vivo* OCT images of the monkey ONH. The user-friendly design enables the extraction of important biomechanical information from *in vivo* images efficiently through an integrated interface, with several useful functions requiring no more than a single click. The program was tested with a set of experimental data obtained under three IOP conditions.

The ALC depth distribution curve reflected the anterior shift of the ALC surface under low IOP. Also, our results indicated that the BMO planarity increased under high IOP and decreased under low IOP, suggesting a deformation of the scleral canal under elevated IOP. The change in the MRW and MRA were relatively small, however both measures increased from baseline under low IOP and decreased with high IOP, indicating that thickness of the neuroretinal rim tissue increases as IOP decreases, and vice versa

Compared with previous studies, we observed a deviation under 15% for the ALC depth, BMO planarity and MRA. We did find a deviation of 35.8% from literature values for the MRW. The reference literature value for the BMO planarity was obtained from human subjects, whereas all the other measurements were obtained from monkeys. This might contribute to explain the difference in BMO planarity, although human and monkey are often regarded to have similar ONH structures and biomechanics [11]. Also, our images were acquired while the animals were under controlled intracranial pressure. The literature with which we compared values provided no information on intracranial pressure. Several recent studies, including some from our group, have demonstrated that variations in intracranial pressure can affect the ONH [6], [12].

While being a powerful computational tool, our Matlab program still has room for improvements. First, while this work presented comparison between our results and literatures, more rigorous validation will be included in future work. Also, we would like to improve robustness to incomplete data, such as when the structures cannot be discerned because of OCT signal shadowing behind blood vessels. Furthermore, future work will involve adding new functionalities to the program, such as analyzing the regional depth and computing shape indexes of the surfaces, allowing the extraction of more valuable information from the OCT images.

5. Conclusion

Our work has produced a set of tools integrated into a Matlab program. The tools compute and visualize several parameters, namely the ALC, BM, ILM surface depth, the BMO planarity, the MRW and MRA, which are important for characterizing the morphology and mechanics of the ONH structures in response to IOP changes. The analyses can be executed easily with a single click on the graphical user interface. The program developed in this work was tested with a set of *in vivo* monkey data, and showed results comparable to the literature. It is ready to be employed in research of the ONH biomechanics and has the potential to be applied to other studies that require similar 3-D surface data analysis.

6. Acknowledgments

The project was funded jointly by the National Institutes of Health (R01 EY023966, EY025011, EY013178, T32 EY017271 and P30 EY008098), Glaucoma Research Foundation Shaffer Grant, the Swanson School of Engineering, and the Office of the Provost.

7. References

- [1] I. C. Campbell, B. Coudrillier, and C. R. Ethier, "Biomechanics of the posterior eye: A critical role in health and disease," *J. Biomech. Eng.*, vol. 136, no. February, Dec. 2013.
- [2] A. Sommer, M. JTielisch, and J. Katz, "Relationship between intraocular pressure and primary open angle glaucoma among white and black americans: The baltimore eye survey," *Arch. Ophthalmol.*, vol. 109, no. 8, pp. 1090–1095, Aug. 1991.
- [3] I. A. Sigal, B. Wang, N. G. Strouthidis, T. Akagi, and M. J. A. Girard, "Recent advances in OCT imaging of the lamina cribrosa," *Br. J. Ophthalmol.*, vol. 98 Suppl 2, no. Suppl 2, p. ii34-9, Jul. 2014.
- [4] M. J. a Girard, W. J. Dupps, M. Baskaran, G. Scarcelli, S. H. Yun, H. a Quigley, I. a Sigal, and N. G. Strouthidis, "Translating Ocular Biomechanics into Clinical Practice: Current State and Future Prospects," *Curr. Eye Res.*, vol. 40, no. April, pp. 1–18, 2014.
- [5] S. Lee, S. X. Han, M. Young, M. F. Beg, M. V. Sarunic, and P. J. Mackenzie, "Optic Nerve Head and Peripapillary Morphometrics in Myopic Glaucoma," *Investig. Ophthalmology Vis. Sci.*, vol. 55, no. 7, p. 4378, Jul. 2014.
- [6] H. Tran, A. P. Voorhees, B. Wang, N.-J. Jan, E. Tyler-Kabara, L. Kagemann, H. Ishikawa, J. S. Schuman, M. A. Smith, G. Wollstein, and I. A. Sigal, "*In vivo* Modulation of Intraocular and Intracranial Pressures Causes Nonlinear and Non-monotonic Deformations of The Lamina Cribrosa," *Assoc. Res. Vis. Ophthalmol.*, 2016.
- [7] W. Jacob, H. Tran, T. Jeremy, A. Voorhees, J. Ten Eyck, D. Tsui, J. R. Drobitch, Y. Shi, W. Walters, B. Wang, M. A. Smith, E. Tyler-Kabara, J. S. Schuman, G. Wollstein, and I. A. Sigal, "Improving 3D Quantification of In-Vivo Monkey Optic Nerve Head Deformations Using Radial Methods on Optical Coherence Tomography Images," *Univ. Pittsburgh-Science 2015*, 2015.
- [8] N. G. Strouthidis, B. Fortune, H. Yang, I. a Sigal, and C. F. Burgoyne, "Longitudinal change detected by spectral domain optical coherence tomography in the optic nerve head and peripapillary retina in experimental glaucoma," *Invest. Ophthalmol. Vis. Sci.*, vol. 52, no. 3, pp. 1206–19, Mar. 2011.
- [9] Y. Suzuki, A. Iwase, M. Araie, T. Yamamoto, H. Abe, S. Shirato, Y. Kuwayama, H. K. Mishima, H. Shimizu, G. Tomita, Y. Inoue, and Y. Kitazawa, "Risk Factors for Open-Angle Glaucoma in a Japanese Population: The Tajimi Study," *Ophthalmology*, vol. 113, no. 9, pp. 1613–1617, 2006.
- [10] B. Fortune, J. Reynaud, C. Hardin, L. Wang, I. A. Sigal, and C. F. Burgoyne, "Experimental Glaucoma Causes Optic Nerve Head Neural Rim Tissue Compression: A Potentially Important Mechanism of Axon Injury," *Investig. Ophthalmology Vis. Sci.*, vol. 57, no. 10, p. 4403, Aug. 2016.
- [11] H. Levkovitch-Verbin, "Animal models of optic nerve diseases," *Eye*, vol. 18, no. 11, pp. 1066–1074, Nov. 2004.
- [12] W. H. Morgan, B. C. Chauhan, D.-Y. Yu, S. J. Cringle, V. a Alder, and P. H. House, "Optic disc movement with variations in intraocular and cerebrospinal fluid pressure.,," *Invest. Ophthalmol. Vis. Sci.*, vol. 43, no. 10, pp. 3236–42, Oct. 2002.

Notes



PITT

University of Pittsburgh
Swanson School of Engineering
151 Benedum Hall
Pittsburgh, PA 15261
412-624-9800
engineering.pitt.edu

NONPROFIT ORG.
U.S. POSTAGE
PAID
PITTSBURGH, PA
PERMIT NO. 511

